

# X-Rays From Galactic Black Holes

## Theory and Observation

Dissertation  
zur Erlangung des Grades eines  
Doktors der Naturwissenschaften  
der Fakultät für Physik  
der Eberhard-Karls-Universität Tübingen

vorgelegt von

Jörn Wilms

aus Tübingen  
1998

Selbstverlegt von:	J. Wilms, Linsenbergr. 33, 72074 Tübingen
Tag der mündlichen Prüfung:	21. April 1998
Dekan:	Prof. Dr. D. Kern
1. Berichterstatter:	Prof. Dr. R. Staubert
2. Berichterstatter:	Prof. Dr. M.C. Begelman

## Erweiterte deutsche Zusammenfassung

Wilms, Jörn

### X-rays from Galactic Black Holes: Theory and Observation

In dieser Dissertation beschäftige ich mich mit den theoretischen Grundlagen der Erzeugung von Röntgen- und Gammastrahlung in dem heißen Plasma nahe eines Schwarzen Lochs und mit dem Vergleich dieser theoretischen Ergebnisse mit modernen Breitbandmessungen der Spektren galaktischer Schwarzkandidaten.

Kapitel 1 führt in die Grundlagen der Astrophysik stellarer Schwarzer Löcher ein. Insbesondere werden die Ergebnisse neuerer Massenbestimmungen referiert, aus denen die Existenz quasi-punktförmiger Objekte mit Massen oberhalb von 5 Sonnenmassen in unserer Milchstraße eindeutig hervorgeht. Da diese Masse oberhalb der maximalen Masse für Neutronensterne liegt, kann nach meiner Ansicht von der Existenz Schwarzer Löcher auch in unserer Milchstraße ausgegangen werden. Die Beobachtung stark verbreiteter Eisen-Fluoreszenzlinien in den Röntgenspektren Aktiver Galaxien ist ebenfalls nur durch die Existenz Schwarzer Löcher erklärbar, die bei Aktiven Galaxien allerdings sehr massereich sind. Aus diesen Gründen soll im folgenden nur von „Schwarzen Löchern“, und nicht, wie im astronomischen Sprachgebrauch oft üblich, von „Schwarzkandidaten“ gesprochen werden.

An dieses einführende Kapitel schließt sich mit Kapitel 2 die Darstellung der Physik der Strahlungserzeugung in Akkretionsscheibenkoronen um galaktische Schwarze Löcher an. Die Röntgenspektren dieser Objekte sind Potenzgesetzspektren mit einem exponentiellen Abbruch bei Photonenenergien von ungefähr 150 keV. Der wahrscheinlichste physikalische Prozeß, der ein solches Spektrum erzeugt, ist die Comptonisierung weicher Strahlung in einem heißen Elektronenplasma, einer Akkretionsscheibenkorona. Diese entsteht wahrscheinlich als Folge hydrodynamischer Instabilitäten in einer Akkretionsscheibe. Unter Comptonisierung versteht man hierbei die Erzeugung harter Photonen durch inverse Comptonstöße in der heißen Elektronenwolke (Abschnitt 2.1.1). Dabei können Photonendichten entstehen, die so groß sind, daß Photon-Photon Paarbildungsprozesse eintreten können (Abschnitt 2.1.2). Unter Verwendung nichtlinearer Monte Carlo Methoden habe ich in Zusammenarbeit mit der Gruppe von Mitchell Begelman (JILA, University of Colorado) das Strahlungstransportproblem in solchen Akkretionsscheibenkoronen selbstkonsistent für verschiedene Geometrien des Akkretionsprozesses gelöst (siehe Anhang A für eine Beschreibung der dabei verwendeten numerischen Methoden). In Abschnitt 2.2 werden die sich aus diesen Rechnungen ergebenden Spektren, Temperaturprofile und anderen physikalischen Parameter dargestellt. Ergebnis ist, daß die früher allgemein angenommene Geometrie einer Akkretionsscheibenkorona, die sich „sandwichförmig“ an eine kalte, optisch dicke Akkretionsscheibe anschmiegt, die Spektren der galaktischen Schwarzen Löcher *nicht* erklären kann, da in dieser Geometrie die Kühlung der Korona durch die weiche Strahlung zu effizient ist (Abschnitt 2.2.2.3). Hingegen ist ein vereinfachtes Modell einer geometrisch dicken ku-

gelförmigen Korona, die sich an eine kalten Akkretionsscheibe anschließt, in der Lage, die beobachteten Parameter zu erklären (Abschnitt 2.2.3). Dieses Ergebnis wird durch neuere theoretische Arbeiten über mögliche „advektionsdominierte“ Akkretionsscheiben in galaktischen Schwarzen Löchern, wesentlich bestärkt. In Abschnitt 2.3 werden dann theoretische Modelle für die Vorhersage der zeitlichen Eigenschaften der Akkretionsscheibenkoronen beschrieben. Die Wechselwirkung zwischen kalter Akkretionsscheibe und heißer Korona führt hierbei zu charakteristischen Beziehungen zwischen den in verschiedenen Energiebändern meßbaren Lichtkurven, die ebenfalls zur Bestimmung der koronalen Parameter verwendet werden können.

Um genaue Parameter für die Koronen in Schwarzen Löchern zu erhalten, müssen die aus den theoretischen Rechnungen erhaltenen Spektren direkt mit Beobachtungsdaten verglichen werden. Hierzu sind simultane Beobachtungen dieser Objekte im Energiebereich von 1 bis 300 keV notwendig, die bis 1995 nur sehr schwierig zu erhalten waren. Seit Anfang 1996 steht dazu der amerikanische Röntgensatellit Rossi X-ray Timing Explorer (RXTE) zur Verfügung. In Kapitel 3 und 4 werden die experimentellen Methoden der Datenanalyse eingeführt und die auf RXTE befindlichen Instrumente beschrieben. Kapitel 5 ist der RXTE Beobachtung des galaktischen Schwarzen Loches Cygnus X-1 gewidmet. Hier zeigt sich, daß unsere Akkretionsscheibenmodelle tatsächlich das Röntgenspektrum beschreiben können. Die optische Tiefe der Korona beträgt hierbei  $\tau = 2.1 \pm 0.1$  und ihre mittlere Temperatur ist  $kT_e = 65.7 \pm 3.3$  keV. Ferner kann aus dem zeitlichen Verhalten der Quelle eine koronale Größe von  $R \lesssim 25 GM/c^2$  abgeleitet werden.

Das abschließende Kapitel 6 beschreibt die bislang längste Beobachtung der zwei hellsten Schwarzen Löcher in der Großen Magellanschen Wolke, LMC X-1 und LMC X-3. Die Spektren dieser Objekte sind wesentlich weicher als das von Cyg X-1 und können vermutlich durch Comptonisierung in einer wesentlich kälteren Korona erklärt werden, die in diesem Fall scheibenförmig ist. Diese Beobachtungen, bei denen wir jeweils (fast) kontinuierlich drei Tage die Quellen beobachten konnten, stellen die erste Detektion von LMC X-1 und LMC X-3 bei Energien oberhalb von 20 keV dar. Zusätzlich wurden noch monatliche Beobachtungen von LMC X-1 und LMC X-3 durchgeführt, die die Entwicklung der spektralen Parameter dieser Quellen über das ganze Jahr 1997 hinweg aufzeigen. Es stellt sich heraus, daß die Röntgenemission von LMC X-3 zeitlich stark variabel ist, was eventuell mit einer durch Strahlungsdruck verbogenen Scheibe erklärbar ist. Die mit der Helligkeitsvariation einhergehende ebenfalls beobachtete Variation der spektralen Parameter ist noch nicht verstanden. Dafür sind weitere, für 1998 geplante, Beobachtungen erforderlich.

## Abstract

Wilms, Jörn

### X-rays from Galactic Black Holes: Theory and Observation

The main subjects of this thesis are the theoretical foundations for the production of X-ray and gamma-ray radiation in a hot plasma close to a black hole and the comparison of the theoretical results with broad-band X-ray observations of the spectra of galactic black hole candidates.

Chapter 1 introduces black holes as astrophysical objects and describes the observational basis for the existence of compact objects with masses above 5 solar masses. Since this mass is above the maximum possible mass of neutron stars, the existence of black holes in our galaxy seems very probable.

After this introductory chapter, the physics of the production of high energy radiation in accretion disk coronae is discussed in detail (chapter 2). I introduce the microphysical processes that are important in coronae, i.e., Compton scattering, photon-photon pair production, and reflection of the hard radiation off colder material (§2.1). The radiative transfer problem for accretion disk coronae is then solved using a non-linear Monte Carlo code (§2.2). I conclude that the generally assumed geometry for the accretion disk corona, a cold accretion disk sandwiched between two hot coronae, is not able to explain the observed spectra. This is mainly due to the fact that the reprocessing of the hard radiation within the disk is too efficient so that the density of low energy photons within the corona is too large. The result is that the corona is very efficiently Compton cooled and cannot sustain the high temperatures needed for the production of the hard spectra (§2.2.2.3). On the other hand, the sphere+disk geometry, where a spherical corona sits on the inside of a cold accretion disk, is able to reproduce the observed spectral parameters (§2.2.3). The last section of the chapter describes theoretical models for the temporal behavior of radiation emerging from a Compton cloud (§2.3). In the case of the sphere+disk geometry, interesting effects caused by the reprocessing of hard radiation within the disk are described.

The second part of the thesis describes the application of the above physical models to observational data. Chapters 3 and 4 describe the observational methods and the instrumentation needed for this task. After this interlude, Chapter 5 describes the results from an observation of the galactic black hole Cygnus X-1 using the Rossi X-ray Timing Explorer. The analysis of these data shows that the thermal accretion disk models are indeed able to describe the X-ray spectrum from 2 to 150 keV. The optical depth of the spherical corona is  $\tau = 2.1 \pm 0.1$  and the average coronal temperature is  $kT_e = 65.7 \pm 3.3$  keV. From the temporal behavior of the source it is possible to put constraints on the size of the Compton corona, which is less than a few  $10GM/c^2$ .

The final chapter 6 describes first results of the longest observation of the two bright black holes in the Large Magellanic Cloud (LMC), LMC X-1 and LMC X-3. The spectra of these objects are softer than those of Cyg X-1, which might be a result of the Comp-

tonizing medium being a “normal” slab-like corona. These observations represent the first detection of these objects at energies above 20 keV. Apart from the results of the long observations I also discuss first results from a monitoring campaign on the LMC performed in 1997. The X-ray emission of LMC X-3 is strongly variable on a time-scale of 200 d. The cause for this emission is not understood yet and further observations are planned for 1998.

The thesis concludes with an outlook on future work planned (chapter 7).

# Contents

---

<b>1</b>	<b>Black Holes in Astronomy</b>	<b>10</b>
1.1	Black Holes as General Relativistic Objects . . . . .	10
1.2	Observational Evidence for Black Holes . . . . .	13
1.3	Black Holes as Astronomical Objects . . . . .	15
1.4	This thesis . . . . .	17
<b>I</b>	<b>Theory</b>	<b>19</b>
<b>2</b>	<b>Radiation Processes Around Black Holes</b>	<b>19</b>
2.1	Physical Processes in ADCs . . . . .	22
2.1.1	Comptonization . . . . .	23
2.1.2	Pair Production and Annihilation . . . . .	28
2.1.3	Reflection . . . . .	31
2.2	Accretion Disk Coronae . . . . .	34
2.2.1	Previous Models for ADCs . . . . .	35
2.2.2	Slab-Corona Models . . . . .	38
2.2.3	The Sphere+Disk Geometry . . . . .	50
2.3	Temporal Signatures of Accretion Disk Coronae . . . . .	60
2.3.1	Compton Shots in the Spherical Geometry . . . . .	61
2.3.2	Compton Shots in the Sphere+Disk Geometry . . . . .	67
<b>II</b>	<b>Observations</b>	<b>73</b>
<b>3</b>	<b>Observational Methods</b>	<b>73</b>
3.1	Spectral Analysis . . . . .	74
3.2	Temporal Analysis . . . . .	77
3.2.1	Timing Analysis with Fourier Techniques . . . . .	77
3.2.2	Coherence and Time Lags . . . . .	82
3.2.3	Stochastic Methods . . . . .	83

<b>4</b>	<b>RXTE</b>	<b>85</b>
4.1	RXTE-PCA . . . . .	87
4.1.1	Introduction . . . . .	87
4.1.2	The PCA Response Matrix . . . . .	89
4.1.3	The PCA Background . . . . .	93
4.2	RXTE-HEXTE . . . . .	95
4.2.1	Introduction . . . . .	95
4.2.2	The HEXTE Background . . . . .	97
4.2.3	The HEXTE Response Matrix . . . . .	98
4.3	RXTE-ASM . . . . .	99
4.4	Summary: Data Extraction for RXTE . . . . .	101
<b>5</b>	<b>Observations of a Hard State Black Hole: Cyg X-1</b>	<b>103</b>
5.1	Cygnus X-1 . . . . .	103
5.2	The Hard State Spectrum of Cygnus X-1 . . . . .	105
5.3	RXTE Observation of Cygnus X-1 . . . . .	110
5.3.1	Observations and Data Analysis . . . . .	111
5.3.2	Spectral Analysis . . . . .	111
5.3.3	Accretion Disk Corona models . . . . .	117
5.4	Discussion and Conclusions . . . . .	120
5.5	Temporal Constraints on ADC Models . . . . .	122
<b>6</b>	<b>RXTE Observations of Soft State Black Holes: LMC X-1 and LMC X-3</b>	<b>127</b>
6.1	Introduction: The Monitoring Campaign . . . . .	127
6.2	LMC X-3 . . . . .	127
6.2.1	Introduction . . . . .	127
6.2.2	The Long Observation . . . . .	129
6.2.3	The Spectral Evolution of LMC X-3 . . . . .	133
6.3	LMC X-1 . . . . .	137
6.3.1	The Long Observation . . . . .	139
6.3.2	No Spectral Evolution in LMC X-1 . . . . .	140
<b>7</b>	<b>Summary and Future Work</b>	<b>143</b>
	<b>Bibliography</b>	<b>146</b>
<b>A</b>	<b>Numerical Methods</b>	<b>152</b>
A.1	Linear Monte Carlo Codes . . . . .	152
A.2	Non-Linear Monte Carlo Codes . . . . .	154
A.2.1	Introduction . . . . .	154
A.2.2	Thermal Pools . . . . .	156
A.2.3	Statistical Fluctuations . . . . .	156
A.2.4	Generation of Models . . . . .	157



<b>B Interpolation of Gridded Spectra</b>	<b>159</b>
B.1 Introduction . . . . .	159
B.2 Finite Element Interpolation Using Delaunay Triangularization . . . . .	159
<b>C Properties of the generalized Gamma- and Weibull-Distributions</b>	<b>162</b>
C.1 The Generalized Gamma Distribution . . . . .	162
C.2 The Weibull Distribution . . . . .	163
List of Abbreviations	165
Acknowledgements	167
Lebenslauf	168

## CHAPTER 1

---

### **Black Holes in Astronomy**

Black holes are without doubt some of the most popular astronomical objects. Popular or semi popular books on black holes, like those from Greenstein (1983), Novikov (1990), Gribbin & Rees (1990), Thorne (1994), Begelman & Rees (1996), and especially the popular books by Stephen Hawking (1988) are among the best selling astronomy and even among the best selling science books on the market. Like no other object class they shape the public perception of astronomy, and, therefore, also determine to a certain extent where the tax-payers' money ends up within the broad field of physics.

Because of the strange physics around black holes, they fascinate not only the general public, but also observational astronomers and theoretical physicists alike. Observationally, black holes seem to exist everywhere. They are almost normal members of stellar systems, in the form of “microquasars” they produce small jets, they have been observed as members of binary systems in the companions of our galaxy, and they might harbor in the center of our galaxy and those of other normal galaxies as well as “monsters” in the centers of Active Galactic Nuclei (AGN). They are made responsible for the production of jets in radio galaxies, and they have, at least for a while, been discussed as the sources of the strange gamma ray bursts. However, although black holes have been assumed to be responsible for many of the phenomena observed in high energy astrophysics, astronomers still speak about all these objects as Black Hole Candidates (BHCs).

This thesis is devoted to the study of the three most prominent galactic BHCs, and therefore a more detailed discussion seems to be in order of what makes a black hole candidate a Black Hole (BH) and what are the observational indications for their existence. In this chapter I will try to give such an overview. Most of the more fundamental physics will only be referenced here and will be derived later, if necessary for the rest of this thesis. In section 1.1 an overview of BH properties from the viewpoint of the general theory of relativity will be given, section 1.2 gives a summary of the physical processes that might be used to discern BHs from other astronomical objects, and section 1.3 gives an overview over the realm of BHs as members of the astronomical community of objects. The chapter concludes with a description of the structure of this thesis (§1.4).

#### *1.1 Black Holes as General Relativistic Objects*

As singularities of space-time, BHs are a direct consequence of the general theory of relativity (GRT) and thus any work on BH observations should at least contain a brief summary on the properties of BHs as seen from the view-point of general relativity.

BHs are a wonderful laboratory for the study of fundamental physical questions, but here I will only be concerned with the properties that might in principle be observable in nature.

A black hole is defined as a body whose mass is so large that its escape velocity is larger than the speed of light. This concept in fact predates the GRT, going back to the English reverend John Michell and the French scientist Pierre Simon Laplace, who independently computed the mass of such a body under the assumption that it was of solar density (Michell 1784; Laplace 1796, 1799). It is doubtful that these early workers really took their ideas more seriously than a pure mind game. Before more work could be done on these strange objects, a better theory of gravitation was needed. This was provided by Einstein's publication of his GRT (Einstein 1916). Briefly after the publication, Karl Schwarzschild, then at the Russian front, obtained the solution for the simplest type of a BH, which is entirely defined by its mass (Schwarzschild 1916). At that time it was unclear, however, how these objects could be physically created since the theory of stellar evolution was still very preliminary. The pioneering work by Subramanian Chandrasekhar (1931a), on white dwarfs, and by Chandrasekhar (1931b) and Baade & Zwicky (1934), on neutron stars, led astronomers to the belief that compact objects might be produced as the end phases of stellar evolution. Oppenheimer and Volkov showed in 1939 that also neutron stars have a maximum mass. Given that stellar evolution can lead to remnants with a mass larger than the Oppenheimer-Volkov mass, the existence of BHs seemed unavoidable. Still, for a while BHs stayed purely in the realm of theoretical physics, studied only by a small number of people like John Archibald Wheeler, who coined the word "black hole" in a popular article (Wheeler 1968). It took more than 20 years before the discovery of active galactic nuclei and of Cygnus X-1 led to the conclusion that black holes might indeed be part of the zoo of cosmic objects. Since 1970, black holes have been studied intensively, from both, theoretical and observational viewpoints. Recent summaries of this field of research are given in the book edited by Hehl, Kiefer & Metzler (1998), in the review by Novikov (1995), and, in more popular form, by the literature given at the beginning of this chapter. Here, only the most important properties of BHs will be referenced.

The most simple geometry for a BH is the Schwarzschild geometry (Schutz 1985), which is the geometry of the vacuum spacetime outside a spherical mass configuration (or a point mass if the metric around a black hole is considered). In the usual units of GRT, where  $G = c = 1$ , the Schwarzschild geometry is defined by the line element

$$ds^2 = - \left(1 - \frac{2M}{r}\right) dt^2 + \left(1 - \frac{2M}{r}\right)^{-1} dr^2 + r^2 d\Omega \quad (1.1)$$

A theorem due to Birkhoff states that in the limit  $t \rightarrow \infty$  the Schwarzschild geometry is the only spherically symmetric, asymptotically flat solution of the Einstein field equations.

The Schwarzschild geometry has a singularity at the Schwarzschild radius

$$R_s = 2M = \frac{2GM}{c^2} = 3 \text{ km} \left( \frac{M}{M_\odot} \right) \quad (1.2)$$

The metric describes the space only outside  $R_s$ . This is sufficient for doing astronomy, since it can be shown that no particle can cross from  $r < R_s$  to  $r > R_s$ . Hence, the Schwarzschild radius defines the radius of the event horizon, the radius of the BH. The singularity on the event horizon is not a true singularity, however, and there exist other coordinate systems that can be used if the behavior of a physical system inside or crossing the horizon is to be studied (see Misner, Thorne & Wheeler 1973 for a discussion).

The orbits of particles in the Schwarzschild geometry can be determined analogous to classical mechanics (see, e.g., Schutz 1985). From invariance arguments, the energy (invariance of the metric with respect to time) and angular momentum (invariance with respect to rotations) of a point-mass can be obtained. It is then possible to show that particles with mass  $m$  move around a BH in an effective potential given by

$$V^2(r) = \left( 1 - \frac{2M}{r} \right) \left( 1 + \frac{L^2}{r^2} \right) \quad (1.3)$$

(Schutz 1985, eq. 11.10) where  $L$  is the angular momentum of the particle. Equating  $V$  to the energy of the particle results in the equation of motion. Depending on the value of  $L$ , the effective potential is either periodic, i.e., the particle will move forever on (complicated) periodic orbits around the central mass, or the potential is non-periodic and the particle will eventually fall into the BH. This latter case occurs for  $L^2 \leq 12M^2$ , corresponding to a minimum possible radius of

$$r = 6M = \frac{6GM}{c^2} = 3R_s \quad (1.4)$$

This is the radius of the marginally stable orbit, which is important in the theory of thin accretion disks which cannot extend closer to the BH than this radius.

The Schwarzschild metric is valid outside all spherical non-rotating mass concentrations. In other words, it is also the correct metric around our sun (neglecting its small angular momentum) or around a neutron star (NS). In these two cases, the predictions of general relativity have been extensively studied: the precession of Mercury's perihelion is exactly as that predicted by GRT celestial mechanics, and the motions observed in the binary pulsar PSR 1513+16 are also exactly as predicted by the equations of motions derivable using the formalism outlined above. These two observations provide good tests for the validity of general relativity and show that the GRT is, for now, the best theory available (see Will 1993 for an extensive discussion of other tests of the GRT). Since the Schwarzschild metric has thus been directly observed in nature and since BHs are just a natural extension of these observations to even higher masses, the existence of BHs seems unavoidable.

More extensive theoretical studies show that the GRT allows more complicated singularities than that of a Schwarzschild BH. It can be shown that BHs can also have

an angular momentum, a charge, and, if magnetic monopoles exist, also a magnetic monopole charge. It is hard to imagine that electrically or magnetically charged astronomical objects really exist, since the electromagnetic force is so much stronger than the gravitational force, leading to the neutralization of any astronomical body, but the existence of rotating (Kerr) BHs might be a possibility.

## 1.2 Observational Evidence for Black Holes

What black holes do exist and how can they be detected? The *only* safe way to determine whether an astronomical object is a BH is the presence of a large amount of mass in a very small volume. Thus, the detection of a compact object whose mass is above the maximum possible mass for a NS, i.e., less than about  $2.9 M_{\odot}$  (Kalogera & Baym 1996), can be considered unequivocal evidence for this object to be a black hole. Since the compact object is invisible in the optical, the binary is a spectroscopic binary and the mass has to be inferred from the measurement of the radial velocity  $v_1$  of the optical companion and from the orbital period  $P$ , using the mass function

$$f(M_*, M_X, i) = \frac{(M_X \sin i)^3}{(M_* + M_X)^2} = \frac{Pv_1^3}{2\pi G} \quad (1.5)$$

where  $M_*$  is the mass of the optical companion,  $M_X$  is the mass of the compact object, and  $i$  is the inclination of the orbit. Note that the mass function gives a lower limit to  $M_2$  so that the compact object can definitively be considered a BH if  $f > 2.9 M_{\odot}$ . If this is not the case, then the inclination of the system and/or the mass of the optical star have to be determined by using standard spectral analysis techniques and optical polarimetry. If the BH is the member of a High Mass X-ray Binary (HMXB), where the optical companion is an O- or B-star, the resulting uncertainty for  $M_*$  can be large (for example, in the case of the HMXB Cyg X-1, different mass estimates range from  $\sim 15 M_{\odot}$  to  $\sim 36 M_{\odot}$  for the optical companion HDE 226868; Gies & Bolton 1986; Herrero et al. 1995), while the determination of the inclination is very difficult in all cases.

Unfortunately, for many X-ray Binary (XRB) systems the mass determination is difficult or impossible. Since the spectral resolution of the currently available X-ray astronomy satellites is too small for the convincing determination of the radial velocity, the measurement of the mass function is only possible when the optical counterpart is known. This knowledge of the optical counterpart is not always available. For example, in the case of LMC X-1 several good candidates for an optical counterpart have been discussed in the past fifteen years and only recently the optical counterpart could be convincingly decided on (Cowley et al. 1995). Thus, many methods have been proposed to “uniquely” identify a BH as a BH from the X-ray measurements alone, but exceptions to almost all of them have more or less rapidly been found due to the similarity of NS accretion and BH accretion (the radius of a NS is just a few Schwarzschild radii). Apart from the dynamical measurements, it appears that there exists no unique method for

identifying black holes (van der Klis 1994; Tanaka & Lewin 1995).

For a long time, X-ray color-color diagrams were thought to be good tools for the characterization of XRBs (White & Marshall 1984; Schulz, Hasinger & Trümper 1989). In analogy to optical color-color diagrams, broad-band X-ray colors (“hardness ratios”) of objects of known type are compared in such a diagram and regions are identified which uniquely identify the class. It turned out, however, that such unique regions do not seem to exist and that NS XRBs and black hole XRBs can have similar broad-band spectral characteristics. For BHs in their soft (high) state, which is characterized by a black-body spectrum plus a very steep power-law, a large number of NS XRBs are known with similar spectra. The same is true for the hard (low) state, the classical example for which is the canonical BH Cyg X-1. As I will discuss in detail in chapter 5, the spectrum of Cyg X-1 is roughly characterized by a power-law with a photon index of  $\Gamma = 1.7$  and an exponential turnover at around 150 keV, which is interpreted as being due to Comptonization in a hot electron gas close to the BH (Sunyaev & Trümper 1979). For a long time, Cyg X-1 was the only BH known with (almost) 100% certainty, and thus people were led to believe that all objects with hard spectra similar to Cyg X-1 might be BHs. However, the discovery of NS Low Mass X-ray Binary (LMXB) systems with hard spectra extending to energies above 200 keV has severely reduced the faith into this assumption (Barret et al. 1991), although more complicated broad-band approaches have been proposed (Barret, McClintock & Grindlay 1996). Finally, the rapid short term variability observed for a long time only in Cyg X-1 has been used as an indicator for the existence of BHs. Again, similar behavior has been discovered in NS XRBs such as Cir X-1 (van der Klis 1994). It remains to be seen whether the values of  $r_{\text{in}} \sin i$  obtained from modeling the observed spectra with the multicolor disk black-body model of (Mitsuda et al. 1984) can be used to detect BHs. In this model,  $r_{\text{in}} \sin i \lesssim 10$  km is seen to be typical for NS XRB, while BHs are found to have typical values larger than  $\sim 20$  km (Tanaka & Lewin 1995), however, further tests are needed to convincingly determine the power of this approach. The same is true for recent attempts by Chakrabarti & Titarchuk (1995) and others to find differences in the accretion flow between objects with event horizons (=BHs) and objects with a hard surface (=NSs).

For the determination of the existence of supermassive BHs, other observational methods have to be used. It appears difficult to explain how the very large luminosities and relativistic jets observed in AGN can be produced without requiring a central massive BH (Rees 1984), but direct observational evidence for testing this paradigm has been missing for a long time. The development of high resolution astronomical observational techniques in the past years has made the direct dynamical test for the presence of BHs in AGN possible. High resolution Hubble Space Telescope (HST) and ground based observations of nearby AGN have shown evidence for large velocities close to the center that can be best modeled by Keplerian motion around a point source of masses in excess of  $10^8 M_{\odot}$  (Macchetto et al. 1997; Kormendy et al. 1997), and also in our own galaxy there is increasing evidence for a central BH (Genzel et al. 1997). Even more convincingly, the discovery of water masers close to the center of NGC 4258 (M 106) by Miyoshi et al. (1995) and Greenhill et al. (1995) has made the mapping of the veloc-

ity field of matter in the inner few parsec of this object possible. Although the details are still debated, the only interpretation for the velocity profile seen is that the masers are situated in an accretion disk around a supermassive BH (Neufeld & Maloney 1995; Lasota et al. 1996). For a review of the dynamical mass estimates see Ford et al. (1997). Even closer to the center of AGN is the emission region of the Fe  $K\alpha$  line. Observations of the broad line profile in MCG–6–30–15 (and subsequently also in other objects) have shown that the observed broad profile is caused by relativistic effects closer than a few Schwarzschild radii to a supermassive black hole (Tanaka et al. 1995; Fabian et al. 1995; Iwasawa et al. 1996). Whether these lines are really generated close to Kerr BHs as opposed to Schwarzschild BHs remains to be proven (Fabian 1997; Reynolds & Begelman 1997). See Fabian (1997) and Wilms, Speith & Reynolds (1998) for a further description of these observations.

### 1.3 Black Holes as Astronomical Objects

Apart from the supermassive BHs in AGN and in the center of our galaxy, about 20–25 XRBs in the galaxy and in the Large Magellanic Cloud are believed to contain a BH. These systems are colloquially referred to as “galactic BHs”. In this section I will give a brief overview on the main properties of these sources as it applies to later sections of this thesis. For recent extensive reviews of galactic black holes, see Cowley (1992) and Tanaka & Lewin (1995); a special review emphasizing the broad band spectral information of the sources has been given by Zhang et al. (1997).

Like NS binaries, the BH XRBs are characterized mainly after the mass of the donor star, into low-mass and high-mass systems. The additional class of sources with a jet, the so-called “microquasars” are described below. Depending on whether the BH is the member of a LMXB (with a K dwarf or later star as companion) or a HMXB (with a B- or O-star as donor), its observational properties are very different.

Except for three sources, all galactic BHs known are found in LMXB systems and all of these appear to be transient sources, i.e., sources whose intensity can vary by several orders of magnitude in a comparably short amount of time. During the outburst, these “Soft X-ray Transient (SXT)” sources or “Black Hole X-ray Novae” can be  $10^4$  times more luminous than during quiescence (if they are observable at all during quiescence). The peak luminosity can be around  $10^{38}$  erg/s. Recent reviews on this class of objects have been given by Wheeler (1996) and Tanaka & Shibasaki (1996). The light curve of the outburst is usually characterized by a very quick rise of a duration of a day or shorter, plus a nearly exponential decline with an  $e$ -folding time of 30...40 d. Sometimes, a deviation from the decline about 60...80 d after the initial outburst is observed, which is called the “reflare”. Depending on the luminosity, a third increase is seen about 200 d after the initial outburst. In most cases, the optical light curve follows the X-ray lightcurve. This regular behavior has been seen, e.g., in GRS 1124–684 (Nova Mus 1991), GS 2000+251, and J0422+32 (Nova Per 1992), while other transients, like GS 2023+338 (V404 Cyg, Nova Cyg 1989), have shown deviations from

this behavior. The X-ray spectrum of the transients is characterized by a soft black body spectrum which can be modeled by thermal emission from an accretion disk, and a power-law at energies above 20 keV, extending out to 400 keV or more. In some objects (like GS 2023+338), the thermal component is missing and the spectrum is a pure power-law, sometimes with an exponential cutoff (in't Zand et al. 1992). The explanation for the temporal behavior is not known. Some authors point at a thermal instability similar to that of dwarf novae, where the accumulation of material in the accretion disk leads to a thermal instability heating the gas until it suddenly ionizes, thereby increasing the disk viscosity so that the mass transfer onto the compact object is rapidly increased followed by a slower cooling of the disk with a decrease in  $\dot{M}$  (Wheeler 1996; Cannizzo 1996). Other authors challenge this disk instability model on the grounds that the observed time scales in BH appear to be less well reproduced by the model and explain the outburst with the transition from an Advection Dominated Accretion Flow (ADAF) to a normal  $\alpha$ -disk (Lasota, Narayan & Yi 1996; Esin, McClintock & Narayan 1997).

Related to the “normal” SXTs by their transient outbursts are the “micro quasars”, GRS 1915+105 and GRO J1655-40 – perhaps some of the least understood objects in current astronomy. Previously only known in AGN, both sources have jets exhibiting apparent superluminal motion (Mirabel & Rodríguez 1996; Rodríguez & Mirabel 1995; Hjellming & Rupen 1995). While the mass function of GRO J1655-40 is known to be well above  $3 M_{\odot}$  (the most recent mass estimate gives  $M = 7.02 \pm 0.22 M_{\odot}$ , Orosz & Bailyn 1997), it is very difficult to measure the mass function of GRS 1915+105 due to its large extinction. Since its behavior is similar to that of GRO J1655-40 it is very probable, though, that also GRS 1915+105 is a BH. Both sources exhibit very violent behavior in all wavelength regimes (Greiner, Morgan & Remillard 1996; Pooley & Fender 1997). The X-ray lightcurves of GRS 1915+105 measured with the Rossi X-ray Timing Explorer (RXTE) show phases of chaotic variability together with phases where the lightcurve is periodically repeating a very complex pattern (Greiner, Morgan & Remillard 1996). QPOs have been detected in GRS 1915+105 at frequencies below 10 Hz, as well as a very stable feature at 67 Hz which might be related to an accretion disk instability (Nowak et al. 1997).

The most important group of BHs within the framework of this thesis is the small and elusive group of HMXB BHs, namely Cyg X-1, LMC X-1, and LMC X-3. All three sources are persistent sources and are continuously observed. For most of the time, Cyg X-1 is found in its “hard state”, which is also sometimes called the  $\gamma_2$  state (Ling et al. 1983) or the “low state”. As mentioned above, this state is characterized by a non-thermal power-law spectrum of photon index  $\Gamma = 1.7$  with an exponential turnover at around 150 keV. Such a spectrum is typically interpreted as being due to Comptonization in a hot electron gas surrounding an accretion disk, an accretion disk corona. See chapter 2 for information on the physical processes that might cause this corona. On several occasions, however, Cyg X-1 has also been found in a state where its luminosity is dominated by a thermal spectrum plus a very steep ( $\Gamma \gtrsim 2$ ) power-law component. The last such state has been observed in 1996 (Cui et al. 1997a,b) and, before that, in 1980 (Ling et al. 1983). In this “soft state”, which is also referred to as the “high state”,



the spectrum of Cyg X-1 is similar to that of the other two BH HMXB, LMC X-1 and LMC X-3. In the “soft state”, the thermal luminosity is above 10% of the Eddington luminosity (the largest luminosity attainable for a BH) and the source variability is stronger. What causes the switching between states is not understood yet, nor is the basic physics of why the states appear to be different. See Nowak (1995) and Esin et al. (1998) for two recent introductions to the different models.

Both states seen in HMXB BH binaries are also sometimes seen in the SXTs and in other transient BH candidates like GX 339-4. Since the persistent sources are the only sources that are always observable, an understanding of their spectra and temporal behavior is crucial for the understanding of the group of galactic BHs as a whole. The rest of this thesis, therefore, is devoted to such an analysis.

#### 1.4 *This thesis*

The rest of this thesis will mainly focus on the theoretical and observational aspects of the hard state X-ray spectrum of galactic BHs. For understanding the physics of the generation of the hard radiation it is necessary to deal with the physics of accretion disk coronae in detail.

In the first part of this volume, therefore, the radiation processes in accretion disks around BHs are described (chapter 2). I present information on the important physics in the coronae, Compton scattering, photon-photon pair production, and Compton reflection. The main part of chapter 2 is devoted to the presentation of results from computations using a new type of Monte Carlo code for the two commonly assumed geometrical configurations of the accretion disk corona. I give information on the spectrum emerging from the corona and on the temperature structure of the corona, emphasizing how these results relate to the observations. Furthermore, the temporal behavior of the emerging radiation is studied.

The second part of this thesis is devoted to the application of these results to real observed black hole systems, mainly Cygnus X-1. The introductory chapters 3 and 4 introduce the observational and experimental techniques used here, i.e., spectral and temporal analysis techniques, as well as the X-ray satellite RXTE which performed the observations on which the concluding chapters 5 and 6 are based. In chapter 5 the broad-band spectrum of Cyg X-1 in its hard state is modeled with the accretion disk corona models, using both a composite non-simultaneous X-ray spectrum as well as a recent RXTE observation. The final observational chapter, chapter 6 describes the results from a monitoring campaign on the two BHs in the large Magellanic cloud, LMC X-1 and LMC X-3, and present first results from one of the longest pointed observations of these sources. A summary and outlook on the future concludes the thesis in chapter 7.



# **PART I**

## **Theory**

---

## Radiation Processes Around Black Holes

As was briefly described in chapter 1, the hard state X-ray spectrum of galactic BHs and AGN is characterized by a power-law spectrum with a photon-index of  $\Gamma \approx 1.5 \dots 1.8$  and an exponential cut-off at photon-energies around 100 keV (Grebenev et al. 1993; Maisack et al. 1993; Wilms et al. 1996, and references therein). At low energies, this spectrum is further modified by features due to the interaction of X-rays with “cold” matter, including an iron fluorescence line at 6.4 keV and the Compton reflection hump (Guilbert & Rees 1988; Nandra et al. 1991; Fabian 1994, and references therein). The simplest model that has been successful at reproducing these spectral signatures is one where soft thermal radiation from an accretion disk is Comptonized in a semirelativistic electron-plasma, an Accretion Disk Corona (ADC), with the reflection features being produced in cold matter in the vicinity of the corona.

Even within the context of these models, the exact geometry and the physical properties of the corona are still unclear, with several models being discussed. Until recently the generally accepted picture for the generation of X-rays was that of an optically thick, cold ( $kT \lesssim 1$  keV) accretion disk sandwiched between two hot plane-parallel coronae. Most of the previous work on Compton coronae concentrated solely on this important configuration (Galeev, Rosner & Vaiana 1979; Field & Rogers 1993; Haardt & Maraschi 1991, 1993; Haardt, Maraschi & Ghisellini 1994, 1997; Nakamura & Osaki 1993; Hua & Titarchuk 1995; Poutanen, Svensson & Stern 1997, and references therein). In all of these papers it was commonly assumed that a substantial fraction of the gravitational accretion energy is directly dissipated in the corona by some unknown physical processes.

The popularity of the slab-ADC is due to the fact that ADC models in this geometry can quantitatively explain the X-ray spectra of Seyfert galaxies. Seyfert galaxies are usually believed to have thin accretion disks even very close to the central engine, and it seems natural that a corona could somehow form out of the disk. In the past few years, a magnetohydrodynamic instability has been discovered which might lead to a natural mechanism for explaining the formation of slab-ADCs (Balbus & Hawley 1991, see also Hawley, Gammie & Balbus 1994 and references therein): This “magnetorotational instability” or “Balbus-Hawley instability” can amplify the turbulent magnetic pressure in a magnetized accretion disk, leading to magnetic flux tubes rising out of the accretion disk to regions where the magnetic pressure is equal to the ambient gas pressure, i.e., the  $\beta$ -parameter is of the order of unity. The result is a weakly magnetized “core” of the disk, surrounded by a magnetized corona (Stone et al. 1996). Analogous to the solar corona these flux tubes are then thought to reconnect, thereby releasing an appreciable

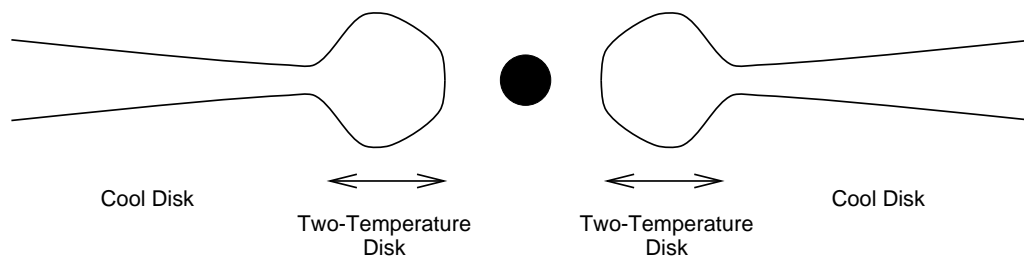


Figure 2.1: Sketch of the alternative disk model of Shapiro, Lightman & Eardley (1976): An optically thin, geometrically thick, two-temperature region inside of a standard optically thick, geometrically thin, one-temperature accretion disk.

amount of the locally available energy into the ambient plasma, heating the corona (Balbus & Hawley 1996). More recent numerical simulations have shown that the turbulent magnetic pressure is increased in low-density regions where it might directly heat the corona (Stone et al. 1996).

Although there is good reason to believe that slab coronae are present in AGN, the evidence for thin accretion disks close to the BH in stellar-mass BHs is less convincing. It was pointed out as early as the mid-seventies that optically thin, hot accretion disk models might be an alternative to the standard optically thick, cold accretion disk (Shapiro, Lightman & Eardley 1976, SLE, see also Lightman & Eardley 1974 and Thorne & Price 1975). In these models, an outer, geometrically thin, optically thick accretion disk turns into a geometrically thick, optically thin two-temperature accretion disk close to the black hole. In the two-temperature region, the ion-temperature is assumed to exceed the electron temperature by about two orders of magnitude (Shapiro, Lightman & Eardley 1976), since the electrons are efficiently Compton cooled. Unfortunately, the SLE-disk was found to be thermally unstable (Piran 1978).

In recent years, however, accretion models have been rediscovered that are stable, at least for some mass-accretion rates (Abramowicz et al. 1996; Esin et al. 1996; Narayan & Yi 1995; Ichimaru 1977, and references therein). Contrary to earlier beliefs, there exist two thermally stable states of the accretion flow exist for mass accretion rates below a certain threshold. One state is the standard optically thick, geometrically thin accretion disk described above, the other solution is the Advection Dominated Accretion Flow (ADAF) (The alternative term “secret guzzlers” for ADAFs, proposed, e.g., by Abramowicz et al. (1996), did not catch on in the literature). In an ADAF the inner region of the accretion flow, close to the BH, is assumed to be optically thin. Under certain circumstances it can happen that the cooling time of the infalling gas is larger than the time it takes for the gas to be accreted into the BH, a time scale of the order of the free-fall time from the marginally stable orbit. Therefore, an appreciable amount of the available energy of the gas is dumped (“advected”) into the BH instead of being radiated away (Narayan 1996a). The result is that the radiative cooling efficiency is very small ( $\eta = L/\dot{M}c^2 \lesssim 0.01$ ) as compared to the standard  $\alpha$ -disk where  $\eta \gtrsim 0.1$  (Abramowicz et al. 1996). It is not yet clear whether the ADAF-mode is always the preferred mode of the accretion disk and the  $\alpha$ -disk mode only exists for  $\dot{M}$  larger than the threshold (dubbed the “strong ADAF

principle” by Svensson 1997), whether the ADAF- and the  $\alpha$ -disk mode are chosen depending on the boundary conditions of the system (the “initial condition principle”), or whether the ADAF-mode is chosen only if no other solution exists (the “weak ADAF principle”). The observed state switches of galactic BHs could be interpreted as indicating that at least the strong ADAF principle does not hold, assuming the state switches are interpreted as being due to a switch from an ADAF to a thin disk solution.

Until a theoretical argument for or against each of the different ADAF principles is found, however, it is not obvious which of the different proposed geometrical configurations is the “only truth”. Since the ability of a model to describe the data is the principal observational support for any of the Compton models, it is very important that the numerical modeling is done as self-consistently as possible. Recently we have performed detailed numerical simulations using the code discussed in appendix A.2 to compute self-consistent models for simplified versions of *both* accretion disk – corona configurations. Our main interest in these simulations was to understand in detail the spectral and temporal behavior of the radiation escaping the system, to a level of quality in the spectra that enables us to use our theoretical results and directly compare them with the observations. This chapter describes the major physical processes at play in ADCs (§2.1), summarizes our results on the spectra of ADCs (§2.2), and presents information on the temporal behavior of ADCs in section 2.3.

Most of the original content of this chapter has been published in the following papers which are not always referenced explicitly in the rest of this chapter:

- Dove, J., Wilms, J., Begelman, M. C., 1997, *Self-Consistent Thermal Accretion Disk Corona Models for Compact Objects: I. Properties of the Corona and the Spectra of Escaping Radiation*, *Astrophys. J.*, **487**, 747–758
- Dove, J., Wilms, J., Maisack, M., Begelman, M. C., 1997, *Self-Consistent Thermal Accretion Disk Corona Models for Compact Objects: II. Application to Cygnus X-1*, *Astrophys. J.*, **487**, 759–768
- Wilms, J., Dove, J., Staubert, R., Begelman, M. C., 1997, *Properties of Accretion Disk Coronae*, in: *The Transparent Universe* (C. Winkler, T. J.-L. Courvoisier, Ph. Durouchoux, eds.), Noordwijk: ESA Publications Division, ESA SP-382, 233–236

## 2.1 Physical Processes in ADCs

In this section a brief overview on the major physical processes that determine the energetics and the emerging photon spectra of ADCs is given. As was explained in the last section there is ample evidence that the X-ray continuum of BHs is produced by Comptonization, i.e., by the upscattering of soft photons by the inverse Compton effect. This process is described in further detail in section 2.1.1. Due to the large photon density in an ADC, photon-photon pair production is an important physical process, provided the photon spectrum is hard enough (section 2.1.2). Finally, the presence of cold matter, i.e., the presence of the accretion disk, is thought to further modify the escaping spectrum: photoabsorption of the hard photons leads to the emission of fluorescence lines, and the interaction of the hard photons with the low-temperature electrons in the matter modifies the emerging continuum (“Compton reflection”). This process is described in

section 2.1.3.

### 2.1.1 Comptonization

#### 2.1.1.1 Compton Scattering

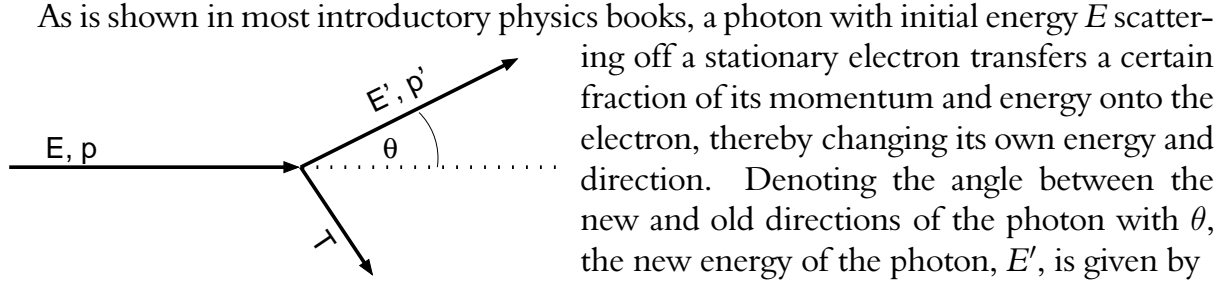


**Figure 2.2:** Geometry for Compton scattering

$$E' = \frac{E}{1 + \frac{E}{m_e c^2} (1 - \cos \theta)} \quad (2.1)$$

This energy change results in a change of the wavelength of the photon given by

$$\lambda' - \lambda = \frac{h}{m_e c} (1 - \cos \theta) \quad (2.2)$$

where  $h/m_e c = 2.426 \times 10^{-10}$  cm is the Compton wavelength. For  $E/m_e c^2 \ll 1$ , eq. (2.1) is

$$E' \approx E \left( 1 - \frac{E}{m_e c^2} (1 - \cos \theta) \right) \quad (2.3)$$

The angular distribution of the electron after the scattering event and the cross section for Compton scattering are given by the Klein-Nishina formula

$$\frac{d\sigma_{\text{es}}}{d\Omega} = \frac{3}{16\pi} \sigma_{\text{T}} \left( \frac{E'}{E} \right)^2 \left( \frac{E}{E'} + \frac{E'}{E} - \sin^2 \theta \right) \quad (2.4)$$

(Klein & Nishina 1929, see also Rybicki & Lightman 1979). Writing  $\epsilon = E/m_e c^2$  and substituting eq. (2.1) results in

$$\frac{d\sigma_{\text{es}}}{d\Omega} = \frac{3}{8\pi} \sigma_{\text{T}} \left( \frac{1 + \cos^2 \theta}{2} \right) \cdot \left( \frac{1}{1 + \epsilon(1 - \cos \theta)} \right)^2 \cdot \left( 1 + \frac{\epsilon^2 (1 - \cos \theta)^2}{(1 + \cos^2 \theta)(1 + \epsilon(1 - \cos \theta))} \right) \quad (2.5)$$

where

$$\sigma_{\text{T}} = \frac{8\pi}{3} r_0^2 = \frac{8\pi}{3} \left( \frac{e^2}{m_e c^2} \right)^2 = 6.652 \times 10^{-25} \text{ cm}^2 \approx 2/3 \text{ barn} \quad (2.6)$$

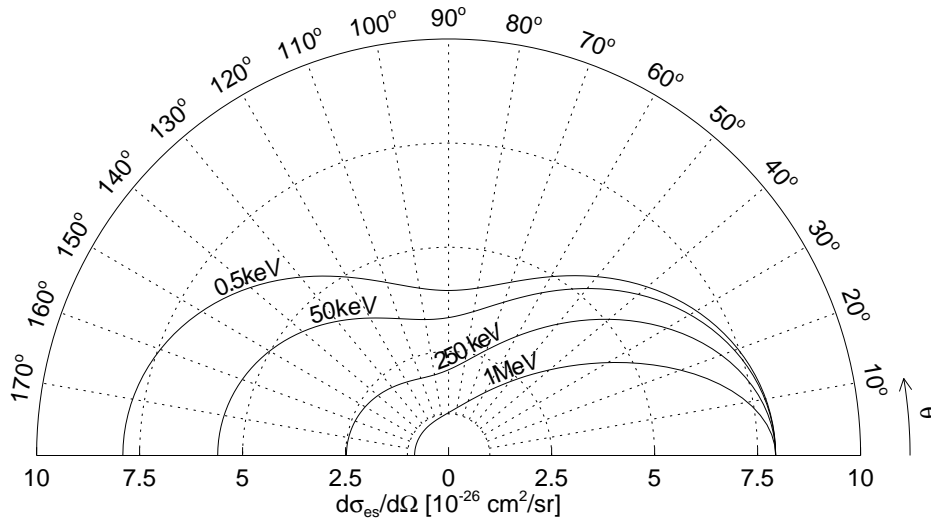


Figure 2.3: Differential Klein-Nishina cross section per electron for different incident photon energies  $E$  of 0.5 keV, 50 keV, 250 keV, and 1 MeV. The photon is coming from the left. Relativistic beaming dominates for large  $E$ .

is the classical Thomson cross section ( $r_0 = 2.82 \times 10^{-13}$  cm is the classical electron radius). A plot of the differential cross section is given in Fig. 2.3. Note that  $\sigma_T$  is proportional to  $m_e^{-2}$ . If one were to apply the scattering theory to other charged particles, e.g., protons, all cross sections would scale as  $(m_e/m_p)^2 \approx 10^{-7}$ . Therefore Compton scattering by particles other than electrons is negligible because almost no momentum can be transferred.

Integrating eq. (2.4) over all scattering angles results in the total cross section

$$\begin{aligned} \sigma_{\text{es}} &= \frac{3}{4} \sigma_T \left[ \frac{1+x}{x^3} \left\{ \frac{2x(1+x)}{1+2x} - \ln(1+2x) \right\} + \frac{1}{2x} \ln(1+2x) - \frac{1+3x}{(1+2x)^2} \right] \\ &= \frac{3}{8} \sigma_T \frac{1}{x} \left\{ \left[ 1 - \frac{2(x+1)}{x^2} \right] \ln(2x+1) + \frac{1}{2} + \frac{4}{x} - \frac{1}{2(2x+1)^2} \right\} \end{aligned} \quad (2.7)$$

(Rybicki & Lightman 1979; Longair 1992). This is the Klein-Nishina formula. For small initial energy  $E$ , the Klein-Nishina formula approaches the classical Thomson formula

$$\frac{d\sigma_T}{d\Omega} = \frac{3}{8\pi} \sigma_T \left( \frac{1 + \cos^2 \theta}{2} \right) \quad (2.8)$$

It has to be stressed that in the derivation of eq. (2.7) it is implicitly assumed that the electron be stationary and free. Neither of these two assumptions is realized in nature. The physics of Compton scattering off a bound electron is described by Evans (1958). The astrophysical implications have been studied by Sunyaev & Churazov (1996) for the case of Compton scattering in a hydrogen gas (the only case where the cross section can be evaluated analytically, see Gorshkov, Mikhailov & Sherman 1973). It turns out, however, that for our purposes these corrections to eq. (2.4) are negligible.



### 2.1.1.2 Thermal Comptonization

If the electrons cannot be assumed stationary, i.e., if they are not “cold”, the formulae given in the last section have to be modified. Within the framework of this thesis the interesting case is that in which the electrons have a (possibly relativistic) Maxwellian distribution characterized by its temperature  $T_e$  and are irradiated by “seed” photons with an initial energy  $E \ll T_e$ . This setup is called the “thermal Comptonization” problem (Hua 1997; Titarchuk 1994; Titarchuk & Hua 1995; Hua & Titarchuk 1995; Pozdnyakov, Sobol & Sunyaev 1983; Sunyaev & Titarchuk 1980, and references therein).

Ignoring the  $\theta$ -dependency of the cross section one can average eq. (2.3) over all  $\Omega$  to obtain an order of magnitude estimate for the average energy-change of a photon scattering off a stationary electron

$$\frac{\Delta E}{E} \approx -\frac{E}{m_e c^2} \quad (2.9)$$

Thus, the average energy change at  $E = 6.4 \text{ keV}$  (the energy of the Fe  $K\alpha$  line) is about  $0.2 \text{ keV}$ . If the electrons are not stationary but have a Maxwellian energy distribution with a temperature that is small compared to the rest-mass energy of the electrons,  $kT_e \ll m_e c^2$ , then the average relative energy change of the seed photon is given by

$$\frac{\Delta E}{E} \approx \frac{4kT_e - E}{m_e c^2} \quad (2.10)$$

(Rybicki & Lightman 1979, eq. 7.36). For  $E < 4kT_e$ , the relative energy change is  $\Delta E/E > 0$  and the photons on average gain energy by being upscattered by the inverse Compton effect. This is the process of Comptonization. A side effect of the upscattering is that the electrons are losing energy and thus inverse Compton scattering is a cooling process for the gas. The average energy amplification of the photons, the Compton amplification factor, is given by

$$A = 4kT_e/m_e c^2 = 4\Theta \quad (2.11)$$

where  $\Theta = kT_e/m_e c^2$ . In reality, there is approximately a Gaussian distribution around  $\Delta E$  with a width given by

$$\frac{\sigma}{E} = \sqrt{\frac{2kT_e}{m_e c^2}} \quad (2.12)$$

(Ross, Weaver & McCray 1978, eqns. [2], [5], and [10]). The approximate total energy change of a photon traversing a medium of optical depth  $\tau_e = n_e \sigma_T R = n_e \sigma_T c t$  can be computed by multiplying the average number of scatterings with the average energy change per scattering. The average energy change per scattering is given by eq. (2.10), while the average number of scatterings is obtained from the theory of random walks as  $n_{\text{scat}} = \max(\tau_e, \tau_e^2)$ . Thus the total energy change of the photon while traversing the medium is given by

$$\gamma = \frac{4kT_e}{m_e c^2} \max(\tau_e, \tau_e^2) \quad (2.13)$$

if the recoil effect can be neglected. This parameter is called the Compton  $\gamma$  parameter. A relativistic generalization of  $\gamma$  is difficult to find. Most people agree that the Compton amplification factor is given by

$$A = 1 + 4\Theta \frac{K_3(1/\Theta)}{K_2(1/\Theta)} \approx 4\Theta + 16\Theta^2 \quad (2.14)$$

(Zdziarski 1985, eqs. [4] and [7]) where the  $K_i$  are the modified Bessel functions of second kind of order  $i$ . A generalization of  $\gamma$  itself is more difficult since the naïve generalization of the nonrelativistic  $\gamma$  does not work (see Pietrini & Krolik 1995, and references therein for a discussion of this problem).

In the limit of a large optical depth, the Comptonization problem can be expressed as a diffusion problem, resulting in the Kompaneets equation

$$\frac{\partial n}{\partial \gamma} = \frac{1}{x^2} \frac{\partial}{\partial x} x^4 \left( n + n^2 + \frac{\partial n}{\partial x} \right) \quad (2.15)$$

where  $n$  is the photon occupation number,  $x = E/kT_e$ , and where  $\gamma$  is the Kompaneets parameter, defined by  $\gamma = (4kT_e/m_e c^2) \sigma_T n_e c t$  (note that the Kompaneets parameter is *not* equal to the Compton- $\gamma$ !). A derivation of eq. (2.15) starting from the Boltzmann equation has been given by Rybicki & Lightman (1979), while a derivation via the Fokker-Planck equation has been presented by Wilms (1996). Note that the Kompaneets equation is valid only in the diffusion limit and assumes  $kT_e \ll m_e c^2$ . Most probably, both assumptions are *not* valid in real astrophysical systems (see below).

With certain additional assumptions on the source geometry and the spatial and energetic distributions of the seed photons it is possible to use eq. (2.15) in order to obtain the photon spectrum emerging from the cloud. See Sunyaev & Titarchuk (1980) for the derivation of this spectrum and Titarchuk (1994) and Hua & Titarchuk (1995) for an extension of the Sunyaev & Titarchuk (1980) work that is also valid for lower optical depths and relativistic temperatures.

For small optical depth and small seed photon energy, the approximate form of the emerging spectrum can be derived (Rybicki & Lightman 1979, p. 212): The probability of a photon to undergo  $n$  scatterings before leaving the cloud is  $p \sim \tau^n$ , while its energy after  $n$  scatterings is  $E \sim E_0 A^n$  where  $A$  is given by eq. (2.14). Assuming that all seed photons had small initial energy, the intensity of the emerging photons at a given energy  $E$  is proportional to the initial seed photon intensity times the probability of the photons to reach  $E$ :

$$I(E) \sim I(E_0) p(E_0 \rightarrow E) \sim I(E_0) \tau^n \sim I(E_0) \left( \frac{E}{E_0} \right)^{\ln \tau / \ln A} \quad (2.16)$$

where the exponent was obtained by multiplying  $n \sim \ln(E/E_0)/\ln A$  with  $\ln \tau$  on both sides. Obviously, at some energy of the order of  $kT$ , the power-law will turn over in an exponential cut-off since the photons cannot be upscattered to higher energies. This limit of the Compton cascade, where the resulting photon spectrum is a power-law, is

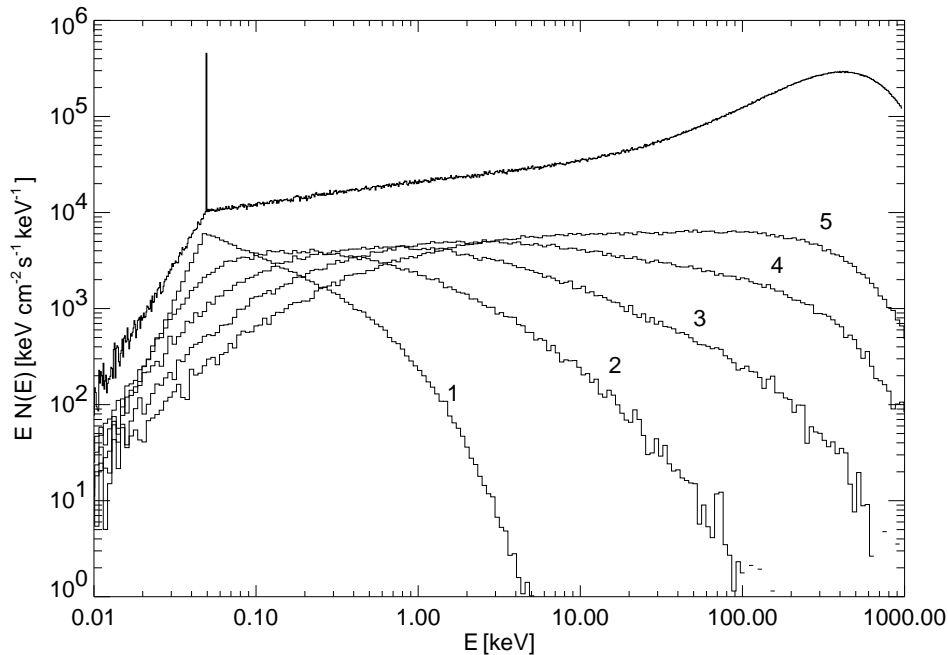


Figure 2.4: Comptonization spectrum for a sphere with a Thomson optical depth of  $\tau = 5$  and a uniform electron temperature of  $kT_e = 0.4m_e c^2 = 204.4$  keV. The seed photons are injected with an energy of  $E = 50$  eV from a point-source at the center of the sphere. The spectra labeled 1 . . . 5 are the emerging spectra for the scattering orders 1 . . . 5, the top spectrum is the total escaping spectrum. The scatter in the spectra is due to noise resulting from the linear Monte Carlo code used to compute the spectra.

also called unsaturated Comptonization since the photons have only a very small probability of reaching an energy comparable to  $kT_e$ .

On the other hand, if the seed photon energy is on the order of the average electron energy, i.e., for  $E \gtrsim kT_e$ , the photon-spectrum emerging the cloud is proportional to  $E^3 \exp(-E/kT_e)$ , i.e., a Wien spectrum. For seed photon energies that high, eq. (2.10) shows that the average energy change of the photons is zero. Due to photon number conservation in Compton scattering, the result is a Wien spectrum (and *not* a Planckian). This Wien hump always forms if enough photons are upscattered to energies of the order of the thermal energy of the electrons, i.e., for large Compton- $\gamma$ . Because the photons pile up at around  $3kT_e$ , this is called the saturated Compton cascade.

I have used an expanded version of the linear Monte Carlo code described in my diploma thesis (Wilms 1996) to illustrate these effects. Fig. 2.4 shows how the final Comptonization spectrum can be thought of as the sum of the Comptonization spectra for the individual scattering orders. For energies up to about 100 keV the escaping photons have only suffered a few scatterings, i.e., the cascade is unsaturated, and a power-law forms. For final photon energies above  $\sim 100$  keV the cascade saturates and a Wien hump forms. In Fig. 2.5 the spectra emerging from spheres with the same temperature but different optical depths are shown. For low optical depth the Compton- $\gamma$  is small

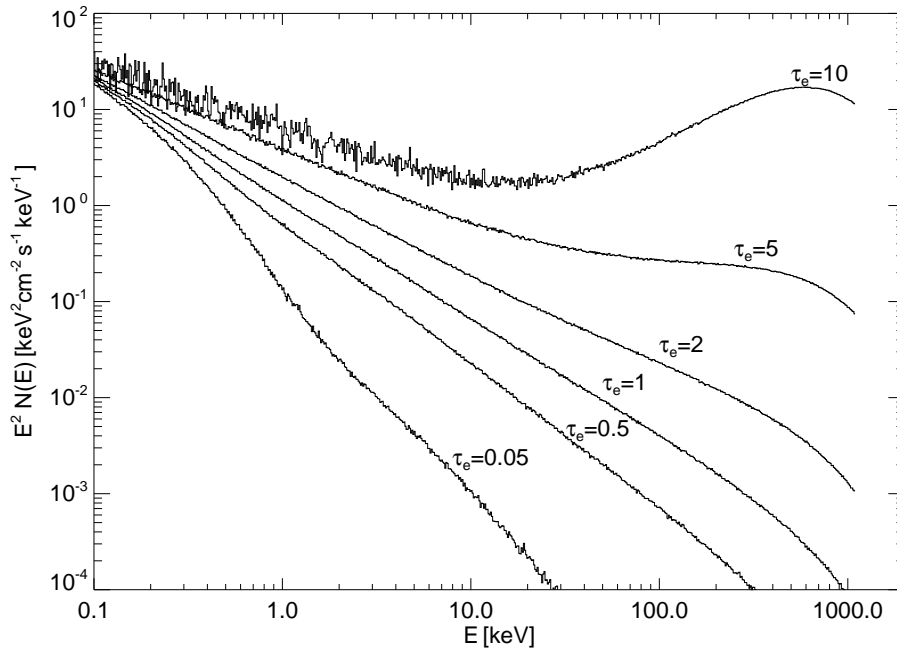


Figure 2.5:  $\nu f_\nu$ -Spectra from a sphere with an electron temperature of  $kT_e = 0.7m_e c^2 \approx 360$  keV for different Thomson optical depths  $\tau_e$ . The spectra harden with increasing  $\tau_e$  until a Wien hump forms. The deviation from a pure power-law in the  $\tau_e = 0.05$  case is due to the contribution of the first scattering order to the spectrum, i.e., the contribution of photons just scattering once before escaping. The noise at low energies in the  $\tau_e = 10$  spectrum is due to the Monte Carlo routine used.

and the spectrum is a pure power-law. With increasing  $\tau$ , i.e., with increasing  $\gamma$ , the Compton cascade starts to saturate and a Wien hump is formed.

### 2.1.2 Pair Production and Annihilation

The second most important physical process in ADCs is photon-photon pair production and its inverse, electron-positron pair annihilation. Perhaps due to the fact that photon-photon pair production is difficult to observe in the laboratory<sup>1</sup> the first papers realizing that photon-photon pair production is a process relevant for high-energy astrophysics have been generally ignored (Nikishov 1962; Jelley 1966). It was only 15 years ago that photon-photon pair production processes have been systematically studied in an high-energy astrophysical context (Zdziarski 1980; Svensson 1982, and references therein).

Photon-photon pair production is the process

$$\gamma + \gamma \longrightarrow e^+ + e^- \quad (2.17)$$

<sup>1</sup>The difficulty of studying photon-photon pair production is mainly due to the difficulty of producing a high enough density of gamma-rays above 511 keV. It has only been very recently that this important process has been detected in the laboratory. See Burke et al. (1997) for a description of this important experiment.

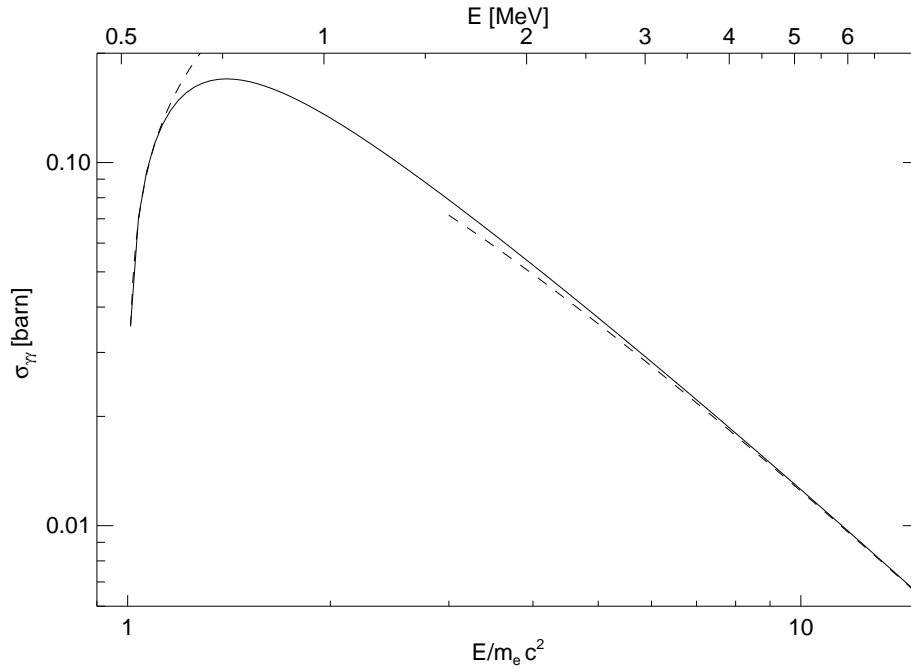


Figure 2.6: Cross section for photon-photon pair production (eq. 2.18; solid line) and the two asymptotics of eq. (2.19) (dashed lines).

The cross section in the center of mass (CM) system is given by

$$\sigma_{\gamma\gamma} = \frac{\pi r_0^2}{\epsilon^2} \left( \left( 2 + \frac{2}{\epsilon^2} - \frac{1}{\epsilon^4} \right) \ln \left( \epsilon + \sqrt{\epsilon^2 - 1} \right) - \sqrt{1 - \frac{1}{\epsilon^2}} \left( 1 + \frac{1}{\epsilon^2} \right) \right) \quad (2.18)$$

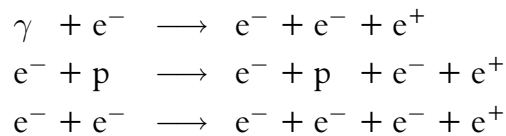
(Akhiezer & Berestetskii 1965; Berestetzki, Lifschitz & Pitajewski 1989) where  $\epsilon = E/m_e c^2$  is the center of mass energy of the photons and  $r_0$  is the classical electron radius (see p. 24). Due to obvious reasons, the threshold CM energy for which pair production is possible is  $E = m_e c^2$ .

The asymptotic behavior of  $\sigma_{\gamma\gamma}$  is given by

$$\sigma_{\gamma\gamma} = \begin{cases} \pi r_0^2 (\epsilon^2 - 1)^{1/2} & \text{for } \epsilon - 1 \ll 1 \\ \pi r_0^2 (2 \ln(2\epsilon) - 1) / \epsilon^2 & \text{for } \epsilon \gg 1 \end{cases} \quad (2.19)$$

(Svensson 1982). In Fig. 2.6 a plot of this cross section is given.

In principle, pairs could likewise be produced by the following processes



Approximate cross sections for these processes have been given by Svensson (1982). He shows that the pair production rate resulting from  $\gamma e^-$ -pair production is more than

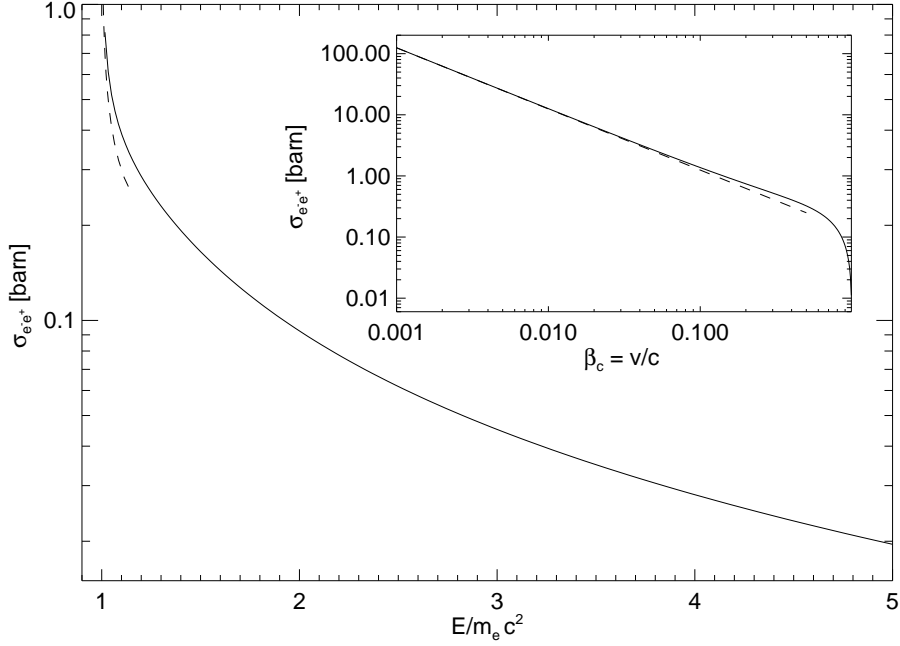


Figure 2.7: CM cross section for pair annihilation (eq. 2.21) as a function of the CM energy (in units of  $m_e c^2$ , including the rest mass of the particle; large plot), and as a function of the CM velocity of one particle (inset). The dashed line is the asymptotic behavior of the cross section for small velocities,  $\sigma_{e^-e^+} \propto 1/\beta_c$ .

one order of magnitude smaller than the pair production rate from  $\gamma\gamma$ -pair production. The rates from the other two processes are more than three orders of magnitude smaller than the  $\gamma\gamma$ -pair production rate. In the computations described later, therefore, only photon-photon pair production is included.

The inverse process to pair production is pair annihilation,



In the CM system the cross section is given by

$$\sigma_{e^-e^+} = \pi r_0^2 \left( \frac{1 - \beta_c^2}{4\beta_c} \right) \left\{ \frac{3 - \beta_c^4}{\beta_c} \ln \left( \frac{1 + \beta_c}{1 - \beta_c} \right) + 2(\beta_c^2 - 2) \right\} \quad (2.21)$$

(Berestetzki, Lifschitz & Pitajewski 1989, eq. 88,15) where  $\beta_c$  is the CM velocity of the electrons in units of the speed of light. For small velocities,  $\sigma_{e^-e^+} \approx \pi r_0^2 / \beta_c$ .

In Fig. 2.7 the pair annihilation cross section is shown.  $\sigma_{e^-e^+}$  is strongly peaked at energies  $E \sim m_e c^2$ , i.e., small velocities, while it asymptotically approaches zero for high velocities since the interaction timescale between the electron and the positron shortens for higher velocities so that annihilation cannot occur.

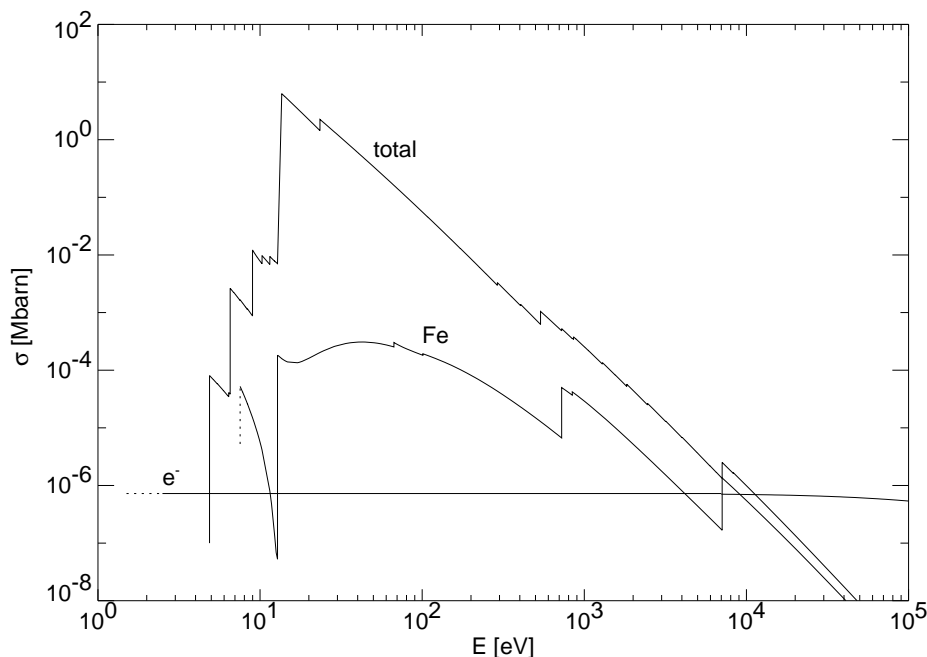


Figure 2.8: Total cross section for photo absorption per hydrogen atom computed using the photoionization cross sections of Verner et al. (1993), contribution of iron to the photo absorption cross section, and the Klein-Nishina cross section, assuming a gas with solar abundances (Anders & Grevesse 1989).

### 2.1.3 Reflection

The last ingredient in the accretion disk corona cauldron is Compton reflection. Compton reflection is always observed when hard photons are generated in the presence of comparably cold material. In Fig. 2.8 the photo ionization cross section  $\sigma_{\text{bf}}$  and the effective cross section for Compton scattering per hydrogen atom for material of solar abundances are shown. For energies below about 15 keV the optical depth for Compton scattering is small compared to that for photo absorption. Therefore, most incident photons with energies smaller than 15 keV are absorbed in the cold medium<sup>1</sup>. On the other hand, photons with  $E \gg 15$  keV will predominantly Compton scatter. Since photons lose energy in Compton scattering off a cold electron (eq. 2.9, p. 25), this results in an energy-dependent effective absorptivity at high energies, with the high energy photons being scattered to lower energies until they are either scattered out of the medium or until they are photoabsorbed. The result of both effects, photo absorption and Compton scattering, is a broad hump in the spectrum between about 10 keV and

<sup>1</sup>The largest contribution to  $\sigma_{\text{bf}}$  in the energy band around 7 keV is due to iron, more precisely the iron K and L shells (Fig. 2.8). Therefore, “cold” in the context of Compton reflection means that at least the iron K and L shells should be (almost) filled, i.e., the dominating ionization stage should be less than Fe XVI. The ionization potential of Fe XVI is about 2900 eV (Allen 1973), so that a (very rough) estimate shows that a “cold temperature” corresponds to disk temperatures less than about  $3 \times 10^7$  K. The observed soft-excess temperatures in galactic black holes are in the ball park of  $kT_{\text{BB}} \lesssim 2$  keV, so that a study of cold reflection is sufficient in the following. For a description of reflection of hard radiation off ionized disks see Done et al. (1992, and references therein).

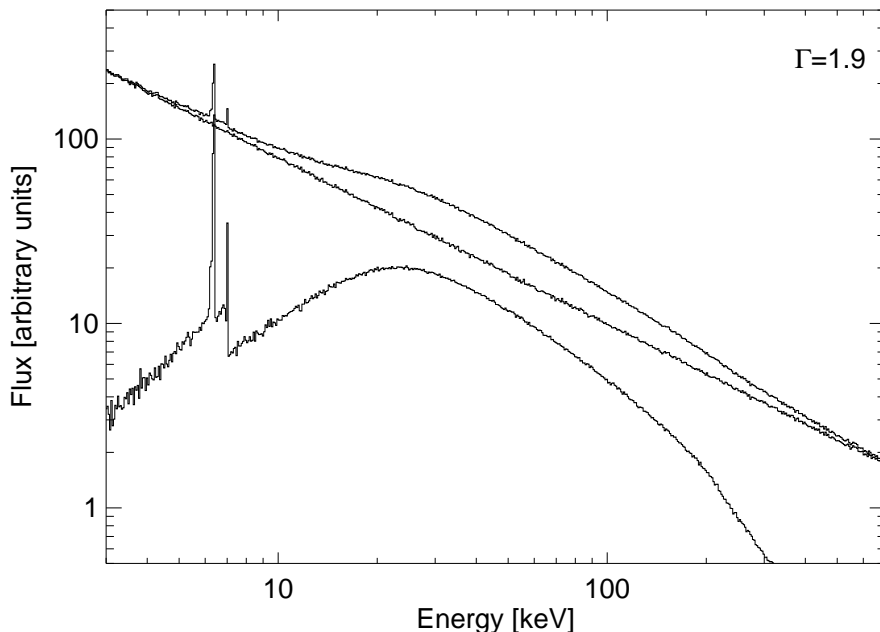


Figure 2.9: Reflection spectrum for a slab of cold matter irradiated by a power-law photon spectrum with photon index  $\Gamma = 1.9$ . The spectrum at the bottom is the resulting reflection spectrum. Note the strong iron edge at 7.1 keV and the strong fluorescent iron  $K\alpha$  and  $K\beta$  lines. The top spectrum is the sum of the incident and the reflected spectrum.

100 keV. In Fig. 2.9 the reflection spectrum and the total emerging spectrum resulting from Compton reflection of an incident isotropic power-law photon spectrum off a cold slab are shown. The Compton reflection hump was first predicted by Lightman & White (1988) and White, Lightman & Zdziarski (1988), followed by numerical computations by George & Fabian (1991), Matt et al. (1992), Matt, Fabian & Ross (1993), and others.

An important side-effect of the photo absorption at low energies is the emission of fluorescent lines following a K-shell absorption event. Due to a combination of its comparatively high cosmic abundance and its high fluorescence yield ( $\omega_{K,Fe} = 0.34$ , Kaastra & Mewe 1993), the iron  $K\alpha$  line is especially strong with a predicted equivalent width of about 150 eV (Fig. 2.9). In addition, other emission lines are present at lower energies (Reynolds et al. 1994). See my diploma thesis for a more detailed description of the relevant atomic physics (Wilms 1996). Spectral hardening due to reflection and emission line features are observed in many galactic and extragalactic sources.

To study the reflection spectrum it is convenient to express the reflection spectrum as a function of the incident spectrum in terms of a Green's function. Then, the reflected spectrum  $I_{\text{ref}}$  can be expressed as

$$I_{\text{ref}}(x; \mu) = \int_0^{\infty} G_{\text{ref}}(\mu, x, x_0) I_{\text{inc}}(x_0) dx_0 \quad (2.22)$$

where  $I_{\text{inc}}(x_0)$  is the incident spectrum,  $G(\mu, x, x_0)$  is the Green's function, and  $x =$



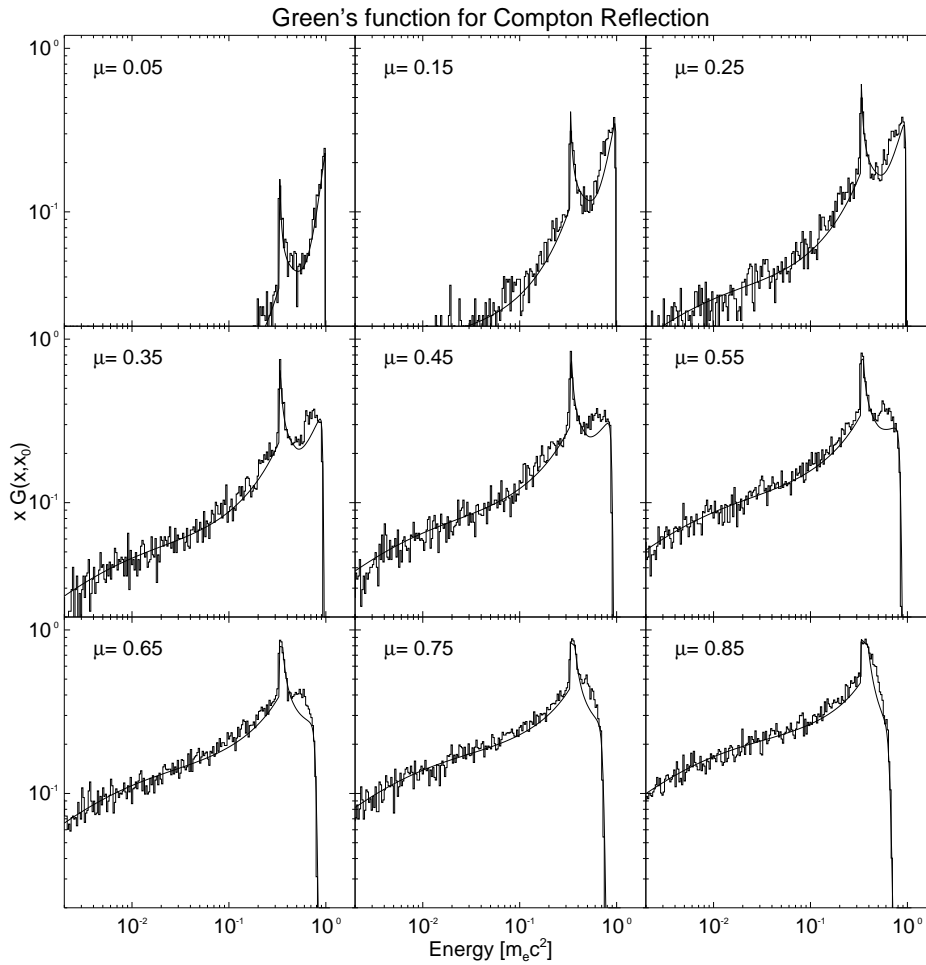


Figure 2.10: Green's functions for the pure Compton reflection obtained with a linear Monte Carlo algorithm based on that described by Wilms (1996) compared to the analytical fits by Magdziarz & Zdziarski (1995). Initial energy of the photons is  $E = m_e c^2$ . The deviation between the simulation and the analytical curves at  $E \sim m_e c^2$  is due to a round-off error in the reflection code used.

$E/m_e c^2$ . The cosine of the angle  $\theta$  between the disk-normal and the direction to the observer is denoted by  $\mu$ . The Green's function is normalized

$$\int_0^\infty \int_0^+ G(\mu, E, E_0) d\mu dE = 1 \quad (2.23)$$

$G$  can be interpreted as the probability-density that a photon of incident energy  $E_0$  is observed at an energy of  $E$  and an incident angle  $\mu$  after the reflection process.

The analytic derivation of  $G$  is very difficult and most workers have resorted to the numerical computation of using Monte Carlo computations. Angle averaged Green's functions have been published by White, Lightman & Zdziarski (1988). Their work has been superseded by Magdziarz & Zdziarski (1995), who give analytical angle-dependent Green's functions with an error of 5% or less. They assumed an angular distribution of the photons proportional to  $\mu$ . In Fig. 2.10 the Green's function for pure Compton

reflection of photons of an initial energy of  $E = m_e c^2$  as obtained with my linear Monte Carlo algorithm is compared to the analytical fits of Magdziarz & Zdziarski (1995). Here, “pure Compton reflection” means that photo absorption has not been taken into account. While this is clearly not the case in nature, ignoring photo absorption allows for a better understanding of the phenomenology of Compton reflection. Looking at the disk almost edge on, i.e., for small  $\mu$ , zeroth and first order Compton scattering dominates. With higher  $\mu$ , higher scattering orders start to dominate and the importance of zeroth order Compton scattering is reduced since the photons observed when looking face on the disk must have suffered at least one head-on Compton scattering before escaping. For a more in depth description of Compton reflection see my diploma thesis (Wilms 1996).

## 2.2 Accretion Disk Coronae

Since the high-energy spectrum of the escaping radiation from an accretion disk corona is primarily a Comptonization spectrum, it depends mainly on the geometry of the system, the Thomson optical depth of the corona,  $\tau_{es}$ , and the temperature of the corona,  $T_c$ . When modeling observational data, typically a geometrical configuration is assumed (most often either a slab geometry or a spherical configuration is chosen), and  $\tau_{es}$  and  $T_c$  are allowed to vary independently until a good fit to the data is achieved. However, it is not clear whether the best-fit parameters found in this process can indeed be interpreted as really being the *physical* parameters of the system. For many configurations, reprocessing of radiation from the corona within the cold accretion disk allows the accretion disk to have a large flux of thermal radiation even if most of the gravitational energy is dissipated within the corona (Haardt & Maraschi 1991). For example, in the case of the slab geometry, a high flux of soft photons results in a high Compton cooling rate, and consequently models with modest optical depths ( $\tau_{es} \gtrsim 0.2$ ) can only have temperatures  $T_c \lesssim 120$  keV (see §2.2.2.3). It has been found empirically that the observed spectrum of Cyg X-1 can be described by a slab-ADC model, with a temperature of  $T_c \sim 150$  keV and an optical depth of  $\tau_{es} \sim 0.3$  (Haardt et al. 1993). These parameters are *not* physically allowed so that their interpretation in terms of a theory of the accretion process in Cyg X-1 might result in erroneous conclusions.

Since our knowledge of the physics of the accretion process in a black hole system depends so strongly on the interpretation of these best-fit parameters, it is important that the computation of ADC-models be done as carefully and self-consistently as possible. In the past few years I have performed such simulations in collaboration with the group of Mitch Begelman at JILA. This section summarizes the results obtained so far, emphasizing the theoretical aspects of the work. The application of our results to real systems is postponed to chapter 5.

### 2.2.1 Previous Models for ADCs

The study of the thermal properties of ADCs and the computation of the escaping spectrum is to a large extent dominated by the computational problems involved with solving the difficult equations coupling the radiation field to the electron plasma: through Comptonization, the properties of the photon spectrum depend on the corona's temperature and opacity. Since Compton cooling is the dominant cooling process, the temperature of the corona, in turn, depends on the spectrum. Additionally, the coronal optical depth and the radiation field are coupled to each other through pair production and pair annihilation. Reprocessing of radiation within the accretion disk, where the radiation is either Compton reflected back into the corona or photo-absorbed and subsequently thermalized, further complicates the problem. To overcome these difficulties, a large variety of different mathematical methods has been developed in the past:

*Analytical methods* solve the Comptonization problem by taking the physical state of the corona, i.e., the temperature structure and the optical depth, as given and then analytically or numerically solving the Kompaneets equation or one of its variants. The analytical methods have been pioneered by Felten & Rees (1972), Illarionov & Sunyaev (1972), Lightman & Rybicki (1980), Lightman, Lamb & Rybicki (1981), and especially Sunyaev & Titarchuk (1980). These theories have been further extended by Sunyaev & Titarchuk (1985), Titarchuk (1994), and Hua & Titarchuk (1995). Since the properties of the corona have to be known before the radiation field can be computed, it is not clear whether the coronal properties are self-consistent with the radiation field. Furthermore, fully analytical solutions are only possible for a limited range of geometrical configurations (sphere, slab, and cylinder), and spatial seed photon input distribution (cf. Sunyaev & Titarchuk 1980). An extension of the formalism to include the fully relativistic, angle-dependent cross sections appears to be very difficult or even impossible (the iterative scattering method developed by Poutanen 1994, Poutanen & Svensson 1996, and Poutanen, Svensson & Stern 1997 might provide a solution of this problem). Furthermore, no analytical method has been presented so far that is capable of taking into account the anisotropy of the radiation field within the corona *and* also self-consistently computes the radiation field resulting from the reprocessing of the incident coronal radiation in the cold disk. The current "state of the art" is to compute the reprocessed component using a different method, for example Green's functions analogous to those of section 2.1.3. This component is then added to the spectrum emerging from the system. It is obvious that possible subsequent interactions between the reflected component and the corona cannot be taken into account this way.

*Solving the kinetic equations* is an extension to the analytical methods just described. Instead of "only" solving the Kompaneets equation the full set of integro-differential equations for the (non-) thermal pair equilibrium and for the radiative transfer is set up and solved. This approach has been taken, e.g., by Fabian et al. (1986), by Lightman & Zdziarski (1987) and by Svensson (1987, and references therein). The state of the art has been described by Coppi (1992) and by Pilla & Shaham (1997). Concerning the flexibility of the method, the approach to solve the kinetic equations suffers from the same

shortcomings as the analytical methods described above, since it is only possible to obtain solutions for a rather small subset of possible geometries. In addition, the equations governing the problem are very complicated so that certain approximations have to be made. Especially the correct treatment of the radiative transfer using the kinetic equations is difficult so that most workers have usually resorted to using an escape probability approach (see, e.g., Coppi 1992).

*Linear Monte Carlo (MC) methods* are based on a philosophy which is very different from that of the methods just described. Instead of looking at the system from a “global” point of view, that is by solving the equations governing the global physics of the ADC, in a MC-code, individual particles are dealt with. For example, in a linear MC-code, individual photons are propagated through a background-medium simulating the particle distribution of the electron plasma. The computational techniques for MC-codes for the Comptonization problem are described by Pozdnyakov, Sobol & Sunyaev (1983) and Górecki & Wilczewski (1984), further improvements have been given by Zdziarski (1986), Hua & Lingenfelter (1992), Hua (1997), and the references therein. The main advantage of these methods is that the microphysics of Compton scattering can be simulated correctly, including all QED corrections, and that the codes are capable of solving the complicated radiative transfer problem. It is difficult, however, to simulate the interaction between the radiation and the corona in a straightforward manner and one has to resort to (messy) iterative methods (see Skibo et al. 1995 for the description of such a method).

*Non-Linear Monte Carlo (NLMC) methods* are a natural extension of the linear Monte Carlo methods. In a NLMC code, the disadvantages of the linear MC method are avoided by directly simulating both the pair-plasma *and* the photon-field in parallel (Stern et al. 1995a; Novikov & Stern 1986; Stern 1985). In other words, instead of simulating one particle at a time, a large number of particles is dealt with. This way, the particles representing the coronal plasma can react directly to changes in the radiation field so that it is very easy to compute self-consistent models for all imaginable geometries with only a modest amount of programming time. A thorough description of the NLMC method is given by Stern et al. (1995a, and references therein), appendix A.2 also gives an introduction to the method. A disadvantage of the non-linear MC method, as well as the linear one, is that the CPU time needed for the computation of one corona model is much higher than for the analytical models (hours compared to minutes on typical workstations).

To summarize, the main advantage of both kinds of analytical methods is that they can be used to gain insight into the physics relevant to the ADC-problem and that they are not very CPU intensive, while their main disadvantage is that an exact solution of the radiative transfer problem is not possible due to problems in the treatment of the coupling between the radiation field and the electron plasma. On the other hand, Monte Carlo methods allow for the exact treatment of all physical processes by being able to simulate the micro-physics in detail, while their disadvantage is that it is difficult to understand the “global picture” due to the large amount of CPU time involved.

The first thermal Comptonization models in which the coupling between the radia-

tion field and the coronal plasma as well as Compton reflection within the cold accretion disk was taken into account were developed in a series of papers by Haardt and collaborators using a hybrid of MC and analytical techniques (Haardt & Maraschi 1991, HM91 henceforth, Haardt & Maraschi 1993, HM93 in the following, and Haardt et al. 1993). These models were done for a plane-parallel accretion disk geometry like that of Fig. 2.11. In the HM93 models, the resulting temperature of the corona was determined by equating Compton cooling with viscous heating. Reprocessing of radiation within the cold accretion disk is also included in their model. While these papers are very important for the current understanding of the physics of ADCs, the models suffer from slight shortcomings that make the application of the resulting spectra to observational data problematic:

1. Since HM93 use the Thomson cross section for the differential cross section instead of the Klein-Nishina cross section, a Wien cutoff rather than a self-consistent spectral shape is used to approximate the spectrum for photon-energies above  $kT_c$  (where  $T_c$  is the coronal temperature). This approximation leads to an underestimation of the pair production rates since the hard tail of the self-consistent spectrum is harder than a Wien tail (Stern et al. 1995b). Recently, Haardt, Maraschi & Ghisellini (1997) have modified the HM93 code such that the high energy roll over is calculated more accurately using a fully relativistic kernel.
2. In addition, the approximation of the high-energy tail by a Wien cutoff leads to a slightly wrong estimate of the Compton cooling rate.
3. Due to the hybrid nature of the HM93 code, line features and the interaction of the Compton reflected spectrum with the corona (and therefore the possibility of multiple reflection) have to be neglected. While this is not a problem for the determination of the thermal balance within the corona, it results in a slightly erroneous estimate of the escaping spectrum that could lead to wrong spectral parameters when applying the model to observational data.
4. The only geometry that can be studied with the HM93 model is the slab-geometry. As I showed in the introduction of this chapter, it is not clear whether this geometry is really the correct geometry in the case of galactic BHs.

In a step towards the inclusion of all relevant physical processes, the work of HM93 was extended by Poutanen and collaborators using the iterative scattering method (Poutanen 1994; Poutanen & Svensson 1996; Poutanen, Svensson & Stern 1997, and references therein). Specifically, Poutanen & Svensson (1996) computed ADC models in which Compton scattering, photon-photon pair production, pair annihilation, bremsstrahlung and double Compton scattering were taken into account, all using the relativistic cross sections. They also included Compton reflection off the accretion disk. With the iterative scattering method it is in principle possible to solve the radiative transfer problem in a “cleaner” way than by using a MC method, but the current implementations of the iterative scattering method that I am aware of are limited to 1D simulations for a finite

number of geometrical configurations and the method is only able to deal with coronae of small optical depth.

Since one of the major aims of the work presented here was to be able to directly compare the spectra resulting from ADC models with the observed spectra of galactic and extragalactic black holes, we decided to use a non-linear Monte Carlo code to compute self-consistent numerical corona models that do not suffer from the shortcomings of the methods described above. The simulated models include the microphysics of electrons, positrons, and photons and their interactions. Although protons and their interactions are not included in the simulations since their cross section for Compton scattering is very small (see p. 24), we specify their initial spatial distribution. Since we enforce charge neutrality and since the electrons are strongly coupled to the protons by Coulomb interactions, the spatial distribution of the electrons (excluding the  $e^- - e^+$ -pairs) is then identical to those of the protons. The physical interactions taken into account are Compton scattering, photon-photon pair production, and pair annihilation, all using the correct quantum-electrodynamical cross sections given in section 2.1. In addition, reprocessing in the accretion disk is taken into account by simulating Compton scattering off cold electrons, photo-absorption in the disk, fluorescent line emission, and thermalization of the irradiated photons in the disk. Contrary to HM93, the reflection component is not simply added to the emerging spectrum but is allowed to interact with the corona like the primary soft radiation from the accretion disk. Therefore, multiple reflections and interactions of reflected photons with the corona are self-consistently taken into account.

In all simulated models the rest-mass energy density of the electrons was several orders of magnitude lower than the radiation energy density. Thus, the collision rate between the electrons and the photons, a measure for the Compton cooling efficiency, was much higher than the collision rate between the electrons and the protons, a measure for the bremsstrahlung cooling rate. Therefore, cooling due to thermal bremsstrahlung can be ignored in the models. In order to allow for a non-uniform temperature distribution within the plasma, the coronae were divided into spatial cells in which the physical conditions (i.e., radiation field, temperature, pair density, etc.) were assumed to be constant. For all models described here, purely thermal electron-positron distributions, i.e., distributions that can be described by a relativistic Maxwellian distribution, were assumed. A brief overview over the technical details of the code is given in appendix A, while a very detailed description of the code, including an users manual, has been presented by Jim Dove in his PhD-Thesis (Dove 1997). The rest of this section is devoted to a description of the results obtained in our simulations.

## 2.2.2 Slab-Corona Models

### 2.2.2.1 Energetics

In the standard plane-parallel slab geometry the electron corona is situated above and below the optically thick, geometrically thin accretion disk (Fig. 2.11). This geometry can be thought of as a simplified picture of the coronae produced by the Balbus-Hawley

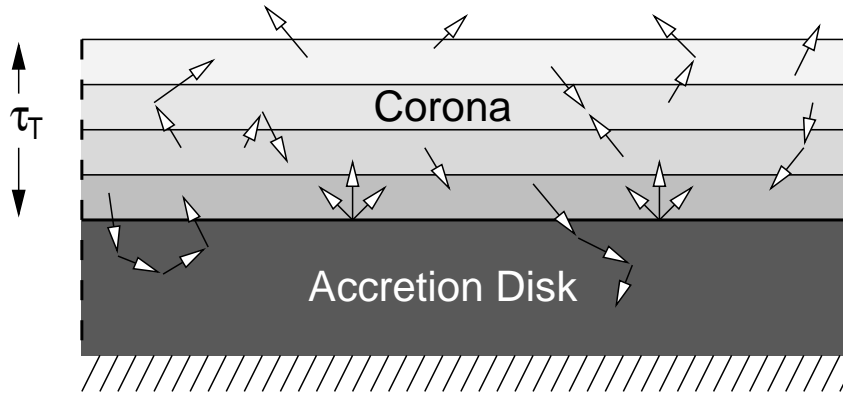


Figure 2.11: Accretion disk corona geometry in slab-geometry: the cold, optically thick accretion disk is sandwiched between two coronae (of which only the upper one is shown). The corona can have a vertical temperature structure. Photons incident onto the disk are either reflected or photoabsorbed (Dove, Wilms & Begelman 1997, Fig. 1).

instability alluded to at the beginning of this chapter. To understand the results of the simulations which will be presented, it is instructive to study the energetics of the system with an analysis analogous to that of HM93. Although this analysis is done here specifically for the slab case, it will be seen later that the analysis is quite general and can be applied to all ADC systems. The flow of energy within the disk-corona system is shown in Fig. 2.12 which will help in understanding the following paragraphs.

Let the total energy dissipated per unit area and unit time interval be  $P_G$ . Of this power, a fraction  $(1-f)P_G$  is dissipated within the accretion disk, while a fraction  $F_c = fP_G$  is directly deposited in the corona. Due to reprocessing of coronal radiation within the disk, the *total* flux of radiation of the accretion disk,  $F_d$ , is due to two parts: the soft photons resulting from the conversion of  $(1-f)P_G$  into radiation, and the flux resulting from the absorption of photons irradiated onto the disk,  $F_{\text{abs}}$ :

$$F_d = (1-f)P_G + F_{\text{abs}} \quad (2.24)$$

while the energetical contribution of the corona is just given by

$$F_c = fP_G \quad (2.25)$$

The absorbed flux,  $F_{\text{abs}}$ , is the fraction of the flux irradiated onto the disk,  $F_c^- = \eta F_c$ , that is not reflected

$$F_{\text{abs}} = F_c^- (1-a) \quad (2.26)$$

where  $a$  is the angle-averaged albedo of the disk. Due to energy conservation the total emitted flux,  $F_{\text{esc}}$  has to be equal to  $P_G$ . Therefore

$$F_{\text{esc}} = F_c - F_{\text{abs}} + F_d = P_G \quad (2.27)$$

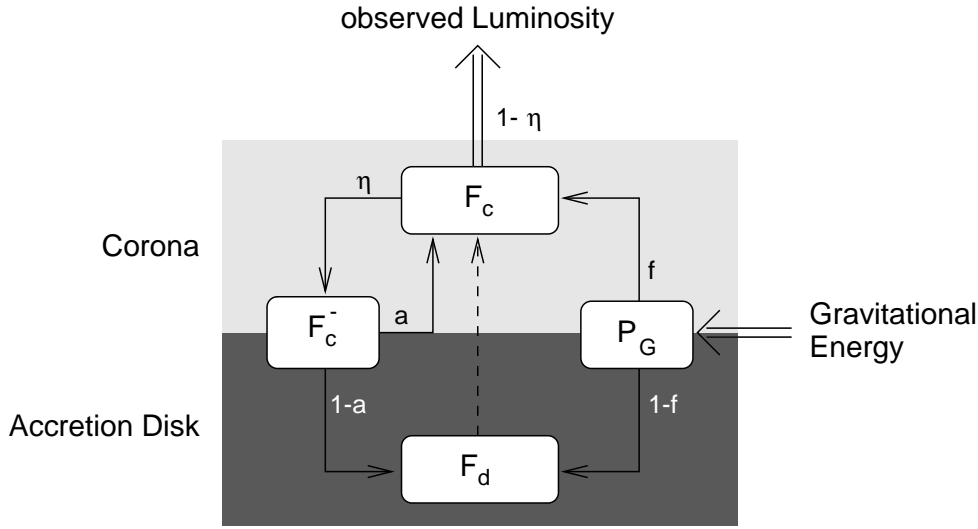


Figure 2.12: Energy flow within the accretion disk-ADC-system.

Instead of working with fluxes it is convenient to express the energy requirement using dimensionless compactnesses, defined by

$$l_i = \frac{\sigma_T}{m_e c^3} z_0 F_i \quad (2.28)$$

where  $i \in \{c, \text{abs}, G, \text{disk}, \text{esc}\}$  and where  $z_0$  is a characteristic length scale of the corona (see the discussion following eq. (2.33) below). The energy requirement of eq. (2.27) can then be written as

$$l_G = l_{\text{esc}} = l_c + l_d - l_{\text{abs}} \quad (2.29)$$

Since the compactnesses are coupled by the energy conservation requirement we are free to set one of them to a predefined value. To simplify programming the NLMC-code, it is a convenient choice to set the intrinsic compactness of the disk,  $(1-f)l_G$ , i.e., the part of  $l_d$  that is due to viscous heating with in the disk, to unity:

$$(1-f)l_G := 1 \quad (2.30)$$

With this (arbitrary) choice the fraction of gravitational energy dissipated into the corona is given by

$$f = \frac{l_c}{1+l_c} \quad (2.31)$$

For  $l_c \gg 1$  this fraction is  $f \approx 1$  and most gravitational energy is dissipated in the corona resulting in  $F_d \approx F_{\text{abs}}$ , while for  $l_c \ll 1$  most gravitational energy is dissipated in the disk and  $F_d \approx P_G$ .



### 2.2.2.2 The Simulations

From the discussion in the preceding section it follows that the corona can be characterized by three parameters, provided that it can be assumed that the disk properties are constant with respect to radius and that the disk is azimuthally symmetric:

1. The seed Thomson optical depth of the electrons,  $\tau_p$ , that is the Thomson optical depth *excluding* the contribution due to the electron-positron-pairs. Since charge neutrality is enforced,  $\tau_p$  is given by

$$\tau_p = \int_0^\infty \sigma_T n_p(z) dz \quad (2.32)$$

where  $n_p = n_{e^-} - n_{e^+}$  is the proton number density.

2. The *local* compactness-parameter of the corona,  $l_c$ , defined as

$$l_c = \frac{\sigma_T}{m_e c^3} z_0 F_c = 0.7 \left( \frac{L_c}{0.1 L_{\text{Edd}}} \right) \left( \frac{100 R_s}{R_c} \right) \left( \frac{z_0}{0.1} \right) \quad (2.33)$$

where  $F_c$  is the rate of energy dissipation per unit area into the corona,  $z_0$  the coronal scale height, and all other symbols have their usual meanings. The parameters are typical for galactic black holes. For the slab geometry,  $l_c$  is related to the *global* compactness parameter used by HM93 by  $l_{c,\text{local}} = l_{c,\text{global}}/\pi$  if  $F_c$  does not vary with height.

3. The temperature of the cold accretion disk,  $T_{\text{BB}}$ , which is thought to be uniform with radius as well – since the Compton cooling is independent of the average seed photon energy, provided that  $kT_{\text{BB}} \ll kT_c$ , this is a good assumption (although it is numerically no problem to relax this assumption as will be shown in §2.2.3).

For each model point defined by  $l_c$ ,  $\tau_e$ , and  $T_{\text{BB}}$ , the NLMC-code was then used to obtain a self-consistent ADC-model for these initial parameters. This model allowed us to obtain the following information:

1. The vertical temperature structure  $T(z)$  of the corona.
2. The total opacity of the ADC,  $\tau_{\text{es}}$ . Since  $\tau_{\text{es}}$  includes a possible contribution caused by pair production, in general  $\tau_{\text{es}} \neq \tau_p$ .
3. The radiation field within the corona.
4. The angle-dependent escaping radiation field, binned into ten bins of equal  $\Delta\mu$  where  $\mu = \cos\theta$  and where  $\theta$  is the angle of the escaping photons with respect to the disk normal.
5. The energy-integrated disk albedo.

In principle, the spatial form of the heating rate is an additional parameter of the code. For the purposes of this thesis, however, only models with a constant heating rate per unit volume were considered.

Contrary to HM93 we did not assume  $f = 1$  when computing the model grid. Instead, models in the range  $0.01 \leq l_c \leq 1000$ , corresponding to  $0.001 \lesssim f \lesssim 1$ , were studied. The disk temperature  $T_{\text{BB}}$  was held fixed for each model, normalizing the total flux of the accretion disk such that the total flux of thermal radiation is consistent with the self-consistent compactness parameter of the disk and assuming the shape of the radiation to be a Planckian. For the models presented here we mainly concentrated on  $T_{\text{BB}} = 200$  eV, a value appropriate for galactic BHs (see chapter 5). Finally, the seed optical depth,  $\tau_p$ , was varied within the range  $0.05 \lesssim \tau_p \lesssim 2$ . Note that varying  $f$ , i.e.,  $l_d$ , and holding  $T_{\text{BB}}$  constant corresponds to varying the scale height  $z_0$  of the disk. Since all of the physical processes considered are linear in the particle density this rescaling does not pose any problem: for a given total optical depth, the self-consistent coronal temperature depends only on the ratio of the coronal compactness to the intrinsic disk compactness, which is a function of  $f$  (see p. 43 and the relevant discussion in HM93 on this topic). In the next sections I describe the results of these simulations in greater detail.

### 2.2.2.3 Thermal Properties of the Corona

In Fig. 2.13 the self-consistent temperature is shown as a function of the total optical depth, for several values of the corona compactness parameter and seed opacities. As was pointed out by HM93, for a given total opacity there is a maximum self-consistent temperature which is independent of the *seed* opacity. The solid line marks this maximum coronal temperature  $T_{\text{max}}(\tau_{\text{es}})$ , as a function of the *total* opacity. This figure is similar to Fig. 1b of HM93 and Fig. 1 of Stern et al. (1995a) but for clarity models that are both pair dominated and non-pair dominated are shown, allowing us to understand how the temperature evolves with the compactness parameter of the corona: for a given total opacity, pair-dominated models reach the maximum temperature with a coronal compactness that is much lower than the corresponding value for non-pair dominated models.

The inset of Fig. 2.13 shows the evolution of models starting with the same seed opacity  $\tau_p = 0.2$  but having a different coronal compactness. For small values of  $l_c$  the temperature increases as a function of  $l_c$  while the opacity remains nearly constant since pair production is negligible for low  $l_c$ . In this regime the Compton cooling rate of the corona is dominated by the soft photons implicitly emitted by the cold accretion disk ( $f \ll 1$ ), and an increase in  $l_c$  corresponds to an increase in the heating rate without much of an increase in the cooling rate. As the corona becomes hotter, the pair production rate increases. Once pair production begins to be significant, the increase in  $\tau_{\text{es}}$  results in an increase of radiation reprocessing within the cold accretion disk. Since most ( $\sim 90\%$ ) of this reprocessed radiation is re-emitted as a thermal blackbody, the increase in the reprocessed radiation causes a very large increase of the Compton cool-

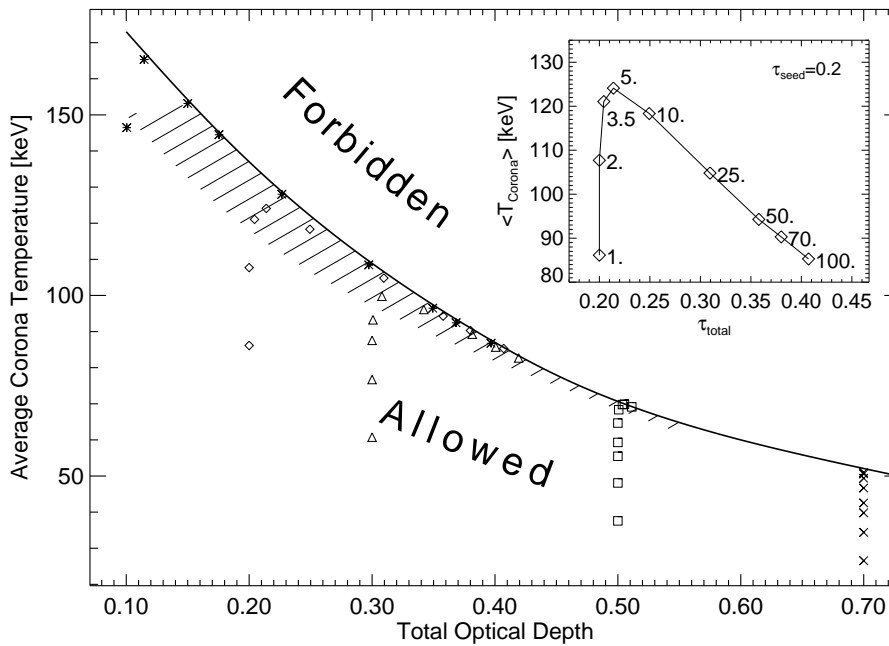


Figure 2.13: Allowed temperature and opacity regime for self-consistent ADC models with a slab geometry. The solid line is derived from a “fit by eye” to the numerical results. For a given total optical depth, temperatures above the solid line are impossible. The hatched region below the solid line marks the parameter space in which the contribution to the total opacity by pairs is significant. The symbols signify models of the same seed opacity but different coronal compactness. For all models, the blackbody temperature of the disk is  $kT_{\text{BB}} = 200$  eV. *Inset:* The average temperature and the total opacity as a function of the coronal compactness parameter (Dove, Wilms & Begelman 1997, Fig. 2).

ing rate within the corona. Thus, through the production of pairs and the increase in reprocessed radiation the Compton cooling rate increases more than linearly with increasing  $l_c$ . Since the heating rate is only proportional to  $l_c$ , the coronal temperature reaches a maximum value and then decreases with increasing  $l_c$  for models where the seed electron optical depth is held constant.

Although  $T_{\text{max}}(\tau_{\text{es}})$  traces the distribution of self-consistent solutions for pair-dominated models, as was mentioned above the maximum temperature (for a given total opacity) is independent of whether the model is pair dominated or not pair dominated. The only difference between these two types of models is that the pair dominated models need a higher coronal compactness to sustain a given total opacity. For the models presented here, the pair-dominated models do not predict an observable annihilation line in the escaping spectrum; thus, for a given total opacity and coronal temperature, the pair-dominated and non pair-dominated models predict the same spectrum of escaping radiation. This degeneracy of models is evident in Fig. 2.13, where models with different seed opacities and compactness parameters sometimes have the same total optical depth and temperature. For this reason, our results are independent of the value of

the intrinsic disk compactness parameter,  $l_G(1-f)$ . This fact justifies our setting of the intrinsic disk compactness to unity (p. 42). If this value were set to a higher value, the Compton cooling rate would be higher, but the same maximum temperatures would be reached with higher  $l_c$  values. If  $l_G(1-f)$  were decreased, the models in which  $l_c \gg 1$  would not be altered since the thermal emission is already dominated by reprocessed radiation. For models where  $l_c \lesssim 1$ , holding the seed opacity constant while decreasing  $l_G(1-f)$  simply reduces the Compton cooling rate and precludes the cooler regions of Fig. 2.13 (lower left region) from being self-consistent. In other words: reducing the value of the intrinsic disk compactness parameter drives the solutions towards the pair-dominated,  $f \sim 1$ , regime. All of these arguments have been confirmed by numerical simulations.

As was mentioned in on p. 42, the black-body temperature used for the models is  $T_{\text{BB}} = 200 \text{ eV}$ . However, the results presented above are very insensitive to the disk temperature. For example, a corona with a total optical depth  $\tau_{\text{es}} = 0.25$  and a disk temperature  $T_{\text{BB}} = 5 \text{ eV}$  has a maximum temperature  $T_{\text{max}} = 117 \text{ keV}$ , compared to  $T_{\text{max}} = 128 \text{ keV}$  for the  $T_{\text{BB}} = 200 \text{ eV}$  case. Therefore, models with very low disk temperatures, which are attractive in the sense that the thermal-excess might not be observable due to the interstellar absorption of ultraviolet radiation, have maximum corona temperatures that are colder than the values presented above. On the other hand, models with a higher black-body temperature predict even larger thermal-excesses than those corresponding to a 200 eV disk.

The major conclusion of this section is that accretion disk coronae cannot have a temperature higher than  $\sim 130 \text{ keV}$  if the total optical depth is greater than about 0.2, regardless of the coronal compactness parameter, the intrinsic accretion disk compactness parameter, and the black-body temperature. Alternatively, ADCs with a temperature  $\gtrsim 150 \text{ keV}$  cannot have an optical depth greater than  $\sim 0.15$  (see Fig. 2.13). This range of parameters corresponds to a minimum value of the photon index of  $\Gamma \sim 1.8$ , which places severe limitations on the applicability of these models to observed black hole spectra<sup>1</sup>. As will be demonstrated in chapter 5, the observed hard power-laws in BHs can only be explained with models having photon-starved sources, where Compton cooling is less efficient and the coronae are allowed to have higher temperatures.

#### 2.2.2.4 Non-Uniform Temperature Structure

Our models allow for the determination of the temperature and opacity within local cells, allowing for the possibility of non-uniform temperature structures.

In Fig. 2.14, the relative temperature deviation ( $\Delta T/T_{\text{avg}}$ ) for assorted values of  $\tau_p$ ,  $T_c$  and  $l_c$  is given. Note that, for optically thin models ( $\tau_p \lesssim 0.3$ ), the temperature is essentially uniform, while the temperature varies up to a factor of three for optically thick models. For  $\tau_p \gtrsim 0.5$ , the region nearest the accretion disk is always the coldest,

<sup>1</sup>Note that due to the ‘‘anisotropy break’’ in the spectrum (HM93) the power-law portion of the spectrum hardens with decreasing inclination angle. For models with  $\tau_{\text{es}} = 0.3$  and  $kT_c = 110 \text{ keV}$  where the angle averaged photon index is  $\Gamma \approx 1.8$ , the angle dependent photon index varies from 2.1 when the corona is seen ‘‘edge on’’ to 1.7 for a ‘‘face on’’ disk.

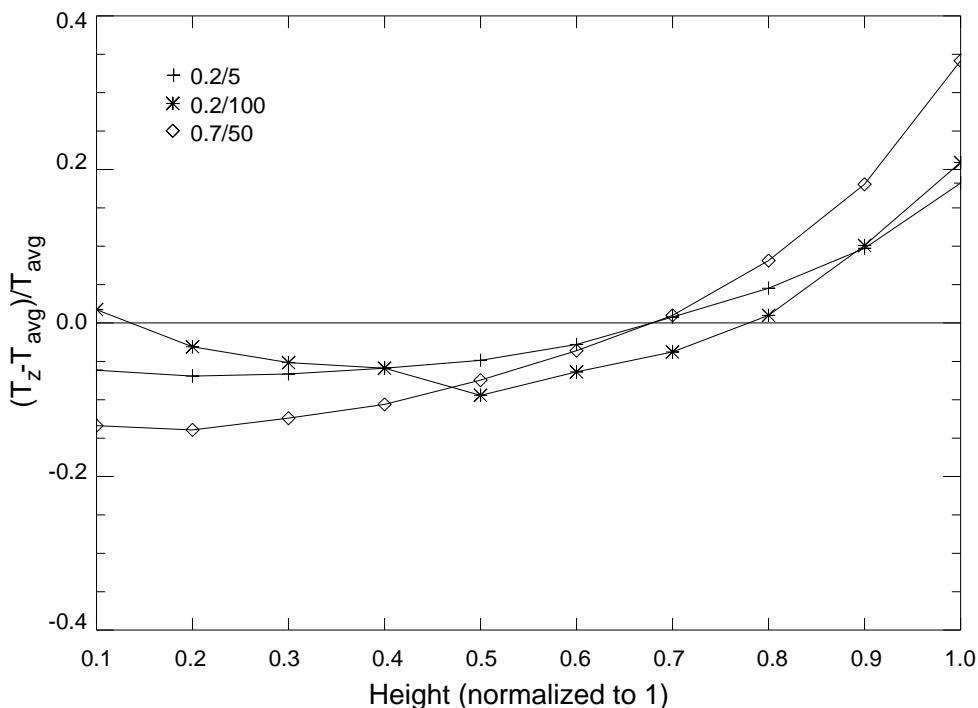


Figure 2.14: Vertical temperature structure of the accretion disk corona expressed as the relative deviation of the local temperature,  $T(z)$ , from the volume averaged corona temperature  $T_{\text{avg}}$ . Several models, with different combinations of the seed optical depth  $\tau_p$  and coronal compactness parameter  $l_c$ , are shown (Dove, Wilms & Begelman 1997, Fig. 3).

while the region farthest away from the disk (largest values of  $z$ ) is the hottest. This is easily understood since the energy density of the radiation field decreases with increasing height, and therefore the Compton cooling rate decreases with  $z$ . In optically thin coronae, on the other hand, the energy density of the radiation field does not vary too much with height, but the average energy of the radiation field does increase due to the hardening of the spectrum of the internal radiation field with increasing height. Therefore, since the Compton cooling rate is proportional to both the average energy,  $\langle \epsilon \rangle$ , and the energy density, the minimum temperature can occur at intermediate heights rather than always at  $z = 0$ .

### 2.2.2.5 The Emerging Spectrum

Fig 2.15 shows the comparison of the spectra resulting from models with a non-uniform temperature structure to those resulting from models where the temperature does not change with height for a range of model parameters. Note that these models are not self-consistent. For the optically thin models the thermal gradients do not give rise to any significant changes in the spectral shape of the radiation field and the fractional difference between the uniform and the nonuniform models is always less than 1%. Therefore, in order to obtain spectra that differ significantly from models with a uniform heating, a nonuniform distribution of the heating rate that significantly amplifies the temperature gradient would be required and Compton cooling alone is not sufficient.

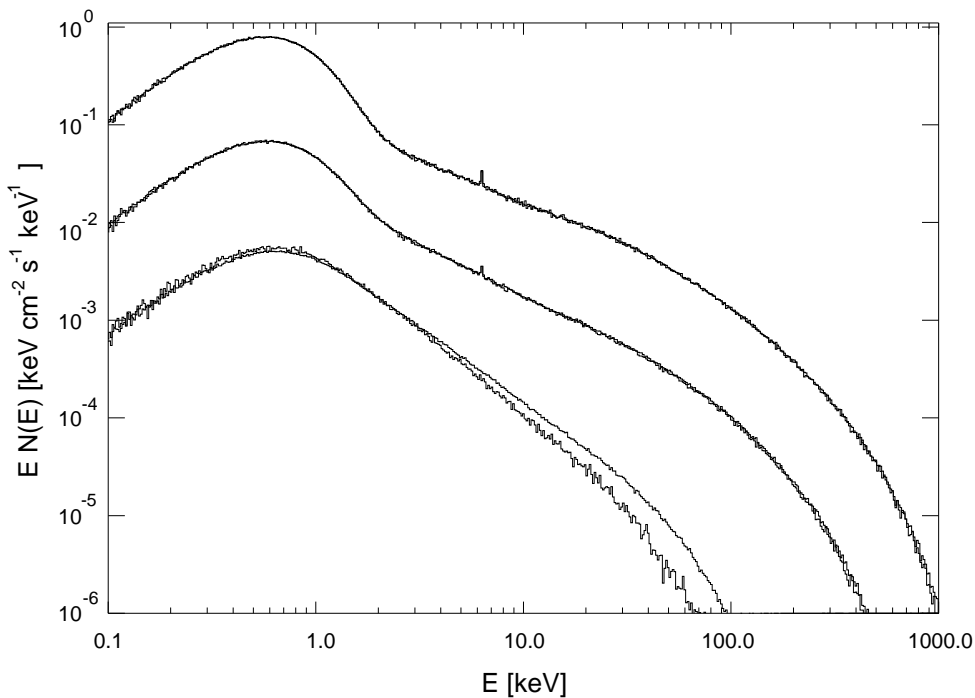


Figure 2.15: A comparison of the spectra emerging from the non-linear ADC models with those emerging from linear models with a uniform vertical temperature distribution. From top to bottom, the average temperature and total optical depth  $\{kT_{\text{avg}}(\text{keV}), \tau_{\text{es}}\}$  are:  $\{118.4, 0.25\}$ ,  $\{69.8, 0.50\}$ , and  $\{15.6, 2.0\}$ . Smooth spectra represent the non-linear models, the noisier ones are spectra emerging from the linear models. For clarity, each spectrum is normalized to an arbitrary value (Dove, Wilms & Begelman 1997, Fig. 4).

For parameters appropriate for low mass X-ray binaries, where  $\tau_{\text{es}} \gtrsim 1$ , the spectrum of the escaping radiation is significantly different than the corresponding spectra resulting from a uniform model, especially at high energies where the non-uniform model produces a slightly harder high energy tail. This hard tail is caused by the small contribution to the spectrum of the uppermost region of the corona, where the temperature is hotter than the average coronal temperature.

#### 2.2.2.6 Anisotropy of the Escaping Radiation Field

In Fig. 2.16 the spectrum of the escaping radiation for several values of the inclination angle is shown. We define  $\mu = \cos(\theta)$ , where  $\theta$  is the angle between the line of sight and the normal of the accretion disk. As expected, the spectral shape does not vary with respect to the inclination angle for optically thick models. However, for optically thin models, the spectral shape of the escaping radiation field (and the internal radiation field) *does* vary with  $\mu$ . Since the effective optical depth for radiation leaving the accretion disk is  $\tau/\mu$ , the fraction of black-body radiation that escapes the system without subsequent interactions with the corona decreases with decreasing  $\mu$ . Consequently, the thermal-excess weakens with decreasing values of  $\mu$ . Finally, as  $\mu$  decreases, the spectrum becomes softer since the magnitude of the reflection ‘hump’ decreases. These

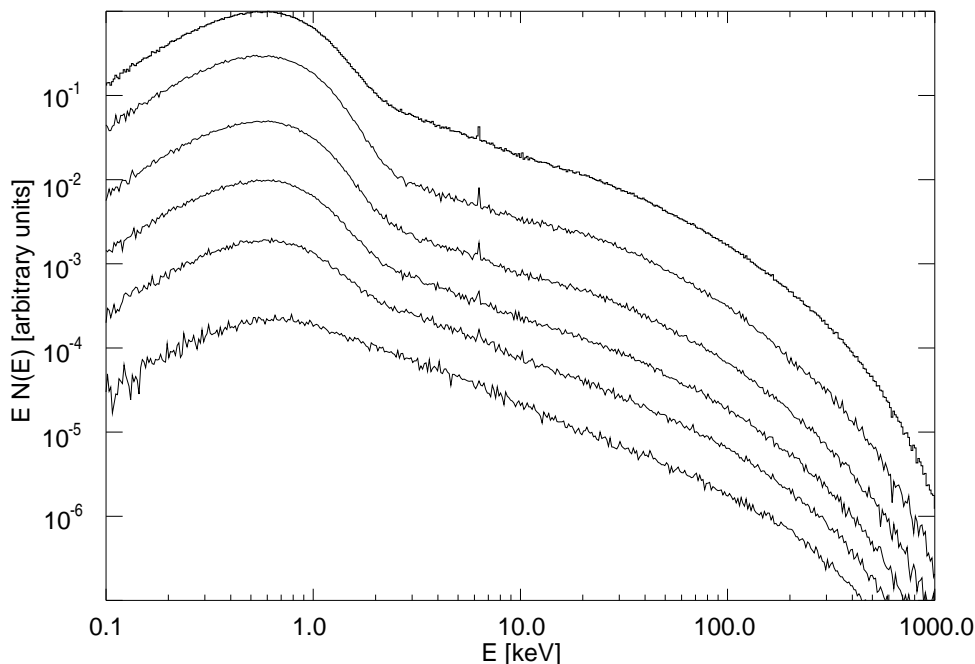


Figure 2.16: The spectrum of escaping radiation for several values of  $\mu = \cos(\theta)$ . The uppermost plot is the spectrum averaged over all angles. Below, in order,  $\mu = 0.9, 0.7, 0.5, 0.3,$  and  $0.1$ . For all cases, the average temperature is  $kT_{\text{avg}} = 118$  keV, the optical depth is  $\tau_{\text{cs}} = 0.25$ , and the black-body temperature of the disk is  $kT_{\text{BB}} = 200$  eV (Dove, Wilms & Begelman 1997, Fig. 5).

results are in agreement with HM93. Therefore, the spectra of ADCs that are seen “face on” ( $\mu = 1$ ) are the hardest, but they also have the largest amount of thermal excess. On the other hand, ADCs viewed “edge on” do not have an observationally recognizable soft-excess in their spectra nor do they contain reprocessing features. If the matter responsible for producing the “reflection features” is the optically thick, cold accretion disk that is producing the seed photons, it does *not* appear possible that the spectra of ADCs can have strong reflection features without also containing a strong soft excess. While a very cold accretion disk (i.e.,  $kT_{\text{BB}} \lesssim 10$  eV) would produce thermal emission that could be “hidden” due to the efficient Galactic absorption of UV radiation, it is questionable whether an accretion disk of a BH, in the radial region where most of the X-rays are produced, could stay so cold without heating up.

### 2.2.2.7 Strength of the Fe $K\alpha$ Fluorescence Line

The strength of the Fe  $K\alpha$  fluorescence line for BHs provides stringent constraints on the properties of ADC models. For a slab geometry, roughly half of the Comptonized radiation field within the corona is reprocessed within the cold accretion disk. For parameters appropriate for BHs, where the radiation field is hard (having a photon index of  $\Gamma \sim 1.5$ ), the large amount of reprocessing gives rise to a very large Equivalent Width

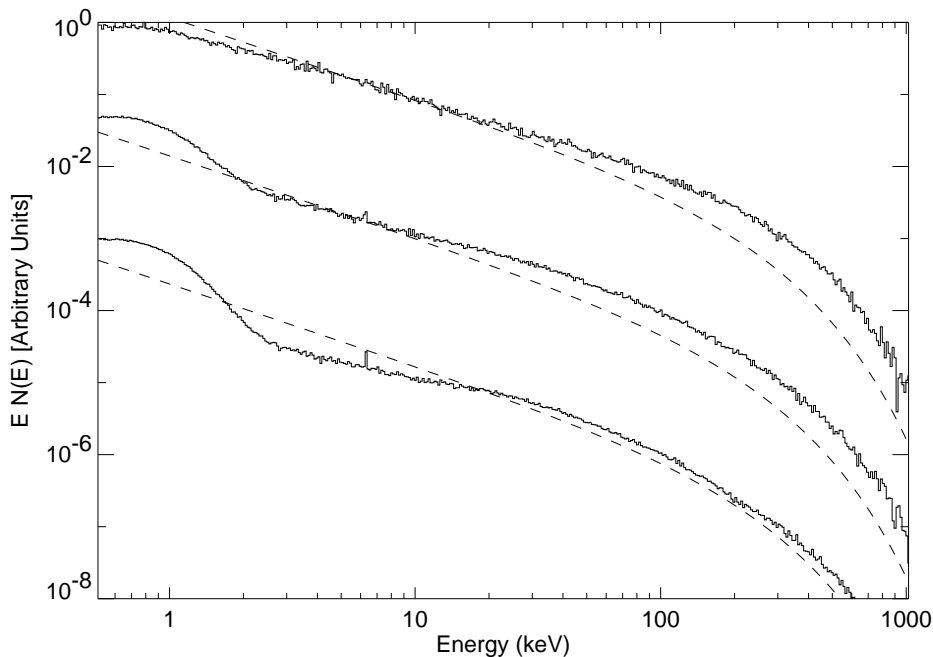


Figure 2.17: Comparison of the predicted spectrum of escaping radiation with the analytic model of Hua & Titarchuk (1995), for several inclination angles. Solid lines correspond to our model, and the dashed lines correspond to Titarchuk’s model. From top to bottom,  $\mu = 0.1, 0.5,$  and  $0.9$ . Again,  $kT_{\text{avg}} = 118$  keV,  $\tau_{\text{cs}} = 0.25$ , and  $kT_{\text{BB}} = 200$  eV (Dove, Wilms & Begelman 1997, Fig. 6).

(EW) of the Fe  $K\alpha$  line. For emission lines the EW is defined as

$$\text{EW} = \int_0^\infty \frac{F(E) - C(E)}{C(E)} dE \quad (2.34)$$

where  $F(E)$  is the total model flux, *including* the emission line, and  $C(E)$  is the pure model continuum, *without* the emission line. For the optically thin, hot corona models, the angle averaged EW varies between about 90 eV and 120 eV. Due to the statistical nature of the simulations it is not possible to determine better values for the EW. The predicted EWs would be even higher than these values if a harder spectrum, i.e., a spectrum with a spectral shape that better describes the observational evidence from Cyg X-1, were incident onto the accretion disk. Simulations with the linear Monte Carlo code indicate that an incident radiation field with  $\Gamma = 1.5$  and an exponential cutoff at 150 keV irradiated onto a cold disk leads to an iron EW of 150 eV for a “face on” orientation (see Wilms 1996 for details). Since the observed EWs are typically  $\lesssim 100$  eV, this is yet another indication that the slab geometry might not be the correct geometry for galactic BHs.

#### 2.2.2.8 Comparisons to Previous Models

The major difference between the self-consistent models and the analytic Comptonization models of Sunyaev & Titarchuk (1980) and Hua & Titarchuk (1995) is that the



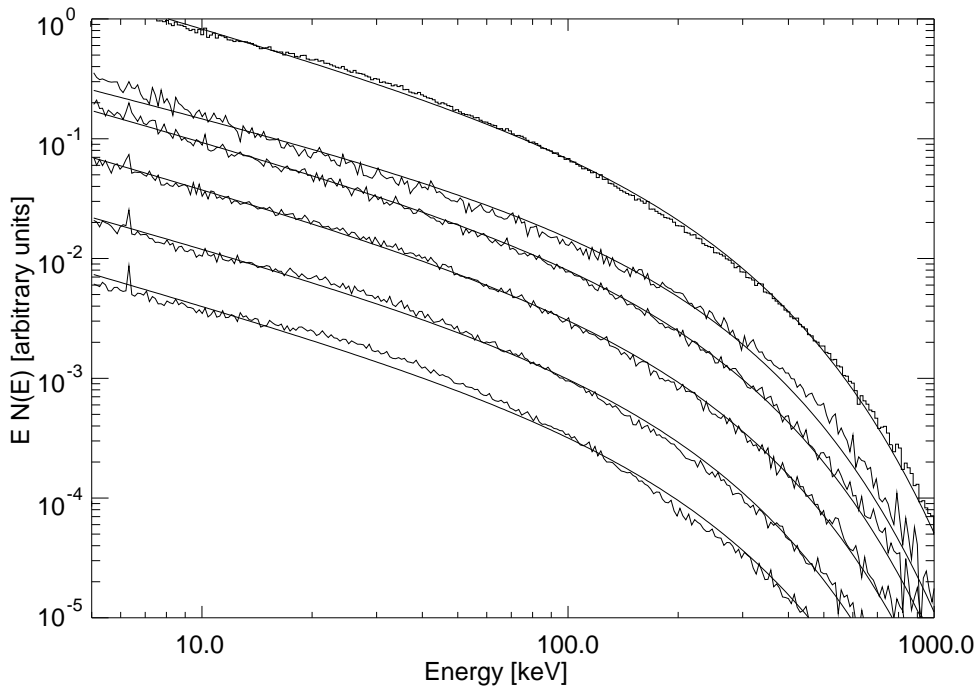


Figure 2.18: Comparison of the predicted spectrum of escaping radiation with spectra of the form  $F(E) \propto E^{-\gamma} \exp(-E/E_{\text{cut}})$ . The uppermost spectrum is the angle-averaged spectrum; then, from top to bottom,  $\mu = 0.1, 0.3, 0.5, 0.7,$  and  $0.9$ . The model parameters are the same as in Fig. 2.17 (Dove, Wilms & Begelman 1997, Fig. 7a).

former models take into account the reprocessing of radiation within the cold accretion disk, giving rise to reflection features in the spectra. In addition, the self-consistent models give a more accurate description of the transition between the thermal blackbody (seed photons) and the Comptonized portion of the spectrum since Titarchuk’s analytical model is only valid for energies much higher than the energy of the seed photons (cf. §2.1.1). It is therefore expected that the two models will predict different spectra of escaping radiation. However, due to the popularity of these analytic models, it is necessary to compare our models with the XSPEC version of the Hua & Titarchuk (1995) models (Fig. 2.17).

Although the two models differ significantly, they *do* agree for energies much higher than  $kT_{\text{BB}}$  if the “reflection” features and the soft excess are ignored. However, the modeled high-energy tails do not decrease with increasing energy as rapidly as those predicted by the analytic model. This disagreement has previously been noted by several other authors (Stern et al. 1995a; Skibo et al. 1995).

As shown in Fig. 2.18, we have also attempted to describe the simulated spectra by a power-law with an exponential cut-off,

$$N_E = F_0 E^{-\alpha} \exp(-E/E_0) \quad (2.35)$$

where  $N_E$  is the photon flux as a function of the energy  $E$ . Although very good fits for the angle-averaged spectra are possible, there are large deviations when looking at the

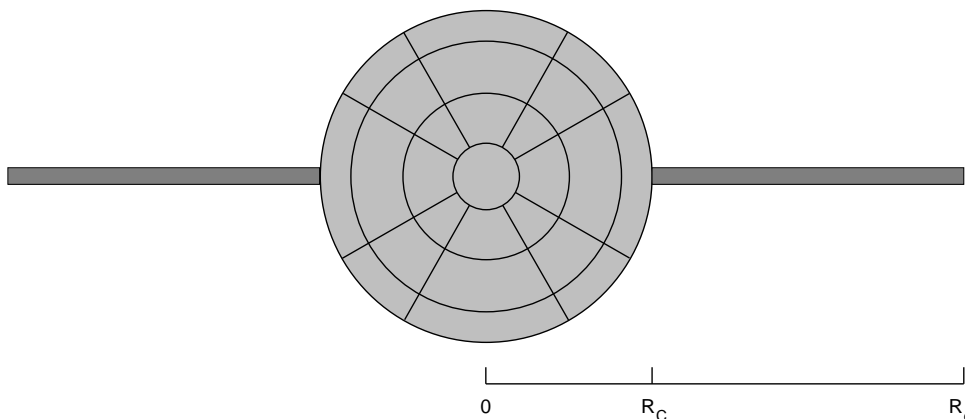


Figure 2.19: The sphere+disk geometry. The inner spherical corona has a radius  $R_c$  and the outer accretion disk (assumed to be optically thick) extends from the inner radius  $R_c$  to the outer radius  $R_d$ . In the computations the disk is assumed to be infinitely thin, the vertical extent shown here is for illustration only. For the computations the corona is subdivided into several radially symmetric zones as indicated to enable the study of the temperature structure (Dove et al. 1997, Fig. 2).

individual angle dependent spectra. This problem is due to the presence of reflection features. The fits become better as the inclination angle increases since the strength of reprocessing features decreases with increasing  $\mu$  (§2.2.2.6). When the reflected component of the radiation field is subtracted from the spectra of escaping radiation, good fits are again possible. The reflected component subtracted from the escaping component is the reflected component evaluated just above the accretion disk. Since subsequent Comptonization of reprocessed radiation is possible, the escaping photon spectrum is not simply the sum of the spectra of the reprocessed radiation and “non-reprocessed” Comptonized radiation. However, this approximation is good for optically thin models since most reprocessed radiation escapes the corona without additional interactions.

Finally, we tried fitting the slab models with functions that include a reflection hump. A corona model with  $kT_{\text{BB}} = 200$  eV,  $k\langle T_c \rangle = 118$  keV,  $\tau_{\text{es}} = 0.25$ , and  $\mu = 0.9$  can be well described with an exponentially cut-off power-law with  $\Gamma = 2$ ,  $E_{\text{cut}} = 400$  keV, and a relative reflection parameter of  $f_{\text{cov}} = 0.48$ . The comparison of the best fit spectrum with the model includes additional structure that shows the danger of simply assuming that a Comptonized unreflected spectrum can always be described by an exponentially cut-off power-law. It is interesting to note that the best-fit covering fraction of the reflection spectrum is  $f < 0.5$ , given that the physical covering fraction for the slab geometry is unity.

### 2.2.3 The Sphere+Disk Geometry

Although the slab corona models give rise to some very interesting physics, their value in explaining observed spectra of galactic black holes seems to be small. The main limitation of the slab geometry models, in regard to explaining the high-energy spectra of the hard state of black holes, is that there is too much reprocessing of coronal radiation in the cold accretion disk resulting in the low maximum temperatures shown in Fig. 2.13.

Therefore, models with the reprocessing matter having a smaller covering fraction (as seen from the corona) are more likely to explain the observations. As I explained in the introduction, one such geometry is a combination of a spherical corona of radius  $R_c$  with an optically thick, geometrically thin, cold accretion disk where the accretion disk (starting at  $R_c$  and extending out to  $R_d$ ) is assumed to be exterior to the sphere (Fig. 2.19). This geometry is very similar to the two-temperature accretion disk model of Shapiro, Lightman & Eardley (1976), although, in the model presented here, the proton temperature is assumed to be equal to the electron temperature. Thus, the geometry is also similar to the advection-dominated disk models by Narayan and collaborators (Narayan 1996b, and references therein), although the seed photons for Comptonization are produced by the accretion disk through thermal emission rather than by bremsstrahlung and synchrotron radiation within the corona.

Similar to the slab geometry, the major model parameters are the coronal compactness parameter  $l_c$  and the optical depth of the corona. For the sphere+disk geometry the coronal compactness parameter can be defined by

$$l_c = \frac{\sigma_T}{m_e c^3} \frac{L_c}{R_c} = 4\pi \left( \frac{m_p}{m_e} \right) \frac{L_c}{L_{\text{edd}}} \frac{R_s}{R_c} = 23 \left( \frac{L_c}{0.1 L_{\text{edd}}} \right) \left( \frac{100 R_s}{R_c} \right) \quad (2.36)$$

where  $R_s$  is the Schwarzschild radius and  $L_c$  is the luminosity of the corona. It is easy to see that the discussion of the energetics of the slab ADC system in section 2.2.2.1 equally applies to the sphere+disk system since nowhere in that discussion was there any reference to any specific parameter of the geometry. This means that we are again allowed to set the intrinsic disk compactness to unity,  $(1-f)l_G = 1$ , without affecting the physical space accessible to the models. With this normalization the fraction of gravitational energy dissipated within the corona is again given by

$$f = \frac{l_c}{1+l_c} \quad (2.37)$$

A major difference in the numerical treatment of the sphere+disk geometry as opposed to the slab geometry is that the whole sphere+disk system has to be simulated in parallel, since the volume in which the Comptonization happens is so far away from the disk. Thus the thermal structure of the accretion disk has to be considered in detail. In the case of the slab disk it was possible to just set the disk temperature to a certain value, in the case of the sphere+disk geometry it is not obvious that a similar treatment is justified. Before presenting the results from the numerical simulations on the sphere+disk geometry, therefore, the consequences of this “global” approach to the ADC system have to be studied. Section 2.2.3.1 is devoted to the presentation of some simple physical models studying the influence of the coronal luminosity on the temperature structure of the disk, while the following section 2.2.3.2 looks at the amount of disk radiation that is leaving the system freely, without ever interacting with the corona. It is this radiation that is responsible for the soft excess observable in galactic BHs. Only after these two analytical sections are the properties of the corona-disk system as a whole described (§2.2.3.3).

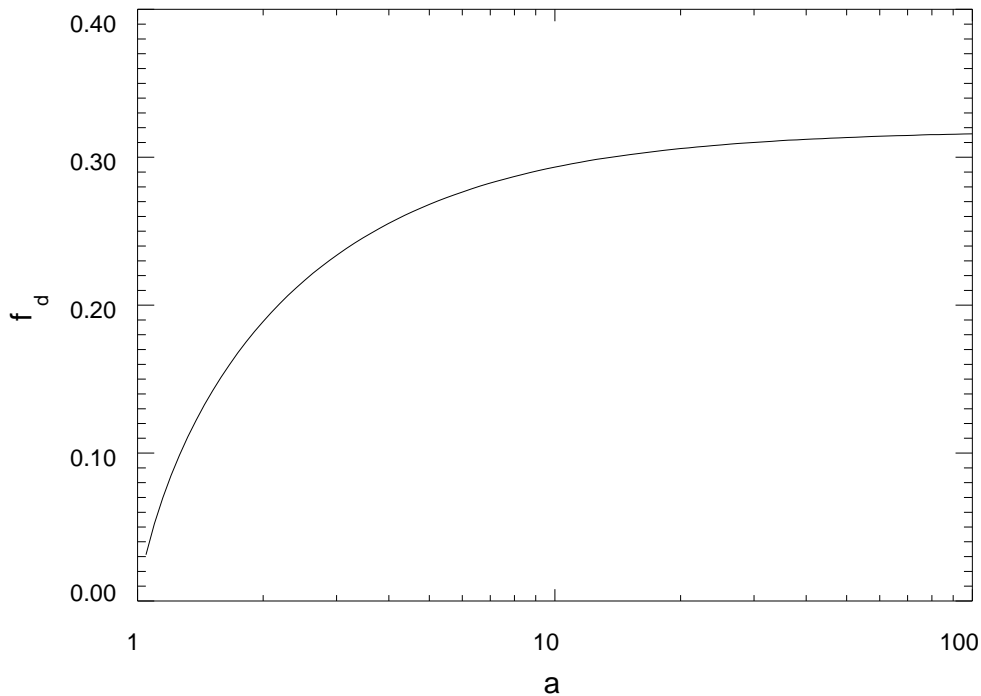


Figure 2.20: Covering fraction  $f_d(a)$  of the accretion disk as a function of the normalized outer radius  $a = R_d/R_c$ , averaged over the surface of the corona (Dove et al. 1997, Fig. 3).

Since many of the results from the slab geometry carry over to the sphere+disk geometry, only physical properties differing from those of the slab geometry are described, mainly the existence of a regime of much hotter coronae.

### 2.2.3.1 The Temperature Structure of the Disk

A description of the physics of centrally illuminated disks as a whole is outside the scope of this thesis, since such a study would also have to include the effects of the internal heating. Thus, this discussion will be concentrating on simple analytical results for some important limiting cases. First, the disk will be looked at from a global point of view to find an expression for the average disk temperature. This expression can then be used to make a statement on local quantities, i.e., to find the radial temperature structure of the disk.

The lowest limit for the temperature of a centrally illuminated disk is obtained by assuming that the disk is heated solely by the hard radiation, that is by assuming that  $f \sim 1$ . Then

$$\pi R_c^2 (a^2 - 1) \sigma_{\text{SB}} \langle T_{\text{BB}} \rangle^4 = (1 - A) \frac{L_c}{2} f_d(a) \quad (2.38)$$

where  $a = R_d/R_c$  is the ratio of the outer disk radius to the corona radius,  $L_c$  is the total luminosity for photons leaving the corona,  $f_d(a)$  is the fraction of these photons that is hitting the disk, and  $A$  is the albedo of the disk. Although  $f_d$  is in general a very complicated function, a good approximation is to assume that the photons leaving the

corona are uniformly distributed over the coronal surface with an isotropic distribution. With these assumptions, the fraction of photons hitting the disk is given by

$$f_d(a) = \frac{\langle \Delta\Omega \rangle}{2\pi} = \frac{1}{2\pi} \int_{\theta_m}^{\pi/2} \sin(\theta) \Delta\Omega(\theta) d\theta, \quad (2.39)$$

where  $\langle \Delta\Omega \rangle$  is the average solid angle of the disk as seen from the surface of the corona. The other terms in the integral are the angle between the normal of the coronal surface and the plane of the disk,  $\theta$ , as well as  $\theta_m = \arcsin(1/a)$ , and

$$\Delta\Omega(\theta) = \int_{\csc\theta}^a \frac{2 \cos \theta}{x^2 + 1 - 2x \sin \theta} \left( \frac{a^2 - x^2}{a^2 + 1 - 2x \sin \theta} \right)^{1/2} dx \quad (2.40)$$

where  $\csc \theta = 1/\sin \theta$ . Both integrals have to be evaluated numerically. Fig. 2.20 shows how the covering fraction depends on  $a$ . For  $a \gtrsim 10$  the covering factor is nearly constant with an asymptotic value of about 0.35, so that the amount of reprocessing of radiation within the accretion disk is insensitive to  $a$  in this regime. This *maximum* possible covering factor should be compared with the covering factor in the slab geometry, where all of the downward directed radiation at the base of the corona interacts with the accretion disk resulting in  $f_{d, \text{slab}} \sim 1$ . Thus, the spectra obtained from the sphere+disk geometry are predicted to contain much weaker reprocessing features than those from the disk geometry – in agreement with the observational evidence from galactic BHs, which also points towards small covering factors.

Since it is very plausible that the outer parts of the accretion region still form a disk with a radial extent that is much larger than the sphere radius, it is very probable that covering factors smaller than 0.35 do not exist in nature. To simulate such realistic systems, we therefore chose to set  $a = 10$  for our computations. Hence, the computed spectra represent models with the maximum amount of reprocessing possible for the sphere+disk geometry.

The exact shape of the spectrum observed from the sphere+disk system depends on the radial temperature structure of the disk. Since even in an  $\alpha$ -disk the radial temperature structure results in a spectrum that is quite different from a pure Planckian (Shakura & Sunyaev 1973), this difference should be even more prominent in the case of the sphere+disk geometry since heating close to the sphere is much more efficient due to the inverse square law. The local temperature is found from the local energy balance by equating the absorbed coronal flux with the with the local thermal emissivity

$$\sigma_{\text{SB}} T_{\text{BB}}^4(r) 2\pi r dr = \frac{1}{2}(1 - A)L_c df_d \quad (2.41)$$

where  $r = R/R_c$ ,  $A$  is the local albedo,  $df_d(r)/dr$  is the differential covering fraction of a ring of radius  $r$ , and  $f_d(r)$  is determined numerically using eq. (2.24). Note that eq. (2.41) is just the derivative of eq. (2.38) with respect to  $r$ . With eq. (2.36), the temperature is then given by

$$T_{\text{BB}}(r) = 150 \left( \frac{df_d(r)}{dr} \right)^{1/4} \left( \frac{l_c}{25} \right)^{1/4} \left( \frac{100R_s}{R_c} \right)^{1/4} \left( \frac{10M_\odot}{M} \right)^{1/4} \text{ eV} \quad (2.42)$$

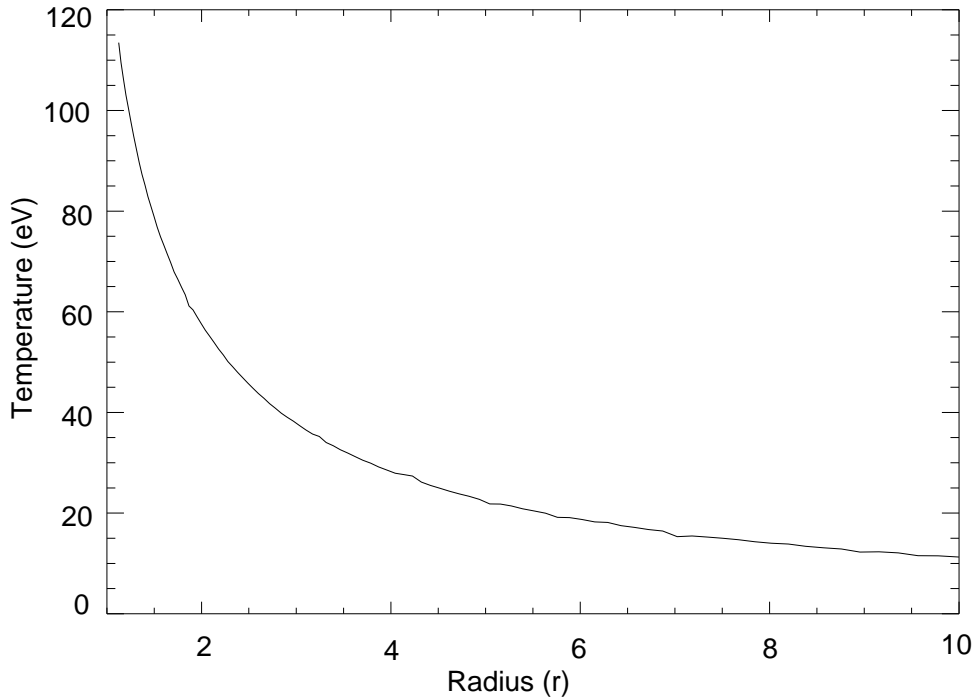


Figure 2.21: Temperature of the accretion disk as a function of radius assuming that the disk is heated solely by hard radiation intercepted from the spherical corona. The profile has been computed for  $l_c = 25$ ,  $M = 10 M_\odot$ , and  $R_c = 100 R_s$  (Dove et al. 1997, Fig. 4).

Therefore the sphere+disk model predicts an “effective” disk temperature that is much lower than in the slab geometry models. Fig. 2.21 shows how  $T_{\text{BB}}(r)$  varies with  $r$ .  $T_{\text{BB}}(r)$  roughly decreases as  $T_{\text{BB}}(r) \propto r^{-1.1}$ , i.e. the disk cools off much faster than the standard  $\alpha$ -disk models where  $T_{\text{BB}}(r) \propto r^{-3/4}$  (Shakura & Sunyaev 1973).

If any accretion-energy were dissipated directly into the accretion disk ( $f < 1$ ), then the disk temperature would be higher than the values given above. In order to determine the relative importance of the internal dissipation of energy, compared to the contribution from coronal illumination, one can look at a model where, for  $R > R_c$ , the accretion disk behaves as the standard optically thick  $\alpha$ -disk, while all of the accretion energy is dissipated in the corona for  $R < R_c$ . In this case the disk temperature can be expressed as

$$\begin{aligned}
 kT_{\text{BB}}(R) &= k \left( \frac{3}{16} \frac{m_{\text{pc}}^5}{GM\sigma_{\text{SB}}\sigma_{\text{T}}} \right)^{1/4} \left( \frac{L_{\text{acc}}}{\eta L_{\text{edd}}} \right)^{1/4} \left( \frac{R}{R_s} \right)^{-3/4} \\
 &= 55 \left( \frac{10M_\odot}{M} \right)^{1/4} \left( \frac{L_{\text{acc}}}{\eta L_{\text{edd}}} \right)^{1/4} \left( \frac{R}{100R_s} \right)^{-3/4} \text{ eV.}
 \end{aligned} \tag{2.43}$$

(see Dove et al. 1997 for a derivation of this formula). Thus the heating rate due to the direct dissipation of accretion energy is comparable to that from coronal illumination showing the need for a better theory of centrally illuminated accretion disks. However, since  $T_{\text{BB}}^4$  is proportional to the total heating rate per unit area, doubling the heating

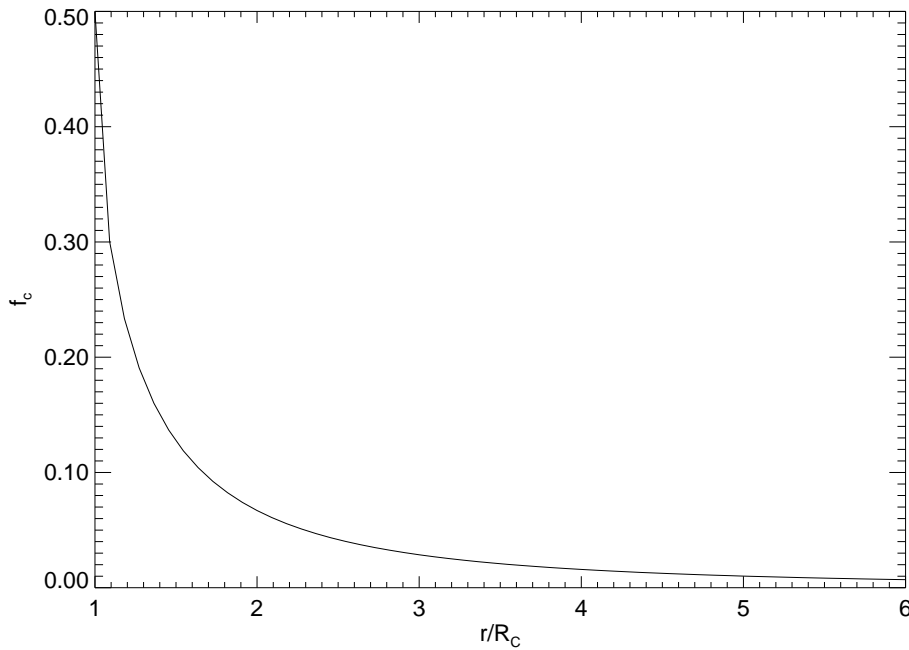


Figure 2.22: Covering factor of the corona as seen from the disk at a distance  $r$  from the center of the sphere (eq. [2.44], Dove et al. 1997, Fig. 5).

rate would only change the resulting disk temperature by a factor of  $2^{(1/4)}$ . Therefore, although the inclusion of direct energy dissipation into the disk would change the disk's total luminosity, the effect on the radial temperature profile would be small.

### 2.2.3.2 The Soft Excess

A major difference between the slab geometry and the sphere+disk geometry is that (by construction) a large amount of soft radiation never has to interact with the sphere. This is exactly what is needed to obtain the higher coronal temperature, but has also a directly observable consequence: even for optically thick coronae there should still be a large excess of soft radiation visible in the emerging spectrum. The covering fraction of the corona, evaluated on the accretion disk at a radial distance  $r$  from the center, is given by

$$f_c(r) = \frac{\Delta\Omega}{2\pi} = \frac{1}{2} \left[ 1 - \sqrt{1 - \left(\frac{R_c}{r}\right)^2} \right] \quad (2.44)$$

This function rapidly decreases with  $r$  (Fig. 2.22). In order to obtain an estimate of what fraction of the energy emitted by the accretion disk interacts with the corona,  $f_c$  is averaged over the accretion disk, weighted by the thermal flux,  $F(r)$ ,

$$\langle f_c \rangle(a) = \frac{\int_1^a 2\pi r f_c(r) F(r) dr}{\int_1^a 2\pi r F(r) dr} \quad (2.45)$$

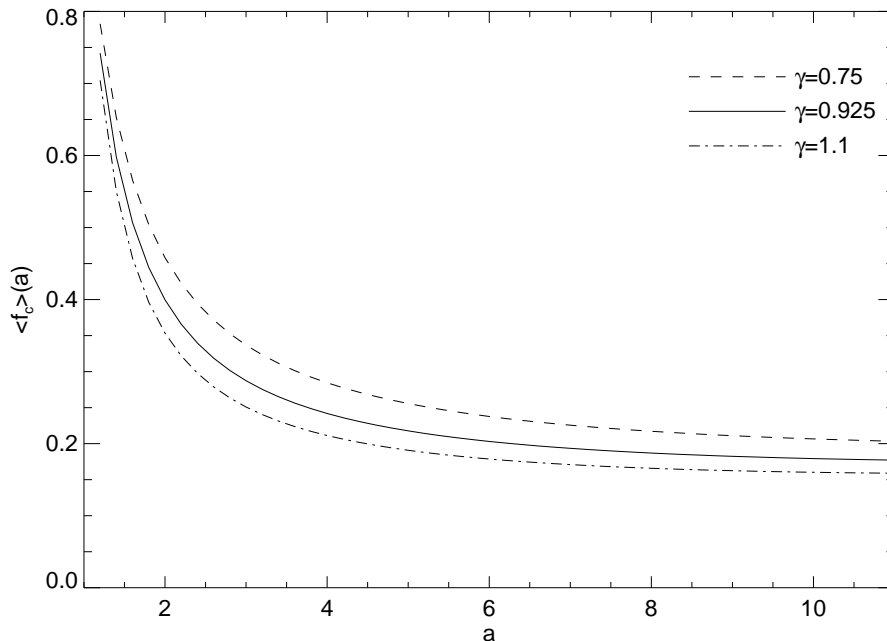


Figure 2.23: Average covering factor of the corona as a function of outer disk radius,  $\langle f_c \rangle(a)$ , for different radial temperature profiles,  $T(r) \propto r^{-\gamma}$ .  $\gamma = 0.75$  corresponds to the  $\alpha$ -disk of Shakura & Sunyaev (1973),  $\gamma = 1.1$  is a centrally illuminated accretion disk (eq. 2.42), and  $\gamma = 0.925$  is the geometric average between the two.

Since  $F(r) \propto T_{\text{BB}}(r)^4$  by Stefan-Boltzmann's law, the exact behavior of  $\langle f_c \rangle(a)$  depends on the radial temperature profile. In the previous section it was shown that to good precision  $T(r) \propto r^{-\gamma}$  where  $\gamma \sim 1.1$  for the centrally illuminated disk and  $\gamma = 3/4$  for the  $\alpha$ -disk. To obtain an estimate for the (more realistic) case in which both effects are equally important one can average these two exponents. Fig. 2.23 shows how the averaged covering fraction depends on  $a$  for these three cases. For  $a \gtrsim 2$ ,  $\langle f_c \rangle \lesssim 0.25$  in all cases and at least 80% of the thermal radiation escapes the system without interacting with the corona. In contrast, for the slab geometry models, all of the thermal radiation must propagate through the corona prior to escaping the system. For that reason the sphere+disk models always predict that a large amount of thermal radiation, relative to the amount of Comptonized radiation, will escape the system. Unless this thermal radiation is absorbed by the interstellar medium (which most of it is since the disk is quite cold, cf. eq. 2.42), it will appear in the observed spectrum as a soft excess.

Neglecting the radiation intercepted by the sphere, the soft spectrum emerging from the system is given by summation over the locally emitted spectra

$$F(E) \propto \int_1^a B_P(T(r)) r dr \quad (2.46)$$

where  $B_P(T)$  is the Planckian distribution. In Fig. 2.24 the flux spectrum resulting from such a centrally heated disk is shown using parameters typical for galactic BHs. The



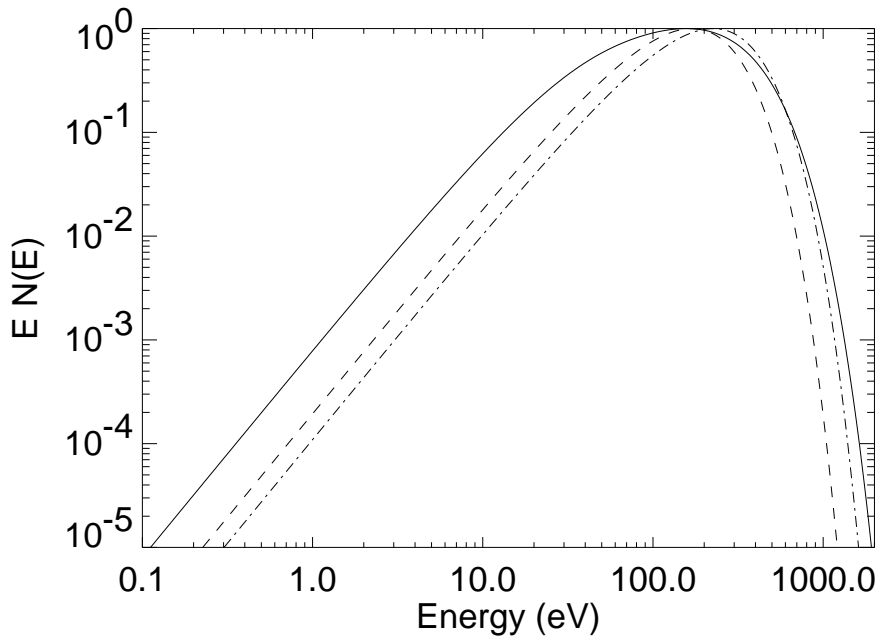


Figure 2.24: Spectrum of thermal radiation emitted from an accretion disk with a radial temperature structure  $T_{\text{BB}}(r)$  as given by eq. (2.42) (solid line), using the same parameters as for Fig. 2.21. the dashed line is the Planckian for a temperature of  $T_{\text{BB}} = 60$  eV, and the dash-dotted line is a Planckian corresponding to  $T_{\text{BB}} = 80$  eV. All distributions are normalized to a maximum flux of unity (Dove et al. 1997, Fig. 7).

hard tail of the disk spectrum can be quite well described by a Planckian with  $T = 80$  eV since the hard tail is dominated by radiation emitted fairly close to the corona. Since it is mainly this radiation from regions of the disk with a comparably high temperature that is Compton upscattered and since the Comptonization spectrum is insensitive to the exact spectral shape of the seed photons, for theoretical modeling purposes the radial temperature distribution can be neglected. Thus, the models presented later in this section have been computed using a constant temperature of 80 eV instead of computing the real disk spectrum. This overestimates the flux in the predicted soft excess by about 10%. For real spectral fitting, however, the shape of the soft excess has to be modeled correctly. Since the exact radial temperature structure strongly depends on the physical assumptions put into the above analytical derivation and since the self-consistent computation of the temperature structure would be very expensive in computer time, we decided to use the radial temperature structure from an  $\alpha$ -disk for computing the models used in chapter 5.

### 2.2.3.3 Physical Properties of the Corona

Using the NLMC code we computed a grid of models, in which the range of seed opacities is  $0.5 \leq \tau_p \leq 4.0$  and the range of coronal compactness parameters is  $0.1 \leq l_c \leq 100$ . The outer radius of the disk was set to  $a = 10$  and the temperature structure of

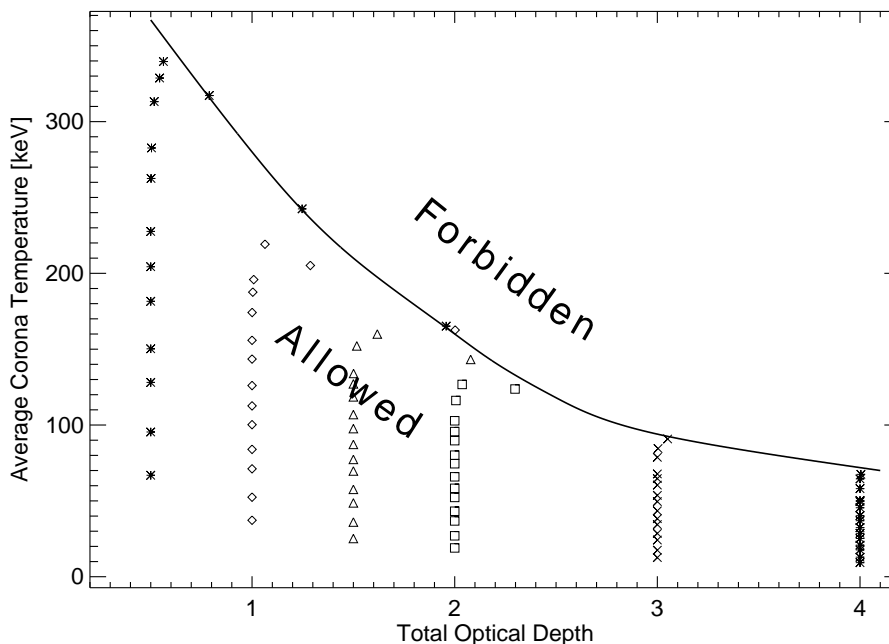


Figure 2.25: Allowed temperature and opacity regime for self-consistent ADC models with a sphere+disk geometry. The solid line is derived from a “fit by eye” to the numerical results. For a given total optical depth, coronae with temperatures above the solid line do not exist. The black body temperature of the disk was assumed to be  $kT_{\text{BB}} = 80 \text{ eV}$  for all models (with no dependency on radius – note that this does only slightly affect the allowed regime!). Different symbols represent models with different seed opacities, while different points having the same symbol represent different coronal compactness parameters (Dove et al. 1997, Fig. 9).

the disk was set to  $kT_{\text{BB}} = 80 \text{ eV}$  with no radial dependence. The computational strategy and the output parameters for these models were the same as for the slab geometry.

As already mentioned several times, the most important difference between the slab-geometry and the sphere+disk geometry is that the spherical corona is able to reach much higher temperatures as compared to the slab models because the corona is “photon-starved,” i.e., the luminosity of the seed photons is much less than the luminosity of the hard X-rays (Zdziarski, Coppi & Lamb 1990). As discussed above, most photons that are reprocessed within the accretion disk do not re-enter the corona. Therefore, the Compton cooling mechanism that prohibits slab geometry coronae from having high temperatures is less efficient in keeping the spherical coronae cool. This can be clearly seen from the allowed regime of optical depths and average corona temperatures for the sphere+disk geometry shown in Fig. 2.25. Observationally, the most important conclusion from this is that there are self-consistent  $\{T_c, \tau_{\text{es}}\}$  combinations such that the observed power-law and cut-off in BHs can be reproduced.

Note that the allowed temperatures are high even for large optical depths of the corona. For this reason the spectra emerging from these systems still have power-law spectra that are quite hard and do not exhibit a Wien hump (Fig. 2.26). At first

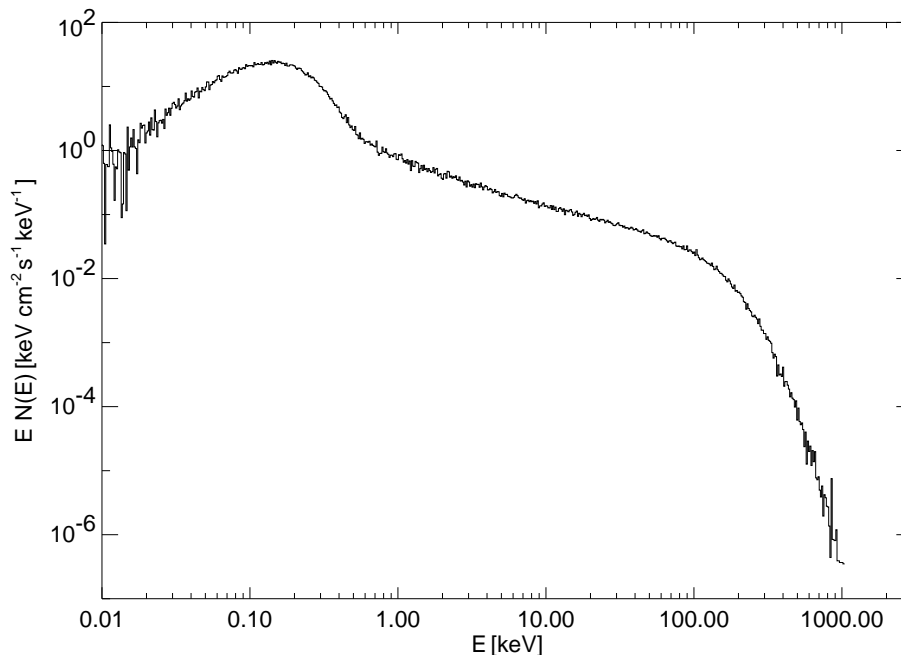


Figure 2.26: Typical spectrum emerging the sphere+disk geometry for  $\tau = 3$  and  $l_c = 1$ , corresponding to an average coronal temperature of 45 keV.

glance, from the discussion on Comptonization in section 2.1.1 this might look counter-intuitive. However, the big difference between the spectra presented, e.g., in Figs. 2.4 and 2.5 and the spectra from the sphere+disk geometry is that the soft photon source is situated in the *center* of the disk for the former models, while the plasma is illuminated from the outside in the case of the sphere+disk geometry. This means that the escaping photons are mainly Compton scattering within the skin of the sphere and not deep within the sphere, so that they have a high probability of reemerging after just a few Compton scatters even if the sphere has a large optical depth. Therefore the “effective” optical depth of the sphere is small for these photons although the total optical depth of the sphere is large. Note also that the soft excess of the spectrum shown in Fig. 2.26 is much stronger than that of the slab models, confirming the discussion in section 2.2.3.2. As was claimed in the previous sections, due to the small covering factor of the disk, the spectrum exhibits no discernible reprocessing features.

Finally, a theoretically interesting feature of the sphere+disk models is the internal temperature structure of the sphere. Even though it was assumed that the heating rate within the sphere is uniform with volume, the self consistent temperature structure was found to vary by 30% for the models with  $\tau_{es} \gtrsim 1$ . For these optical depths, the outer shells of the corona are the hottest while the center region is the coldest. This is caused by the symmetry of the system: the center region is illuminated from all sides so that Compton cooling is most efficient in this region. The variation is not large enough, however, for the predicted spectra to contain a “hardening” feature that mimics the hardening due to Compton reflection as proposed by Skibo & Dermer (1995).

### 2.3 Temporal Signatures of Accretion Disk Coronae

The results of the ADC simulations presented so far concentrated solely on the physical conditions within the ADC as well as the escaping spectrum. Although X- and  $\gamma$ -ray astronomy are traditionally focused on the photon energy spectrum, there is much knowledge to be gained from the temporal behavior of sources containing ADCs. What knowledge can be gained, however, is not obvious from the results presented so far and additional computations need to be done.

To understand qualitatively what is happening in a Comptonizing medium, we consider a spherical electron cloud of uniform electron density. A burst of soft photons emitted at the center of the cloud will Compton scatter through the cloud and finally diffuse outwards. The time a photon stays in the cloud obviously depends on its path length within the cloud, which, in turn, is dependent on the number of scatterings the photon experiences before emerging. Since many scattering orders contribute to the emerging spectrum, the initially very narrow photon burst will be spread out in time when the photons emerge the cloud. Because the average energy gain of the photon per scattering is approximately constant (eq. 2.9, p. 25), different scattering orders also correspond to different final photon energies. Thus the time at which the photons escape from the cloud is different for different final energies. If the seed photon intensity is time dependent, not only will this variability be mirrored in the observed X-ray light-curve, but likewise there will be a time-lag between different energy bands in the observed X-ray lightcurve, such that the hard photons lag the softer ones. Such time-lags have indeed been observed (Nowak & Vaughan 1996; Miyamoto et al. 1992, and references therein; see also chapter 5).

If it can be assumed that the Comptonizing medium is static, then the observed light curve in the energy band  $E_1, E_2$  can be written as

$$I_{E_1, E_2}(t) = \int_{-\infty}^t G_{E_1, E_2}(E_0; t, t_0) I_{\text{intrinsic}}(E_0; t_0) dt_0 \quad (2.47)$$

where  $I_{\text{intrinsic}}(E_0; t_0)$  is the intrinsic intensity variation of seed photons emitted with an energy  $E_0$  at time  $t_0$ , and  $G_{E_1, E_2}(E_0; t, t_0)$  is the probability that such a seed photon emerges from the Comptonizing system at time  $t$  with an energy in the energy band from  $E_1$  to  $E_2$ . Since this probability is also dependent on the shape of the emerging spectrum, only the total Green's function,  $G_{0, \infty}$ , is normalized to unity,

$$\int_{t_0}^{\infty} G_{0, \infty}(E_0; t, t_0) dt = 1 \quad (2.48)$$

while  $G_{E_1, E_2}$  is normalized to the relative photon flux in the energy band from  $E_1$  to  $E_2$ . Since  $G$  is the light curve resulting from a  $\delta$ -function like seed photon input light curve, the Green's function is colloquially called a "Compton shot". By virtue of eq. (2.47) it is sufficient to compute  $G$  to be able to characterize the effects caused on the intrinsic light curve by the electron cloud. In the next two sections I describe the properties of Compton shots resulting from Monte Carlo computations. Due to its physical simplicity I will first describe the properties of Compton shots from a spherical geometry,

where the photon source is situated in the center (§2.3.1). After this the results of the computations for the more complicated sphere+disk geometry are described (§2.3.2). All results presented in this section have been obtained using an extended version of the linear Monte Carlo code described in my diploma thesis (Wilms 1996), which is primarily based on the algorithms presented by Pozdnyakov, Sobol & Sunyaev (1983) and Hua (1997). A brief description of the code can be found in appendix A.1

### 2.3.1 Compton Shots in the Spherical Geometry

#### 2.3.1.1 Introduction

The simplest geometry to compute Compton shots is that of an electron sphere with radius  $R$ , uniform electron density  $n_e$  and uniform temperature  $kT_e$ . The source of the seed photons is situated at the center of the sphere. Due to its simplicity, this geometry is the only geometry which has been extensively studied in the literature. In fact, *all* published studies presenting Compton shots concentrated on the spherical geometry. First analytical considerations for the shape of the Compton shot in the limit of  $\tau_{es} \gg 1$  were done by Payne (1980) and by Sunyaev & Titarchuk (1980). The latter authors concentrated especially on the case of a spatial seed photon distribution  $N(R) \propto \sin(\pi n_e \sigma_T R / \tau) / R$  for which they could show that  $G_{0,\infty}(t, 0) \propto \beta \exp(-\beta u)$ , where  $u$  is proportional to the time. Later simulations were stimulated by the discovery of possible time lags between different energy bands in Cyg X-2 and GX 5-1 (see van der Klis 1995 for a description of these observations using newer data). Stollman et al. (1987) quantitatively studied the dependency of the time lag on  $\tau_{es}$  for  $\tau_{es} \in [5, 15]$ . They also looked at the case where the optical depth itself was time dependent. In a second paper using the same code and the same range of parameters, Wijers, van Paradijs & Lewin (1987) focused on the dependency of the time lag on the seed photon temperature. The properties of the shots emerging from a sphere with a point source in the center were also studied by Kylafis & Klimis (1987) and Kylafis & Phinney (1989), using a larger range of parameters and a combination of analytical methods and Monte Carlo simulations. These latter authors, however, did not include any information on the energy dependency of the shot.

With the availability of X-ray observations of high temporal resolution as those I will present in chapter 5.5 and with the availability of new time series analysis methods, the study of Compton time lags has had a revival. In a series of papers, Hua, Kazanas, and collaborators have studied the influence of the density profile on the time lag observed from a spherical electron cloud that is symmetrically *irradiated* with soft photons (Kazanas, Hua & Titarchuk 1997; Hua, Kazanas & Titarchuk 1997; Hua, Kazanas & Cui 1998), concentrating not on the Green's function but on the predicted periodogram obtainable from such a system. This geometry is qualitatively closer to the sphere+disk geometry studied in section 2.3.2.

In his study of time-dependent Comptonization, Payne (1980) found that in the limit of large optical depth the Green's function for monochromatic seed photons with energy

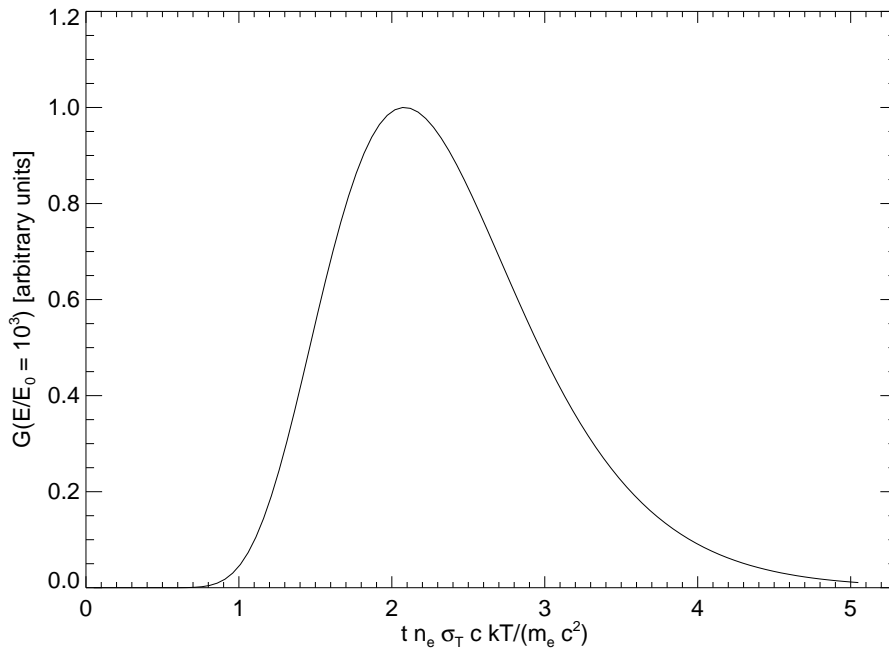


Figure 2.27: Compton shot computed using Payne’s formula (eq. 2.49), for an optical depth of  $\tau_{\text{es}} = 5.$ , a temperature of  $kT = 0.5m_e c^2$ , and  $E/E_0 = 10^3$ . Note that  $G$  is distinctly asymmetric, even for large optical depths.

$E_0$  is given by

$$G_{E,E}(E_0; \tilde{t}) = \frac{4\alpha}{\gamma} \frac{1}{(4\pi\tilde{t})^{1/2}} \frac{1}{E_0} \exp\left(-\left(\frac{9}{4} + \frac{4\alpha}{\gamma}\right)\tilde{t}\right) \left(\frac{E}{E_0}\right)^{(3/2 - \ln(E/E_0)/(4\tilde{t}))} \quad (2.49)$$

where

$$\tilde{t} = \frac{kT}{m_e c^2} n_e \sigma_T c t \quad (2.50)$$

$$\alpha = \pi^2/3 \quad \text{for a sphere} \quad (2.51)$$

$$\gamma = \frac{4kT}{m_e c^2} \tau_{\text{es}}^2 \quad (2.52)$$

Fig. 2.27 gives an example for the shape of  $G$  computed from the Payne (1980) theory.

### 2.3.1.2 Simulations

Payne’s analytical theory (and similar results from Kylafis & Klimis 1987) are quite able to reproduce the exact Monte Carlo results for high optical depths, but they break down for lower optical depths. This is unfortunate since the last sections showed that the hot ADCs observed have to have low optical depths. For low  $\tau_{\text{es}}$ , the individual scattering orders have a strong influence on the shape of the shot. It is therefore necessary to overcome the problem of the analytical theory by “brute force”, i.e., to compute Compton

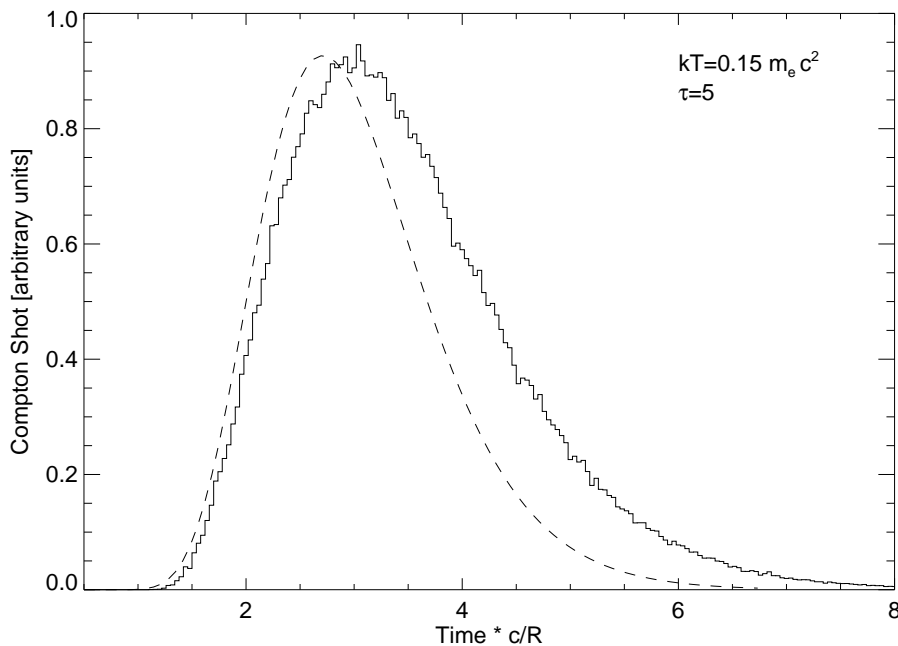


Figure 2.28: Comparison between a Compton shot simulated with the linear Monte Carlo code and the Compton shot computed from Payne's theory (dashed), for an optical depth of  $\tau_{\text{es}} = 5$  and a moderately hot corona with  $kT_e = 0.15m_e c^2 \approx 75 \text{ keV}$ .

shots using a MC code. Using the linear MC code described in appendix A.1, therefore, a large grid of models was computed, covering the optical depth range from  $\tau_{\text{es}} = 0.25$  to 10, and the temperature range from  $kT = 0.1m_e c^2$  to  $0.7m_e c^2$ . This large range of models allows for a study of the low optical depth shots occurring in nature, including relativistic temperatures. On the other hand, the large optical depths included in the grid allow for a study of the regime where the numerical theory approaches the analytical solution of eq. (2.49). For all models, the total emerging Compton shot, for all energies, was computed, as well as shots for narrow energy bands.

Fig. 2.28 compares the shot profile obtained with the Monte Carlo code to the profile given by eq. (2.49), for an optical depth of  $\tau_{\text{es}} = 5$  and an electron temperature of  $kT_e = 0.15m_e c^2$ . As with all profiles shown here, the time is normalized to the time it takes a photon to travel a distance corresponding to the radius of the sphere,  $R$  (called “light crossing time” from now on). The shapes of the theoretical shot and the simulated shot are in quite good agreement. The shot profile computed from Payne's theory is narrower, however. The main cause for this disagreement is that in his analytical theory only the lowest eigenvalue of the diffusion problem is taken into account, corresponding to an underestimation of the higher scattering orders. Since photons of higher scattering orders stay in the corona for a longer time, the tail of the Compton shot is underestimated. This build up of a Compton shot from the different scattering orders is shown in Fig. 2.29. Note the analogy to the build up of the photon energy spectrum shown in Fig. 2.4, p. 27. When the optical depth is small, as is the case for the model of

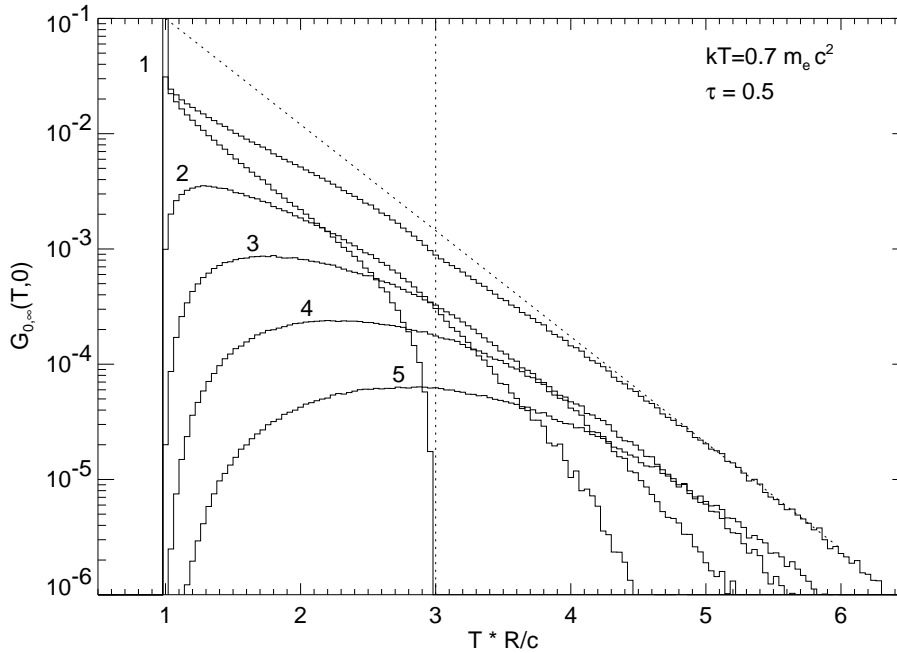


Figure 2.29: Contribution of the first five scattering orders (numbers) to the total emerging Compton shot. The dotted line at  $TR/c = 3$  shows the maximal time-lag for photons suffering exactly one time-lag, while the dotted power-law is the extrapolation of the asymptotically reached power-law reached for large time lags, to smaller  $t$ .

Fig. 2.29, then the total emerging Compton shot has a characteristic break at  $t = 3$  light crossing times, indicated by the dotted vertical line in the figure. This break is caused by the contribution of the first scattering order to the shot, because these photons can stay in the cloud maximally for this length of time (traveling from the center to the edge of the cloud, suffering a head on collision, and traveling back to emerge on the opposite side of the sphere). Note also that for high time lags the shot asymptotically reaches an exponential, while there are large deviations from the exponential for smaller lags.

For a systematic study of the Compton lags in the spherical geometry many models need to be computed using up a large amount of CPU time. Since quite a lot of data are produced this way the results are not very instructive at first. If these data could be presented in a compact form, then they would be easier to understand and it would be easier to use the time lags in analyzing the observations. For larger escape times, Fig. 2.29 suggests an exponential behavior of the shot (in agreement with the proportionality found by Sunyaev & Titarchuk 1980, quoted in the introduction to this section), which is modified for smaller times. Empirically it was found that for all seed photon energies the Green's function can be well described by

$$G_{E_{\min}, E_{\max}}(t; A, t_1, \alpha, \beta, \gamma) = \begin{cases} \frac{\alpha}{\beta} \frac{A}{\Gamma(\frac{1+\gamma}{\alpha})} \left(\frac{t-t_1}{\beta}\right)^\gamma \exp\left(-\left(\frac{t-t_1}{\beta}\right)^\alpha\right) & \text{for } t > t_1 \\ 0 & \text{for } t \leq t_1 \end{cases} \quad (2.53)$$



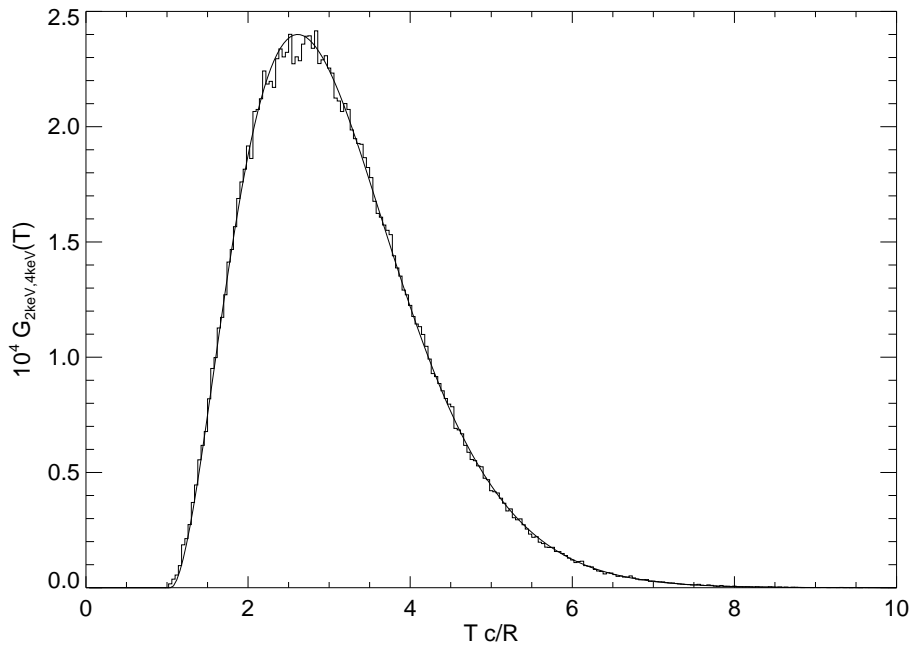


Figure 2.30: Simulated Green's function for a sphere with  $\tau = 1.5$  and  $kT = 0.2m_e c^2$ , for the energy band from 2 keV to 4 keV (histogram), and the best-fit generalized Gamma function  $6 \times 10^{-4} G(T|x_1 = 1, \alpha = 1.36, \beta = 1.27, \gamma = 1.81)$  (solid line).

where  $\alpha$ ,  $\beta$ , and  $\gamma$  are the parameters of the distribution,  $A$  is a normalization constant, and where  $\Gamma(x)$  is Euler's Gamma function. All fit-parameters depend on the seed photon energy. The probability density of (2.53) is called a generalized Gamma distribution<sup>1</sup>. It is one of the most general one-sided probability distributions used in statistics. In the special case of  $\gamma = \alpha - 1$  the generalized Gamma distribution is called a Weibull distribution. The properties of the generalized Gamma and the Weibull distribution are discussed in detail in appendix C.1.

### 2.3.1.3 Results

Fits to eq. (2.53) have been performed for the whole grid simulated (60 models and  $\sim 350$  shots total). The Gamma distribution is able to represent the shot profile to a very high precision (see Fig. 2.30 for an example). This makes it possible to characterize each shot by just five parameters so that a study of the behavior of the shots is simplified.

Fig. 2.31 shows the dependency of the normalized shot profile from the energy of the escaping photons, for several energy bands. Note that for the higher energies the

<sup>1</sup>In their analysis of the Compton shots from a sphere with a density gradient that is irradiated from the outside, Hua, Kazanas & Cui (1998) model their profiles with the Gamma distribution,

$$g_{\text{Hua}}(t) = \begin{cases} t^{\alpha-1} \exp(-t/\beta) & \text{for } t \geq 0 \\ 0 & \text{otherwise} \end{cases} \quad (2.54)$$

This simpler fit function does not work with all shot profiles obtained in my simulations.

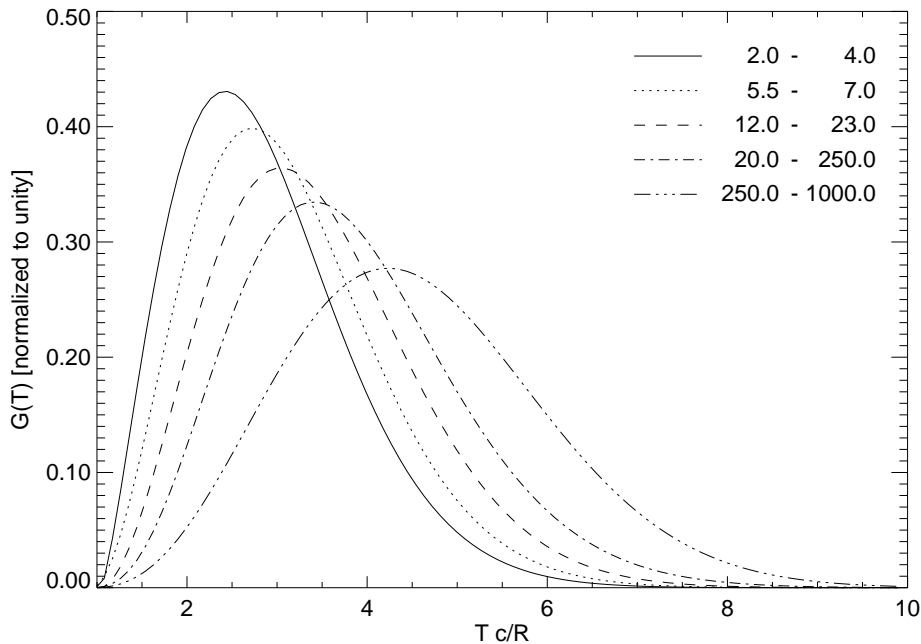


Figure 2.31: Dependency of the normalized shot profiles from the final energy of the photons for a model with  $\tau = 0.75$  and  $kT = 0.25 m_e c^2$ .

shot is broader and the most probable escaping time of the photons occurs at a later time. Since the average energy change in one Compton scattering is proportional to  $kT$  (cf. eq. [2.9] on p. 25), photons escaping with a higher energy have on average suffered more Compton scatterings than photons escaping in lower energy bands. Therefore, the time these photons spent in the sphere is larger and consequently they escape at a later time than low energy photons. The larger average number of Compton scatterings is also the cause for the larger width in the high energy shot profile. Note, however, that the width of the shot profile also depends on the width of the energy band for which the profile was computed – it is difficult to disentangle these two effects in simulations of the kind performed here.

For a given energy band, the time lag *decreases* with increasing temperature of the cloud (Fig. 2.32). Again, this is mainly due to the smaller number of scatterings photons need to undergo before reaching a given energy. In agreement with the discussion of the previous paragraph, the time lag increases with higher photon bands. Fig. 2.32 indicates that in models with lower temperatures, which have softer spectra, the difference in time lags between adjacent energy bands is slightly larger (compare, e.g., the time lags for  $kT = 0.1 m_e c^2$  with those for  $kT = 0.7 m_e c^2$ ). In the figure this behavior results in a decrease of the curvature of the plot with increasing temperature. Observationally this indicates that the measurement of the time lag between two energy bands in a source that has a Comptonization spectrum is characteristic of the physical parameters in the source, an idea brought forth by Vaughan & Nowak (1997), Nowak & Vaughan (1996), and the papers referenced in these publications. The measurement of the time lag can thus be

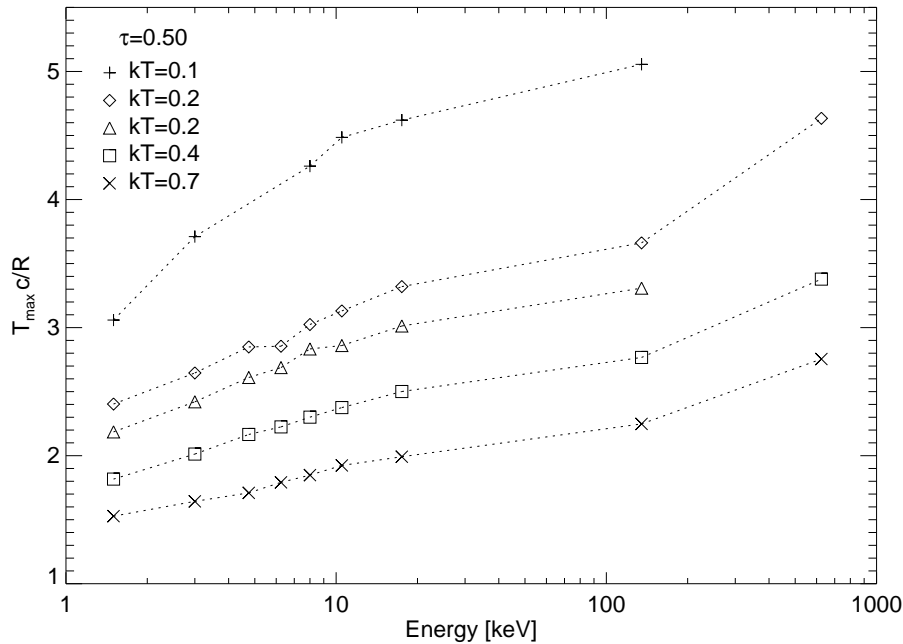


Figure 2.32: Time lag of photons escaping the sphere in a given energy band (here characterized by the mean energy of the band [not weighted by photon number!]) for spheres with an optical depth of  $\tau = 0.5$  and different temperatures. The lag is characterized by the most probable time for a photon to escape, i.e., by the time at which the shot profile has its maximum. Points missing at high photon energies are due to the low photon number in that bin due to the soft spectrum. The high energy point for the  $kT = 0.2 m_e c^2$  model has a large statistical uncertainty.

used, in principle, to check whether the physical parameters obtained from the spectral fitting are consistent with those predicted for the temporal behavior of the source.

A similar behavior of the time-lag can also be seen when looking at the second parameter determining the model, the optical depth (Fig. 2.33). For any given energy band the most probable time for the photons to escape with that energy shortens with increasing optical depth. This seems counterintuitive at first glance, but is a consequence of the scaling of the time unit in terms of the light crossing time. In this parametrization a higher optical depth results in an increase of the electron number density. Since the number of scatterings to reach a given output energy band is constant for a given electron temperature, increasing the electron density means that the scattering frequency is increased and therefore the time before these photons escape is reduced. Note that this effect is also apparent in eq. (2.49) where the profile is given in terms of  $\tilde{t}$  which is proportional to  $\tau$  times the light crossing time.

## 2.3.2 Compton Shots in the Sphere+Disk Geometry

### 2.3.2.1 Introduction

The results presented for an electron sphere with a source in the center are quite general and carry over for a much more complicated system, the sphere+disk geometry. Apart

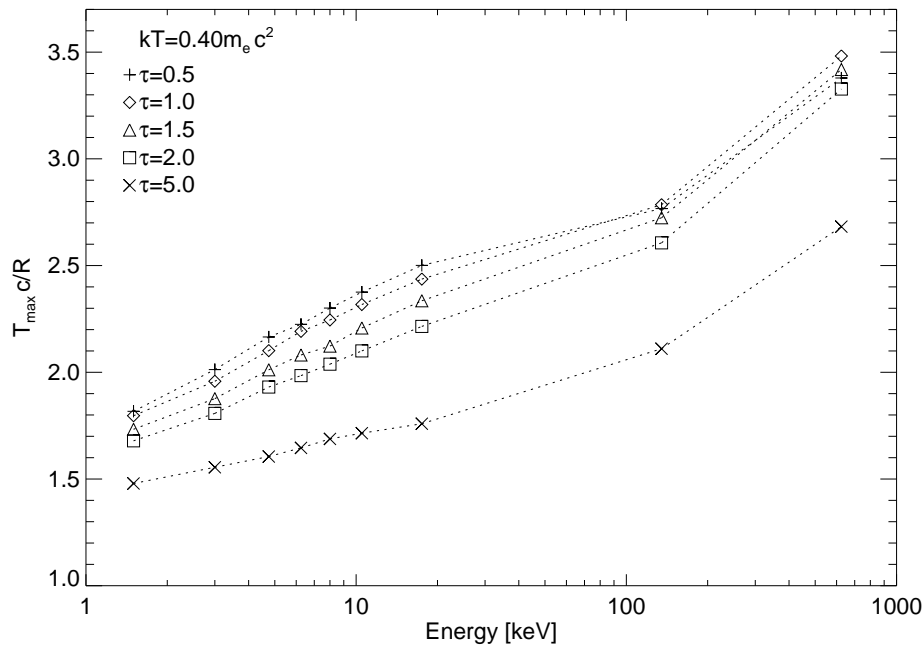


Figure 2.33: Most probable escape time in a given energy band, for a sphere with temperature  $kT = 0.4 m_e c^2$  and varying optical depth. As in Fig. 2.32 the uppermost energy bands are not too significant.

from the different geometry, the major difference between the systems is the presence of cold matter within the sphere+disk geometry. Due to reprocessing of the hard radiation within the accretion disk, which results in reflected photons or in the emission of thermalized photons in the form of black body photons, the Comptonizing medium and the accretion disk are coupled: the effect of thermalization is to cause “echos” in the temporal response of the system to an initial  $\delta$ -function like burst of photons, since the thermalized photons are again able to produce hard photons by Comptonization in the sphere. In the implementation of the MC code this means that several programming tricks are necessary to ensure energy conservation. These are discussed in appendix A.1.

Due to the size of the whole sphere+disk system, the time lag of the photons emerging the system is not only caused by the different light travel time of the photons within the sphere, but also by the time it takes the photons to travel from their initial point of emission on the accretion disk to the sphere. In addition, hard photons emitted from the different “sides” of the sphere have different travel times to the observer (who is assumed to be far away from the sphere). In the computations presented below, this phase shift was taken care of by adding the travel time of the photons to a plane perpendicular to the photon’s direction, which is at a large distance (50 sphere radii) from the center of the cloud, to the total travel time of the photon. Thus, in contrast to the shot profiles presented in section 2.3.1, the times that will be given in this section are only relative times. Thermalization and Compton reflection do *not* affect the final computed time lag: Compton reflection mainly happens within the first few optical depths of the ac-

cretion disk. Since the disk has a very high density this volume is very small compared to the size of the system, so that Compton reflection occurs virtually instantaneously. Thermalization in the accretion disk occurs primarily via photoabsorption of a photon followed by the emission of either a photo-electron or Auger electrons, both which have typical energies on the order of a few keV or less. The electrons then lose their energy primarily via Coulomb interactions with other electrons. The typical relaxation timescale for thermalization is given by (Frank, King & Raine 1992, eq. 3.32)

$$t \sim \frac{m_e^2 v^3}{8\pi n_e e^4 \ln \Lambda} \frac{m_e v^2}{2kT} = \frac{m_e^{1/2}}{2^{3/2} \pi e^4 \ln \Lambda} \frac{E^{5/2}}{n_e kT} \quad (2.55)$$

$$\sim 10^{-5} \text{ s} \left( \frac{E}{10 \text{ keV}} \right)^{5/2} \left( \frac{n_e}{10^{16}/\text{cm}^3} \right)^{-1} \left( \frac{kT}{1 \text{ keV}} \right)^{-1}$$

where  $E = m_e v^2/2$  is the initial energy of the electron,  $n_e$  the electron number density,  $e$  the elementary charge,  $T$  the temperature of the plasma, and  $\ln \Lambda \approx 15$  is the Coulomb logarithm. Since the thermalization timescale is small compared to the light-crossing time of the spherical disk and the light-travel time from the accretion disk to the sphere, it can be assumed that thermalization occurs quasi-instantaneously. Consequently the time spent by the photons within the accretion-disk was not taken into account in the determination of the time-lag.

### 2.3.2.2 Simulations

Using the MC code, I have computed a grid of models for a large range of parameters, i.e., optical depth and temperature of the cloud, seed photon temperature, and radius of emission of the first seed photon. Instead of just *one* generalized Gamma distribution as in the case of the pure sphere geometry, the sum of *two* generalized Gamma distributions is needed to describe the resulting shot profiles. The second distribution, which contains less flux than the first one, can be attributed to the presence of the photon “echo” in the shot. From the numerical fits it turned out that the starting times  $t_1$  of these two distributions were almost identical. Furthermore, it turned out that the fit parameters of the individual shots were coupled such that  $\gamma \approx \alpha - 1$  in all fits. It turned out that forcing  $\gamma = \alpha - 1$  resulted in equally good fits to the computed profiles. A generalized Gamma distribution with  $\gamma = \alpha - 1$  is called a Weibull distribution, its properties are described in appendix C.2 on p. 163. The final fit-function chosen for the description of the Compton shots was therefore

$$G_{E_1, E_2} = A_1 P_W(t; \alpha_1, \beta_1, t_1) + A_2 P_W(t; \alpha_2, \beta_2, t_1) \quad (2.56)$$

resulting in very good fits for all models computed. Thus, as in the case of the sphere geometry, only five parameters are needed to describe the shot profile. Fig. 2.34 gives examples for the shot profiles obtained this way.

Since the major behavior of the shots, like their dependency on the temperature and the optical depth, are similar to those in the pure sphere geometry, they will not be

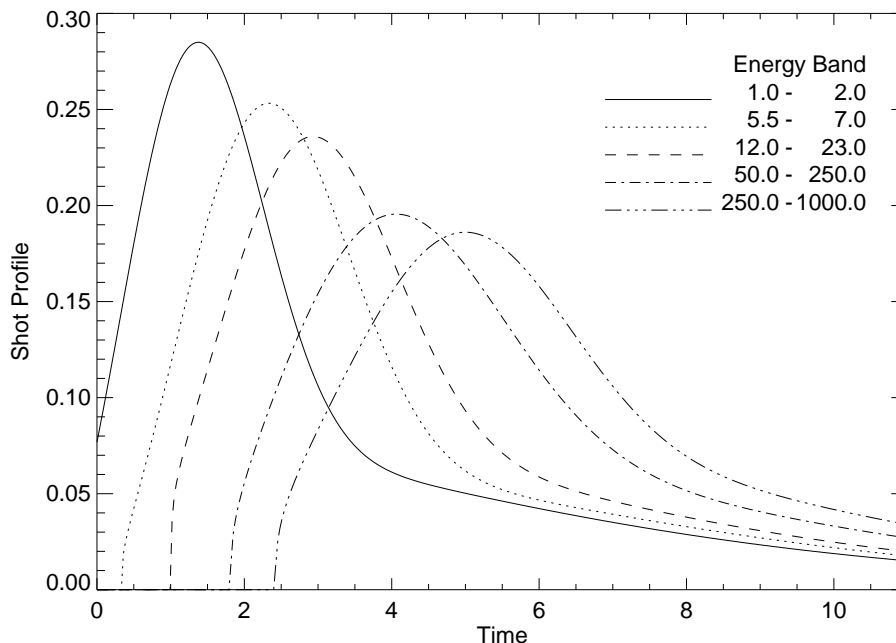


Figure 2.34: Profile of the Compton shots from the sphere+disk geometry for different final energy bands. Note the tail caused by the photon “echo”. The radius at which the primary photon was emitted is at  $r_{\text{in}} = 1.5$  sphere radii, and the seed photon energy is 214.4 eV.

repeated here. I will focus instead on the dependency of the shot profile on the initial seed photon energy, and on the effects due to the radius of emission of the seed photons. All examples given are for a sphere with  $\tau = 2.1$  and a temperature of  $kT = 66$  keV, corresponding to parameters found for Cyg X-1 (chapter 5).

To be able to study the effect of radially symmetric disturbances of the accretion disk on the temporal behavior of the emerging Comptonization spectrum, the Green’s function for photons emitted from a ring of radius  $r$  was computed. Fig. 2.35 compares the average time photons take to escape the system as a function of the initial radius at which the seed photon was emitted. Contrary to the previous section, the lag time is defined by the *mean* time the photons need to escape (computed using the expressions in appendix C.2) and not by the most probable time. Since the energy bands considered in the figure have energies that are large compared to the seed photon energy, all photons entering the plot have been Comptonized within the corona. Obviously, the time lag for photons emitted at large radii is longer because of the larger distance from outer radii to the corona. For the same two energy bands, however, it is empirically found that the time lag between these bands appears to be slightly shorter for larger initial radii (Fig. 2.36). The explanation for this result is at present unknown, but might be caused by the difference in the illumination of the central sphere for different initial seed photon radii. One possible application of this effect would be the measurement of radial symmetric instabilities in accretion disks. If the seed photons observed were coming from such an instability, then the response between lower and higher energy

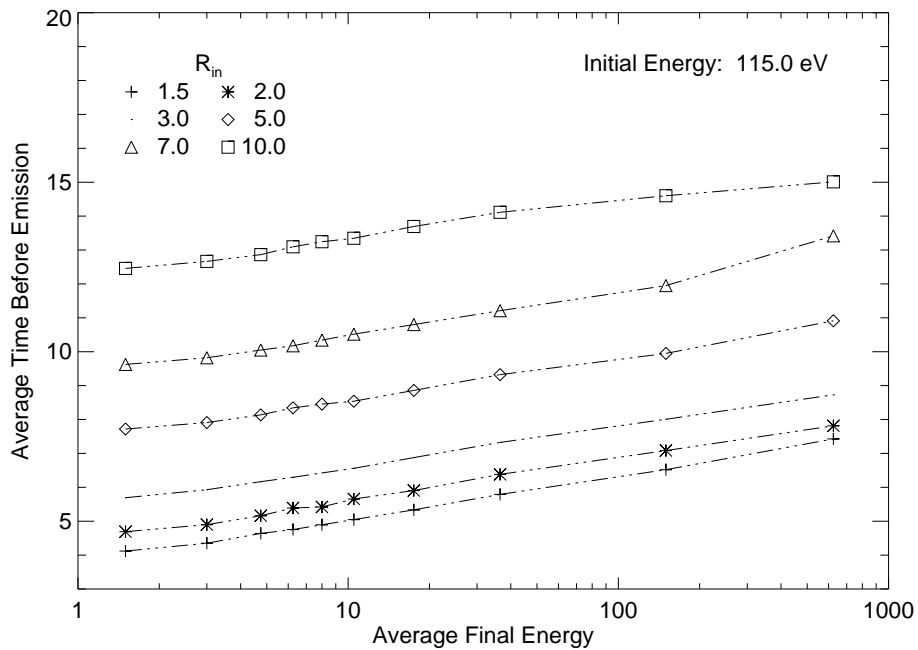


Figure 2.35: Average Compton lag (defined through the first moment of the shot, see text) for photons with an initial energy of 115 eV and different radii of emission. The offset of the time-system is arbitrary.

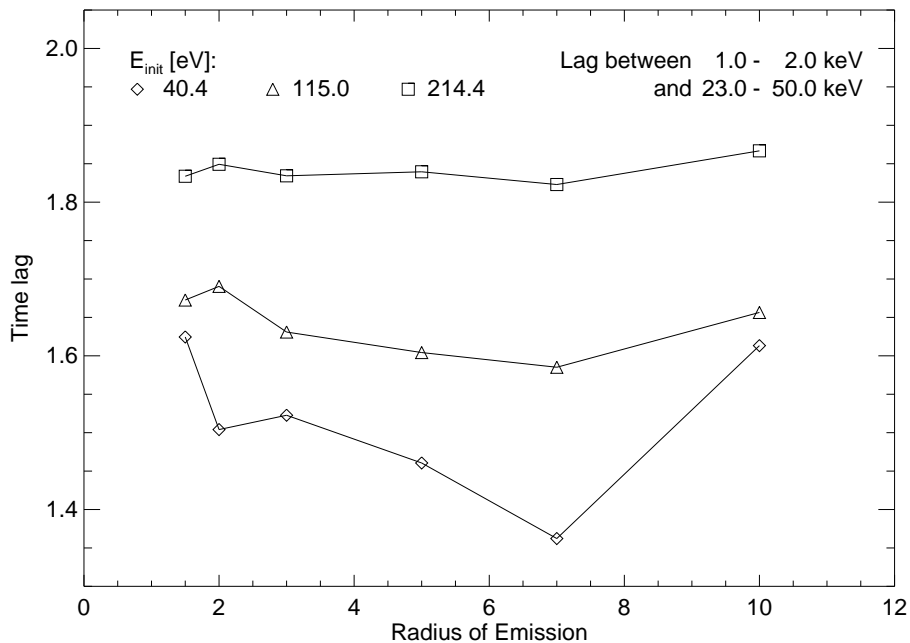


Figure 2.36: Time lag between different energy bands as a function of initial photon energy. The time lag is computed as the difference between the average escape times of the photons for these bands, as a function of the initial radius at which the seed photons were emitted. The 40.4 eV,  $r = 10$  point is uncertain due to numerical noise.

bands should become slightly shorter as the disturbance propagates inwards. A more detailed study using a much larger number of models than those computed here would be necessary, however, to quantify this empirically found effect.



**PART II**  
**Observations**

## CHAPTER 3

---

### Observational Methods

The previous chapters were devoted to a theoretical study of ADCs. In the rest of this thesis these results will be applied to X-ray observations of Black Hole systems to test whether the theory is in agreement with the observations. Before this can be done, however, it is necessary to define the techniques used in the data analysis and to introduce the instruments used.

In this chapter the observational methods are defined: section 3.1 gives a brief introduction to the X-ray spectral analysis methodology and section 3.2 defines the techniques used in the temporal analysis. The description of the X-ray instruments used to gather the data will be given in Chapter 4.

#### 3.1 Spectral Analysis

The major drawback of X-ray spectral analysis as compared to optical spectral analysis is without doubt the limited spectral resolution of the X-ray detectors currently in orbit. The spectral resolution of an X-ray instrument is usually characterized by the ratio  $\Delta E/E$ , where  $\Delta E$  is the Full Width at Half Maximum (FWHM) of the energy dispersion at energy  $E$ . Typical values for instruments sensitive in the 1...10 keV range are 15% at 5.9 keV for proportional counters, and about 3% for semiconductor devices (Zombeck 1990, p. 364). For other energies,  $\Delta E/E \propto E^{-1/2}$ . In contrast, optical prisms have resolutions of  $\lambda/\Delta\lambda \approx 1.5 \times 10^4$  (Kitchin 1984, eq. 4.1.44), corresponding to  $\Delta E/E < 0.01\%$ ! Due to these reasons it is clear that the spectral analysis process in X-ray astronomy has to use comparably complicated methods to be able to extract a physical meaning from the measured data.

This measured X-ray spectrum, i.e., the detected information analyzed in the Pulse Height Analyzer (PHA) of the instrument, can be written as the convolution of the true photon spectrum of the observed source,  $N_{\text{ph}}(E)$ , with a function characterizing the properties of the detecting instrument. The source spectrum is typically given in units of photons per unit area, per unit time, and per unit energy interval,  $[N_{\text{ph}}] = \text{ph cm}^{-2} \text{s}^{-1} \text{keV}^{-1}$ . The instrument is characterized by its (energy dependent) efficiency, which can be expressed in terms of an “effective” collecting area,  $A(E)$ , and by the probability function that a photon of energy  $E$  is detected as a photon of energy  $E'$  by the detector,  $R(E', E)$ . The probability  $R$  is often referred to as the redistribution function of the detector, while the product of  $A(E)$  and  $R(E, E')$  is called the response function of the detector. To first order,  $R(E', E)$  is a Gaussian centered on energy  $E$  with a width

corresponding to the energy resolution of the detector. Higher order effects in the detector (escape peaks, nonlinearities, etc.) lead to deviations from this behavior. Examples of real redistribution functions  $R(E, E')$  are discussed in chapter 4. Thus, for each PHA channel  $i$  the rate of photons detected,  $d_i$ , i.e., the PHA spectrum, can be computed from the incident photon spectrum  $N_{\text{ph}}(E)$  by

$$d_i = b_i + \int_{E'_i}^{E'_i + \Delta E'_i} dE' \int_0^\infty R(E', E) A(E) N_{\text{ph}}(E) dE \quad (3.1)$$

where  $E'_i$  the energy corresponding to PHA channel  $i$ , and  $\Delta E'_i$  is the energy width of the channel. Note the presence of a detector background term,  $b_i$ , which might be caused by cosmic radiation, radioactivity within the detector, the cosmic X-ray background, or other nuisances (cf. §4.1.3, p. 93). The units of  $d_i$  and  $b_i$  are  $[d_i], [b_i] = \text{cts s}^{-1}$ . It is commonplace to approximate eq. (3.1) by a sum, so that a matrix equation for the PHA spectrum results. In matrix form,  $R * A$  is called the Response Matrix Function (RMF).

Since both  $R$  and  $A$  have quite a complicated form, all attempts in the literature to solve eq. (3.1) directly for the source spectrum did not succeed (cf. Blissett & Cruise 1979, and references therein). Instead, the approach used is to *assume* that the observed X-ray source has a certain spectrum (the “model” spectrum) and then to use eq. (3.1) to predict what the model spectrum would look like in the X-ray detector. By minimizing the deviation between the predicted model spectrum and the measured data one then obtains a “best fit” to the data. The minimization is typically done using a Levenberg-Marquardt method as described, e.g., by Bevington & Robinson (1992). To quantify the correspondence between the model and the data, a statistical test is performed. Due to its statistical properties, it is standard practice in X-ray astronomy to take the sum

$$S = \sum_i \frac{((D_i - B_i) - M_i)^2}{\sigma_i^2} \quad (3.2)$$

as a measure for the deviation between the data and the model (Gorenstein, Gursky & Garmire 1968). Here,  $D_i$  is the number of photons registered in PHA channel  $i$  over the duration  $T$  of the observation,  $D_i = d_i T$  (and ditto for the other uppercase variables),  $D_i - B_i$  is the background subtracted measured spectrum,  $M_i$  is the model spectrum (which might depend on model parameters), and  $\sigma_i^2$  is the variance of the data in PHA channel  $i$ . If the measured events are statistically independent and if a large number of photons has been detected,  $D$  is Poisson distributed and the variance can be estimated by  $\sigma_i^2 = D_i + B_i$ . In real life  $\sigma_i$  might also be affected by a systematic error, which might be caused, for example, by uncertainties in the determination of  $R$ . This systematic error is added in quadrature to the uncertainty of the data to obtain the final variance of the PHA channel<sup>1</sup>. If it can be assumed that the measured data have a Poissonian distribution

<sup>1</sup>An alternative approach to estimating  $\sigma_i^2$  is to compute  $\sigma_i^2$  from the model (e.g., by assuming Poissonian statistics) instead of estimating it from the data. The way I have described here is the default of the X-ray analysis package XSPEC, while the latter way of computing  $\sigma_i^2$  is the one preferred in statistics (Lampton, Margon & Bowyer 1976; Horowitz 1997). For good fits, where  $D_i - B_i \approx M_i$ , these two choices obviously result in almost identical model parameters, but the resulting confidence intervals will be slightly different. For consistency, I used the XSPEC default throughout.

(which is usually the case, but see below!), then  $S$  is  $\chi^2$  distributed with  $N - p$  degrees of freedom where  $p$  is the number of estimated model parameters. This  $\chi^2$ -property of  $S$  can be used to test the statistical significance of the agreement between the model and the data: the confidence of the fit is given by (Lampton, Margon & Bowyer 1976, eq. 3)

$$\alpha_{\text{obs}} = \int_S^{\infty} f_{\chi^2}(\nu = N - p | \chi^2) d\chi^2 \quad (3.3)$$

where  $f_{\chi^2}(\nu = N - p | \chi^2)$  is the probability distribution function of the  $\chi^2$  distribution with  $N - p$  degrees of freedom. From the asymptotic expansion of eq. (3.3) (see Diem & Lentner 1970, p. 167) one can show that  $S/(N - p) \sim 1$  for a fit with a high confidence. The ratio  $\chi_{\text{red}}^2 := S/(N - p)$  is called the “reduced chi-squared”. In the X-ray astronomical literature it is standard practice to use the notation “ $\chi^2/\text{dof}$ ” for the reduced  $\chi^2$ , e.g.,  $\chi^2/124 = 0.9$  means that the reduced  $\chi^2$  of a fit with 124 degrees of freedom was 0.9. For the fitting of spectral models to the data and for the computation of the statistical uncertainties, the spectral fitting package XSPEC, version 10.0 (Arnaud 1996; Shafer et al. 1991), was used for all fits presented in this thesis.

The above fitting strategy only yields meaningful results if  $S$  is at least reasonably  $\chi^2$  distributed. This caveat is generally taken to mean that there should be at least 20 counts per spectral bin (cf., e.g., Nandra et al. 1997). If this is not the case, the data need to be rebinned, i.e., the data in adjacent PHA channels need to be added, taking care of the small number statistics involved when computing the statistical uncertainty of the newly formed bin (Gehrels 1986; Kraft, Burrows & Nousek 1991; Nousek 1992). When only a small *total* number of photons has been observed, rebinning does not help and one has to use a different approach to data modeling (see Cash 1979).

If the fit to the model was successful, i.e., if the confidence computed from eq. (3.3) is better than at least 0.9, confidence intervals for the model parameters can be computed. This is typically done following a prescription given by Lampton, Margon & Bowyer (1976). To compute the uncertainty of the interesting model parameter  $X$ , this parameter is varied around its best fit value. For each value of  $X$  in this range, a new model fit is done holding  $X$  at its preset value and allowing the other parameters to vary. This new fit results in a new  $\chi^2$  value. Using the addition theorem of the  $\chi^2$  distribution ( $\chi_{N-p}^2 + \chi_p^2 = \chi_N^2$ ), it is possible to show that the range of  $X$  for which  $S < S_{\text{min}} + \chi_p^2(\alpha)$  contains the “real” value of  $X$  with a probability of  $1 - \alpha$ . This range is then called the confidence interval of  $X$ . Here,  $\chi_p^2(\alpha)$  is the value of the  $\chi^2$  distribution for  $p$  parameters of freedom and significance  $\alpha$ . Where not noted otherwise, the uncertainties given in this work are confidence intervals for one parameter ( $p = 1$ ) at the 90% level ( $\alpha = 0.1$ ), and  $\chi_1^2(0.1) = 2.71$ . See Lampton, Margon & Bowyer (1976, Tab. 1) for other values of  $\chi_p^2$ . Note that this X-ray astronomical definition of the confidence interval is *not* what is called a confidence interval by statisticians. See Akritas (1997, answers 7, 8, and 33) for a discussions of these subtleties and Horowitz (1997) for a polemic discussion of the ways X-ray astronomical fitting is done as seen from the viewpoint of a statistician.

### 3.2 Temporal Analysis

Apart from the physical insight that can be gained from the spectral analysis, the temporal behavior of astronomical sources is a very important source of information. In this section the methods used in this thesis are defined. The traditional way to analyze time series in astronomy has been to use Fourier techniques. These methods are described in section 3.2.1. If the time series is non-periodic, then the analysis using the stochastic processes presented in section 3.2.3 might be more appropriate. These processes are especially well suited for an analysis directly in the time domain.

For an extensive review on the use of Fourier techniques in X-ray astronomy, see Lewin, van Paradijs & van der Klis (1988) and van der Klis (1989), while an introduction of the stochastic methods from a general point of view is given by Scargle (1981). New developments have been extensively covered by König (1997) and Pottschmidt (1997).

#### 3.2.1 Timing Analysis with Fourier Techniques

##### 3.2.1.1 Power Spectral Density

The analysis of time series with Fourier techniques is mainly suited for equidistant time series, i.e., for time series where the count-rate  $x(t_i) =: x_i$  has been determined at times  $t_i = t_0 + i\Delta t$  where  $\Delta t$  is the time-step,  $i$  is a natural number going from 0 to  $N - 1$ ,  $N$  is the number of points in the time series, and  $t_0$  is the start of the time series<sup>1</sup>. Without loss of generality it will always be assumed that  $t_0 = 0$ . For such an equidistant time series, the Discrete Fourier Transform (DFT) is defined by

$$X_j = \sum_{k=0}^{N-1} x_k e^{2\pi i j k / N} \quad \text{where } j \in [-(N/2) \dots (N/2) - 1] \quad (3.4)$$

and the frequency  $\omega_j$  for which the Fourier coefficient  $X_j$  is computed, is

$$\omega_j = 2\pi\nu_j = 2\pi j / (N\Delta t) \quad (3.5)$$

The highest frequency for which  $X_j$  can be computed is the Nyquist frequency,  $\nu_{N/2} = 1/(2\Delta t)$ . The zeroth coefficient of the Fourier-transform,  $X_0$ , is related to the total number of photons,  $N_{\text{ph}}$  observed,

$$X_0 = \sum_{k=0}^{N-1} x_k = \frac{1}{\Delta t} \sum_{k=0}^{N-1} x_k \Delta t = \frac{N_{\text{ph}}}{\Delta t} = N \langle x \rangle \quad (3.6)$$

where  $\langle x \rangle$  is the average count-rate. With this definition of the DFT, the periodogram of a time series is defined as the squared absolute value of the Fourier coefficients, multiplied by a normalization constant  $A$

$$P_j = A |X_j|^2 \quad \text{where } j \in [0 \dots N/2] \quad (3.7)$$

<sup>1</sup>A source of confusion is that some authors, most notably van der Klis (1989), use the total number of photons per time-bin instead of the count-rate in their definitions.

Since the count rates are real numbers,  $X_j = X_{-j}^*$  and therefore  $|X_j|^2 = |X_{-j}|^2$ , so that the periodogram needs to be defined only for positive frequencies (the star, \*, denotes complex conjugation). The continuous counterpart of the periodogram is the Power Spectrum Density (PSD), in astronomy both terms are typically used without distinguishing the continuous and the discrete versions. Note that it is common practice to subtract the mean count rate from the data before computing the periodogram, i.e., to force  $X_0 = 0$ .

For a strictly sinusoidal time series the PSD has a pronounced peak at the frequency of the signal, while a Quasi-Periodic Oscillation (QPO) is characterized by a broad peak centered on the QPO frequency. Non-periodic phenomena (“noise”) are characterized by the broad band behavior of the PSD. For “white noise” the periodogram is flat, while for “red noise” the PSD is characterized by the power-law exponent resulting from the fit of a power-law to the data. Other processes result in even more complicated shapes of the periodogram. Of these, the “shot-noise” process has been used extensively in X-ray astronomy (Belloni & Hasinger 1990b; Lochner, Swank & Szymkowiak 1991). The simplest shot-noise process is a time series consisting of a sequence of statistically independent, exponentially decaying “shots” with a decay time  $\tau$ . The PSD of the shot noise process is given by

$$P_{\text{SN}}(\omega) \propto \frac{\lambda}{(1/\tau)^2 + \omega} \quad (3.8)$$

(Lehto 1989) for  $\omega \neq 0$ . More complicated shot noise processes are discussed by Papoulis (1991, chapter 11).

The normalization constant of the periodogram,  $A$ , is one of the big mysteries of time series analysis, with almost as many definitions as there are authors. The following normalizations are in use in the X-ray astronomical literature:

$A_{\text{Leahy}} = 2\Delta t^2/N_{\text{ph}} = 2\Delta t/X_0$ : This normalization, due to Leahy et al. (1983) and promoted by van der Klis (1989), is very often used in the QPO literature<sup>1</sup>. If the statistical fluctuations in the time series are Poissonian, then the ensemble averaged power is equal to 2 and the variance of the  $P_j$  is  $s_j = 4(1 + 1/N_{\text{ph}})$  (Leahy et al. 1983). In the limit of large  $N_{\text{ph}}$ ,  $P_j$  is distributed as a  $\chi^2$ -distribution with two degrees of freedom. If the periodograms from  $M$  data segments (of equal length and same time binning) are summed to yield a total power-spectrum, the points in the spectrum are distributed as a  $\chi^2$ -distribution with  $2M$  degrees of freedom (Leahy et al. 1983).

$A_{\text{Miyamoto}} = 2\Delta t^2/(N_{\text{ph}}\langle x \rangle) = A_{\text{Leahy}}/\langle x \rangle$ : This normalization has been used mainly by Miyamoto and co-workers (Miyamoto et al. 1991, 1992) and formally defined by van der Klis (1995). Note that they have sometimes given confusing and contradictory definitions of their normalization. In the Miyamoto normalization, the

<sup>1</sup>Note that the definitions given here assume that  $x_i$  is the *count rate* at time  $t_i$ . Some authors prefer to do the analysis using the *total* number of photons detected in the time interval  $\Delta t$ . In order to obtain the same periodograms, the factor of  $\Delta t^2$  has been introduced in the normalization.

periodogram in the Leahy normalization is divided by the mean count-rate of the source to obtain a count-rate independent periodogram. This has the advantage that the shapes of periodograms from different sources can be easily compared. The integrated periodogram, i.e., the area under the PSD estimated by the periodogram, defines the square of the total rms variability of the time series, i.e., the fractional amount by which the lightcurve is sinusoidally modulated (Nowak et al. 1998a).

$A_{\text{Schlittgen}} = 1/N$ : This is a normalization that is mainly used in mathematical time series analysis (Schlittgen & Streitberg 1995). It has been used at IAAT in the analysis of the periodogram of Cyg X-1 by Pottschmidt (1997), and by König (1997) in the analysis of the light curves of active galactic nuclei. The main advantage of this normalization is that the mathematical description of the periodogram is very easy. On the other hand, absolute measurements of power, which are needed, e.g., when a comparison with published data is to be made, are not possible since in the Schlittgen & Streitberg (1995)-normalization of the periodogram depends on the count-rate and on the temporal binning.

Due to the large variance of the  $P_j$  when determined from just one time series it is common practice to average individually determined periodograms and/or to rebin the periodogram in frequency space. See van der Klis (1989) for a description of this process. Note also that interrupted time series suffer from “spectral leakage”, the redistribution of power to other frequencies, which complicates the interpretation of the periodogram and can result in spurious features in the periodogram (Deeter & Boynton 1982).

### 3.2.1.2 Counting Statistics and the Effect of Dead Time

The time series observed in X-ray astronomy are usually from very weak sources and no continuous signal is measured, but the time series is obtained from counting the photons arriving in the detector in the interval  $\Delta t$ . Thus, the measured time series is influenced by two (statistically independent) processes: the temporal behavior of the source itself *and* additional noise due to the measurement process. Obviously, the periodogram computed using eq. (3.7) is influenced by both processes. Since one is not interested in the noise caused by the measurement process, means are sought for to remove the effect of the measurement process from the measured periodogram. Based on the fact that the measurement process and the statistical fluctuations of the source are statistically independent of each other, it can be assumed that the total measured periodogram is the sum of the signal and the noise powers

$$P_j = P_{j, \text{signal}} + P_{j, \text{noise}} \quad (3.9)$$

(van der Klis 1989, eq. 3.1). If the noise-contribution  $P_{j, \text{noise}}$  were known, therefore, it could be subtracted from the measured periodogram to obtain the true signal periodogram. Often it is assumed that the measurement process is dominated by pure photon statistics, i.e., a Poisson process. If this is the case, then  $P_{j, \text{noise}} = 2$  in the Leahy et al. (1983) normalization.

If the measurement process is purely Poissonian, the  $\chi^2$  property of the PSD (in Leahy normalization) can be used to separate the signal- and noise-components. The probability for the Poisson noise to exceed a threshold level  $P_{\text{threshold}}$  is given by

$$\text{Prob}(P_{j,\text{noise}}) = Q_{\chi^2}(P_{\text{threshold}}|n) = \left[2^{n/2}\Gamma(n/2)\right]^{-1} \int_{P_{\text{threshold}}}^{\infty} t^{n/2-1} \exp(-t/2) dt \quad (3.10)$$

where  $n = 2$  or  $n = 2M$ , depending on whether the periodograms have been averaged or not.

With a real detector, however, the simple assumption that the measurement process introduces pure Poisson noise no longer holds: After the detection of a photon in an X-ray detector, the detector cannot detect another photon for a certain amount of time, since, for example, the detector gas needs some time to discharge, the detector electronics need time to process the signal, etc. This effect is called the dead time. Because dead time usually operates on small time scales, the measured periodogram is mainly distorted at frequencies close to the Nyquist frequency. Monte Carlo simulations performed by Weisskopf in 1985 reported by van der Klis (1989) show that the expectation value for the noise power in Leahy et al. (1983) normalization is approximately given by

$$\langle P_{\nu, \text{noise}} \rangle = 2(1 - \langle x \rangle \tau_{\text{dead}}) \left[ 1 + 2 \left( \frac{\langle x \rangle \tau_{\text{dead}}}{1 - \langle x \rangle \tau_{\text{dead}}} \right) \left( \frac{\tau_{\text{dead}}}{\Delta t} \right) \sin^2 \frac{\pi \nu}{2\nu_{N/2}} \right] \quad (3.11)$$

where  $\langle x \rangle$  is the measured count-rate,  $\tau_{\text{dead}}$  the dead time, and  $\nu_{N/2}$  the Nyquist frequency. For the PCA on RXTE, the dead-time due to electronics is about  $10 \mu\text{s}$  (Zhang & Jahoda 1996), which results in a noise-level at the Nyquist frequency of about 1.95 for the count rate of Cyg X-1 (assumed to be 850 counts/detector), fairly close to the measured value (chapter 5.5). In a recent work, Zhang et al. (1995) derive the correct shape of  $\langle P_{\nu, \text{noise}} \rangle$  from first principles. These authors show that eq. (3.11) is sufficient for the description of the count rate effects, provided that the time resolution of the light curve is much larger than the dead time.

### 3.2.1.3 Period Determination with unevenly spaced sampling

The Fourier methods described in the last two sections are well suited for the description of the temporal behavior of an astronomical source provided that the data do not contain gaps (resulting in spectral leakage) and provided that the data are not unevenly sampled. Unfortunately, it is a main characteristic of astronomical time series that they usually do contain both effects, unevenly sampling and missing data, except for the few special cases where the data have been measured over one cloudless night or only cover one satellite orbit. Thus the Fourier-based periodogram described in the last two sections can only be used to characterize the short term behavior of an astronomical source while other methods have to be used to describe the long term behavior. Within the framework of this thesis, the main interest in the description of the long term time scales is in searching for possible periodicities in the data which might be caused by orbital motion, precessing accretion disks, or other effects.



In an in-depth analysis of the periodogram as applied to astronomical time series, Scargle (1982) concluded that a modified periodogram, first presented by Lomb (1976), should be used instead of eq. (3.7) for the period search in the frequency domain. This modified Lomb-Scargle periodogram is defined by

$$P(\omega) = \frac{1}{2} \left\{ \frac{\left[ \sum_{k=0}^{N-1} \tilde{x}_k \cos \omega(t_k - \tau) \right]^2}{\sum_{k=0}^{N-1} \cos^2 \omega(t_k - \tau)} + \frac{\left[ \sum_{k=0}^{N-1} \tilde{x}_k \sin \omega(t_k - \tau) \right]^2}{\sum_{k=0}^{N-1} \sin^2 \omega(t_k - \tau)} \right\} \quad (3.12)$$

(Scargle 1982, eq. 10), where  $\tau$  is given by

$$\tan(2\omega\tau) = \frac{\sum_{k=0}^{N-1} \sin 2\omega t_k}{\sum_{k=0}^{N-1} \cos 2\omega t_k} \quad (3.13)$$

and where  $\omega$  is the frequency at which the power is computed. In eq. (3.12), the  $t_k$  are the times at which the signal was sampled, and  $\tilde{x}_k$  is the time series normalized to mean zero and variance unity, i.e.,  $\tilde{x}_k = (x_k - \langle x \rangle) / \sigma$ , where  $\langle x \rangle$  is the mean count rate and  $\sigma$  is the standard deviation of the data (cf. Horne & Baliunas 1986 for a clear explanation of this choice of normalization). The Lomb-Scargle periodogram is time invariant, i.e., replacing  $t_k$  by  $t_k - T$ , where  $T$  is a constant, does not change  $P(\omega)$ . For a fast implementation of the Lomb-Scargle periodogram, see Press & Rybicki (1989).

The probability of the Lomb-Scargle periodogram to exceed a given value  $Z$  is exponentially distributed, i.e.,

$$\Pr(Z > z) = 1 - (1 - \exp(-z))^{N_i} \quad (3.14)$$

which can be used to check the significance of detected periods. In eq. (3.14),  $N_i$  is the number of statistically independent frequencies in the periodogram, given approximately by

$$N_i = -6.362 + 1.193N + 0.00098N^2 \quad (3.15)$$

(Horne & Baliunas 1986, eq. 13). This formula is chosen such that it overestimates the true number of statistical independent frequencies, thus in reality  $\Pr(Z > z)$  could only be larger.

The uncertainty to which it is possible to detect the frequency of a periodic signal with the Lomb-Scargle periodogram is still affected by aliasing. The approach recommended by Scargle (1982) is to compute the window function by calculating the periodogram of a periodic signal of high frequency sampled at the same times as the original data. An approximate formula for the standard deviation of the frequency is

$$\delta\omega = \frac{3\pi\sigma_N}{2N^{1/2}TA} \quad (3.16)$$

(Horne & Baliunas 1986, eq. 14) where  $\sigma_N$  is the standard deviation of the residual time series after the sinusoidal signal has been subtracted,  $T$  is the total length of the time series, and  $A$  is the amplitude of the signal.

### 3.2.2 Coherence and Time Lags

Although the periodogram is very powerful in describing the variability properties of a time series, not all information available from the time series is contained in the periodogram and the comparison of different time series using their periodograms will not reveal all physics behind the process generating the time series. For example, in section 2.3 it was shown that the presence of a Comptonizing medium leads to characteristic time lags between different energy bands. Since a time lag corresponds to a phase lag in Fourier space, a measurement of these lags using the periodogram is impossible since the phase is lost when squaring the Fourier coefficients. For comparing different time series, therefore, other methods have to be used. Of these methods, the cross spectrum and the coherence function are convenient. The use of these functions in X-ray astronomy is described by Nowak & Vaughan (1996) and Vaughan & Nowak (1997), while a brief introduction from a mathematical point of view has been given by Brockwell & Davis (1991, chapter 11).

For extracting the desired information, the computation is best done in Fourier space. In the following, the two time series to be compared are designated by the indices 1 and 2. The average phase lag is given from the complex cross-spectrum, defined by

$$C_j = X_{j,1}^* X_{j,2} \quad (3.17)$$

To obtain a more physical quantity, it is convenient to express this phase lag in terms of the time delay at frequency  $\nu_j$ ,

$$(\delta t)_j = \frac{\arg(C_j)}{2\pi\nu_j} \quad (3.18)$$

The phase lag or time delay computed this way, however, does not contain any information on how strict the phase relationship is between the two light curves. For example, even for purely random time series there might be by chance some phase lag between two series at a given frequency. To measure how strict the phase relationship between the two time series is, the time series is divided into many subseries and the cross spectrum is computed for each of these time series. These individual cross spectra are averaged. If there is a strong phase relationship, then the average cross spectrum is non-zero, while for a weak or non-existent phase relationship the individual cross spectra are randomly distributed and average to zero. In more formal terms, this averaging is done by computing the coherence function, defined by

$$\gamma_j^2 = \frac{|\langle C_j \rangle|^2}{\langle |X_{j,1}|^2 \rangle \langle |X_{j,2}|^2 \rangle} \quad (3.19)$$

If there is a linear relationship between the two time series, then the Fourier coefficients are related by virtue of the convolution theorem (Vaughan & Nowak 1997, assuming a continuous light curve for simplicity)

$$x_2(t) = \int_{-\infty}^{+\infty} h(t - \tau)x_1(\tau) d\tau \quad \iff \quad X_2(\nu) = H(\nu)X_1(\nu) \quad (3.20)$$

in this case the cross-spectrum is

$$|\langle C \rangle|^2 = |\langle X_1^* X_2 \rangle|^2 = |\langle H X_1^* X_1 \rangle|^2 = |H|^2 \langle |X_1|^2 \rangle^2 = \langle |X_1|^2 \rangle \langle |X_2|^2 \rangle \quad (3.21)$$

since

$$\langle |X_2|^2 \rangle = \langle |H X_1|^2 \rangle = |H|^2 \langle |X_1|^2 \rangle \quad (3.22)$$

Thus, the coherence function is unity if a linear relationship exists between the two time series. Within the framework of this thesis the most important example for such a linear relationship is that coherence is preserved by Compton scattering, *provided that the Compton cloud itself is static* (Nowak & Vaughan 1996). Other examples for how physical processes can modify or preserve the coherence function are given by Vaughan & Nowak (1997).

In the above discussion, the influence of the measurement process on the determination of the cross spectrum and the coherence was deliberately omitted. It turns out that the Poisson noise introduced by the measurement process as well as the dead time of the detector are important modifiers for the coherence, so that the measured coherence function is not the coherence function intrinsic to the observed source. A recipe for determining the intrinsic coherence function from measured X-ray data as well as information on the significance of the coherence function determined from this recipe are given by Vaughan & Nowak (1997).

### 3.2.3 Stochastic Methods

Although Fourier techniques are typically used to characterize the temporal behavior of the observed X-ray sources, they are not the only tools that can be used for describing this behavior. An alternative approach is the description of the observed time series using stochastic models directly in the time domain. In recent years it was found that the class of autoregressive processes is of special importance for astronomy. This class has been found to be able to reproduce a wide variety of observed temporal phenomena (Scargle 1981; König & Timmer 1997; Pottschmidt et al. 1998). Outside of astronomy, similar processes have been used in a variety of fields like the medical sciences, stock exchange rates, and many more.

An autoregressive process of order  $p$  (called an AR[ $p$ ]-process for short), is defined by

$$\tilde{x}_j = \sum_{i=1}^p a_i \tilde{x}_{j-i} + \epsilon_j(\sigma_\epsilon^2) \quad (3.23)$$

where  $\epsilon_j(\sigma_\epsilon^2)$  is a Gaussian random variable with variance  $\sigma_\epsilon^2$  and mean zero, while  $\tilde{x}$  represents the time series (the tilde denotes that the time series is normalized to mean zero and variance unity). The coefficients  $a_i$  determine how strongly  $\tilde{x}_j$  is correlated to the previous values of the time series (hence the name autoregressive process). Obviously, for a stationary process  $|a_i| < 1$ , and only positive values of  $a_i$  lead to physically meaningful models. Of special importance for this thesis is the AR[1] process, which can

be interpreted as the stochastic superposition of exponential shots with time constant  $\tau = -1/\log |a_1|$  (analogous but *not identical* to simple shot noise), which is empirically found to be able to describe the light curves from galactic BHs as well as from active galactic nuclei (König, Staubert & Wilms 1997; Pottschmidt et al. 1998).

Although the major physical behavior of a source might be able to be described with eq. (3.23), the observed time series will not look like  $\tilde{x}_j$  since the observational process, e.g., the Poisson noise introduced by the finite size of the detector, influences the observation. It can be shown that this observational noise leads to an underestimation of the true temporal parameters of the system (König & Timmer 1997). In analogy to Fourier techniques, where the measured periodogram is given by the sum of the signal  $P_{\text{signal}}$  and an additional component,  $P_{\text{noise}}$ , that is due to the measurement process (cf. eq. [3.9]), extensions to eq. (3.23) have been developed which allow for the explicit modeling of the observational process. Of these, the Linear State Space Model (LSSM) is of special importance. The LSSM of first order, LSSM[1], is defined by

$$\tilde{x}_j = a\tilde{x}_{j-1} + \epsilon_j(\sigma_\epsilon^2) \quad (3.24a)$$

$$\tilde{y}_j = c\tilde{x}_j + \eta_j(\sigma_\eta^2) \quad (3.24b)$$

where  $\eta$  is Gaussian noise with mean  $\sigma_\eta^2$ . Eq. (3.24a) is the AR[1] process describing the variability attributed to the physical system, while eq. (3.24b) models the observational process, resulting in the observed light curve  $\tilde{y}_j$ . There are powerful methods that allow to estimate the system parameters from  $\tilde{y}_j$ . By working in the time domain and directly modeling the observed data, problems like spectral leakage and aliasing arising in the frequency domain are avoided. A description of these methods has been given by König (1997) and König & Timmer (1997).

The PSD resulting from such an LSSM[1] model is given by

$$P_{\text{LSSM}}(\omega) = \frac{\sigma_\epsilon^2}{1 + a^2 - 2a \cos \omega} + \sigma_\eta^2 \quad (3.25)$$

Especially for noisy data, fitting the periodogram with a PSD of this shape leads to larger uncertainties for  $a$  and  $\sigma_\epsilon^2$  than working in the time domain (König & Timmer 1997).

## CHAPTER 4

---

### RXTE

The observations presented in this thesis rely mainly on results obtained with the Rossi X-ray Timing Explorer (RXTE). RXTE was launched on a Delta II Rocket from Cape Canaveral on 1995 December 30. Its circular orbit has an altitude of about 580 km above ground, corresponding to an orbital period of about 96 minutes, with an inclination of  $23^\circ$ .

According to a popular brochure about RXTE, the general purpose of the mission is to “take the pulse of the universe”, i.e., to make the measurement of lightcurves with a temporal resolution in the ms to  $\mu\text{s}$  range possible while also providing a moderate energy resolution from 2 to 250 keV. See Bradt (1983) for a first description of the scientific objectives of an “X-ray timing mission”, and Bradt, Swank & Rothschild (1990, 1991) for pre-launch summaries of the satellite instrumentation and capabilities. A very extensive technical description of the instruments is given in Appendix F to the National Aeronautics and Space Administration (NASA) Research Announcement for RXTE (NASA 1997, unless noted otherwise, the rest of this chapter is based on this publication), while an overview on the management procedures has been given in an internal NASA report (NASA 1996).

The RXTE spacecraft is based on NASA’s Medium Explorer class of spacecraft (see Fig. 4.1 for a sketch of the spacecraft). Compared to previous X-ray missions like the Advanced Satellite for Cosmology and Astronomy (ASCA) and the Röntgensatellit (ROSAT), this spacecraft provides a much larger flexibility: due to its rotating solar panels the spacecraft is able to observe almost any region of the sky<sup>1</sup>. Furthermore, RXTE has two (flat) high gain antennae that are able to track different Tracking and Data Relay Satellites (TDRS), allowing the spacecraft to be in (almost) real time connection with the Science Operations Facility (SOF) at Goddard Space Flight Center (GSFC). The daily average telemetry rate of the spacecraft resulting from these connections is 40 kbps, with much higher peak rates of up to 256 kbps for 30 min per day being possible. For onboard data storage, 1 GB of solid state RAM are available. Finally, the onboard software of the spacecraft is more intelligent than has been the case in previous missions. For example, pointing the instruments to a different source just requires the specification of the source position ( $\alpha$  and  $\delta$ ) and of a slewing-rate, the rest is done autonomously by the spacecraft (Rothschild 1997). This flexibility has allowed the SOF to react very quickly when necessary, with response times as small as 3 hours.

Onboard RXTE are two pointing instruments that are used to make long observations

---

<sup>1</sup>Because of thermal control considerations the spacecraft is not pointed closer than  $30^\circ$  to the sun.

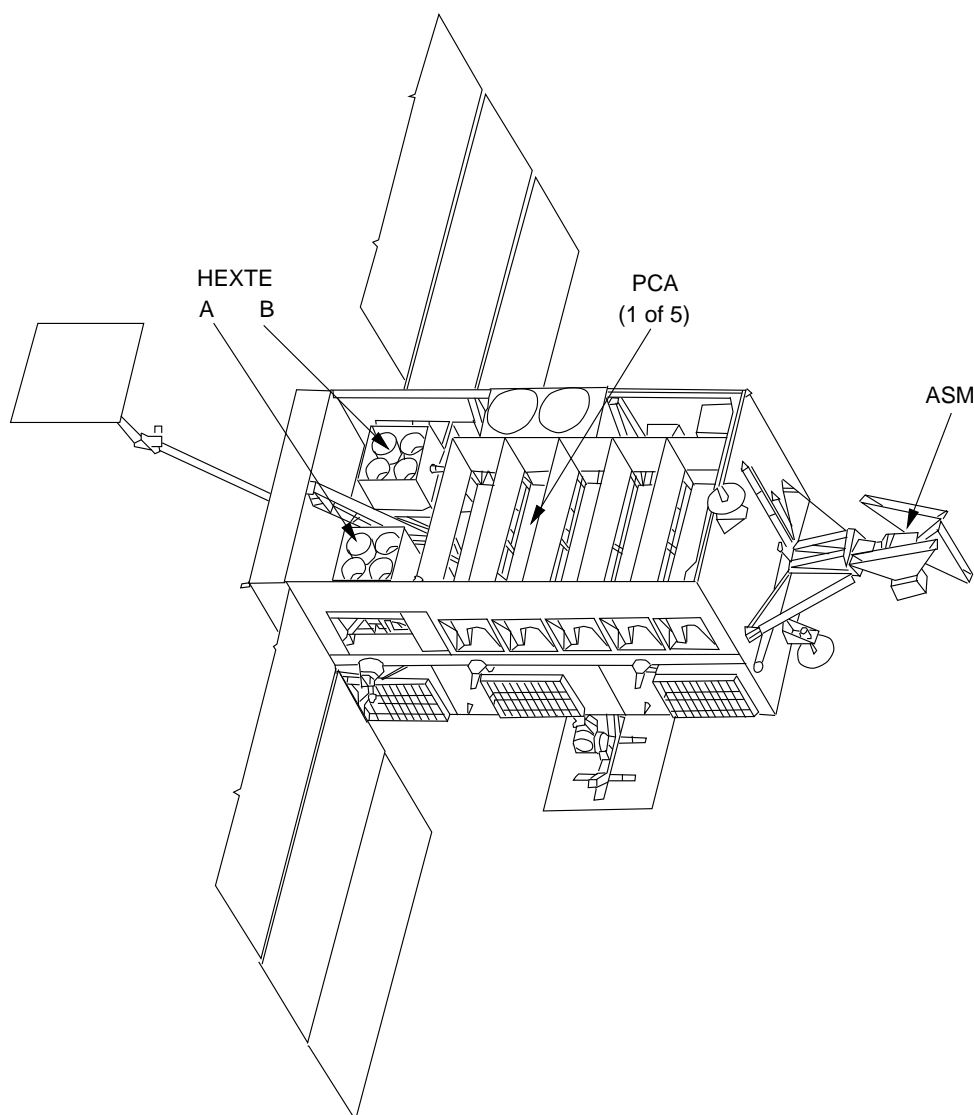


Figure 4.1: The RXTE spacecraft (after Rothschild et al. 1998, Fig. 1)

of individual cosmic X-ray sources: the Proportional Counter Array (PCA), which is sensitive to photons in the energy range from about 3 to about 100 keV, and the High Energy X-ray Timing Experiment (HEXTE), which is sensitive to photons in the energy range from about 15 to about 250 keV. In addition, the All Sky Monitor (ASM), an array of shadow cameras scanning the whole sky visible from the spacecraft for five to ten times per day, provides almost uninterrupted information about the long-term behavior of bright X-ray sources. The rest of this chapter is devoted to a description of the scientific instruments upon RXTE in greater detail and to a definition of the data extraction methods used to analyze data obtained from these instruments. Section 4.1 describes the PCA, section 4.2 is devoted to HEXTE, and section 4.3 describes the ASM. The chapter ends in section 4.4 with a summary of the data extraction process used in the analysis of RXTE data.

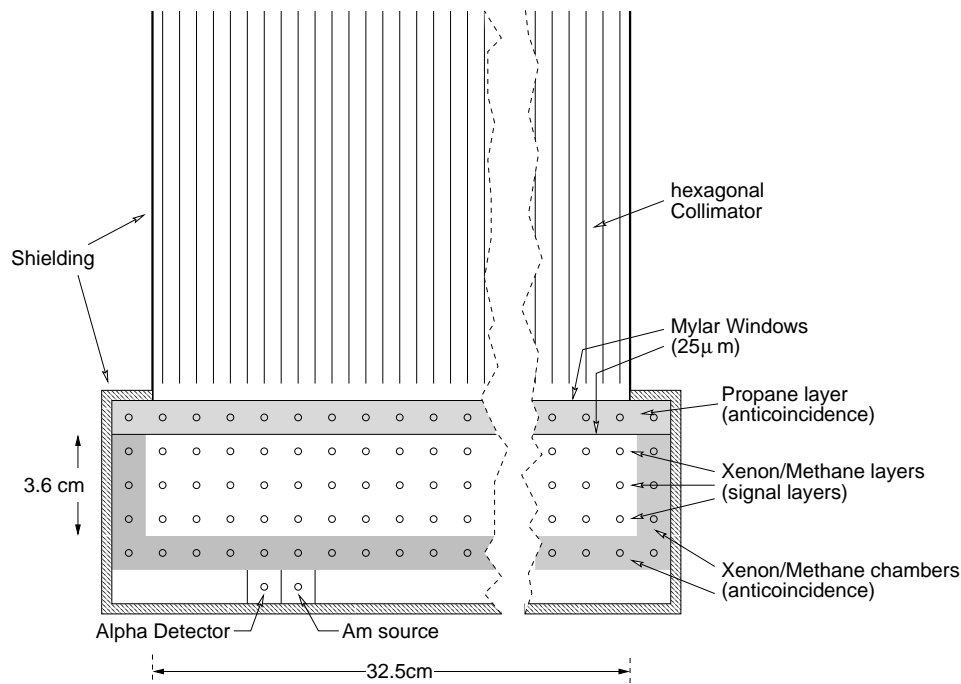


Figure 4.2: Sketch of the structure of one proportional counter unit of the PCA (after Bradt, Swank & Rothschild 1990, Fig. 3).

## 4.1 RXTE-PCA

### 4.1.1 Introduction

The Proportional Counter Array (PCA) onboard RXTE was built in house by NASA's GSFC. It is a direct descendant of the HEAO-1 A-2 instrument (Rothschild et al. 1979, and references therein), with a much larger effective area and much higher temporal resolution. The PCA is an array of five coaligned Proportional Counter Units (PCUs), one of which is shown in Fig. 4.2. From top to bottom, each PCU consists of a Propane anticoincidence layer, three Xenon/Methane science layers, and a final Xenon/Methane anticoincidence layer. The side anodes of the Xe-chamber are connected to provide further anticoincidence information and the detectors are wrapped with a graded shield (Tl and Zn) to provide additional passive background reduction. Gain control and calibration is done using a tagged  $^{241}\text{Am}$  source in each of the PCUs.  $^{241}\text{Am}$  is unstable to  $\alpha$ -decays that are coincident with the emission of a 59.6 keV photon. A photon registered in the PCU simultaneously with the detection of an  $\alpha$ -particle in the detector attached to the Am-probe is assumed to be produced in the Am source and can be used for calibration purposes, e.g., to perform automatic gain control (see Jahoda et al. 1997, for a description). Since the PCA is not position sensitive, BeCu collimators are used to provide a field of view of  $1^\circ$  FWHM. By accident, these collimators are slightly misaligned with respect to each other. Since the misalignment is small, it is not a problem for the standard data analysis. The misalignment has even proven to be useful since it allows for a coarse determination of source positions within the field of view (Jahoda et al.

1997). The total collecting area of the detectors is  $6250 \text{ cm}^2$  with a temporal resolution of  $1 \mu\text{s}$  and an energy resolution of 18% at 6 keV.

Due to the large effective area of the instrument the count rates are so high that it would be easy to max out the telemetry constraints of the satellite if all event information measured within the PCA were transmitted to ground. Thus, the measured raw data has to be compressed by selecting only the information desired by the observer in the observing proposal, throwing away unnecessary information. This is the task of the Experiment Data System (EDS). A very large set of observational modes is available, providing the observer with many choices on what is finally transmitted to Earth. For example, it is possible to ignore part of the spectral information by fully ignoring certain PHA channels or rebinning others, and the temporal resolution of the transmitted data can be reduced by ignoring the lower bits in the time word. Furthermore, individual photon event information can be transmitted (“event data”) as well as whole spectra accumulated over specific time intervals (“science array data”). Up to seven different modes can be treated in parallel by the EDS, allowing fine tuning of the returned information. Of these seven modes, two modes are reserved for the “standard mode data”: the standard 1 data with a temporal resolution of 0.125 sec, including PCU count rate information (without spectral information) and various indicators for the observed background (see p. 93f.) and the standard 2 data with a temporal resolution of 16 sec, which include 129 PHA channel spectra for each PCU layer, 33 PHA channel Propane spectra, and various other detector and layer specific information. The standard 2 data are the basis of most of the spectral work presented in chapters 5 and 6. The standard mode data are *not* gain shifted using the  $^{241}\text{Am}$  source, while all other modes are.

In the first 70 days after launch the PCA high voltage was set to the planned value of 2000 V. During passage through the South Atlantic Anomaly (SAA) the voltage was reduced to 1000 V. In mid 1996 March, two of the five detectors exhibited signs of occasional break-downs that were most probably caused by sparks within the Xe-chamber followed by polymerization of the quenching gas around the anodes (Jahoda et al. 1997, see Smith & Turner 1982 and references therein for laboratory studies concerning this effect). This phase of the first 70 d after launch is usually called the epoch 1. As a reaction to the sparks, a reconfiguration of the PCA was undertaken, reducing the high voltage setting to about 1950 V and switching the detectors off during the SAA passage. The transitional period where the detector gain was changed is called the epoch 2. Finally, since 1996 April 15 all detectors are operated at  $\sim 1950 \text{ V}$ , and detectors 4 and 5 are turned off in phases of high particle background<sup>1</sup>. This phase, called epoch 3, started in 1996 May and lasts until today. Since the flaky PCUs still occasionally exhibit an unstable behavior they are switched off approximately every third day, so that any given observation can consist of parts where all five detectors, four detectors, or only three detectors are working.

---

<sup>1</sup>The detector numbering scheme for the individual PCUs is very confusing. Depending on whether the PCU is seen in the context of the EDS, or in the context of the communication with the PCA electronics, the detectors are numbered from 0 to 4 or from 1 to 5 (Jahoda et al. 1997).



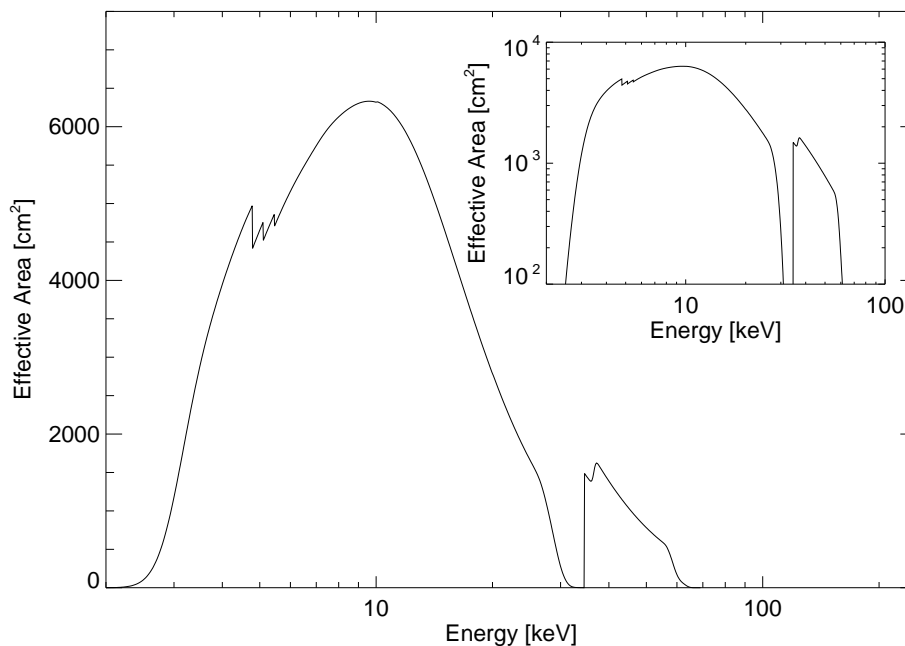


Figure 4.3: The PCA effective area as a function of energy. The inset shows the effective area in the (more often used) logarithmic form.

In the next two sections I give a description of the two experimental aspects of the PCA that are most important for the practical work with PCA-data. In section 4.1.2 the response matrix of the PCA is described, and in section 4.1.3 the background subtraction strategies for the PCA are explained. For further information of the hardware aspects of the PCA see the papers by Zhang et al. (1993), Jahoda et al. (1997), and the NASA Research Announcement for RXTE (NASA 1997, appendix F, chapter 4).

#### 4.1.2 The PCA Response Matrix

Apart from the selection of the observing modes the “normal” user of RXTE needs not to be concerned too much with the hardware aspects of the detectors. An important aspect, however, is how to interpret the PHA data after an observation has been made. For this a thorough understanding of the PCA response matrix is necessary. Due to the changes of the PCU voltage, the energy sensitivity and response of the detectors is different for epochs 1 through 3. Since all observations presented here have been made during epoch 3, special emphasis will be given to this epoch. For a description of epoch 1 data see Kreykenbohm (1997) and Kreykenbohm et al. (1998). Summaries on the PCA calibration effort have been given by Jahoda (1996) and Jahoda et al. (1996), a final calibration paper was unavailable at the time of writing (1997 December).

The PCA is the largest proportional counter ever flown on an X-ray astronomy satellite, with an effective area that is 50% larger than that of the next largest counter, the Large Area Counter (LAC) onboard *Ginga*. Due to its sheer size the calibration of the

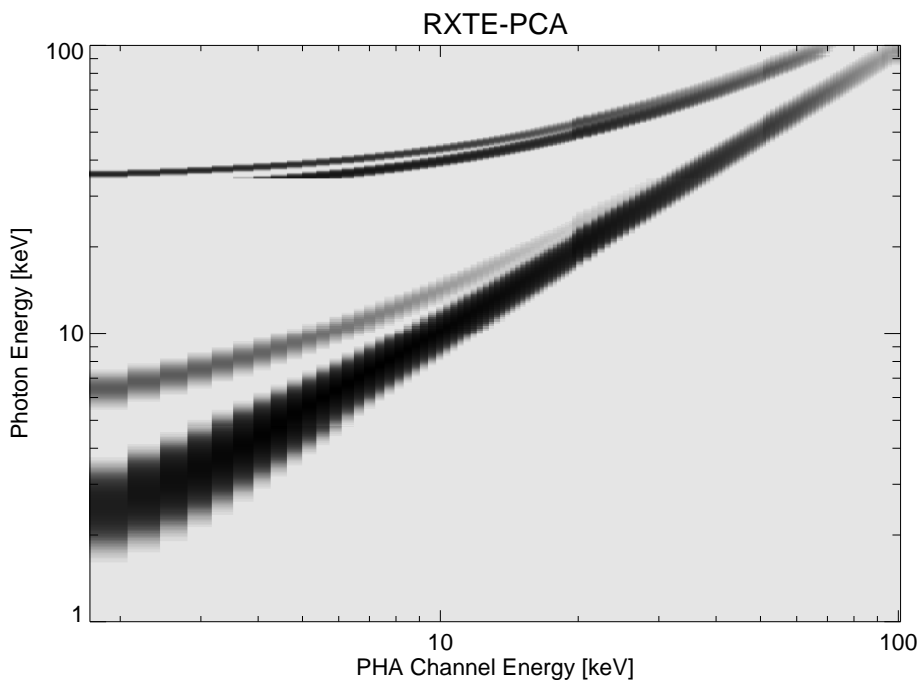


Figure 4.4: The PCA Response Matrix 2.2.1. The varying gray levels depict the probability that a photon of a given primary energy will be detected in a certain PHA-channel. The gray level scale is very non-linear! For example, only 1% of the 10 keV photons are detected in the PHA-channels around  $\sim 6$  keV.

instrument is rather difficult, since physical effects need to be taken into account that could be ignored for the smaller detector arrays of the past. For example, higher order effects in the generation of the primary electron cloud become important. Furthermore, due to the collimator, for any observed source the effective area of the detector depends on the current instrument pointing. Finally, since for standard 2 data the PHA to energy conversion depends on the (temporally variable) detector gain, it is typically not possible to use the same detector response function for all observed data. Instead a response matrix generation program, called `pcarmf`, has been developed by GSFC that builds an individual response matrix for each observation using the gain shift information and the satellite attitude information. In Fig. 4.3 the effective area of the instrument is shown. According to this figure the useful energy range of the PCA is from about 2.5 keV to an energy of about 50 keV. Note the jumps in the effective area at the Xe L edges (at energies of 5.45, 5.10, and 4.78 keV respectively, Henke et al. 1982), and the strong decrease below the Xe K edge at 34.6 keV. It is these strong changes in the detector sensitivity that cause the most difficulties and result in a systematic uncertainty of about 5% around the L edge, i.e., in the astronomically important iron K band, so that the released matrix generated with `pcarmf` is not too useful for our purposes (cf. Fig. 4.5c for an illustration of the nature of these uncertainties).

For the purposes of this thesis it was therefore decided to use a pre-released copy of version 2.2.1 of the RMF that was kindly provided by Keith Jahoda (Jahoda, 1997, priv.

comm.). These matrices assume that the source is on axis, which was the case in all observations analyzed here. In Fig. 4.4 the response-behavior of the detector resulting from this matrix is shown in a schematic way (see Kretschmar 1996, Fig. 3.3, for a similar schematic for the HEXE detector). The figure displays the probability that a photon with a given incident energy is detected in a certain PHA channel as a sequence of gray levels. Darker colors correspond to a higher probability of detection. Since the detector is linear to first order, i.e., since most photons of photon energy  $E$  are detected in the PHA channel corresponding to energy  $E$ , the gray scale had to be chosen to be very non-linear – the probability corresponding to the “lightest” features shown in the figure is very small. The figure is still very instructive, however, since the major properties of the detector can be clearly seen. The diagonal blackish line is due to the photopeak. It shows the linearity of the detector: for any incident photon energy the probability is very high that the photon is detected at this energy. The width of the photopeak corresponds to the energy resolution of the detector, which goes as  $\Delta E/E = 0.18(E/6 \text{ keV})^{-1/2}$  where  $\Delta E$  is the FWHM. The “side bands” of the diagonal are caused by the escape peaks: the detection of a photon in the PCU is mainly due to photoabsorption by the K or L shell of the detector gas. A consequence of this absorption event is that either Auger electrons are set free, or that a fluorescent photon is emitted. If this photon is not detected by a subsequent interaction with the detector gas, then the amount of energy corresponding to the fluorescence energy of Xe is lost. The net effect is that the detected signal is interpreted as coming from an initial photon of lower energy. If the observed source were monochromatic (as it is in most laboratory experiments), then the observed PHA spectrum would have a dominant peak at the photon energy (the photopeak) and a second weaker peak at  $E - E_{\text{esc}}$  due to the escaping photons (which have energy  $E_{\text{esc}}$ ). This second peak is called the escape peak. In a visualization of the response like that of Fig. 4.4, the escape peak is visible as a band at PHA energies close to the photopeak. For the PCA, the active component is the Xe gas. Since low energy photons interact with the Xe L shell, the escape peak is caused by the Xe  $L\alpha$  photons having an energy of 4.11 keV (Bearden 1967). For higher incident photon energies the major interaction is with the Xe K shell and thus the main escape peak is caused by the Xe  $K\alpha$  photons ( $E_{K\alpha} = 29.46 \text{ keV}$ , Bearden 1967). In this case, however, a second escape peak is present due to Xe  $L\alpha$  photons escaping after the interaction of the first fluorescent photon with the detector gas, as well as an escape peak caused by the (very improbable) interaction of high energy primary photons with the Xe L shell. The secondary escape peaks are weak, however, and are only visible in Fig. 4.4 due to the non-linearity of the gray scale.

The uncertainty of a RMF can be checked by looking at the residues of a spectral fit to the observation of a source with a known spectrum. The source traditionally used for this purpose is the Crab pulsar which has a pure synchrotron spectrum of the form  $N_{\text{ph}} \propto E^{-2.08}$ , absorbed by a column equivalent to  $N_{\text{H}} = 3 \times 10^{21} \text{ cm}^{-2}$  (Toor & Seward 1974). At higher energies, above about 70 keV, the spectrum has been reported to soften, i.e., the power-law index increases (Strickman, Johnson & Kurfess 1979, and references therein). To study the long-term stability of the detectors on RXTE, the Crab pulsar is observed by the satellite in approximately monthly intervals. The RXTE instrument

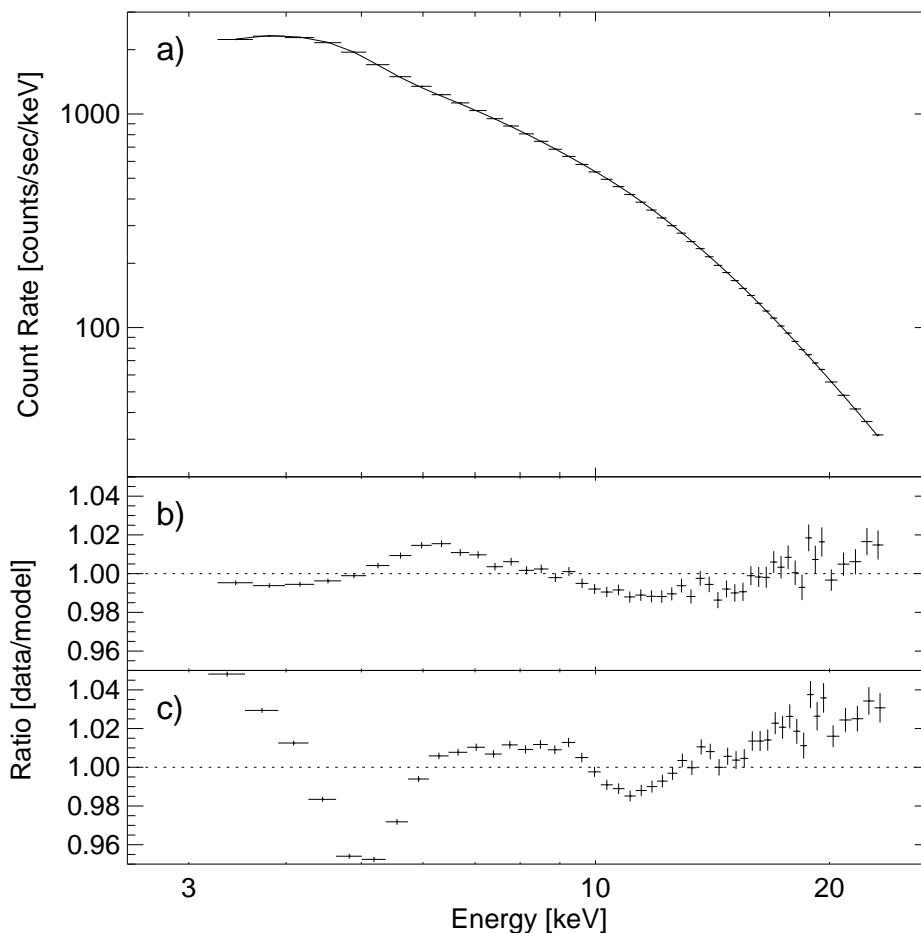


Figure 4.5: Fit to an observation of the Crab pulsar. a) Observed data and best fit using the PCA response matrix, version 2.2.1. b) Ratio between the best fit of subfigure a) and the data. c) Ratio between the data and the best fit obtained with the older matrix generated with `pcarmf`. Note the improvement between c) and b).

team provided me with 1200 s of one of these monitoring observations, measured 1997 January 31 (OBS-ID 10200-01-20-00, Jahoda, 1997, priv. comm.). These data were then extracted using the standard procedures employed at the IAAT (see §4.4, p. 101) and a spectral fit to an absorbed power-law was done. In Fig. 4.5 the resulting spectrum and the ratio between the model and the observation are shown<sup>1</sup>. For comparison, Fig. 4.5c shows the same ratio obtained with a fit using the older version of the RMF. It is obvious that version 2.2.1 of the matrix is a large improvement over the old `pcarmf` matrix,

<sup>1</sup>Traditionally, X-ray astronomers used the  $O - C$  residue or some variant of it to characterize the deviations between the observation and the model. In the case of a strongly varying source spectrum this approach is not very instructive and can mislead the observer. The ratio between the observation and the model is better in this respect since it is independent of the measured count rate. Furthermore, in the presence of known deviations between the assumed detector response and the true RMF, the significance of deviations between the model and the observation can be understood by comparing the measured ratio to that of a calibration observation. For this reason, only ratio plots are given in this thesis.

although there are still characteristic deviations between the model and the observation due to some ill-understood effects in the detector. These uncertainties are especially apparent below 3 keV (corresponding to PHA channel 6) and around and above the Xe K edge. Furthermore, the channels around the L edge still have some slight deviations which might be caused by uncertainties in the modeling of the energy to channel conversion. The overall uncertainty in the response is around 1%, i.e., comparable to or even better than the uncertainty in the RMF in previously flown proportional counters (the *Ginga* LAC had a final calibration uncertainty of about 2%, Turner et al. 1989). This study suggests that for bright sources like Cyg X-1, where the uncertainty in the background is negligible, the assumption of a systematic error of about 1% results in meaningful  $\chi^2$  values. For weaker sources, PHA channel dependent systematic errors should be assumed, which put less weight on the PHA channels with the largest uncertainty. This was not necessary for any object described in this thesis.

Finally it should be noted that an even better signal to noise ratio could be reached by ignoring data from the less well calibrated detectors (dets. 3 and 4), and by only using information from the top layer of the detector (Remillard, 1997, priv. comm.). For the purposes of this thesis I decided not to adopt this strategy, because

1. Throwing data away from some detectors would result in a much smaller signal which would be prohibitive in the study of the weak sources like LMC X-1, especially when detectors 4 and 5 were turned off at the time of the observation. In this case, ignoring detector 3 would mean to ignore 33% of the available data.
2. The effective area of the topmost layer drops significantly at energies above 10 keV which makes broad band observations of sources with steep spectra difficult, especially if they are weak. In the case of a bright source like Cyg X-1, the signal to noise ratio is dominated by the source and ignoring the lower layers only results in a small change in the resultant response uncertainty while the overall sensitivity of the detector is strongly reduced.

Due to these reasons it seems that for demonstrating the applicability of ADC models to observational data, using all available data while keeping in mind the slightly increased calibration uncertainty is the correct choice. For later refined studies, however, single-detector analysis, and ignoring information from the lower layers are methods that might be useful.

### 4.1.3 The PCA Background

The background seen in any X-ray detector is the sum of three parts: first, background produced by interactions of cosmic ray particles with the detector material and, second, the background produced by short-term radioactivity from isotopes produced by spallation in the detector during the transition through the SAA (about 50% of all RXTE orbits lead through the SAA). These two components of the background are called the detector internal background. In addition, there is a third contamination of the source-spectrum due to the soft X-ray sky background, i.e., soft radiation thought to be produced by the

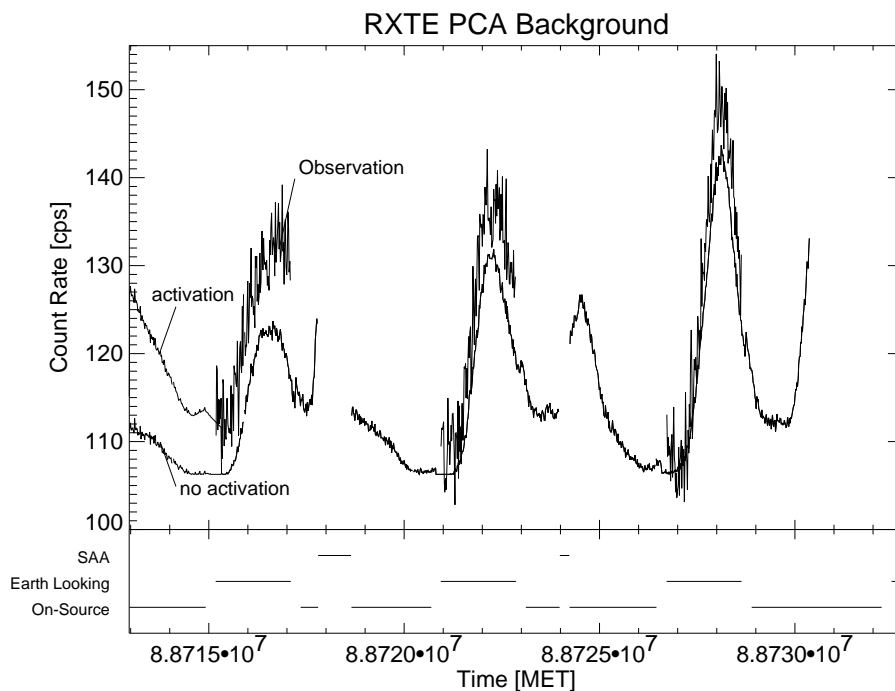


Figure 4.6: Estimated and measured background for the first part of the Cyg X-1 observation of section 5.3. The bars at the bottom of the figure indicate times during which the Earth was occulting the source, or the satellite was passing through the South Atlantic Anomaly (SAA), and times during which the satellite was looking onto the source. No data are available or can be generated for the direct SAA passages. MET is the mission elapsed time, a time system used in the RXTE data.

superposition of spectra of many weak active galactic nuclei (Fabian & Barcons 1992, and references therein). Since the PCA is not an imaging instrument and does no source-background-swapping measurements like HEXTE (see §4.2.2, p. 97), these three components of the background cannot be observed directly and the background has to be found by other means. There are two possible strategies to find the background:

1. Since the PCA detectors are turned off only during the SAA passage it is possible to extract a spectrum for the time when the instruments are looking at the Earth. At energies below about 20 keV and when the detector is not looking at the Earth's limb (which is bright in soft X-rays, Rothschild et al. 1979), the Earth's X-ray luminosity is almost zero so that the observation results in a measurement of the detector internal background. A problem with this approach is that the particle environment of the instrument during Earth occultation varies from the particle environment during the source observation since the Earth's magnetic field is not uniform. Furthermore, the activation component of the background is strongly variable during the on-source time because it has a characteristic decay time of only half an orbit.

2. Using onboard measurements for the particle background and information about the position of the satellite in the magnetic field of the Earth, a background model for the detector can be built. This is usually done by using many blank sky measurements and Earth occultations. These are correlated with the Very Large Event (VLE) count-rate, which is a measure for the current particle background, and with the orbital information to find the background model. For this thesis, the current background-model as implemented in version 1.5 of the program `pcabackest` was used. A description of the “background” of `pcabackest` has been given by Jahoda (1996). The major problem of uncritically using the PCA background model is that, at the time of writing, there were still large systematic uncertainties associated with it.

Due to the problems associated with both methods I performed tests to be able to quantify their uncertainty. In fig. 4.6 the background observed during the Earth occultation is compared with the background predicted by `pcabackest`, taking into account the VLE- and the activation model. During the Earth occultations, the `pcabackest` generated background and the measured background show the same general behavior. The difference between the model and the measurement is reduced with decreasing importance of the activation, indicating that the activation model is still the weakest part of the background model. This can also be seen when comparing the measured background with another possible background model, based on the so-called q6 count rate. Again, the main difference between the real background and the modeled background is in phases directly after the SAA.

Although these problems exist, using the background model is still preferable to using the Earth occultation background since the long term variation of the background can be taken into account<sup>1</sup>. Since no current PCA background estimator is able always to correctly model the activation component it is necessary to manually check any generated background model. I have done this by comparing the modeled background variation with Earth occultation measurements, and by testing whether the high channels in the PCA, where the count rate is background dominated, are sufficiently close to zero. If these precautions are taken into account it is usually possible to obtain a sufficiently good background subtraction.

## 4.2 *RXTE-HEXTE*

### 4.2.1 *Introduction*

The High Energy X-ray Timing Experiment (HEXTE) on RXTE has been built by the Center for Astrophysics and Space Sciences (CASS) of the University of California at San Diego (UCSD), La Jolla, CA, as a direct descendant of the HEAO-A4 detector (Matteson 1978). A pre-launch description of the detectors is given in the paper by

---

<sup>1</sup>This might be different for epoch 1 data where our tests indicated that `pcabackest` was unable to reproduce the Earth occultation data measured during a long observation of Vela X-1 (Kreykenbohm et al. 1998).

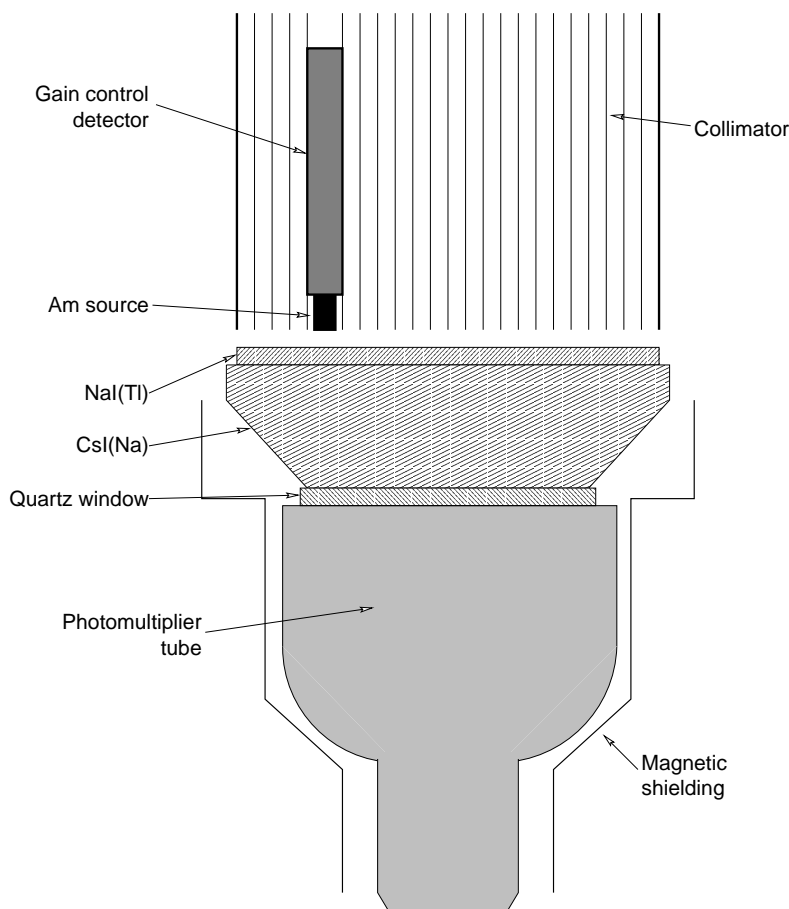


Figure 4.7: Sketch of the structure of one of the HEXTE counters (after Bradt, Swank & Rothschild 1990, Fig. 4c).

Gruber et al. (1996), while the post-launch calibration efforts have been described by Rothschild et al. (1998).

The main elements of HEXTE are two clusters of four NaI(Tl)/CsI phoswich scintillation counters, named cluster A and B, respectively, that are collimated with a lead honeycomb collimator. In Fig. 4.7 a sketch of one scintillator is given. The field of view of the collimator is  $1^\circ$  FWHM and the detector is coaligned with the PCA. Each scintillator has an effective area of  $200 \text{ cm}^2$ . Since the PHA analyzer of one of the detectors in cluster B failed on 1996 March 6, the total effective area of HEXTE is  $1400 \text{ cm}^2$  (see Fig. 4.8). The temporal resolution of the detectors is  $7 \mu\text{s}$ . As in the PCA, the gain correction is done onboard using a  $^{241}\text{Am}$  source. For all observations used in this thesis, HEXTE was operated in a mode in which all individual events are returned.

After the launch of RXTE it turned out that the HEXTE electronics suffers from a dead-time which is severely prolonged compared to pre-launch expectations. The effective observing time, the “live time”, is thus shortened by an appreciable fraction of the total on-source time (40% on average). See Rothschild et al. (1998) for a detailed description of this effect. The correction of the dead-time has to be done using special software written by the UCSD HEXTE-team. I mainly used pre-release software and



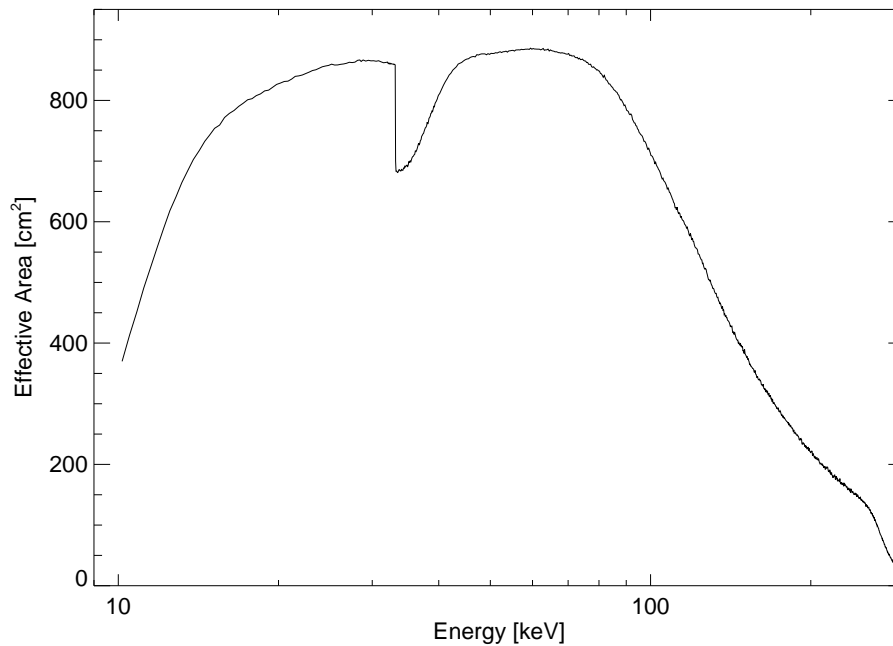


Figure 4.8: The energy dependent effective area of HEXTE cluster A, without taking into account the detector dead-time and the misaligned collimator.

internal UCSD software for the extraction of the spectra presented in chapters 5 and 6 (Gruber & Heindl, 1997, priv. comm.). The unfortunate result of the unexpectedly high dead-time and of an additional misalignment of the detector collimator (see below, p. 99) is that the real effective area of the instrument is about 50% of the pre-launch expectations, which makes it comparable with the HEXE detector built by MPE /AIT and placed onboard the Mir space station since 1987 (Reppin et al. 1983).

#### 4.2.2 The HEXTE Background

The internal background in the detectors is reduced by the phoswich design of the detectors, where raise-time discrimination is used to accept only events from within the NaI crystal as scientific events (Rothschild et al. 1998). Four plastic anticoincidence detectors around each crystal perform additional active background shielding. The resulting instrumental background is reduced to a level of about 100 cps by these procedures. To enable the observer to subtract this final background, HEXTE performs source-background rocking: each of the clusters can be displaced by  $1.5^\circ$  and by  $3^\circ$  away from its nominal pointing position. In standard HEXTE operations, one cluster is observing the source, while the other observes a background field. Source and background swapping is done every 16 s (or multiples of 16 s), with the phasing of the swapping ensuring that one detector always observes the source. Although the internal detector background turned out to be stronger than estimated before launch (see Gruber et al. 1996 for the pre-launch estimates), the background subtraction in the HEXTE func-

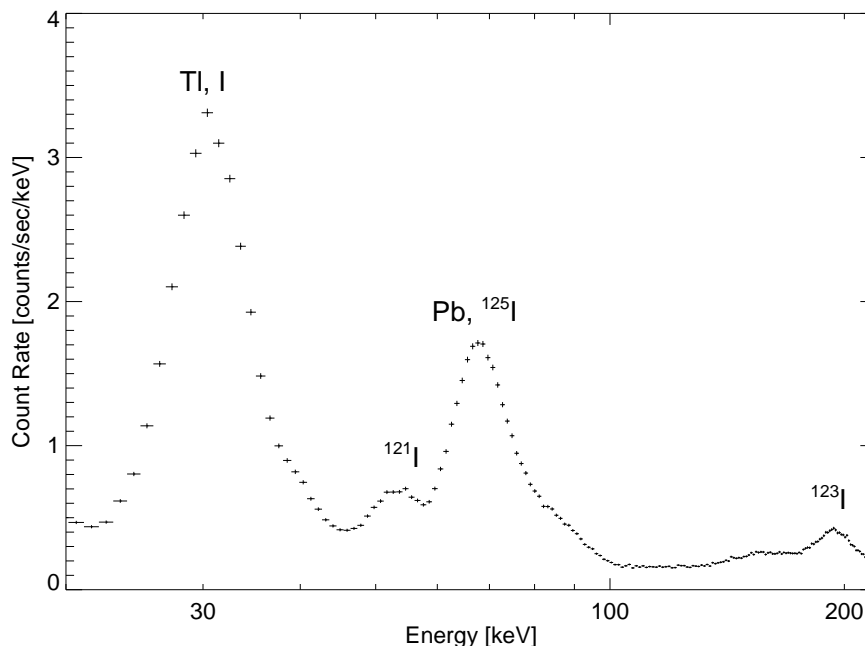


Figure 4.9: The HEXTE background spectrum for cluster A (background for the observation of Cyg X-1 presented in chapter 5, live time 3833 sec on the background fields), indicating possible sources for the major line features (Rothschild et al. 1998, Gruber, 1997, priv. comm.): a Pb line from the collimator material in the band from 60 to 90 keV, a 58 keV line from  $^{121}\text{I}$  which is the result of activation in the SAA, as well as K lines in the 25 to 30 keV range resulting from spallation products of the detector material.

tions perfectly. This can be nicely seen in our LMC observations (chapter 6), where the background was flawlessly subtracted even in the 132 ksec long observations (Fig. 6.2, p. 131). In Fig. 4.9 a background spectrum is shown. Since almost all astronomical X-ray sources are background dominated in the HEXTE band, the disappearance of the line features in a background subtracted spectrum can be used to check whether the deadtime algorithm works properly.

#### 4.2.3 The HEXTE Response Matrix

The HEXTE response matrix is well understood (see Rothschild et al. 1998 for the details of the calibration). Fig. 4.10 gives a graphical representation of the matrix. The energy resolution of the detectors is 16% at 60 keV, with an  $E^{-1/2}$  proportionality. A comparison of the current matrix with the observed Crab spectrum analogous to section 4.1.2 indicates that the systematic uncertainty of the matrix is smaller than 2%, with a break around 30 keV caused by the K edge of Iodine and K escape photons (Fig. 4.11c). Further empirical corrections can be introduced into this matrix to remove the remaining uncertainties. Figs. 4.11a and 4.11b illustrate the resulting quality of the calibration using a pure power-law fit to the Crab spectrum.

There still is a discrepancy in the relative normalization of the HEXTE and the PCA,

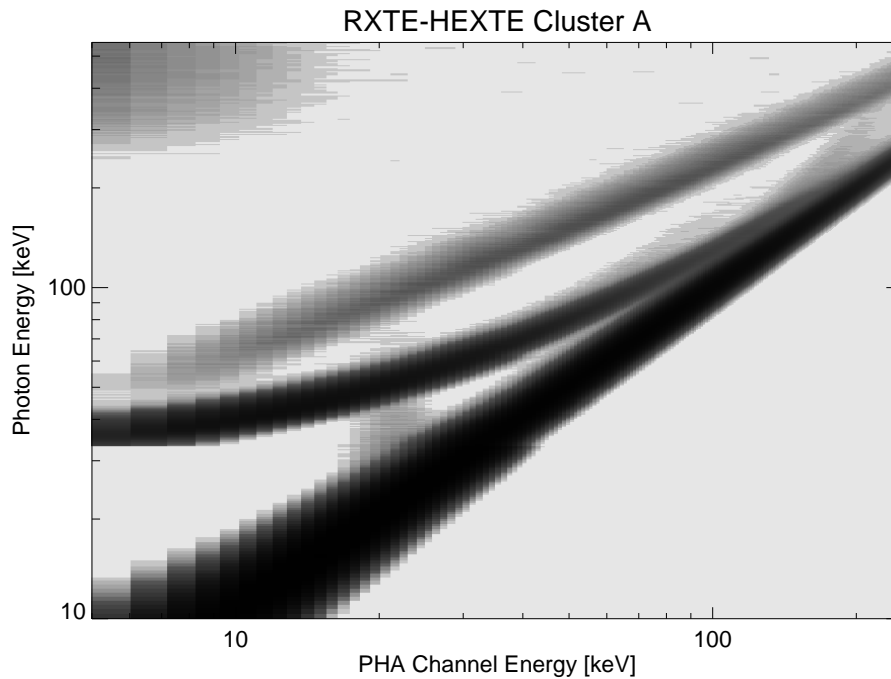


Figure 4.10: The Response Matrix for cluster A of HEXTE. A nonlinear table of gray-values was used to emphasize the physically important features of the matrix like the escape peak.

as HEXTE consistently predicts fluxes that are about 25% smaller than those measured with other instruments. Recent investigations by the HEXTE team indicate that this discrepancy is caused by a slight misalignment of the HEXTE collimator, resulting in an effective area that is smaller than that assumed in the generation of the HEXTE response matrices (Heindl, 1997, priv. comm.). Since the spectral form is unaffected by the discrepancy, the misalignment can be taken care of in the spectral fitting procedure by either letting the normalization of the spectra free in spectral fits or, alternatively, by introducing a multiplicative constant in the spectral fits and perform all normalizations with respect to the PCA. I chose to adopt this latter procedure here.

### 4.3 RXTE-ASM

The third instrument on RXTE is the All Sky Monitor (ASM). The ASM consists of three triangular shadow mask cameras with a field of view of  $6^\circ \times 90^\circ$  FWHM and a spatial resolution of  $3' \times 15'$ . The detectors are Xe/CO<sub>2</sub> Position Sensitive Proportional Counters (PSPCs) with a total effective area of 90 cm<sup>2</sup> for all three detectors combined. See Fig. 4.12 for a sketch of one ASM detector. The cameras are mounted on the “rear” of the spacecraft on a rotateable platform (cf. Fig. 4.1) that is moved such that 80% of the sky passes through the field of view of the ASM during each RXTE orbit. This allows the ASM to continuously monitor the intensity and the broad-band spectral evolution of the  $\sim 150$  brightest X-ray sources in the 1.5 to 12 keV band. Due to problems with

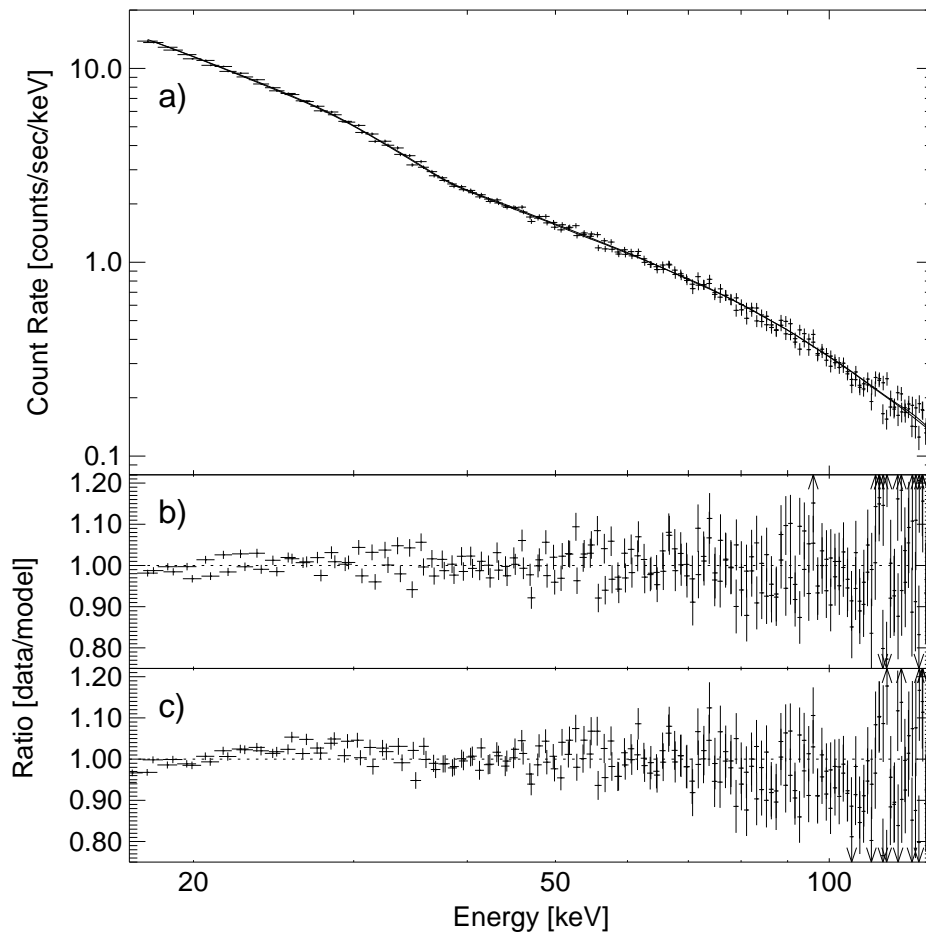


Figure 4.11: Fit of a pure power-law spectrum to the HEXTE measurement of the Crab pulsar made in 1996 January 6 (total live time 1150 s per cluster). The data were taken before the detectors in cluster B failed so that the cluster count rates are comparable. a) Data and the best fit power-law using the 1997 March 20 crab fudged matrix. b) Ratio between the data and the model, using the fudged matrix. c) Ratio between the data and the model using the unfudged matrix.

sparks in the PSPCs at the beginning of the mission, ASM data is not available for about 50 days after the beginning of the mission. The technical background of the ASM is described by Levine et al. (1996), the history and ideas behind the construction of the ASM are described by Doty (1994).

In contrast to data gathered from the pointing instruments, which are only released after a proprietary period of (nominally) one year after the observation, the ASM data are available to the astronomical community directly after the observation. First results from a quick-look analysis of the ASM data are typically published within 24 hours after the observation and can be obtained via the World Wide Web (WWW). In longer intervals these data are reprocessed and calibrated and are made available electronically by the High Energy Astrophysics Archive (HEASARC) at GSFC. The relevant data products and file formats are described by Lochner & Remillard (1997).

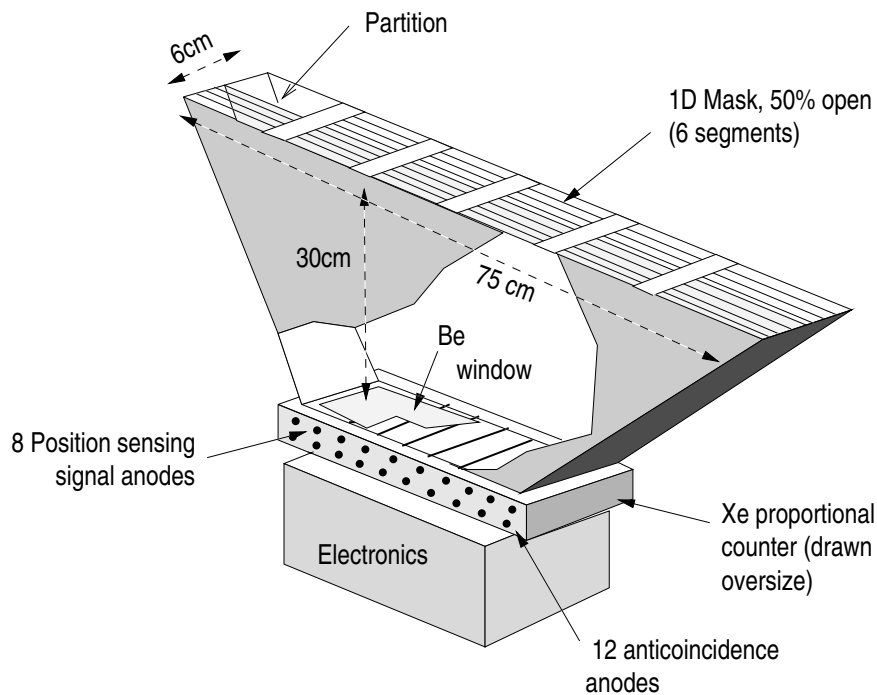


Figure 4.12: Schematic diagram of one ASM detector (not drawn to size; in reality, one segment of the mask has the size of the detector window). After Levine et al. (1996, Fig. 1).

For the purposes of this thesis, only “1 dwell” solutions to the ASM data were used, i.e., data containing count rates from the individual detectors. These individual light curves were then rebinned from their original unevenly spaced temporal binning to evenly spaced light curves with a temporal resolution of (typically) 0.5 to 1 day, depending on source brightness.

#### 4.4 Summary: Data Extraction for RXTE

To summarize, the data extraction procedure adopted for the spectra analyzed here consisted of the following steps:

- Using the orbital ephemeris and information on the high voltage in the PCA, a list of the available good time intervals is created. To avoid possible contamination from X-rays from the Earth’s limb, only data taken at elevations more than  $10^\circ$  above the horizon were used. Since the response matrices used for the PCA (version 2.2.1) and HEXTE (version dated 1997 March 20, crab fudged) do not include collimator effects, only data taken when the real satellite pointing position was closer than  $0^\circ 01'$  to the nominal position.
- Using the RXTE extraction software (ftools 4.0), spectra for these good time intervals were extracted. Separate spectra were generated for phases in which one or more PCA detectors were turned off. These spectra were *not* combined to obtain a final spectrum, but were treated individually in the spectral analysis process.
- For HEXTE, software obtained from UCSD was used to perform the dead time

correction. The success of the dead time computations was checked by looking at the source light curve and by looking at the precision of the background subtraction as described in section 4.2.2.

- For the PCA, a background estimate was generated for the good “on source” times, as well as for the Earth looking intervals (when available). To control the quality of the background model, the modeled background was compared to the Earth looking data. In addition, the background subtraction was checked by testing whether the background dominated PCA channels had zero count rates within their statistical fluctuations (see the description in §4.1.3). In the case of any problems, the good time intervals around the SAA were enlarged to minimize the effects of activation using a prescription given by the RXTE Guest Observers Facility (GOF) in one of their RXTE recipes. If this enlargement was not sufficient, the good time intervals were shortened even more.

For the spectral analysis, XSPEC version 10.0 (Arnaud 1996; Shafer et al. 1991) was used. This XSPEC version contains patches that are necessary to be able to correctly read the HEXTE PHA files.

The extraction process is described in further detail in the “RXTE cheatsheet” prepared at IAAT (Kreykenbohm & Wilms 1997).

---

## Observations of a Hard State Black Hole: Cyg X-1

The previous chapters laid out the framework of the theoretical and observational study of systems containing ADCs. In the next two chapters these methods will be applied to conduct an observational study of these systems. This chapter is devoted to black holes in the hard state, which is mainly characterized by a hard power-law. Most of this paper focuses on the prime example of a hard-state black hole, Cygnus X-1, although several other black holes will also be mentioned. In the following chapter 6, observations of the soft-state black holes LMC X-1 and LMC X-3 will be described.

This chapter is organized as follows: in section 5.1 the system Cyg X-1 is introduced with a description of the relevant observational parameters, in section 5.2 non-simultaneous data from Cyg X-1 are analyzed using ADC models, in section 5.3 data from a 10 ksec RXTE observation are studied. The result of these observations is that ADC models work satisfactory to explain the X-ray spectrum. Whether the temporal behavior can likewise be explained is the subject of section 5.5. The chapter ends with a summary of the observational results on Cyg X-1 and other black hole systems.

This chapter is based on the following papers, which are not always quoted explicitly:

- Dove, J., Wilms, J., Maisack, M., Begelman, M. C., 1997, *Self-Consistent Thermal Accretion Disk Corona Models for Compact Objects: II. Application to Cygnus X-1*, *Astrophys. J.*, **487**, 759–768
- Dove, J., Wilms, J., Nowak, M. A., Vaughan, B. A., and M. C. Begelman, 1998, *RXTE Observation of Cygnus X-1: I. Spectral Analysis*, *Month. Not. Royal Astron. Soc.*, submitted.
- Wilms, J., Dove, J., Maisack, M., Staubert, R., 1996, *The Broad-Band High-Energy Spectrum of Cyg X-1*, *Astron. Astrophys. Suppl.*, **120**, C159–C162
- Wilms, J., Dove, J., Nowak, M. A., Vaughan, B. A., *RXTE Observation of Cyg X-1: Spectra and Timing*, in: *Proc. 4<sup>th</sup> Compton Symposium*, Williamsburg, VA, (C. D. Dermer, M. S. Strickman, J. D. Kurfess, eds.), AIP Conf. Proc. 410, Woodbury, NY: AIP, 849–853

### 5.1 Cygnus X-1

Cygnus X-1 is one of the most firmly established persistent galactic BHCs. Discovered in a rocket flight in 1964 (Bowyer et al. 1965), the object was one of the first X-ray sources known, although its exact nature was not clear until its optical identification with the O-star HDE 226868 (Hjellming 1973). Since then, Cyg X-1 has been the subject of observations by almost all X-ray missions. In-depth reviews on the system have been published by Oda (1977) and Liang & Nolan (1984). Tab. 5.1 gives an overview on the most important parameters relevant for the interpretation of observations of Cyg X-1, for a more extensive discussion of the system parameters see Wilms (1996).

Table 5.1: Parameters for the system Cyg X-1/HDE 226868. Values in parentheses are uncertainties in units of the last digit. Table prepared in collaboration with Katja Pottschmidt (Pottschmidt 1997).

	Optical Companion HDE 226868	Compact Object Cyg X-1	References
Position:			
J2000.0: $\alpha, \delta$	19 <sup>h</sup> 58 <sup>m</sup> 21 <sup>s</sup> .700, +35°12'05".82		1
galactic: $l_{\text{II}}, b_{\text{II}}$	71:33, +3:07		1
Spectral Type	O9.7 Iab		3
$T_{\text{eff}}$ [K]	32 000		4
$E_{\text{B-V}}$	0.95(7)		8
$N_{\text{H}}$ [cm <sup>-2</sup> ]	6(2) × 10 <sup>21</sup>		8,2
Distance [kpc]	2.5(3)		5
$m_{\text{V}}$ [mag]	8.84		6
$B_{\text{T}}$ [mag]	9.828(22)		6
$V_{\text{T}}$ [mag]	9.020(17)		6
B – V [mag]	+0.81		9
U – B [mag]	–0.28		9
Luminosity [ $L_{\odot}$ ]	10 <sup>5.4</sup>	10 <sup>4</sup>	4,10
Luminosity [erg/s]	10 <sup>39</sup>	4 · 10 <sup>37</sup>	
Inclination		35°	11
$a \sin i$ [km]		5.82(8) × 10 <sup>6</sup>	7
Orbital Period [d]		5.59974(8)	7
Major Axis [ $R_{\odot}$ ]	14.6	26.3	11
$v \sin i$ [km/s]	75.6(10)		7
Mass Function [ $M_{\odot}$ ]		0.252(10)	7
Mass [ $M_{\odot}$ ]	18	10	11
Radius	17 $R_{\odot}$	30 km <sup>†</sup>	4
Separation [ $R_{\odot}$ ]		41	11
Mass loss rate [ $M_{\odot}/\text{a}$ ]		3 × 10 <sup>-6</sup>	4
Wind velocity [km/s]	2100		11

<sup>1</sup>Turon et al. (1992), <sup>2</sup>Bałucińska-Church et al. (1995), <sup>3</sup>Walborn (1973), <sup>4</sup>Herrero et al. (1995),

<sup>5</sup>Ninkov, Walker & Yang (1987b), <sup>6</sup>ESA (1997), Volume 9, <sup>7</sup>Gies & Bolton (1982), <sup>8</sup>Wu et al. (1982),

<sup>9</sup>Lutz & Lutz (1972), <sup>10</sup>Liang & Nolan (1984) <sup>11</sup> see text for further explanation.

<sup>†</sup> Schwarzschild radius



The value of the mass given in Tab. 5.1 is lower than the usually quoted value of  $16 \pm 5 M_{\odot}$  determined by Gies & Bolton (1986). These authors determined the mass by using a relationship between the rotational broadening of the absorption lines of HDE 226868 and the radial velocity, stating that these two values only depend on the mass ratio. By modeling the light curve of HDE 226868 they found  $M = 33 \pm 9 M_{\odot}$  for HDE 226868. Using the value for the mass function given in Tab. 5.1 the black hole mass given above was determined. This fairly high value of the BH mass quickly propagated into the literature and is the mass value that is quoted in most reviews on black holes (e.g., Tanaka & Lewin 1995). It should be noted, however, that the method used by Gies & Bolton (1986) is not a standard method and their mass measurement for HDE 226868 disagrees with those obtained by other independent methods. Masses obtained from the rotational light curve of the system are in the range of  $16 \pm 2 M_{\odot}$  for HDE 226868 and  $8 \pm 3 M_{\odot}$  for the black hole (Balog, Goncharskiĭ & Cherepashchuk 1981; Hutchings 1978), and masses following from a determination of the  $\log g$  value of the O-star atmosphere of HDE 226868 typically result in masses around  $15 M_{\odot}$  (Herrero et al. 1995; Sokolov 1987; Aab et al. 1984, and references therein). Since the work by Herrero et al. (1995) represents the “state of the art” in the theory of hot stellar atmospheres including wind loss, I decided to use their value for the mass of HDE 226868 (and consequently a smaller black hole mass) in this thesis. This mass is still high enough to point without doubt at the presence of a black hole in the system.

A problem intimately connected with the determination of the BH mass is the determination of the inclination. The value of  $35^{\circ}$  given in Tab. 5.1 is given without a statement on its uncertainty. This is due to the fact that the uncertainty of the inclination measurements is very large since the inclination has to be determined from difficult optical polarization measurements<sup>1</sup> and the values found for the inclination thus scatter in the range from about  $26^{\circ}$  to  $67^{\circ}$  (Bochkarĕv et al. 1986; Ninkov, Walker & Yang 1987a,b; Dolan 1992, and references therein) with most people estimating rather lower inclinations. Due to these reasons I decided to use  $i = 35^{\circ}$ , the value adopted by Herrero et al. (1995) in their mass determination.

## 5.2 *The Hard State Spectrum of Cygnus X-1*

Cyg X-1 is usually found in the so-called “hard”, or X-ray low, state, where the X-ray spectrum can be roughly described by a power-law with a photon-index  $\Gamma \sim 1.65$ , modified by an exponential cutoff with an e-folding energy  $E_f \sim 150$  keV (Ebisawa et al. 1996; Gierliński et al. 1997; Sunyaev & Trümper 1979, and references therein). Below about 1 keV, there is evidence for a soft-excess, usually interpreted as thermal radiation from a cold accretion disk having a temperature  $kT_{\text{BB}} \approx 0.1\text{--}0.3$  keV (Bałucińska-Church et al. 1995; Ebisawa et al. 1996). In addition, the spectrum is found to

<sup>1</sup>One can assume that HDE 226868 (almost) fills its Roche lobe, so that the star is not a sphere. The non-sphericity of the O-star results in a partial polarization of the radiation emerging the atmosphere, a measurement of which can be used to infer the size and orientation of the Roche lobe and thus the inclination.

contain a weak iron line feature at  $\approx 6.4$  keV and a slight hardening above 10 keV, often interpreted as being due to Compton reflection (Barr, White & Page 1985; Ebisawa et al. 1996, and references therein).

All of these features in the X-ray spectrum point towards the presence of an ADC in the system. The geometric configuration of the corona and the cold disk, however, is still unclear. In most prior work, the geometry has been assumed to be a cold accretion disk embedded between two hot coronae in a slab configuration (Haardt, Maraschi & Ghisellini 1997; Haardt & Maraschi 1993, and references therein). From the simulations presented in chapter 2, however, there is evidence that such a geometry might not be able explain the observed spectrum. This evidence relies on the result that there exists a maximum temperature for each optical depth, regardless of the compactness parameter or the disk temperature (cf. §2.2.2.3, Fig. 2.13, p. 43). For  $\tau_{\text{es}} \gtrsim 0.2$ , this maximum temperature is 140 keV, colder than the temperature inferred from spectral fitting with Comptonization models. Different evidence, pointing in the same direction, has also been presented by Gierliński et al. (1997). These authors analyzed simultaneous *Ginga*-OSSE data of *Cyg X-1* and found that the strength of the reflection component is too small to be consistent with a slab geometry. Due to these reasons we decided to model the spectrum of *Cyg X-1* using our synthetic ADC spectra.

The direct observational study of the geometry of the ADC in *Cyg X-1* is complicated by the fact that, until recently, no simultaneous X-ray observation of *Cyg X-1* was available. Either the observations concentrated on the low energy spectrum and the soft excess, or the data was taken in the energy range above 100 keV to study the high energy tail of the spectrum. For the purposes of applying our theory to the observations we therefore compiled a broad band spectrum using non-simultaneous data from several experiments. The detailed properties of the data and information on the instruments is given in my diploma thesis (Wilms 1996, see also Wilms et al. 1996). For the low-energy part of the spectrum (below  $\approx 10$  keV) we used archival data from the Broad Band X-Ray Telescope (BBRXT) which have been reported by Marshall et al. (1993). Only the spectrum measured outside the dips is used, and the spectrum is heavily rebinned to take care of the response matrix uncertainties around 2 keV<sup>1</sup>. The energy range from 10 to 200 keV is covered by observations from the Coded Mask Imaging Spectrometer (COMIS-TTM) and the High Energy X-ray Experiment (HEXE) upon the Russian space station Mir. The HEXE data have been previously presented by Döbereiner et al. (1995), while the joint HEXE-TTM data have been analyzed by Borkus et al. (1995). The high-energy part of the spectrum is represented by the average OSSE spectrum presented by Kurfess (1995) and Philips et al. (1996). Except for the BBRXT data, the

<sup>1</sup>These uncertainties were not known to us at the time when the first paper on the composite spectrum was written (Wilms et al. 1996). By accident, the matrix uncertainties are located at the energies of the Sulfur and the Silicon  $K\alpha$  lines. Due to an unfortunate bug in the treatment of reflection in the NLMC code at that time, in which the relative weight of Compton reflection and thermalization were reversed, our models produced very strong S and Si  $K\alpha$  lines and much softer spectra. This led us to the wrong conclusion that the slab geometry *could* explain the observed spectrum. Only after the publication became it clear to us that the uncertainties in the BBRXT response matrix around the absorption edges in the detector material were too optimistic and that the “line features” were bogus features.

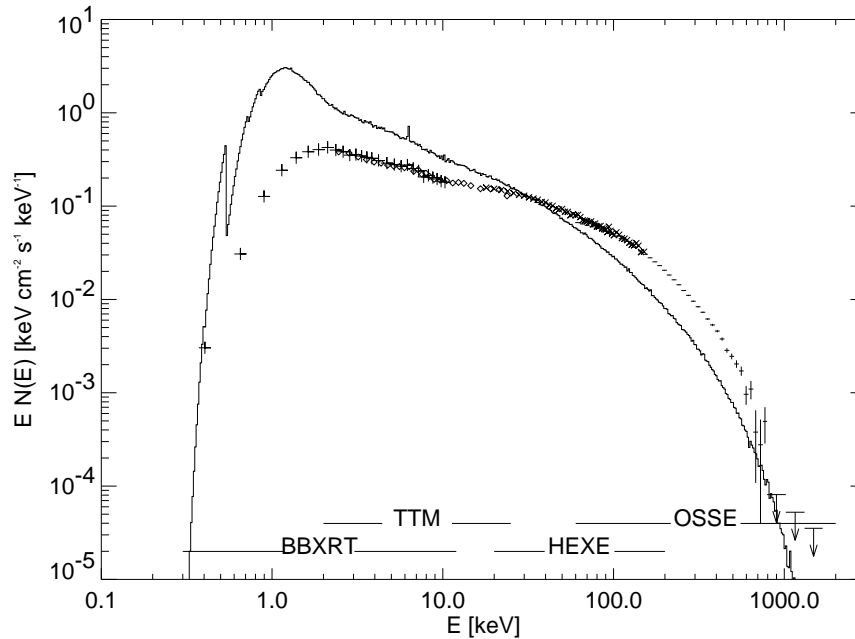


Figure 5.1: Comparison of the unfolded composite spectrum with the slab ADC model (modified by interstellar absorption,  $N_{\text{H}} = 6 \times 10^{21} \text{ cm}^{-2}$ ). The model shown has  $T_{\text{BB}} = 200 \text{ eV}$ ,  $\tau_{\text{es}} = 0.28$ ,  $T_{\text{c}} = 110 \text{ keV}$  and was fitted to the tail of the data (Dove et al. 1997, Fig. 1).

unfolded spectra presented by these authors were used to produce our final composite spectrum. In the case of the BBRXT observation, the unfolded spectrum was produced by myself using an absorbed power-law model. For all instruments the individual spectral models had sufficiently good  $\chi_{\text{red}}^2$  values that the individual unfolded spectra can be regarded as a good representation of the actually observed photon spectrum. Therefore, even though the comparison is done in photon space and not in detector space, the results shown should not be sensitive to the deconvolution procedure.

In Fig. 5.1 the by-eye “best-fit” of the predicted angle averaged spectrum for the slab geometry to the composite spectrum is shown. The model spectrum shown is the hardest spectrum possible in slab geometry that still has a cutoff energy larger than 100 keV. Although such a spectrum might be able to fit the hard tail, it is apparent from the figure that the spectrum is much softer than the observed spectrum. Out of the entire grid of models computed, the hardest spectrum predicted has a photon-index of  $\Gamma = 1.8$ , while the spectral index of Cyg X-1 is  $\Gamma \sim 1.6 \dots 1.7$ . Simulations with the linear code indicate that *only* models with  $\tau \gtrsim 0.3$  might be able to explain the spectrum. This is consistent with the results of Haardt et al. (1993) and Titarchuk (1994) who found these values in their application of the slab-geometry to Cyg X-1. *Such models, however, are not self-consistent.* Even if additional cooling mechanisms such as bremsstrahlung were included in the code, the resulting temperatures would only be smaller than the temperatures found by just including Compton cooling. Thus the  $T$ - $\tau$ -relation shown in Fig. 2.13 represents indeed the *maximum* possible temperature so that harder spectra

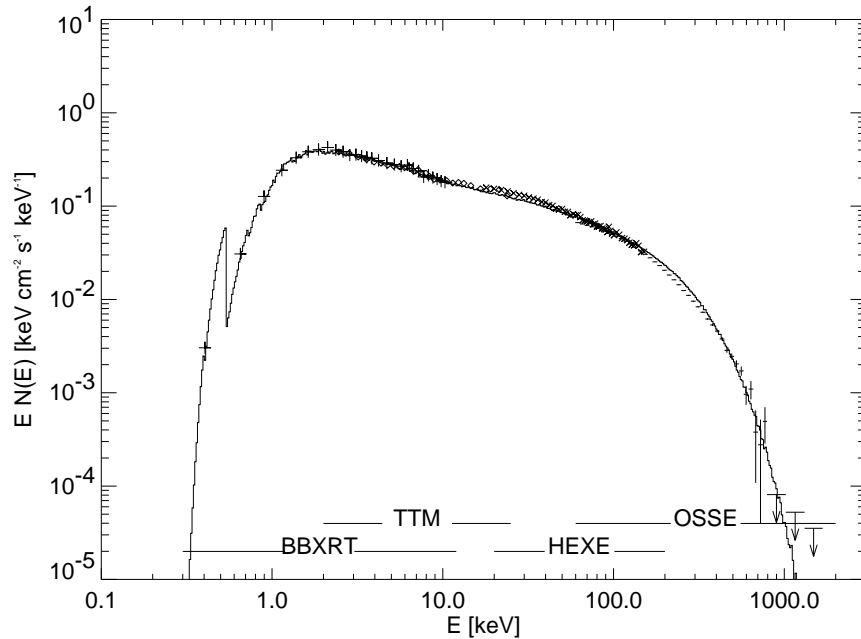


Figure 5.2: Comparison between the “best-fit” model for the sphere+disk geometry grids with  $T_{\text{BB}} = 50 \text{ eV}$  and absorbed by  $N_{\text{H}} = 6 \times 10^{21} \text{ cm}^{-2}$  to the composite spectrum. The agreement between the data and the model is very good. For this model,  $\tau_{\text{es}} = 1.5$ ,  $T_{\text{c}} = 90 \text{ keV}$  (Dove et al. 1997, Fig. 8).

are not possible using this setup.

Apart from predicting the wrong power-law index, the slab geometry also suffers from other problems. The strength of the iron line in the model spectra is larger than the observed spectrum in all simulated models having hard spectra. For example, the model of Fig. 5.1 predicts an EW of about 120 eV, while the observed value is rather below 50 eV (Ebisawa et al. 1996), and in all models the soft excess is far too strong. Since all slab models with hard spectra have to have fairly low coronal optical depths, most of the thermal emission from the disk can escape the system without modification. Although part of the soft excess can be “hidden” from the observer by absorption in the ISM ( $N_{\text{H}} = 6 \times 10^{21} \text{ cm}^{-2}$ , cf. Tab. 5.1), the column is not sufficient to hide the soft excess for a disk with  $kT_{\text{BB}} \sim 200 \text{ eV}$ . Note that the BBRXT observation used for the preparation of Fig. 5.1 was unique because a soft excess was not observed (Marshall et al. 1993). However, even when using data containing a soft excess (Bałucińska & Hasinger 1991; Bałucińska-Church et al. 1995; Ebisawa et al. 1996), the modeled soft-excess is still much stronger than the measured one. Therefore, it can be concluded that *self-consistent accretion disk corona models with slab geometry are not capable of reproducing the observed broad band X-ray spectrum of Cyg X-1.*

Most of these problems are due to the cold disk of the slab ADC model having a covering fraction of unity (i.e., all downward directed coronal radiation is reprocessed in the cold disk). ADCs having a geometry with a smaller covering fraction have weaker repro-

cessing features, are less efficiently Compton cooled, and thereby allow higher coronal temperatures for a given optical depth. An example for this is the hot coronal sphere that is surrounded by an exterior cold, optically thick and geometrically thin, accretion disk studied in section 2.2.3. Using the grid of models described in section 2.2.3 it is indeed possible to obtain a very satisfactory description of the composite spectrum. Fig 5.2 shows the best fit obtained with the sphere+disk models with a uniform temperature of  $T_{\text{BB}} = 50$  eV. The agreement between the data and the model is very good. Although the soft-excess in the models is even larger than in the slab geometry models, the lower disk temperatures predicted for centrally illuminated accretion disks helps in hiding this soft excess from the observer. In fact, the soft excess predicted by the model appears to be consistent with the observations. The quality of the data available to us, however, is insufficient to make a final statement on the soft-excess.

Because of the smaller covering fraction of the accretion disk, the models predict weaker reprocessing features in the radiation field as compared to the slab models. In principle this could be used to constrain the outer radius of the accretion disk by looking at the EW of the iron fluorescence line, which is proportional to the solid angle of the disk. The best-fit model of Fig. 5.2, where  $R_d/R_c = 10$ , has an EW of about 60 eV, consistent with the EW  $\lesssim 70$  eV found in the spectrum (Ebisawa et al. 1996; Gierliński et al. 1997). Models with smaller  $R_d/R_c$  would predict much smaller equivalent widths, so that our result is consistent with the presence of a comparably large accretion disk outside the corona. Although this is not an exciting result *per se*, it is at least nice to see that what everybody believes is true and that the outer radius of the disk in BHs is larger than a few Schwarzschild radii.

There are two caveats associated with the good “fit” found for the sphere+disk geometry. First, the unfolded spectrum used in the “fit” is not unique and there might be other spectra that reproduce the data measured in the detector. We have addressed this question by simulating observations for ROSAT, HEXE, and the RXTE PCA using the above best-fit sphere+disk model. The simulated observations were then fit with the empirical spectral models used by previous workers in the field to see whether our physical model agrees with their spectral fits. The result of these comparisons was that the model reproduces the measured spectral parameters for these satellites (see the appendix of Dove et al. 1997 for a detailed discussion of how this comparison was done).

The second caveat is caused by the rather low soft-excess temperature predicted from the sphere+disk models, which might result in an observability of the soft excess in the ultraviolet. We have therefore compared the flux predicted by our model in the 1200 to 1950 Å band with the flux observed in this band by the International Ultraviolet Explorer (IUE). The predicted flux is 2–3 orders of magnitude smaller than the flux in a typical IUE low-dispersion spectrum of HDE 226868 made 1980 June 25 (specifically, the spectrum SWP09421 was used in which the measured background subtracted flux is about  $2 \times 10^{-13}$  erg cm<sup>-2</sup> s<sup>-1</sup> Å<sup>-1</sup>). This is consistent with earlier results that the ultraviolet spectrum of the system is dominated by emission from the O star (Treves et al. 1980; Pravdo et al. 1980). Therefore, IUE observations cannot be used to constrain the disk temperature of the models.

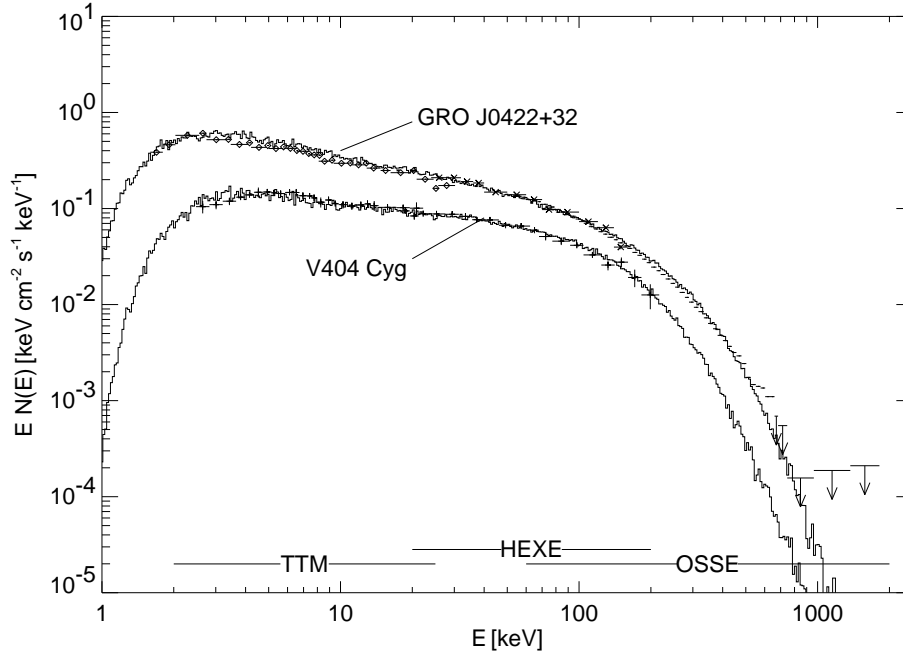


Figure 5.3: Comparison between the best-fit sphere+disk models and data for composite spectra of GRO J0422+32 (Döbereiner et al. 1994; Kroeger et al. 1996) and V404 Cyg (in't Zand et al. 1992; Döbereiner et al. 1994, 1989 June 20 spectrum). The spectra have been scaled arbitrarily. For V404 Cyg, the best fit parameters are  $kT = 52$  keV,  $\tau_{\text{es}} = 3.4$ , and  $N_{\text{H}} = 2.4 \times 10^{22} \text{ cm}^{-2}$ , while for GRO J0422+32 the parameters are  $kT = 75$  keV,  $\tau_{\text{es}} = 1.9$ , and  $N_{\text{H}} = 1.6 \times 10^{22} \text{ cm}^{-2}$  (Dove et al. 1997, Fig. 10).

The results obtained for Cyg X-1 are also applicable to other hard-state BHCs. Although the spectrum of SXTs is typically dominated by a soft component, occasionally they have spectra that are similar to the hard-state of the non-transient BHs. In Fig. 5.3 the spectra of two of these SXTs, V404 Cyg (GS 2023+338) and GRO J0422+32, are compared to spectra resulting from the sphere+disk geometry. Therefore it appears that photon-starved ADC models, such as the sphere+disk model, are applicable to explaining the observed X-ray spectra of many BHs. In the case of the transient sources, this result might shed light on the physical circumstances triggering the outburst.

### 5.3 RXTE Observation of Cygnus X-1

Thus, as was shown in the previous section, there is plenty of observational evidence that the slab corona model is unable to explain the observed spectrum. This statement, however, has been criticized by several people since the observations on which the composite spectrum of Figs. 5.1 and 5.2 is based were not taken simultaneously. Although the smooth transition between individual observations taken by different instruments invalidates this argument (at least in my opinion), simultaneous broad-band spectral observations are necessary to further constrain the coronal parameters. In this section I

present the results from the spectral analysis of 10 ksec of RXTE data on Cyg X-1, taken on 1996 October 26 and 27. Section 5.3.1 describes how the observations were performed, in section 5.3.2 the results from spectral modeling of the Cyg X-1 spectrum using “standard” simplified models and self-consistent ADC models are given, and in section 5.4 the results of these fits are discussed.

### 5.3.1 Observations and Data Analysis

RXTE observed Cyg X-1 for a total of 22.5 ksec on 1996 October 23 and 24. The data were extracted and screened as described in section 4.4. Due to problems in the RXTE SOF concerning the data repackaging, only the first 10 ksec of the standard-mode PCA data were available to us (the rest of the data got only delivered in 1997 November – too late for an inclusion of the results in this thesis). This duration is sufficient for the spectral analysis, as the PCA count-rate is high ( $\approx 4300$  cps, compared to a background count-rate of  $\approx 150$  cps). The comparison between the background obtained from Earth occultation and the background derived from `pcabackest` indicates that the `pcabackest` derived background using the VLE model is suitable for the spectral analysis of this observation (see §4.1.3, especially Fig. 4.6 on p. 94). Due to the PCA calibration uncertainties, PHA channels above 30 keV and below 3 keV were ignored, and a 2% channel independent systematic error was assumed in the data analysis. The HEXTE data was extracted using  $\beta$ -test versions of the HEXTE data extraction and dead time correction software. Changes made in the software after the extraction of the HEXTE spectra does not influence the results presented here. Due to the calibration uncertainty of HEXTE, only data for PHA channels above 20 keV was used. The rapidly decreasing signal to noise ratio forced us to rebin the spectrum by a factor of 3 for channels between 50 and 100 keV, and by a factor of 10 for higher channels.

### 5.3.2 Spectral Analysis

#### 5.3.2.1 Standard Models

To facilitate the comparison of this observation with previous observations, spectral fitting was performed using the following models, which had been used in the past to describe the spectrum of Cyg X-1: a power-law, a power-law with an exponential cutoff, a power-law with an exponential cutoff plus a cold reflection component, and thermal Comptonization models. In addition, a Gaussian line with energy and width fixed to 6.4 keV and 0.1 keV, respectively, was added to several of these models. The low-energy absorption was fixed to an equivalent cold Hydrogen column of  $N_{\text{H}} = 6 \times 10^{21} \text{ cm}^{-2}$ , the value suggested by the soft X-ray spectrum and interstellar reddening measurements of HDE 226868 (Bałucińska & Hasinger 1991; Wu et al. 1982, see also Tab. 5.1). The results of the spectral fits are given in table 5.2<sup>1</sup>.

<sup>1</sup>To account for the known discrepancies in the relative normalization of PCA and HEXTE (see §4.2.3, p. 98), a multiplicative constant was introduced in the spectral models that represents the relative normalization between the data-sets. The relative normalization between HEXTE and PCA was always found to be  $0.74 \pm 0.01$  and is therefore not listed in table 5.2.

Table 5.2: Results of spectral fitting to the Cyg X-1 RXTE data.

Model	$\Gamma$	$A_{\text{pl}}$	$E_f$ [keV]	$kT_{\text{BB}}$ [keV]	$A_{\text{BB}}$ $10^{-2}$	$f$ $10^{-2}$	$kT_c$ keV	$\tau_{\text{T}}$	$A_c$	$A_L$ $10^{-3}$	$\chi^2/\text{dof}$
pl	1.70	1.78	...	...	...	...	...	...	...	...	2315/171
plxp	1.63 $^{+0.01}_{-0.01}$	1.48 $^{+0.03}_{-0.04}$	364 $^{+28}_{-25}$	...	...	...	...	...	...	...	806/169
plxp+bb	1.45 $^{+0.01}_{-0.02}$	0.91 $^{+0.03}_{-0.04}$	162 $^{+9}_{-8}$	1.2 $^{+0.0}_{-0.1}$	2.2 $^{+0.1}_{-0.2}$	...	...	...	...	...	173/167
plxp+bb+g	1.45 $^{+0.02}_{-0.01}$	0.91 $^{+0.04}_{-0.01}$	164 $^{+9}_{-8}$	1.1 $^{+0.1}_{-0.0}$	2.1 $^{+0.2}_{-0.1}$	...	...	...	...	3.3 $^{+2.5}_{-2.6}$	170/166
pexrav	1.71 $^{+0.02}_{-0.02}$	1.67 $^{+0.05}_{-0.06}$	924 $^{+400}_{-250}$	...	...	20 $^{+5}_{-5}$	...	...	...	...	752/168
pexrav+bb	1.45 $^{+0.02}_{-0.01}$	0.92 $^{+0.06}_{-0.05}$	164 $^{+10}_{-10}$	1.2 $^{+0.1}_{-0.1}$	2.2 $^{+0.1}_{-0.2}$	0.01 $^{+0.00}_{-0.01}$	...	...	...	...	173/166
pexrav+bb+g	1.44 $^{+0.02}_{-0.01}$	0.89 $^{+0.04}_{-0.03}$	161 $^{+9}_{-8}$	1.2 $^{+0.1}_{-0.1}$	1.9 $^{+0.1}_{-0.2}$	0.00 $^{+0.00}_{-0.00}$	...	...	...	3.9 $^{+2.5}_{-2.6}$	156/165
comptt+bb	...	...	...	1.1 $^{+0.1}_{-0.1}$	1.4 $^{+0.1}_{-0.1}$	...	40 $^{+1}_{-2}$	3.6 $^{+0.1}_{-0.1}$	0.47 $^{+0.01}_{-0.02}$	...	244/167
comptt+bb+g	...	...	...	1.0 $^{+0.1}_{-0.1}$	1.3 $^{+0.2}_{-0.1}$	...	40 $^{+1}_{-2}$	3.6 $^{+0.1}_{-0.1}$	0.47 $^{+0.02}_{-0.01}$	5.9 $^{+2.7}_{-2.6}$	232/166
s+d	...	...	...	...	...	...	65.7 $^{+3.3}_{-3.3}$	2.1 $^{+0.1}_{-0.1}$	6.48 $^{+0.06}_{-0.05}$	...	152/155

$N_{\text{H}}$  was fixed at  $6 \times 10^{21} \text{ cm}^{-2}$ . Uncertainties given are at the 90% level for one interesting parameter ( $\Delta\chi^2 = 2.7$ ). pl: power-law with photon-index  $\Gamma$  and normalization  $A_{\text{pl}}$  (photon-flux at 1 keV); plxp: power-law with exponential cutoff [ $A_{\text{pl}} E^{-\Gamma} \exp(-E/E_f)$ ]; bb: black body with temperature  $kT_{\text{BB}}$ ; the normalization  $A_{\text{BB}}$  is defined in units of  $L_{39}/R_{10}^2$  where  $L_{39}$  is the luminosity in units of  $10^{39} \text{ erg/s}$  and  $R_{10}$  is the distance in units of 10 kpc; pexrav: power-law with exponential cutoff reflected off cold matter (using Green's functions of Magdziarz & Zdziarski 1995),  $f$  is the ratio between the incident and the reflected flux; comptt: Comptonization spectrum after Hta & Titarchuk (1995) and Titarchuk (1994), with a coronal temperature of  $kT_c$  and the total optical depth  $\tau_{\text{T}}$ , seed-photon temperature is 10 eV; g: Gaussian line, with energy and width fixed to 6.4 keV, 0.1 keV, respectively;  $A_L$  is the amplitude of the line in total number of photons/cm $^2$ /s in the line.  $A_L = 3.3 \times 10^{-3}$  corresponds to an equivalent width of  $\approx 45 \text{ eV}$ . s+d: ADC model with sphere+disk geometry, total optical depth of the corona is  $\tau_{\text{T}}$ , the coronal temperature is  $kT_c$ , the temperature profile of the cold disk is  $kT_{\text{BB}}(R) = 150 (R/R_c)^{-3/4} \text{ eV}$ .



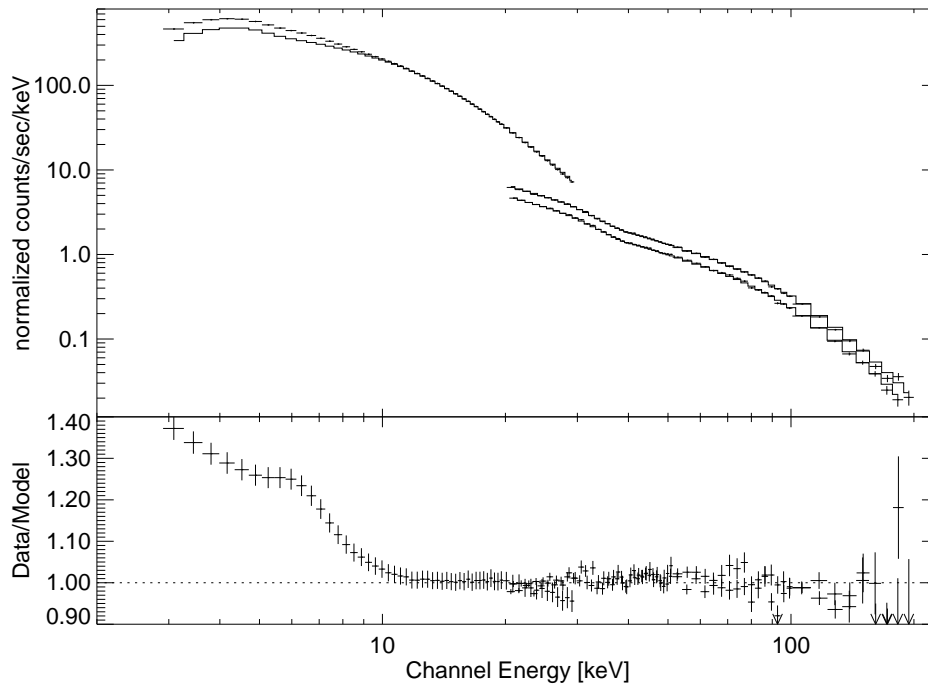


Figure 5.4: Fit of a power-law with an exponential cutoff to the Cyg X-1 data, including only data measured above 10 keV in the fit to illustrate the importance of the soft excess. The top part of the figure displays the data and the model (lines), while the bottom display indicates the ratio between data and model. Uncertainties shown are  $1\sigma$ .

For energies  $E \gtrsim 10$  keV, a power-law with an exponential cutoff provides a good description of the data (Fig. 5.4). The value for the  $e$ -folding energy,  $E_f$ , is well constrained due to the quality of the HEXTE data. The analysis of the residuals of this fit indicates the presence of a soft excess at energies  $\lesssim 8$  keV. Adding a black-body component with a temperature  $kT_{\text{BB}} \approx 1$  keV and a Gaussian at 6.4 keV with an equivalent width of 46.4 eV, to this model improves the quality of the fit, resulting in a good description of the data over the whole energy range ( $\chi^2_{\text{red}} = 169/166$ ; Fig. 5.5). The PCA residuals between 20 and 30 keV seen in Fig. 5.5 are consistent with those seen for power-law fits to the Crab shown in the last chapter (Fig. 4.5, p. 92).

It is important to note that a literal interpretation of the black-body component as being due to disk emission is difficult. The black body component is simply added phenomenologically to measure the magnitude of the data's deviation from a power-law. Other components like a soft excess resulting from a temperature distribution in an accretion disk ("disk black body", see section 6.3 for a description of this model), or a bremsstrahlung model result in an equally good description of the data. Due to the unavailability of simultaneous low-energy data covering the energy range from 0.1 to 3 keV, a decision of which soft excess model describes the observed deviation best is impossible. This inability to distinguish between different physical causes for the soft excess, however, does not influence the results presented below concerning the ADC geometry, and should only be considered a slight nuisance.

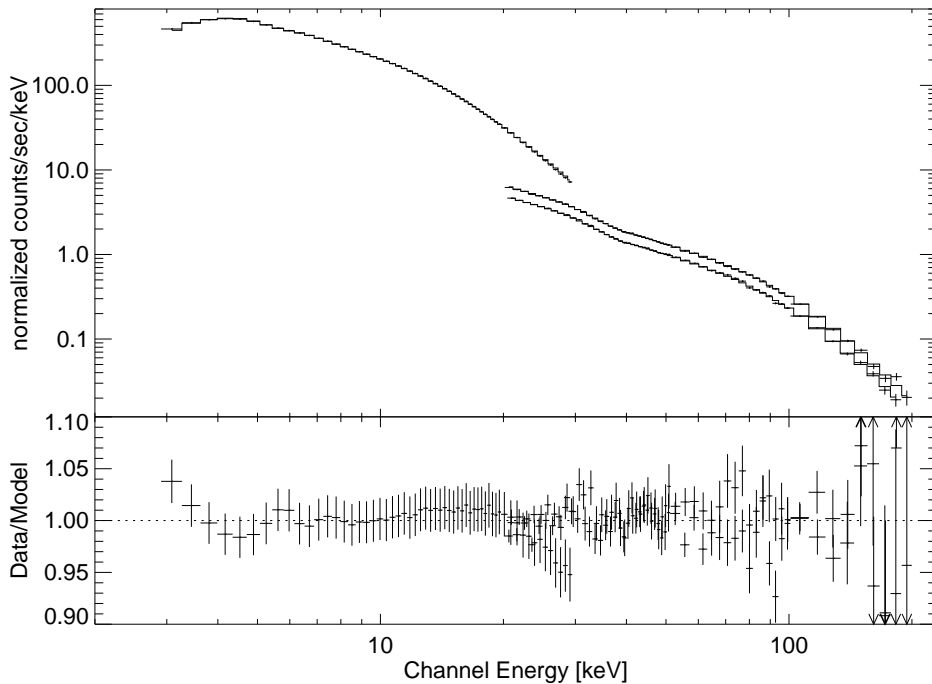


Figure 5.5: Fit to the whole spectrum from 3 keV to 200 keV using a model with a blackbody of  $kT_{\text{BB}} = 1.1$  keV, a Gaussian at 6.4 keV with an equivalent width of 46.4 eV, and a power-law with a photon-index of  $\Gamma = 1.45$  a high-energy cutoff with a folding energy of  $E_f = 163$  keV. The fit is very satisfactory, with the remaining residuals present being consistent with the detector uncertainty (cf. Figs. 4.5 and 4.11).

The addition of a reflection component to the best fit  $\text{plexp}+\text{bb}+\text{g}$  model *does not* improve the quality of the fit. The best-fit value for the fraction of incident radiation that is Compton reflected by cold matter is  $f \lesssim 0.02$ . Even though we only considered PCA data in the 3...30 keV range, the power-law index of the continuum is well constrained by the HEXTE data, and there is no evidence that the spectral slope of the data for the two instruments disagree within the energy range of the overlap (the turn over in the PCA ratio above 20 keV is due to the calibration uncertainty at the Xe K edge).

There is a strong deviation between these measured parameters and spectral parameters found in the earlier literature. The power-law is harder and the reflection component is definitely much weaker than in previous observations. The most probable explanation for this behavior is that these new parameters are due to the description of the entire 3–200 keV spectral band with a single model. Previous broad-band observations were to a large extent made using *Ginga* and OSSE data and therefore had relatively poor spectral coverage in the energy range  $\sim 30$ –100 keV (the composite spectrum presented earlier in this chapter does not suffer from these problems and consequently is entirely consistent with the findings from the RXTE data). To check to what extent the best-fit is influenced by the remaining RXTE calibration uncertainties (which are smaller than those for the *Ginga* LAC, see p. 93), we restricted the RXTE data to 3–30 keV and 100–200 keV, that is to an energy band that roughly covers the energy range

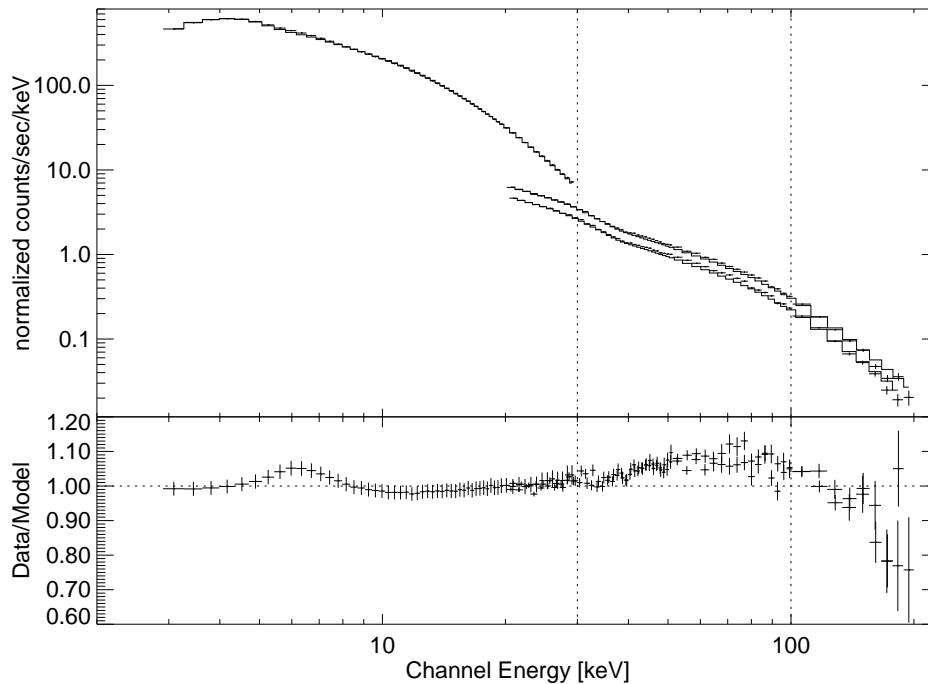


Figure 5.6: Fit to the data using the reflection model of Magdziarz & Zdziarski (1995). To simulate previous observations, only the data below 30 keV and above 100 keV were used. Adding these data back in shows that the spectrum exhibits an excess over the otherwise satisfactory model.

of the *Ginga* and OSSE observations. If this is done, the resulting best-fit parameters are similar to those previously found for Cyg X-1, although, due to the higher signal to noise ratio in our measurement, deviations are still present. Specifically, for this restricted data range, a reflected power-law with  $\Gamma = 1.81 \pm 0.01$  and covering fraction  $f = 0.35 \pm 0.02$  yields  $\chi^2/\text{dof} = 157/90 = 1.75$  (Fig. 5.6). Adding back the HEXTE data in the 30–100 keV range, significantly reduces the quality of the fit ( $\chi^2/77 = 8.7$ ). Being able to fit a reflected power-law with a large disk covering fraction is thus seen to be partly a consequence of ignoring the data in the  $\sim 30$ –100 keV range.

It is this 30–100 keV energy range that is crucial for constraining a power-law index since these energies are uncontaminated by reprocessing or reflection features. We therefore postulate that the observed 10–30 keV “hardening” feature typically found in observations with a smaller energy range appears to be the beginning of a hard power-law that continues to  $\sim 100$  keV, and that the  $\sim 1$ –10 keV portion of the spectrum has a softer power-law due to contamination from the thermal excess. This contamination could be due to Comptonization of the thermal radiation emitted by the cold disk with an effective blackbody temperature  $kT_{\text{BB}} \sim 150$  eV, since, for energies less than about  $10kT_{\text{BB}}$ , the Comptonized spectrum is not expected to be a pure power-law.

Note that this result does not indicate that there are no reflection features in the observed spectrum of Cyg X-1. As shown below, the ADC model with a sphere+disk geometry is able to describe the observation, and this model does include reflection. The reflection feature predicted from the sphere+disk geometry, however, differs from

the reflection features predicted by the phenomenological reflection models, in which a pure power law with exponential cutoff is assumed as the spectrum incident onto the slab-accretion disk. In the sphere+disk geometry, the incident spectrum is the spectrum emerging from the spherical corona, which is different from a pure power-law. This is especially important in the energy region around 10 keV, where the soft thermal radiation is only slightly Comptonized so that the spectrum is not a pure power-law.

Although the residuals of the power-law fits clearly indicate the presence of an Fe  $K\alpha$  line, the  $\sim 2\%$  uncertainty in the PCA response matrix at 6 keV make a determination of the line equivalent width problematic. One possible way out of this problem is to try to perform a spectral analysis which is independent of these uncertainties. For this, the measured PHA spectrum is divided by the spectrum of a source which is known to be featureless, for example the Crab spectrum. If the spectrum of Cyg X-1 were featureless and if the detector were ideal, then the ratio between the spectrum of the Crab and the spectrum of Cyg X-1 would be

$$\frac{\text{Cyg X-1}}{\text{Crab}} = \frac{A_1 E^{-\Gamma}}{A_2 E^{-2.08}} \propto E^{2.08-\Gamma} \quad (5.1)$$

so that a plot of this ratio divided by  $E^{2.08-\Gamma}$  would result in a straight line if the spectrum of Cyg X-1 were a pure featureless power-law continuum. If this assumption were wrong and the spectrum contained features, they would be seen as deviations from the straight line. Fig. 5.7 shows the result of the division of the Cyg X-1 data by the Crab spectrum described in section 4.1.2 on p. 91f. If a power-law spectrum with  $\Gamma = 1.42$  is assumed for Cyg X-1, i.e., a power-law with an index that is approximately equal to the best fit values given in Tab. 5.2, then the corrected ratio above 10 keV is indeed flat, indicating that the spectrum is a pure power-law in this region. Below 10 keV, the soft excess is clearly visible, as is the iron line feature at 6.4 keV. Unfortunately, problems with the channels above 30 keV, which start to contain an appreciable fraction of background photons, prevent the use of this method to look for the characteristic curvature of the spectrum caused by reflection. Furthermore, due to different detector gains in the two observations, it is also not possible to use the divided spectrum to estimate the equivalent width of the line<sup>1</sup>. Therefore, due to our inability to decide on the exact strength and shape of the line we included a Gaussian line in most of our fits presented in table 5.2, fixing the line energy at 6.4 keV and fixing the line width at 100 eV, i.e., at the typical values found in the ASCA observations of Ebisawa et al. (1996). Using these values and just fitting the normalization of the line results in  $EW \approx 60 \pm 35$  eV. Fits where the line width was not fixed always resulted in unphysical line widths of around 600 eV due to the remaining calibration uncertainties and due to the only moderate energy resolution of the detector. Although undoubtedly influenced by the uncertainties in the RMF, the best-fit EW with a fixed width does indicate the contribution from an intrinsic line to the spectrum and is probably in agreement with the results based on four

<sup>1</sup>Our general experience with the ‘‘Crab division method’’ indicates that it is very difficult to make specific statements about spectral parameters obtained this way so that the method should only be used to verify information gained by other means (Kreykenbohm et al. 1998).

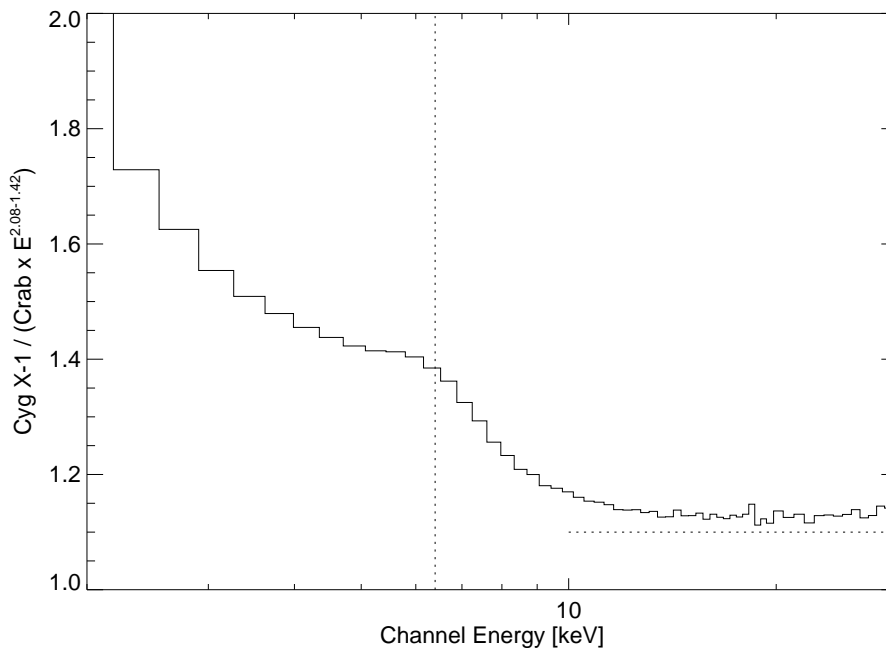


Figure 5.7: Division of the measured Cyg X-1 data by the spectrum of the Crab pulsar, divided by  $E^{2.08-1.42}$ . The flattening in the ratio above  $\sim 10$  keV (dotted horizontal line) shows that the spectrum can be well described by a power-law in this regime, while at lower energies the soft excess and the iron line are visible (the dotted horizontal line is at 6.4 keV).

days of ASCA observations presented by Ebisawa et al. (1996), who found a comparably weak Fe line with  $EW \lesssim 30$  eV.

Thermal Comptonization is a more physical model for the observed energy spectrum of Cyg X-1 than a power-law. Applying the model of Titarchuk (1994) to the data it is found that a thermal Comptonization spectrum, resulting from a spherical geometry with  $\tau \approx 3.6$  and  $kT_c \approx 40$  keV, with an additional soft component, can give an acceptable description of the data, although the model underestimates the flux at energies  $\gtrsim 150$  keV (Fig. 5.8). The semi-relativistic, optically thin model of Titarchuk (1994), for either a slab geometry or a spherical geometry, was unable to explain the data.

Although the traditional models can be reasonably successful in describing the observed broad band spectrum of Cyg X-1, they do not yield a physical interpretation of the emitting mechanisms responsible for the production of the high-energy radiation. There is not necessarily a one-to-one correspondence between a phenomenological model component and a physical interpretation. This can only be obtained by more physical coronal models like the sphere+disk ADC models.

### 5.3.3 Accretion Disk Corona models

The spectra obtained for the ADC models described in chapter 2 have been implemented into the data reduction software XSPEC (version 10.0, Arnaud 1996) for use in spectral fitting. The radial temperature structure of the accretion disk was assumed

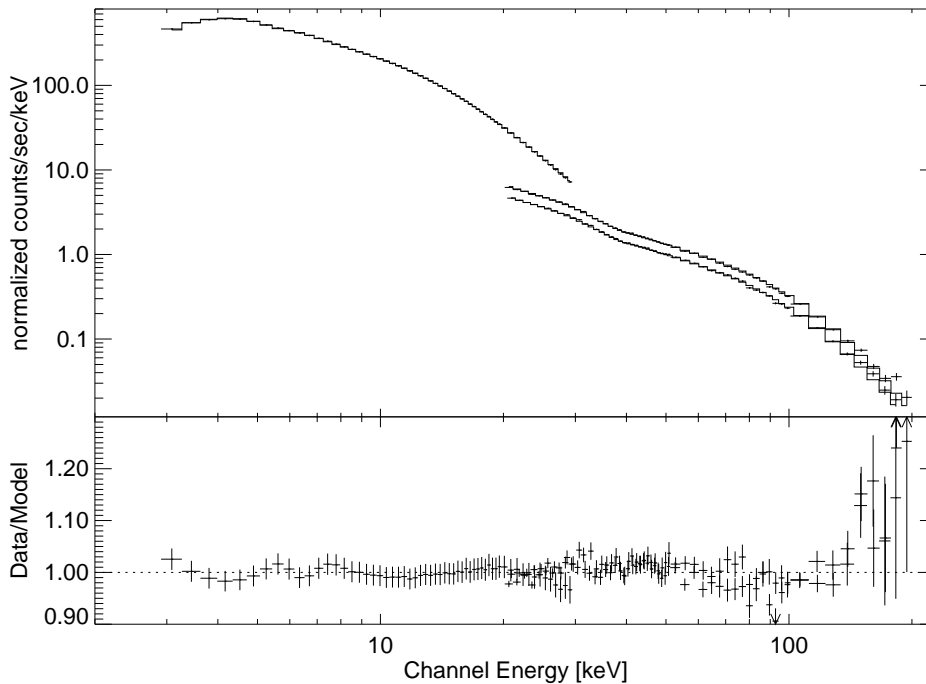


Figure 5.8: Fit to the spectrum using the analytical Comptonization theory of Titarchuk (1994) for the high energy spectrum, and including a Gaussian and a black body in the low energy spectrum. Note the deviations above about 100 keV.

to be  $T_{\text{BB}} \propto (R/R_c)^{-3/4}$ , where  $R$  is the disk radius and  $R_c$  is the radius of the coronal sphere (see p. 57). The implicit flux of the disk (i.e., the radiation emitted due to viscous energy dissipation and not due to reprocessing of coronal radiation) is given by  $F(R) = \sigma_{\text{SB}} T^4(R)$ , and the spectral shape is determined by the local disk temperature (so that the disk spectrum seen at infinity is a superposition of thermal Planckian distributions analogous to eq. 2.46, p. 56). A description of the interpolation algorithm used is given in appendix B.

Slab-corona models do not result in good fits, as the predicted spectra are always much softer than the observed spectrum ( $\chi_{\text{red}}^2 \sim 80$ ). This result is consistent with the findings from non-simultaneous data presented in section 5.2.

The sphere+disk ADC model does provide a good description to the data (cf. Tab. 5.2 and Fig. 5.9)<sup>1</sup>. The formal  $\chi^2$ -value of the best-fit model ( $\chi_{\text{red}}^2 = 1.55$ ) is larger than the values found for some of the phenomenological models discussed in section 5.3.2.1. Considering that the model has only three parameters (seed optical depth, coronal compactness, overall normalization, plus the “hidden” parameter  $T_{\text{BB}}$ , which is fixed at 150 eV during the fitting procedure), and considering that the model is *physically self-consistent*, the level of agreement with the data is quite good. The major disagreement between the model and the data occurs in the  $\sim 5 \dots 10$  keV range, where the residuals

<sup>1</sup>Note that, even though the free parameters of each grid of models are the coronal seed opacity and the coronal compactness parameter, for convenience the corresponding average coronal temperature and total optical depth are listed in Tab. 5.2.

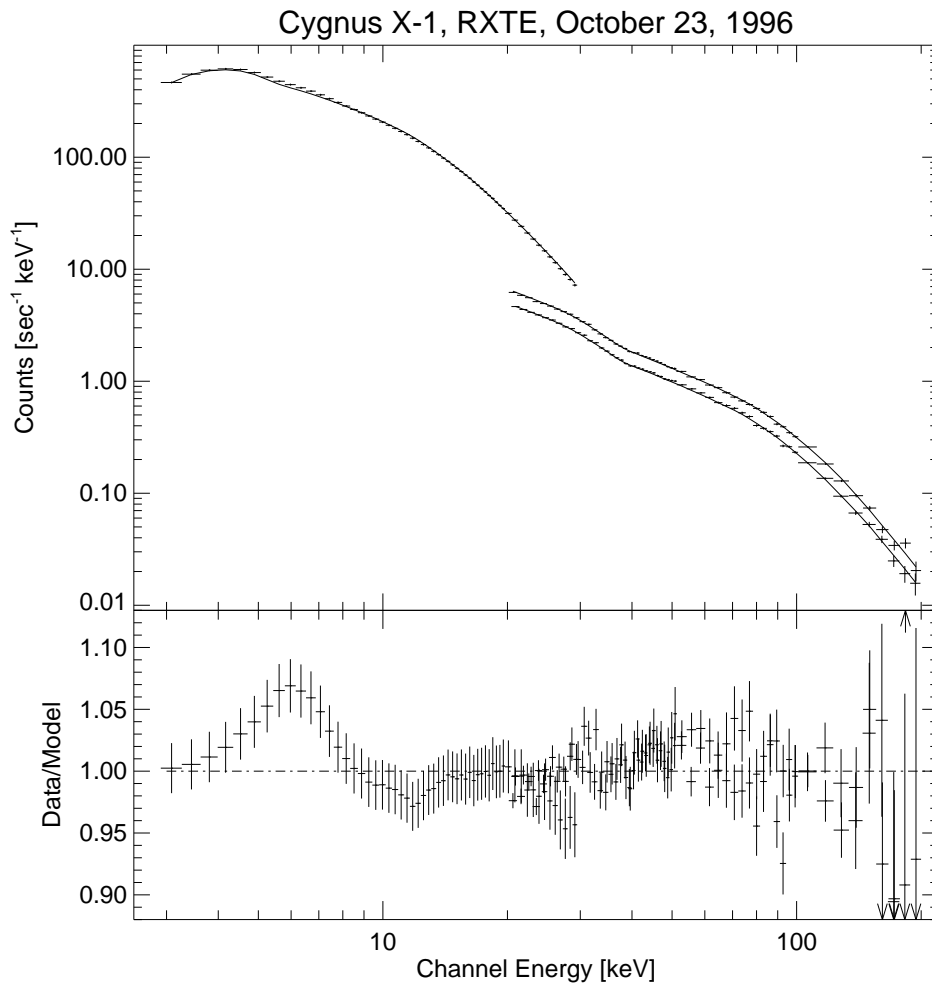


Figure 5.9: Fit of the sphere+disk model to the data, indicating good overall agreement between the accretion disk corona model and the observations. See text for further explanation, especially on the deviations in the iron band.

are as large as 7%. In section 5.4 several ways in which slight modifications to the model might result in improved fits to the data are discussed.

Contrary to the results of Gierliński et al. (1997), we were able to fit the high-energy tail with a *single* Comptonizing component. This result might be due to the  $\sim 15\%$  variation of the coronal temperature in the models, which is due to the non-uniform radiation field within the corona and gives rise to a non-uniform Compton cooling rate. We also tried sphere+disk models in which the inner temperature of the disk is 300 eV or 800 eV, the latter temperature roughly being consistent with the best-fit black-body temperature found in the previous section. However, since sphere+disk models calculate the flux emitted by the disk self-consistently, both of these models predict much more of a soft-excess than observed. This result reinforces the conclusion that the 1 keV black-body component that was added to the exponentially truncated power-law model

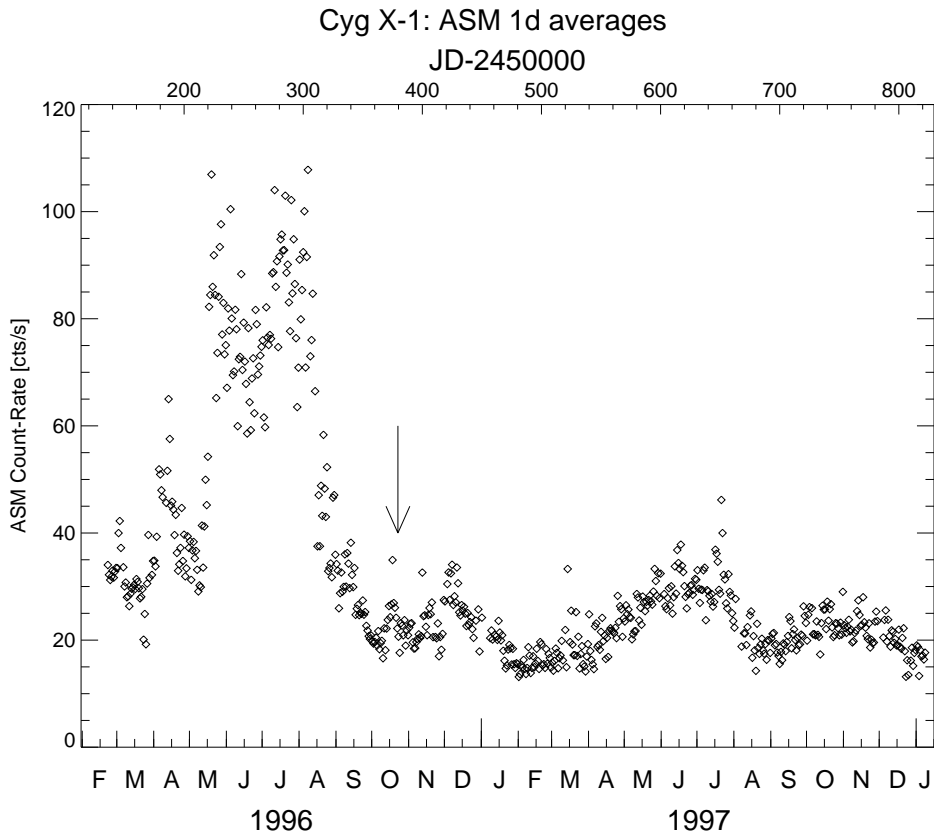


Figure 5.10: The RXTE-ASM count-rates for Cyg X-1 from the beginning of the ASM measurements until 1997 December. The time of the observation analyzed here is indicated with the arrow. Note the soft state (characterized by the high ASM count rates) shortly before the observation.

should not be interpreted literally as disk emission.

#### 5.4 Discussion and Conclusions

We have applied a variety of spectral models to an RXTE observation of Cyg X-1. We find that the observed spectrum in the 3.0–200 keV range is well described by a power-law with a photon index  $\Gamma = 1.45^{+0.01}_{-0.02}$  modified by an exponential tail with an  $e$ -folding energy  $E_f \approx 160$  keV, and a soft excess that was modeled as a black-body (although other broad distribution models are capable of explaining the soft-excess) having a temperature  $kT_{\text{BB}} \approx 1.2$  keV. The measured value of  $\Gamma$  is lower than those found in previous broad-band analyses, which find a  $\Gamma \sim 1.65$  (Gierliński et al. 1997; Döbereiner et al. 1994). In addition, the observed strength of the Compton reflection feature is weak, as the best-fit covering fraction, determined by fitting the data with a power-law reflection model (Magdziarz & Zdziarski 1995), is found to be  $\approx 0.2$  when no soft excess component is included, and is found to be  $\lesssim 0.02$  when one is included. The latter value is considerably lower than the  $f \approx 0.3$  found by Gierliński et al. (1997).

Two weeks prior to our observation, Cyg X-1 transited from a soft (“high”) state to



a hard (“low”) state (Fig. 5.10). For a description of the properties the Cyg X-1 soft state, see Cui et al. (1997b). The proximity of our observation to this transition might have influenced our results, leading to a harder spectrum and weaker reflection components than what has usually been observed from this source. However, we believe that our best-fit parameters are also due to our fitting the entire 3–200 keV spectral band, as discussed in section 5.3.2.1.

ADC models having a slab geometry are unable to explain the observed hard power-law and the small amount of reprocessing, consistent with the results of Dove et al. (1997), Gierliński et al. (1997), and Poutanen, Krolik & Ryde (1997). In contrast, the sphere+disk ADC models provide a good explanation of the data, and furthermore these models are *physically self-consistent*. The sphere+disk models seem to under-produce “reprocessing features”, especially the Fe line, even though reprocessing is self-consistently included within these models (as shown in chapter 2, the geometrical covering fraction of the accretion disk, as seen from the surface of the corona, is  $f_G \approx 0.30$ ). If these residuals, which represent less than 1% of the total flux from Cyg X-1, are due to underestimating reprocessing, several possibilities come to mind. First, our model has a sharp transition between the cold (flat) disk and the corona. It is possible that these two regions overlap to some extent, and thereby produce stronger reprocessing features. Poutanen, Krolik & Ryde (1997) suggest that these regions overlap to a large extent during the high state, which ended only two weeks prior to our observation. Another possibility is that we are observing a hot transition layer between the disk and corona. Our disk also remains flat out to its outer edge. If the disk flares, which is likely due to X-ray heating, it is not flat anymore and reprocessing features will be enhanced. Finally, the iron abundance in the disk of Cyg X-1 could be higher than the solar value that we used in our model.

Due to the data’s broad energy range, the physical properties of the corona are well constrained. However, it is premature to claim that the sphere+disk configuration is indeed the correct geometry. Other, albeit unknown, geometries in which a small fraction of coronal radiation is reprocessed by the disk, may also be able to describe the data. The spectral features due to the reprocessing of coronal radiation in the cold disk (i.e., the Fe  $K\alpha$  fluorescence line, the Compton reflection “bump”, and the soft-excess due to thermalization of the coronal radiation) occur for energies in the  $\sim 0.1$ –20 keV range, and different geometries will predict slightly different reprocessing features. Since data below 3 keV had to be ignored, we were unable to constrain the model parameters which deal with the soft-excess due to thermal radiation emitted by the cold disk, nor can the strength or width of the iron line be measured directly (due to the uncertainty of the PCA response matrix at 5.5 keV). Therefore, more low energy data are needed to further constrain ADC models for Cyg X-1 on the basis of spectral data alone.

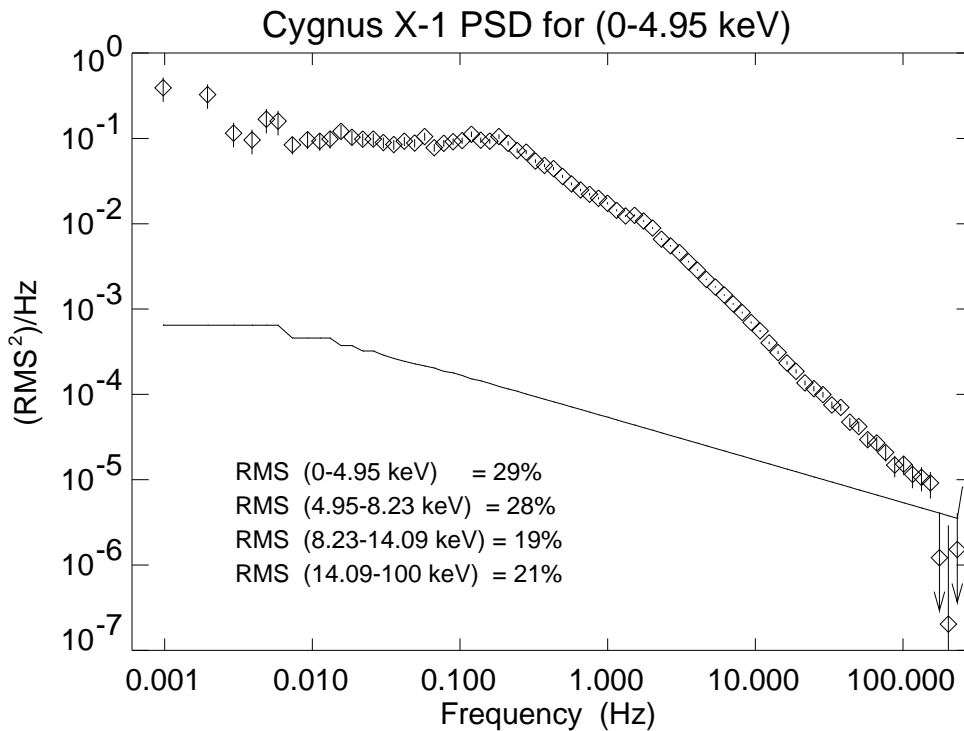


Figure 5.11: Periodogram for the energy band below 4.95 keV in Miyamoto et al. (1992) normalization. Note the distinctive breaks at about 0.2 Hz and 2 Hz. The rms-noise has been subtracted from the PSD, the sensitivity level of which is indicated by the thin line. The rms levels of the PSDs for the other spectral bands are given in the inset.

### 5.5 Temporal Constraints on ADC Models

Additional constraints to the ADC models can come from measurements of time-lags and the temporal coherence between several energy bands from the source. These measurements can be compared with the time-lags and coherence function predicted using the physical parameters of the geometry found from spectral fitting (Vaughan & Nowak 1997; Nowak & Vaughan 1996). Only a geometry in which both the spectral and the temporal data can be explained should be considered a valid candidate for Cyg X-1. Due to its complexity, however, the combined temporal and spectral analysis of the Cyg X-1 observation is outside the scope of this thesis. What I present in this section, therefore, is mainly a short overview on the observed temporal properties. The extensive analysis of these data is postponed to later studies. See Nowak et al. (1998a) and Wilms et al. (1997a) for previous discussions of these data.

Cyg X-1 was the first X-ray source where temporal variability on time scales less than 1 s was observed (Oda et al. 1971). These fluctuations have been typically described in terms of shot-noise models, although the shape and temporal distribution of the shots has been the subject of much debate (Nolan et al. 1981; Lochner, Swank & Szymkowiak 1991; Negoro et al. 1995). Typically, some form of exponentially decaying shot was assumed or, alternatively, symmetric shot profiles. I am not aware of any study using realistic non-symmetric profiles comparable to those shown in section 2.3. The peri-

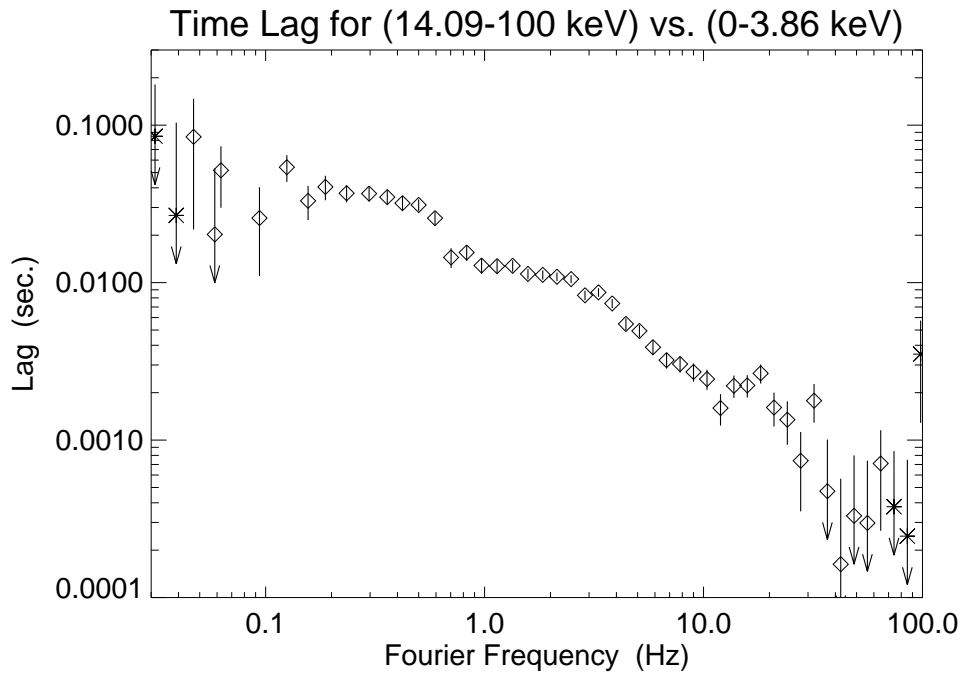


Figure 5.12: Time lag as a function of Fourier frequency for the band from 14.09 to 100 keV vs. the band below 3.86 keV. Open diamonds indicate frequencies where the hard photons lag the soft photons, stars indicate frequencies where the hard photons lead the soft photons.

odogram was then fitted with the theoretical PSD obtained from the shot model to obtain a description of the shot properties. As an example for the measured periodogram, the PSD of Cyg X-1 as obtained from our RXTE observation is given in Fig. 5.11. Over the frequency range shown the PSD can be roughly described by

$$\frac{\text{PSD}}{\text{rms}^2/\text{Hz}} = \begin{cases} 0.091 & \text{for } f < 0.2 \text{ Hz} \\ 0.017f^{-1.04} & \text{for } 0.2 \text{ Hz} \leq f < 2.4 \text{ Hz} \\ 0.031f^{-1.71} & \text{for } 2.4 \text{ Hz} \leq f \end{cases} \quad (5.2)$$

where the break frequencies and power-law slopes have been determined numerically. This shape of the PSD is similar to previous observations (Miyamoto et al. 1992; Belloni & Hasinger 1990a,b), although, due to the quality of the RXTE data, the shape could be determined to a higher precision than was previously possible. Thus, the PSD is characterized by a flat top at low frequencies, and two red noise components at higher frequencies (note that the shape of the periodogram appears to be variable on long timescales Belloni & Hasinger 1990b). For very small frequencies, i.e., large time scales, additional low frequency noise might be present, indicated by the increase at frequencies below  $6 \times 10^{-3}$  Hz in Fig. 5.11.

As was shown in section 3.2.2, for the physical interpretation of the temporal variability of Cyg X-1 within the framework of Comptonization models, the time lags between different energy bands can be used. Fig 5.12 displays the measured frequency dependent

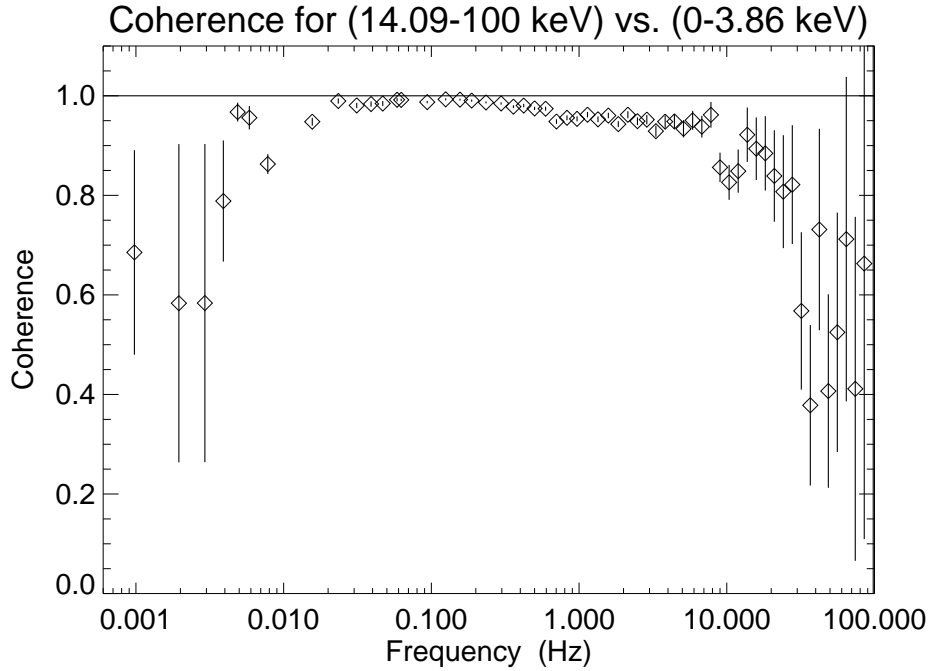


Figure 5.13: Coherence function as a function of Fourier frequency for the same bands as the time lags shown in Fig. 5.12. The coherence is unity from about 0.02 Hz to 10 Hz, the coherence loss at larger time scales is real. The loss of coherence at high frequencies might be influenced by uncertainties associated with the Poisson noise subtraction.

time lag between the lowest band accessible in the RXTE observation ( $E < 3.86$  keV) and the highest energy band ( $E > 14.09$  keV). In agreement with the previous *Ginga* results presented by Miyamoto et al. (1992), the observed time lag is a function decreasing with frequency that has two characteristic breaks at  $\sim 0.6$  Hz and at  $\sim 10$  Hz. Compared to the previous data, however, our measurement could determine the time lag to a much higher precision. Note that the time lag erratically changes sign for frequencies above  $\sim 20$  Hz, as well as for frequencies below  $\sim 0.08$  Hz. This indicates that no strong phase relationship can be found in these frequency regimes. Consistent with this result is that the coherence function is unity to a high precision in the frequency range from 0.08 Hz to 20 Hz, while coherence is not preserved outside this range (Fig. 5.13).

This strong phase relationship over a large frequency range is still a major puzzle for the astrophysics of BH systems. Typical time scales in Cyg X-1 are on the order of

$$T = 5 \times 10^{-5} \text{ s} \left( \frac{R}{GM/c^2} \right) \left( \frac{\nu}{c} \right)^{-1} \left( \frac{M}{10 M_{\odot}} \right) \quad (5.3)$$

If the observed time lag were due to the light travel time of the photons through the medium producing the radiation, the observed shortest time lag of about  $10^{-3}$  s points to sizes of smaller than  $10 GM/c^2$ , or about 150 km, while the longest time lag of 0.05 s corresponds to a size of  $1000 GM/c^2$ . Thus, these sizes are at least in the correct physical regime (i.e., km as opposed to AU). If the transport of information between the regions

radiating coherently were moving with velocities smaller than  $c$ , the resulting sizes would be even smaller. As pointed out by Nowak et al. (1998a), the longest time lag observed is longer than the expected free fall time in an ADAF model, so that it appears that these models are not able to reproduce the observed temporal behavior of Cyg X-1. Further studies are needed, however, to understand whether this claim is true or not. For Comptonization models in the diffusion limit, the minimum time lag observed is the difference in the diffusion times for the hard and the soft photons. If the minimum time lag observed is  $10^{-3}$  s, then the theory of Miller (1994) and Nowak & Vaughan (1996) yields a coronal radius of  $10 GM/c^2$  for the system. Since this minimum time scale might be influenced by the measurement uncertainties, perhaps a better choice for the minimum time lag is  $2 \times 10^{-3}$  s, resulting in a coronal radius of  $45 GM/c^2$  (Nowak et al. 1998a). For the sphere+disk geometry, the simulations presented in Fig. 2.36, p. 71, indicate that the observed time lag corresponds to about 1.7 light crossing times. In this case the measurements point towards  $25 GM/c^2$ . To summarize, independent from the estimates used, the time lag arguments lead to coronal sizes between 10 and 20 Schwarzschild radii. Note that these sizes are smaller than the 100 Schwarzschild radii predicted from the simple ADAF solution (Esin et al. 1998).

How realistic are these coronal sizes? An independent check of these time lag arguments can be obtained from a study of the temporal behavior of the source in time space. In her diploma thesis, Katja Pottschmidt analyzed all available EXOSAT data using the LSSM approach (Pottschmidt 1997; Pottschmidt & König 1997). She finds that these data can be successfully modeled using LSSM[1] models. The relaxation time inferred from the AR[1] process describing the system is  $\tau = 0.19$  s. To understand how this measured parameter translates into a physical parameter, we used the theoretical Compton profiles for the sphere+disk geometry presented in section 2.3.2 to generate synthetic shot noise light curves. These time series were then analyzed with the LSSM code and it was shown that the time series could be well represented by AR[1] processes. The relaxation time scales determined from this modeling were found to correspond to  $3 \dots 6R_c/c$ , where  $R_c$  is the coronal radius. Translating this to a physical size by using the value measured for Cyg X-1, the coronal radius appears to be on the order of 500 to 1000  $GM/c^2$  (Pottschmidt et al. 1998).

Thus, depending on the method used the values for the coronal size appear to be quite different. One explanation for this might be that the LSSM solution is sensitive to a different kind of temporal structures than the time lags. The measurements for the coronal size in the case of the time lags are derived from the argument of a minimal local size and quite deliberately no attempt was made to build a self-consistent model that is able to describe the whole frequency range of time lags. On the other hand, the relaxation time obtained from the LSSM model describes the shape of the individual shots seen. If the seed photons were generated by a radially symmetric disturbance moving inwards, then the simple toy model presented by Nowak et al. (1998a) shows that it is possible to quantitatively reproduce the range of time lags seen and the range of frequencies where coherence is preserved. In such a case, however, the *observed* shot profiles would look different from those computed in section 2.3.2: roughly, the

shot profile is given by the integral of the Green's functions for Compton scattering for the individual radii, weighted by a function describing the shape of the disturbance. Thus, the resulting shot profile would be much broader than the profile obtained from an individual shot and the ratio between  $\tau$  as estimated from the AR[1] model and the coronal light crossing time would be larger. Therefore the coronal size inferred from the observation would be much smaller. Since the development of such a theory requires the detailed modeling of the different oscillating modes of the accretion disk, it is well outside the scope of this thesis. First results will be presented in a forthcoming paper (Nowak et al. 1998b).

---

## RXTE Observations of Soft State Black Holes: LMC X-1 and LMC X-3

### 6.1 Introduction: The Monitoring Campaign

In this chapter first results from observations of the two only persistent soft state black holes are presented. LMC X-1 and LMC X-3 were discovered by *Uhuru* during the scans of the Large Magellanic Cloud (LMC) in 1970 December and 1971 January, where also the very soft photon spectrum of these sources was noted (Leong et al. 1971). Although the luminosity of both objects is quite high (a few  $10^{38}$  erg/sec), the distance of the LMC prevented the study of these objects for a long time. Only with the advent of detectors with a large effective area, a systematic approach on analyzing these objects has become possible. *Ginga* results on LMC X-1 and LMC X-3 presented by Ebisawa, Mitsuda & Hanawa (1991) and Ebisawa et al. (1993) revealed that both sources exhibit very interesting physical behavior. While LMC X-1 was found to exhibit a 0.08 Hz QPO during part of the observation, LMC X-3 was found to be variable on long time scales of a couple of 100 d (Cowley et al. 1991). No systematic monitoring could be done by *Ginga*, however, and due to the absence of an instrument sensitive above 20 keV, no information about the high energy spectrum was obtained.

Since the end of 1996 RXTE has therefore monitored the two black hole candidates in the LMC in three to four weekly intervals, providing a unique opportunity to study their long term behavior. In this chapter I present first results on the evolution of the spectral parameters of the sources from the first twenty pointings. As part of the campaign, RXTE also performed one long (170 ksec) observation for each of BH. Even though their spectrum is very soft ( $\Gamma = 2.5$  and softer), RXTE detected a significant signal at energies up to 50 keV. In the first part of the chapter, in section 6.2, I describe the results from the observations of the more luminous of the two objects, LMC X-3, while section 6.3 will be devoted to LMC X-1. Note that the results presented here are preliminary since the campaign will be continued for all of 1998.

### 6.2 LMC X-3

#### 6.2.1 Introduction

LMC X-3 is the most luminous BH in the LMC. The object has a peak X-ray luminosity of about  $4 \times 10^{38}$  erg/s and is variable by a factor of about four on time scales of 100 d or

200 d (Cowley et al. 1991, see below). The optical counterpart is a well established B3 V star with a mass function of  $f = 2.3 M_{\odot}$  (Cowley et al. 1983; van der Klis, Tjemkes & van Paradijs 1983) in a 1.7 d orbit. The analysis of the stellar spectrum is complicated by the presence of a fair amount of radiation from an extended accretion disk in the system (Cowley et al. 1983, 1994). Using the absence of X-ray eclipses to determine an upper limit for the inclination the mass of the compact object is found to be above  $9 M_{\odot}$  (Cowley et al. 1983). The position of the source is  $\alpha_{2000.0} = 05^{\text{h}}38^{\text{m}}56^{\text{s}}.4$ ,  $\delta_{2000.0} = -64^{\circ}05'01''$ .

The soft X-ray spectrum of LMC X-3 was first studied in detail by White & Marshall (1984), who noted in their HEAO 1 data that the spectrum of the source is considerably softer above 3 keV than below this energy (their value for the photon-index above 3 keV is  $\Gamma = 3.1 \pm 0.2$ ) and correctly comment that the spectrum is similar to that of Cyg X-1 in its high (=soft) state. White & Marshall (1984) also detected that the spectrum is variable, although they were not able to quantify the variability due to lack of data. Due to the availability of the many EXOSAT observations of LMC X-3 made in 1983 December and 1984 December, the soft spectrum below 10 keV and its variability could be quantified to a larger extent. Treves et al. (1988) were able to model these data with optically thick Comptonization models, other models like a pure black body and thermal bremsstrahlung did not result in satisfactory fits. Due to the soft spectrum of the source the optical depth resulting from the fits is high,  $\tau = 22 \dots 28$ , while the temperature of the electron cloud is around 1 keV. Treves et al. (1988) also find a negative correlation between the optical depth and the gas temperature, i.e., higher temperatures lead to smaller optical depths. Note that these model spectra closely resemble pure black bodies with a very steep power-law. In their later analysis of *Ginga* observations of LMC X-3, the same authors note that such a model, represented by a multicolor disk black body model plus a soft power-law (perhaps the result of Comptonization), indeed gives a better and physically meaningful description of the data (Treves et al. 1990). These authors quote an inner disk temperature of about 1.1 keV and a photon index of  $\Gamma = 2.77$  with  $N_{\text{H}} = 3.6 \times 10^{21} \text{ cm}^{-2}$ . The multicolor disk black body is an approximation to the spectrum of an accretion disk with  $T(r) \propto r^{-3/4}$ , i.e., a simple  $\alpha$ -disk. See Mitsuda et al. (1984, eq. 4) for a detailed description of this model.

*Ginga* observations have also been published by Ebisawa et al. (1993), who concentrated especially on the spectral variability of the object. The disk component of the spectrum is well described by a multicolor disk model with fixed  $r_{\text{in}}^2 \cos i$  and varying temperature, as might be the result of a varying mass accretion rate. On the other hand, the power-law component was found to vary independently from the soft component. One physical interpretation for the power-law put forth by Ebisawa et al. (1993) is that it is produced in a cold Compton corona.

Although the multicolor disk blackbody is found empirically to provide a good description of the soft X-ray hump, its physical interpretation is difficult since the temperature structure of the disk close to the BH is affected by relativistic corrections. See Ebisawa, Mitsuda & Hanawa (1991) and Ebisawa et al. (1993) for a more detailed description of these problems and for the description of a generalized accretion disk model



that does not suffer from these problems. Since most previous work on LMC X-1 and LMC X-3 used the multicolor disk black body, it was decided to use this model for the analysis of the observations presented here. The analysis of the data using more physical models will be presented at a later time.

As mentioned above, LMC X-3 is variable by about a factor of four with a period of either 99 or 198 d (Cowley et al. 1991, see also Fig. 6.3, p. 133 below). For energies below 13 keV, these authors found a positive correlation between the intensity and the hardness, while the hard energies did not show such a correlation. There also appears to be a correlation between the optical light curve and the X-ray light curve, which show similar behavior with the optical light lagging the X-rays by about 20 days. This long-term variability is usually interpreted by the precession of the accretion disk, by analogy with objects like Her X-1. Since the disk is optically thick, the precession results in a changing aspect angle between the line of sight and the surface of the disk, so that “limb darkening” effects lead to a changing disk luminosity.

### 6.2.2 *The Long Observation*

As part of the monitoring campaign, LMC X-3 was observed almost continuously during the course of the first week of 1996 December. Fig. 6.1 displays the light curve of the object during this observation. The figure reveals that LMC X-3 was significantly variable by a factor of about ten percent over the course of the week-long observation. During the first interval of the data, the background subtracted PCA count rate rises from about 410 cps to 450 cps. A second “flare”-like event is seen during the second observing block on 1996 December 2, while it returned to a count rate of 410 cps during the last block, on 1996 December 4 and 5, although significant variability on about half day timescales is still observable. This last block of data will be called the “non-flare” data from now on.

To analyze whether any spectral changes are observable during the flare and the non-flare, the flare and non-flare data were analyzed separately. The data were extracted using the methods described in chapter 4.4, except that PCA data measured up to 30 minutes after the SAA were ignored. The total usable PCA time was 132 ksec. Only data where all PCUs were on was included in the present analysis. Due to the length of the observation it was also possible to measure a significant flux with HEXTE (total on-source live time is 50 ksec for each cluster). This is the first time that spectral information for the band above 20 keV was obtained for this object. The average background subtracted count rates for the whole long observation were 416 cps for the PCA, and 0.76 cps and 0.41 cps for HEXTE clusters A and B, respectively. The background count rate in HEXTE cluster A is 56.5 cps. A 1% channel independent systematic error was assumed for all PCA data. For the long observation, the PCA data is usable to 20 keV, while the HEXTE data yields meaningful data below 50 keV. This latter energy is the hardest energy at which

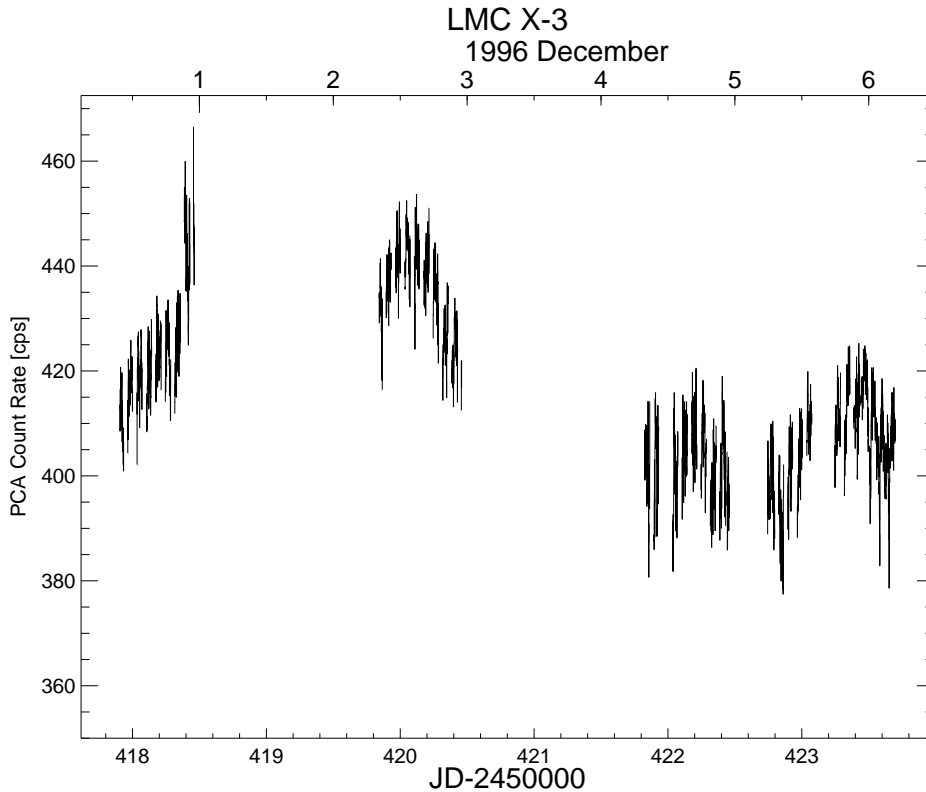


Figure 6.1: Background subtracted PCA count rates for the long observation of LMC X-3. The short gaps in the data are due to SAA passages and Earth occultations of the source.

LMC X-3 has ever been detected<sup>1</sup>.

To describe the data, the popular spectral models for the BH soft state were used. Tab. 6.1 presents the results of these fits. From the broad band data available here, thermal Comptonization can be shown not to be the source of the observed spectrum. Not only is the overall quality of the fit bad ( $\chi^2_{\text{red}} = 3$ ), but the fit indicates that thermal Comptonization (modeled using the theory of Hua & Titarchuk 1995) fails to explain the data at energies above 10 keV. Whether this completely rules out Comptonization as a model for the spectrum of LMC X-3 remains to be seen, however, since the “best-fit” parameters found for the data are outside the range of validity of this Comptonization model. Modeling the spectrum with Comptonization, however, requires thermal Comptonization models that correctly describe the transition regime where the Comptonized radiation and the seed photon spectrum overlap. The computation of such models using the NLMC code is planned for the future.

A better description of the spectrum is given by the sum of a high energy power-law and a model for the soft excess. The soft excess can approximately be described with a black body spectrum (Tab. 6.1), however, the best description is given by modeling the

<sup>1</sup>The Compton Telescope (COMPTEL) flux limits presented by McConnell et al. (1996) for LMC X-1 and LMC X-3 are rather high compared to the extrapolation of the high energy power-law. Their most probable explanation is that they are due to source confusion (McConnell et al. 1996).

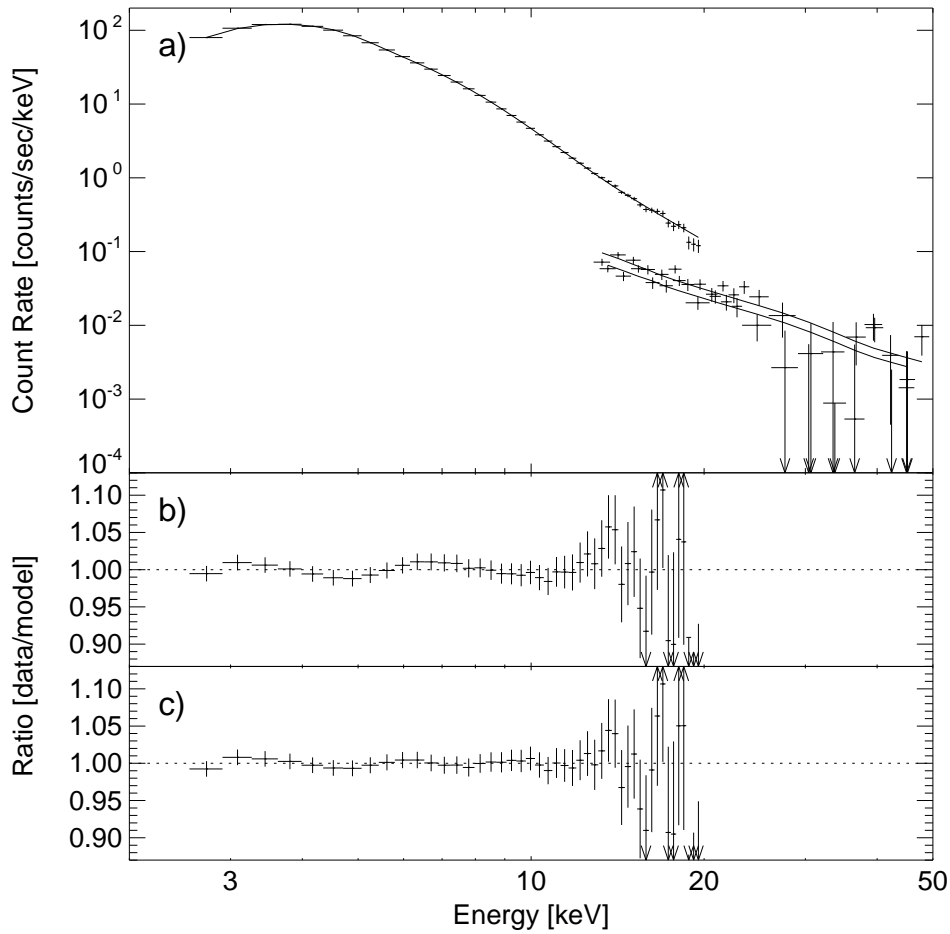


Figure 6.2: Best-fit of the disk black body plus power-law model to the total long observation of LMC X-3. Panel a) displays the observed data and the model, while panel b) gives the ratio between the PCA data and the best fit model. Panel c) shows the effect of adding a Gaussian line to the model.

soft excess with a disk black body after Mitsuda et al. (1984) and Makishima et al. (1986). This is in accordance with the results of Ebisawa et al. (1993) reported in section 6.2.1.

Fig. 6.2 displays the best fit spectrum and its residuals. No high energy turnover is seen in the data – an indication that the power law extends to at least 50 keV. The ratio between the model and the data reveals that the best fit model agrees with the data to better than 2% so that this model is sufficient to explain the observation over the whole range from 2.5 to 50 keV. The deviation between the model and the data in the iron line band, however, is slightly larger than that observed in the fit of the Crab pulsar. Adding a Gaussian at the iron line energy to the spectral model indeed results in a slightly better fit ( $\chi^2/\text{dof} = 107/115$ ), and the value found for the EW of the line, 75 eV, is reasonable. It is premature, however, to interpret this as a real detection of an iron line feature and the subsequent fits were done without including the line feature. Note that the column density could not be constrained very well, even though the quality of

Table 6.1: Results from spectral fitting to the long observation of LMC X-3.

	Total	Flare	Non-Flare
Comptonization			
$N_{\text{H}}$ [ $10^{21} \text{ cm}^{-2}$ ]	0	...	...
$kT_0$ [keV]	0.74	...	...
$kT_c$ [keV]	14.5	...	...
$\tau$	0.23	...	...
$A$	0.02	...	...
$\chi^2/\text{dof}$	534/118	...	...
Black body plus power-law			
$N_{\text{H}}$ [ $10^{21} \text{ cm}^{-2}$ ]	$0_{-0}^{+2.1}$	$0.0_{-0.0}^{+3.6}$	$0.0_{-0}^{+10}$
$kT_{\text{BB}}$ [keV]	$0.973_{-0.005}^{+0.005}$	$0.98_{-0.01}^{+0.00}$	$0.98_{-0.01}^{+0.00}$
$A_{\text{BB}}$ [ $10^{-3}$ ]	$8.9_{-0.2}^{+0.2}$	$9.3_{-0.3}^{+0.2}$	$8.9_{-0.2}^{+0.2}$
$\Gamma$	$3.40_{-0.04}^{+0.05}$	$3.40_{-0.05}^{+0.09}$	$3.6_{-0.1}^{+0.3}$
$A_{\text{PL}}$ [ $\text{ph cm}^{-2} \text{ s}^{-1} \text{ keV}^{-1}$ ]	$1.0_{-0.1}^{+0.1}$	$1.0_{-0.1}^{+0.4}$	$1.2_{-0.1}^{+1.2}$
$\chi^2/\text{dof}$	140/117	111/117	122/117
Disk black body plus power-law			
$N_{\text{H}}$ [ $10^{21} \text{ cm}^{-2}$ ]	$2.3_{-2.1}^{+2.3}$	$2_{-0}^{+2}$	$2_{-2}^{+0.8}$
$kT_{\text{in}}$ [keV]	$1.25_{-0.01}^{+0.01}$	$1.26_{-0.01}^{+0.01}$	$1.24_{-0.01}^{+0.01}$
$A_{\text{DB}}$	$31.5_{-1.6}^{+1.6}$	$32.1_{-1.7}^{+1.7}$	$32.4_{-1.0}^{+1.5}$
$\Gamma$	$2.5_{-0.2}^{+0.2}$	$2.3_{-0.1}^{+0.2}$	$2.5_{-0.3}^{+0.2}$
$A_{\text{PL}}$ [ $\text{ph cm}^{-2} \text{ s}^{-1} \text{ keV}^{-1}$ ]	$0.07_{-0.03}^{+0.05}$	$0.05_{-0.02}^{+0.05}$	$0.04_{-0.02}^{+0.07}$
$\chi^2/\text{dof}$	114/117	98/117	107/117

*Comptonization*: Comptonization model after Hua & Titarchuk (1995) and Titarchuk (1994),  $kT_0$ : seed photon temperature (the seed photons are described by a Wien hump),  $kT_c$ : temperature of the electron gas,  $\tau$  optical depth of the spherical cloud,  $A$ : normalization. *Black body*:  $kT_{\text{BB}}$ : temperature of the black body,  $A_{\text{BB}}$  normalization in  $10^{39} (D/10 \text{ kpc})^2 \text{ erg/sec}$  where  $D$  is the distance, *power-law*:  $\Gamma$ : photon index,  $A_{\text{PL}}$ : photon flux at 1 keV, *Disk black body*: disk black body after Mitsuda et al. (1984) and Makishima et al. (1986),  $kT_{\text{in}}$ : temperature at inner disk radius,  $A_{\text{DB}} = ((r_{\text{in}}/\text{km})/(D/10 \text{ kpc}))^2 \cos i$  where  $r_{\text{in}}$  is the inner disk radius,  $D$  the distance of the object, and  $i$  the inclination angle. Uncertainties given are at the 90% level for one interesting parameter ( $\Delta\chi^2 = 2.7$ ). The uncertainty in the relative normalization between the PCA and HEXTE was taken care of by introducing a multiplicative constant which is not shown in the table.

the data is high. Since data below 3 keV were not included in the fit due to response matrix reasons, this is not astonishing. Simulations reveal that even for a bright source like Her X-1 measuring precise column densities with RXTE is a very challenging task when  $N_{\text{H}} < 10^{22} \text{ cm}^{-2}$  (Stelzer et al. 1998). Since the column to LMC X-3 is less than  $5 \times 10^{21} \text{ cm}^{-2}$  it is no surprise, therefore, that  $N_{\text{H}}$  could not be constrained very well.

Comparing the “flare” and the “non-flare” data results in almost the same fit parameters. As is also evident from looking at the spectrum in detector space, only the normalization of the spectrum changes between the flare and the non-flare state, while the shape of the spectrum stays the same. A more detailed analysis of shorter time intervals during this observation is necessary to enable us to make a final statement on the variability of the source on timescales of a day<sup>1</sup>.

<sup>1</sup>Between the long observation and observation 02 of the monitoring campaign (presented in the next section),  $T_{\text{in}}$  changed by about 0.01 keV/day. Thus the result that the physical parameters are almost constant over the long observation is consistent with the long term variability of the source presented in section 6.2.3.

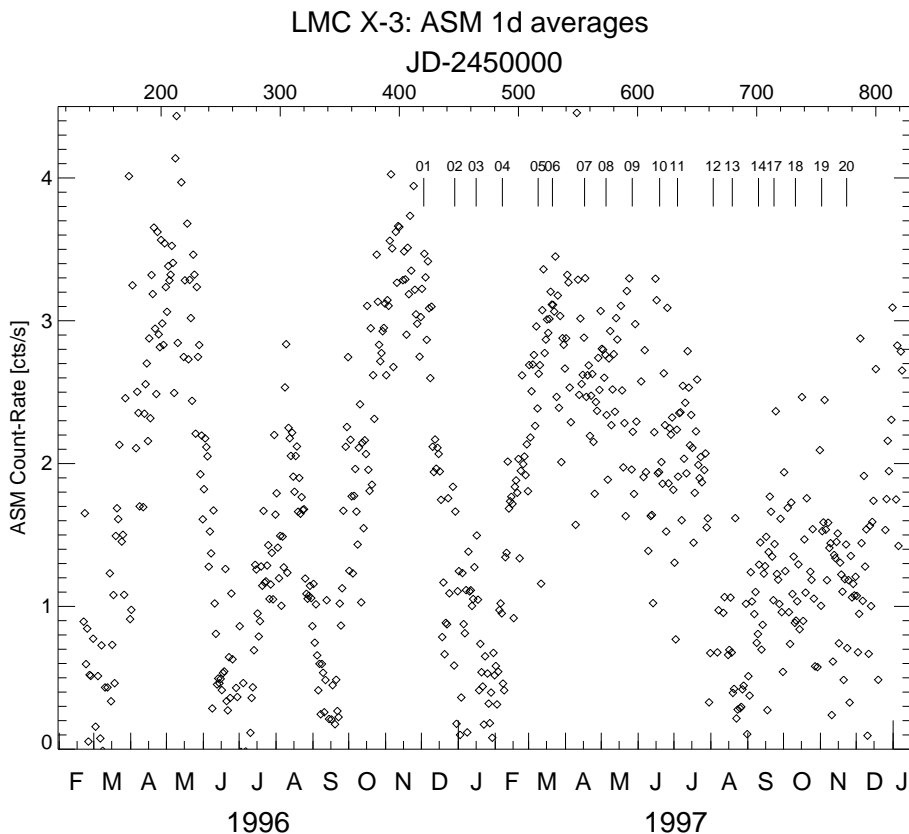


Figure 6.3: RXTE/ASM lightcurve of LMC X-3 for 1996 and 1997. The numbered dashes indicate the dates at which the RXTE monitoring observations were performed. Observation 15 occurred shortly after observation 14, and observation 16 briefly before observation 17. For clarity these observations are not shown. See Tab. 6.2 for the observing log.

### 6.2.3 The Spectral Evolution of LMC X-3

Fig. 6.3 displays the temporal variability of LMC X-3 for 1996 and 1997. The source is clearly variable on timescales of several weeks, with a possible periodicity on a timescale of 200 days. Note the strong peak to peak variation by more than a factor of eight of the amplitude which is definitively not a simple sinusoidal and looks very different from the behavior seen by HEAO 1 (Cowley et al. 1991). The Lomb-Scargle periodogram of this lightcurve, shown in Fig. 6.4, reveals the presence of a period of about 180 d, as well as a possible second period at about 110 d. Since the basis of the measurement is only about 600 days, these periods cannot be given to a higher precision. It is not possible to decide whether the lower period is just a sidelobe of the dominant 180 d period since the small peak at 90 d and the peak at 110 d are just separated by one frequency bin. At least two more years of continuous monitoring are necessary to be able to speak the final word about the periodicity.

To study the long term variability of LMC X-3, RXTE performed an approximately three weekly monitoring of the source starting at the beginning of 1996 December with the long observation described in section 6.2.2 above. A log of the observations is given

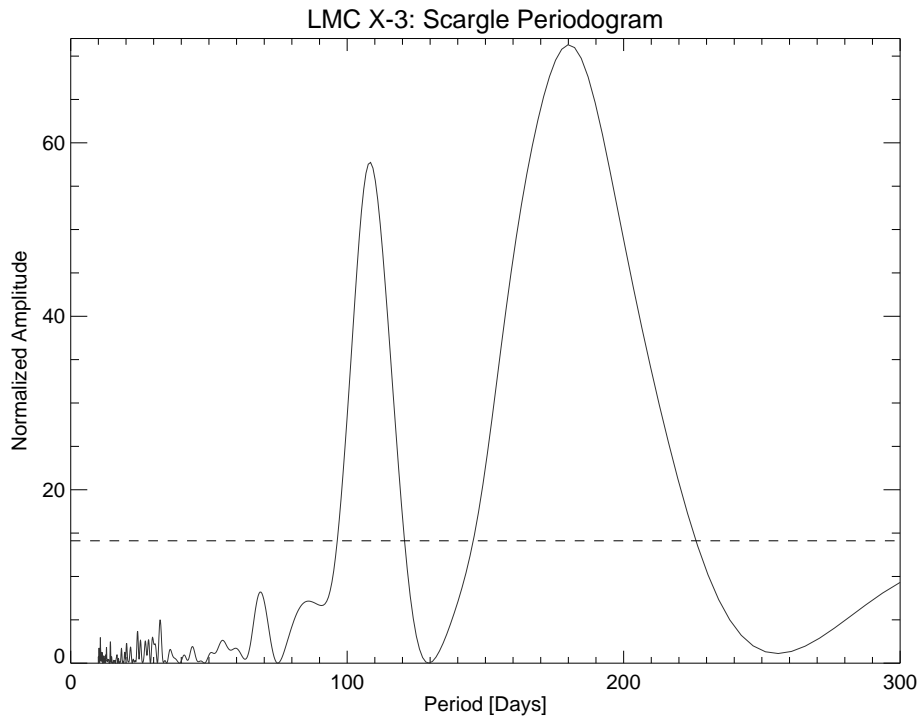


Figure 6.4: Lomb-Scargle periodogram of the data of Fig. 6.3. The dashed line denotes a false alarm probability of 0.001.

Table 6.2: Observing log for the monitoring campaign on LMC X-3. The date is the starting date of the observation, the duration is the total on-source time for which all PCA detectors were turned on, rounded to the closest 100 seconds.

Obs.	Date	Duration	Obs.	Date	Duration
01	1996.11.30	132100	11	1997.07.04	7300
02	1996.12.29	8700	12	1997.08.03	5900
03	1997.01.16	3000	13	1997.08.19	8100
04	1997.02.07	9400	14	1997.09.09	9300
05	1997.03.09	8000	15	1997.09.12	7900
06	1997.03.21	7400	16	1997.09.19	3200
07	1997.04.17	9000	17	1997.09.23	10000
08	1997.05.05	7500	18	1997.10.11	7400
09	1997.05.27	8400	19	1997.11.02	8400
10	1997.06.18	8100	20	1997.11.23	8900

Table 6.3: Results from fitting the LMC X-3 monitoring observations.

Obs	$T_{\text{in}}[\text{keV}]$	norm	$\Gamma$	$A_{\text{PL}}$	$\chi^2/\text{dof}$	$\chi^2_{\text{red}}$
01	$1.25^{+0.01}_{-0.01}$	$31.5^{+1.6}_{-1.6}$	$2.5^{+0.2}_{-0.2}$	$0.07^{+0.05}_{-0.03}$	114/117	1.0
02	$0.97^{+0.02}_{-0.02}$	$24.2^{+3.4}_{-3.3}$	$3.5^{+0.2}_{-0.3}$	$0.21^{+0.10}_{-0.10}$	25.2/30	0.8
03	$0.97^{+0.03}_{-0.02}$	$18.5^{+4.1}_{-3.8}$	$3.3^{+0.2}_{-0.2}$	$0.27^{+0.10}_{-0.10}$	24.0/30	0.8
04	$1.01^{+0.02}_{-0.01}$	$30.4^{+2.7}_{-3.2}$	$3.3^{+0.5}_{-2.5}$	$0.07^{+0.10}_{-0.07}$	24.6/30	0.8
05	$1.22^{+0.01}_{-0.01}$	$31.1^{+1.4}_{-1.7}$	$2.6^{+0.3}_{-0.4}$	$0.09^{+0.08}_{-0.06}$	21.3/30	0.7
06	$1.24^{+0.03}_{-0.10}$	$33.6^{+1.0}_{-0.9}$	$1.5^{+0.7}_{-0.4}$	$0.01^{+0.00}_{-0.01}$	20.0/30	0.7
07	$1.23^{+0.05}_{-0.05}$	$29.7^{+0.7}_{-2.0}$	...	...	57/32	1.8
08	$1.23^{+0.10}_{-0.00}$	$30.6^{+0.6}_{-0.4}$	...	...	16/32	0.5
09	$1.22^{+0.01}_{-0.01}$	$28.8^{+0.4}_{-0.3}$	...	...	40/32	1.3
10	$1.18^{+0.01}_{-0.01}$	$27.7^{+0.5}_{-0.4}$	$4.3^{+0.6}_{-0.4}$	$0.20^{+0.16}_{-0.08}$	90/30	3.0
11	$1.18^{+0.01}_{-0.01}$	$27.2^{+0.5}_{-0.4}$	$4.4^{+0.9}_{-0.5}$	$0.15^{+0.17}_{-0.07}$	108/30	3.6
12	$1.04^{+0.01}_{-0.01}$	$26.6^{+1.2}_{-1.2}$	$2.8^{+0.1}_{-0.1}$	$0.09^{+0.03}_{-0.03}$	84.8/30	2.8
13	$0.70^{+0.02}_{-0.02}$	$27.4^{+3.7}_{-3.4}$	$2.8^{+0.1}_{-0.1}$	$0.08^{+0.02}_{-0.02}$	52.9/30	1.8
14	$1.00^{+0.01}_{-0.01}$	$27.4^{+1.3}_{-1.2}$	$3.7^{+0.4}_{-0.4}$	$0.07^{+0.05}_{-0.04}$	73.3/30	2.4
15	$1.02^{+0.01}_{-0.01}$	$27.3^{+0.9}_{-1.6}$	$3.4^{+0.5}_{-0.6}$	$0.05^{+0.05}_{-0.03}$	20.0/20	1.2
16	$1.07^{+0.01}_{-0.01}$	$26.4^{+1.8}_{-1.5}$	$5.5^{+3.2}_{-1.3}$	$0.62^{+0.50}_{-0.60}$	26.6/30	0.8
17	$1.07^{+0.01}_{-0.01}$	$27.8^{+1.0}_{-1.0}$	$3.4^{+0.2}_{-0.2}$	$0.09^{+0.04}_{-0.03}$	65.3/30	2.2
18	$1.04^{+0.01}_{-0.01}$	$28.3^{+0.6}_{-1.0}$	$3.9^{+0.7}_{-0.6}$	$0.07^{+0.08}_{-0.04}$	70/30	2.3
19	$1.07^{+0.01}_{-0.01}$	$29.3^{+0.8}_{-1.0}$	$2.9^{+0.4}_{-0.7}$	$0.02^{+0.03}_{-0.02}$	74/30	2.5
20	$1.02^{+0.01}_{-0.01}$	$26.3^{+1.3}_{-1.2}$	$3.6^{+0.3}_{-0.4}$	$0.07^{+0.05}_{-0.04}$	50/30	1.7

$N_{\text{H}}$  was fixed at  $3.6 \times 10^{21} \text{ cm}^{-2}$ . Uncertainties given are at the 90% level for one interesting parameter ( $\Delta\chi^2 = 2.7$ ). Due to the weakness of the source, only the energy band from 3 to 10 keV was included in this analysis.

in Tab. 6.2. To visualize the position of the observations within the ASM lightcurve of LMC X-3, the observations are also indicated in Fig. 6.3. For describing the observations the data were fitted with the disk black body plus power-law model that has proven to be successful in the long observation. Since it is not possible to constrain  $N_{\text{H}}$  in any way from these short observations, it was fixed at  $3.6 \times 10^{21} \text{ cm}^{-2}$  for the fits. The results from spectral modeling are given in Tab. 6.3 and are also displayed in Fig. 6.5.

There is a clear correlation between the inner disk temperature  $T_{\text{in}}$  and the total soft X-ray flux as observed by the ASM. For about the first half of the observations, the normalization of the disk black body,  $r^2 \sin i$ , is also correlated to the ASM flux, while it appears to be constant for the second half of the monitoring campaign. This latter behavior, where the variation of the soft flux is solely due to the varying  $T_{\text{in}}$ , has also been seen by *Ginga* and has been interpreted as the observation of a varying mass accretion rate in the system (Ebisawa et al. 1993).

The first part of our monitoring campaign, however, indicates that this interpretation does not always hold:  $r^2 \sin i$  is not constant during that time interval. That LMC X-3

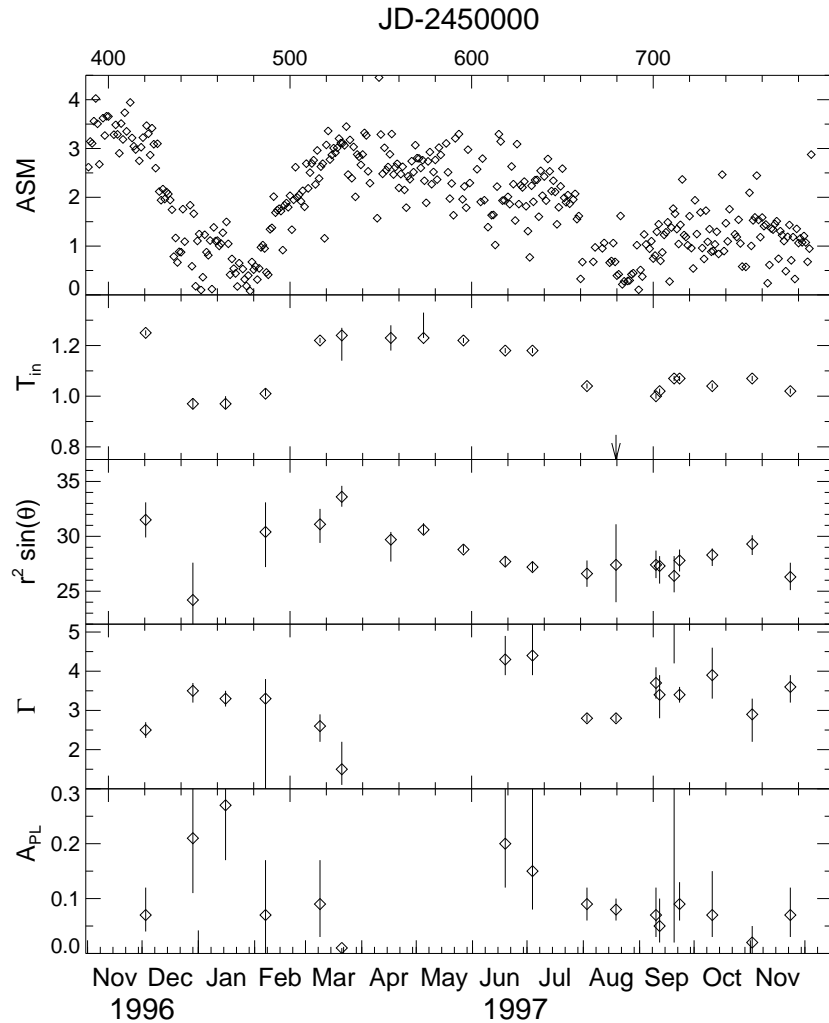


Figure 6.5: Temporal variability of LMC X-3 using the fit-parameters from Tab. 6.3. The error bars indicate the 90% uncertainties from the table.

behaved differently during the first half of 1997 is also evident from the hard component. For the first few pointings, from 1996 November to 1997 March, the photon index appears to be weakly anticorrelated with the flux, i.e., a softer power-law is observed when the source luminosity is low. However, from 1997 January to March, the total flux in the hard component decreased, and no evidence for this component was found in the monitoring observations 07 to 09. After that the hard component appears again. For the second half of 1997, the photon index of the power-law is almost constant and its flux traces the soft component fairly reasonably. This behavior of the power-law is different from that seen in the *Ginga* observations presented by Ebisawa et al. (1993). These authors found no correlation between the soft and the hard spectral components at all. The cause for this discrepancy is at present unknown. It should be noted, however, that the data presented here are the result from an analysis of data from all PCA layers



and are thus very sensitive to the uncertainties in the background subtraction process. Before the final word on the apparent correlations between the power-law normalization and the soft component can be spoken, a better PCA background model needs to be available and the analysis ought to be done for the two topmost PCA layers only. Such an analysis has to wait for the end of the second year of the monitoring campaign and will be presented in a later paper.

### 6.3 LMC X-1

The optical counterpart of LMC X-1 has been a mystery for a long time since the field around the X-ray source is very crowded. Using a large number of ROSAT HRI observations, Cowley et al. (1995) were finally able to identify the counterpart with “star number 32” of Cowley, Crampton & Hutchings (1978), an object that has long been one of the most probable counterparts (Hutchings, Crampton & Cowley 1983, and references therein). The position of the source is  $\alpha_{2000.0} = 05^{\text{h}}39^{\text{m}}39^{\text{s}}.5$ ,  $\delta_{2000.0} = -69^{\circ}44'36''.6$ . The counterpart is surrounded by a He II nebula that might be photoionized by the X-rays from LMC X-1 (Bianchi & Pakull 1985; Pakull & Angebault 1986). Star 32 itself is a O(7-9) III star with  $m_V = 14.8$  in a 4.2 d orbit with an object of  $M > 4 M_{\odot}$ , assuming a mass function of  $f = 0.144 M_{\odot}$  (Hutchings, Crampton & Cowley 1983; Hutchings et al. 1987). Hutchings et al. (1987) assume a most probable mass of  $6 M_{\odot}$  for the compact object, with an uncertainty of about  $2 M_{\odot}$  mainly due to the uncertainty in the inclination, where only an upper limit could be inferred from the absence of X-ray eclipses. The luminosity of the object is about  $2 \times 10^{38}$  erg/s (Long, Helfand & Grabelsky 1981) and was not found to be variable (Syunyaev et al. 1990).

In the *Ginga* observations of LMC X-1, the X-ray spectrum could be well described by a black-body with  $kT_{\text{BB}} = 0.70 \pm 0.01$  keV plus a power-law with photon index  $\Gamma = 2.52 \pm 0.05$  in 1987 April and  $\Gamma = 2.85 \pm 0.12$  in 1987 June (Ebisawa, Mitsuda & Inoue 1989). The parameters of the blackbody were found to be constant during both observations. Instead of using a Planckian blackbody, the disk black body model was found to be able to describe the soft excess even better. The spectral fits to the disk black body resulted in an inner temperature of the disk of  $kT_{\text{in}} = 0.94 \pm 0.03$  keV, and a slightly harder power-law with  $\Gamma = 2.25 \pm 0.08$  in April and  $\Gamma = 2.43 \pm 0.13$  in June (Ebisawa, Mitsuda & Inoue 1989). In addition to the continuum, there was weak evidence for an iron  $K\alpha$  line with  $\text{EW} \approx 75$  eV at 6.8 keV in the spectrum. These results for the spectral continuum have been verified in the BBRXT observation presented by Schlegel et al. (1994), although the disk temperature was found to be slightly lower. Furthermore, these authors present evidence for additional small line features at 5.1 keV and 7.1 keV, respectively. Whether these features are real, however, remains to be seen.

Information on the spectrum of LMC X-1 (and LMC X-3) at energies below 20 keV can also be obtained from the TTM observations described by Syunyaev et al. (1990). These authors model the data with a pure power-law with index  $\Gamma = 3.6 \pm 0.1$ , absorbed by  $N_{\text{H}} = (6.6 \pm 0.4) \times 10^{22}$  cm $^{-2}$ . This latter value for the absorption appears high com-

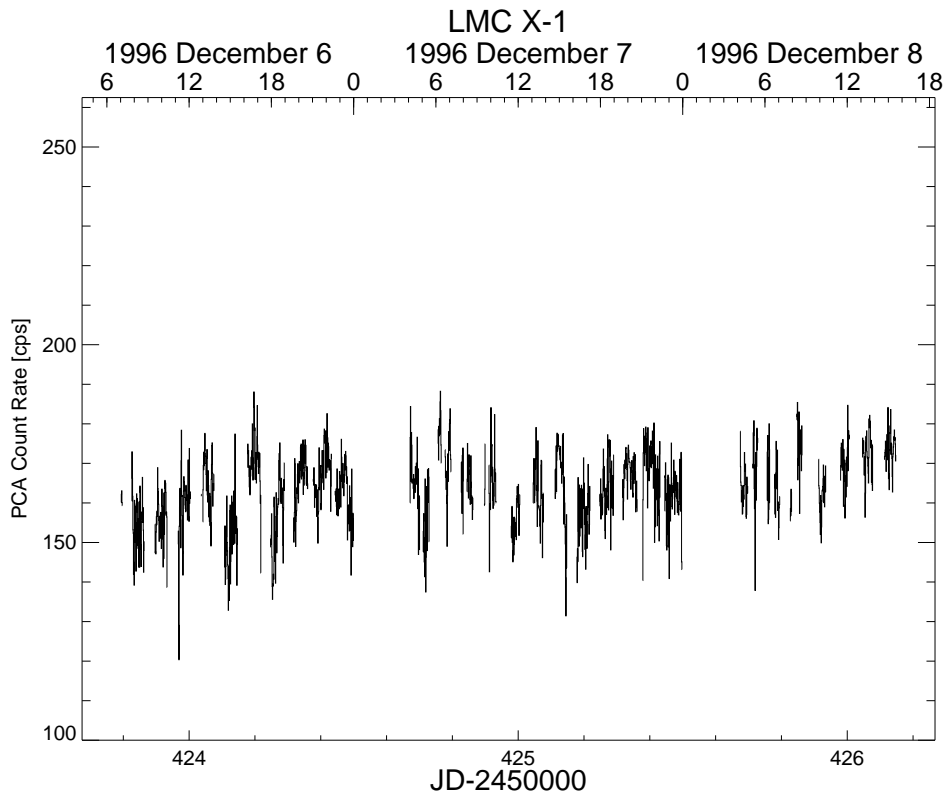


Figure 6.6: Background subtracted PCA count rates for the long observation of LMC X-1.

pared to the *Ginga* and BBRXT measurements, which both yielded  $N_{\text{H}} \approx 5 \times 10^{21} \text{ cm}^{-2}$  over the same energy range (Ebisawa, Mitsuda & Inoue 1989; Schlegel et al. 1994), and a similar small value for  $N_{\text{H}}$  can also be inferred from the interstellar extinction to the object ( $E_{\text{B}-\text{V}} = 0.35$ , Hutchings et al. 1987). Since Syunyaev et al. (1990) did not attempt to describe the measured spectrum with an additional soft excess component, this deviation might be due to the large  $N_{\text{H}}$  “mimicking” the soft excess (note also that these authors do not indicate the quality of their fit). Further studies are needed to solve this puzzle.

The short term temporal behavior of LMC X-1 is not studied very well. Ebisawa, Mitsuda & Inoue (1989) present evidence for a QPO of 0.075 Hz in the first 40 minutes of the *Ginga* observation in 1987 April. During their later 1987 June observation, no QPO was observed, ditto in the ROSAT HRI observations presented by Cowley et al. (1995) and in the BBRXT observations presented by Schlegel et al. (1994). Note that the strength of the QPO reported by Ebisawa, Mitsuda & Inoue (1989) is only slightly above the Poisson limit and that observations with a higher signal to noise ratio are necessary to test whether their claim of a detection of a QPO is real or not (Nowak 1995).

Table 6.4: The best-fit disk black body model for the long observation of LMC X-1.

Disk black body plus power-law	
$kT_{\text{in}}$ [keV]	$1.00^{+0.02}_{-0.04}$
$A_{\text{DB}}$	$29.4^{+1.1}_{-1.0}$
$\Gamma$	$3.65^{+0.05}_{-0.07}$
$A_{\text{PL}}$ [ph cm <sup>-2</sup> s <sup>-1</sup> keV <sup>-1</sup> ]	$0.57^{+0.08}_{-0.09}$
$\chi^2/\text{dof}$	50.5/30

See Tab. 6.1 for an explanation of the spectral models and abbreviations used. Uncertainties given are at the 90% level for one interesting parameter ( $\Delta\chi^2 = 2.7$ ), except for  $kT_{\text{in}}$  which is at the 90% level for two interesting parameters. The uncertainty in the relative normalization between the PCA and HEXTE was taken care of by introducing a multiplicative constant, see text.  $N_{\text{H}}$  was fixed to  $3 \times 10^{21}$  cm<sup>-2</sup>.

### 6.3.1 The Long Observation

RXTE observed LMC X-1 continuously from 1996 December 6 to 1996 December 8 while the source was circumpolar as seen from the satellite. The observed lightcurve is shown in Fig. 6.6. No variability outside the systematic uncertainty associated with the background variability is evident during these three days so that the observation can be analyzed as a whole without any dangers.

The data were extracted using the same methods as those employed for LMC X-3. Only PCA data where all four detectors had been turned on is included in the present analysis, resulting in a total of 75 ksec of on-source PCA data. The background subtracted count-rate for the PCA is 164 cps. For the HEXTE, a total of 55 ksec of live time per cluster was obtained. LMC X-1 was barely detected with the high energy instrument, the count-rate being 0.2 cps. Since the spectrum of LMC X-1 is both weak and very soft, PCA data above 10 keV had to be ignored. A meaningful HEXTE flux was detected up to an energy of 25 keV. Due to the soft spectrum of the source, though, the signal to noise ratio of the HEXTE data is not good enough to obtain more information than just the presence of the source.

As in the case of LMC X-3, neither Comptonization nor a black body with a high energy power-law result in a satisfactory description of the data, while the disk black body model is again able to describe the data. HEXTE can only be used to constrain the high energy spectrum, but this is sufficient to obtain a good handle on the high energy spectrum. In Tab. 6.4 the parameters of the best fit disk black body model are shown. The parameters are in qualitative agreement with the earlier observations, although the photon index of the power-law is significantly softer. The residuals show no evidence for additional line features.

Compared to LMC X-3, the power-law component is stronger in the spectrum. Plotting the unfolded spectrum reveals that for energies above 8 keV the power-law dominates the observed flux. This is a crucial region in the X-ray spectrum since, by chance, there also is the 7 keV iron K absorption edge. The presence of residuals in this energy band seen in the *Ginga* observations of LMC X-1 has prompted Ebisawa (1991) to

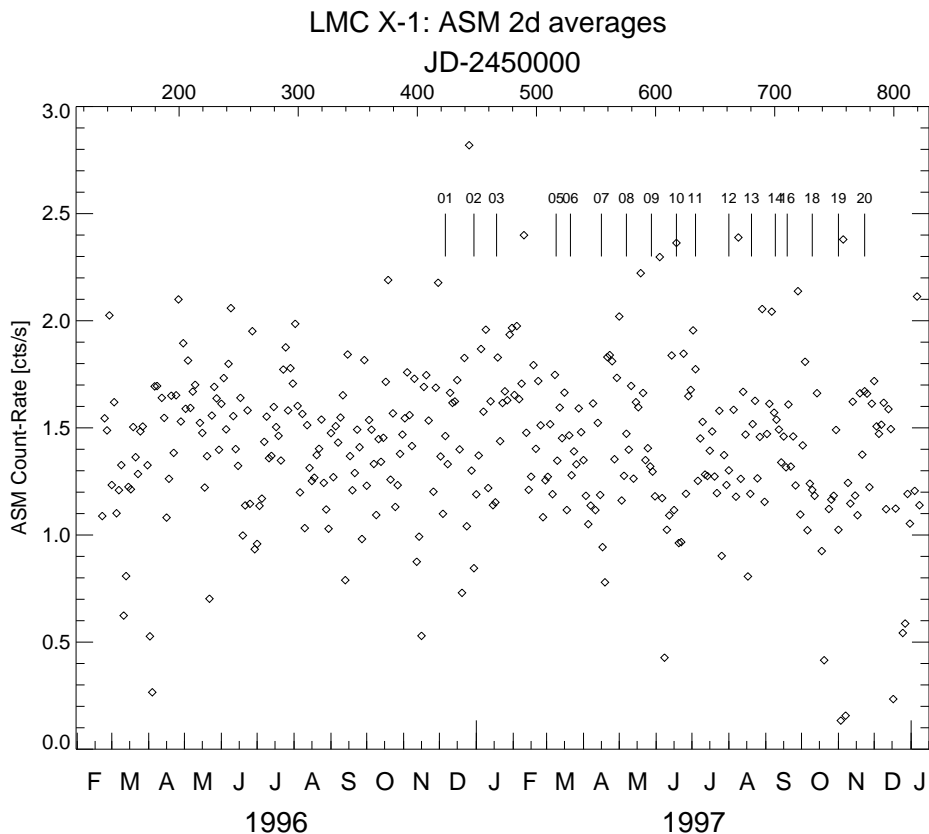


Figure 6.7: RXTE/ASM lightcurve of LMC X-1 for 1996 and 1997. The numbered dashes indicate the dates at which the RXTE monitoring observations were performed. See Tab. 6.5 for the observing log.

describe these residuals with a Doppler-smearred iron edge. No such feature is found in the long observation presented here: the inclusion of such a feature in the spectral models lead consistently to optical depths of zero at the edge energy. However, there are residuals in this regime that are due to the transition between the soft excess and the power-law. One explanation for these residuals is that the power-law is the result of Comptonization of the seed photons from the disk in a comparably cold corona. In this case, the transitional regime does not look like the sum of the seed photon spectrum and the high energy power-law. Therefore, the computation of additional Comptonization models is necessary before a final decision on the nature of the residuals in the iron edge band can be made.

### 6.3.2 No Spectral Evolution in LMC X-1

As in the case of LMC X-3, short (10 ks) monitoring observations on LMC X-1 were done for all of 1997 in intervals of approximately three to four weeks. A log of the observations is given in Tab. 6.5. As is revealed by the ASM lightcurve of LMC X-1, no clear temporal variability is seen from the object. The results from the spectral modeling of the monitoring observations presented in Tab. 6.6 reveal the same picture: None

Table 6.5: Observing log for the monitoring campaign on LMC X-1. The date is the starting date of the observation, the duration is the total on-source time for which all PCA detectors were turned on, rounded to the closest 100 seconds.

Obs.	Date	Duration	Obs.	Date	Duration
01	1996.12.06	75300	11	1997.07.04	3400
02	1996.12.30	4000	12	1997.08.01	8500
03	1997.01.18	8100	13	1997.08.20	8000
05	1997.03.09	5400	14	1997.09.09	6100
06	1997.03.21	8800	15	1997.09.12	8800
07	1997.04.16	10600	16	1997.09.19	7200
08	1997.05.07	8700	18	1997.10.10	9600
09	1997.05.28	5900	19	1997.11.01	8800
10	1997.06.18	3600	20	1997.11.23	4700

PCU 4 was off for all of Observation 04, while Observation 17 had not yet been delivered at the time of writing (1998 January).

Table 6.6: Results from fitting the LMC X-1 monitoring observations.

Obs	$T_{\text{in}}[\text{keV}]$	norm	$\Gamma$	$A_{\text{PL}}$	$\chi^2$
03	$1.05^{+0.03}_{-0.03}$	$22.7^{+4.9}_{-4.3}$	$3.2^{+0.2}_{-0.2}$	$0.43^{+0.15}_{-0.13}$	16.5
05	$0.95^{+0.02}_{-0.02}$	$43.1^{+7.0}_{-6.9}$	$3.3^{+0.3}_{-0.3}$	$0.25^{+0.17}_{-0.14}$	12.2
06	$0.95^{+0.02}_{-0.01}$	$43.2^{+6.5}_{-6.7}$	$3.2^{+0.3}_{-0.3}$	$0.24^{+0.16}_{-0.13}$	9.5
07	$0.93^{+0.02}_{-0.01}$	$48.3^{+7.2}_{-7.2}$	$3.3^{+0.2}_{-0.2}$	$0.31^{+0.17}_{-0.14}$	19.3
08	$0.96^{+0.02}_{-0.02}$	$43.0^{+6.7}_{-6.5}$	$3.3^{+0.2}_{-0.3}$	$0.31^{+0.17}_{-0.14}$	15.3
09	$0.95^{+0.03}_{-0.02}$	$40.2^{+8.3}_{-8.3}$	$3.2^{+0.3}_{-0.4}$	$0.23^{+0.19}_{-0.14}$	18.0
10	$0.93^{+0.02}_{-0.02}$	$47.5^{+8.3}_{-8.3}$	$3.3^{+0.2}_{-0.3}$	$0.32^{+0.19}_{-0.15}$	21.7
11	$0.88^{+0.02}_{-0.01}$	$69.3^{+8.5}_{-11}$	$2.9^{+0.4}_{-0.7}$	$0.12^{+0.16}_{-0.10}$	12.6
11	$0.91^{+0.02}_{-0.01}$	$55.6^{+8.5}_{-9.6}$	$3.2^{+0.3}_{-0.5}$	$0.18^{+0.19}_{-0.12}$	14.5
12	$1.01^{+0.03}_{-0.02}$	$28.5^{+5.2}_{-4.9}$	$3.2^{+0.2}_{-0.2}$	$0.29^{+0.14}_{-0.12}$	12.3
13	$0.97^{+0.01}_{-0.01}$	$46.1^{+5.3}_{-6.0}$	$3.0^{+0.3}_{-0.5}$	$0.15^{+0.14}_{-0.10}$	14.6
14	$1.01^{+0.02}_{-0.02}$	$30.7^{+5.3}_{-5.2}$	$3.0^{+0.2}_{-0.3}$	$0.22^{+0.13}_{-0.11}$	10.6
15	$0.92^{+0.02}_{-0.01}$	$56.6^{+6.9}_{-7.6}$	$3.2^{+0.3}_{-0.4}$	$0.20^{+0.16}_{-0.12}$	12.5
16	$0.96^{+0.02}_{-0.02}$	$40.8^{+6.3}_{-6.8}$	$3.0^{+0.3}_{-0.4}$	$0.18^{+0.15}_{-0.11}$	11.9
18	$1.08^{+0.03}_{-0.03}$	$18.9^{+3.8}_{-3.4}$	$3.1^{+0.2}_{-0.2}$	$0.26^{+0.11}_{-0.10}$	13.2
19	$1.03^{+0.02}_{-0.02}$	$26.9^{+4.2}_{-4.1}$	$2.9^{+0.3}_{-0.4}$	$0.15^{+0.10}_{-0.08}$	8.2
20	$1.09^{+0.03}_{-0.03}$	$20.0^{+4.2}_{-3.4}$	$3.2^{+0.2}_{-0.2}$	$0.33^{+0.14}_{-0.12}$	15.1

$N_{\text{H}}$  was fixed at  $3.6 \times 10^{21} \text{ cm}^{-2}$ . Uncertainties given are at the 90% level for one interesting parameter ( $\Delta\chi^2 = 2.7$ ), all  $\chi^2$ -values are for 16 degrees of freedom. The two parameter sets given for observation 11 are for the first and the second part of that observation.

of the spectral parameters is deviating significantly from the values found in the long observation.

Both objects are quite similar (both donors are high mass stars, orbital periods are on the order of a few days) but the X-ray luminosities differ by a factor of two. The failure to detect any variability in LMC X-1 might put constraints on those physical models that attempt to interpret the variability of LMC X-3, which is usually explained with the presence of a warped, precessing accretion disk in the system. Physical processes responsible for the warping might be an accretion disk wind (Schandl 1996) or strong radiation pressure onto the disk (Maloney, Begelman & Pringle 1996). Both effects lead to a torque on the disk and eventually to a disk precession. Note that it has been suggested that the torque due to the wind might be weaker than the radiation torque, due to the inefficiency of X-ray heating (Maloney & Begelman 1997, Begelman, 1998, priv. comm.). Since LMC X-1 does not exhibit any variability, this might indicate that the crucial factor in determining whether the warping instability operates is the X-ray luminosity of the object.

---

## Summary and Future Work

The major result of this thesis is that the simple slab ADC appears not to exist in galactic black holes. The major physical cause for this is that the slab ADC cannot have a temperature high enough to explain the observed X-ray spectrum since the large covering factor of the accretion disk leads to strong reprocessing in the disk, which increases the Compton cooling. Additional constraints come from the fact that the observed equivalent width of the iron line in the hard state is too small compared to the predictions of the ADC models and that the predicted soft-excess is much stronger than that seen in the observations. Independent from this work, basically the same result has also been found by Gierliński et al. (1997) and Poutanen, Krolik & Ryde (1997). We were able to verify our conclusion by unsuccessfully attempting to model hard state observations of Cyg X-1 and two other galactic black holes with the slab ADC spectra.

We were also able to find a possible geometry that can reproduce the observed spectra. The sphere+disk geometry or similar geometries with a reduced covering fraction have less reprocessing and therefore less Compton cooling. As a result the coronal temperatures are high enough to produce the observed spectra and the Compton reflection features from this geometry are much weaker than those for the slab geometry. A further advantage of the sphere+disk geometry is that it appears to fit within the framework of currently discussed models on the soft to hard state transitions (Esin et al. 1998; Poutanen, Krolik & Ryde 1997).

Finally, I've presented results from the first year of the monitoring of LMC X-1 and LMC X-3. These preliminary results appear to put constraints on the mechanisms triggering the long term variability in soft-state black holes, although much more data is necessary to be able to quantify these constraints.

What will the future bring? In many places new questions have arisen from the computations and the observations presented here. This work started out in a different direction and has subsequently evolved – science just is not a linear process. From the results presented here, however, at least the rough direction of our work for the next couple of years appears to be set.

We will continue the analysis of broad-band data from Cyg X-1. To study transient dips in the system we have been awarded  $4 \times 20$  ksec of RXTE time. The dips are thought to be caused by material from the accretion stream, moving into our line of sight and photo absorbing the radiation from the black hole (Kitamoto et al. 1984; Bałucińska-Church et al. 1997). No detailed study of these dips has ever been done, and even very basic questions remain unanswered so far: What is the real cause of the dips,

clumps in the stellar wind or the accretion stream? Is there any periodicity in the dips or in substructures of the dips that could help us in understanding where the dipping material is situated? What is the ionization state of the absorbing material? A side-effect of this plan is that we realized that the ephemeris of the BH is outdated. We will therefore attempt to redetermine the ephemeris using optical spectroscopy.

Since not all of our planned observations will be successful in the sense that they contain dips, the non-dip observations will be used to further refine the ADC models. A first observation, made in 1997 December, has already been briefly looked at. The observation did not contain any dip so that a PCA spectrum with a very high signal to noise ratio could be extracted from the data. The analysis of these data shows that the observation presented in chapter 5 is indeed special, in the sense that the spectrum is softer than that usually observed (but still too hard for the slab ADC models). This might be an indication that the hard-state had not yet been completely settled down when our first observation was done. Note, however, that this harder spectrum does not change the claim that the accretion geometry in the system is not a pure slab – all slab spectra are much softer! We will also look at X-ray data from the black hole GX 339-4 in its hard state, which is very similar to Cyg X-1. This will further increase the number of black holes of which the coronal parameters are known, perhaps enabling us in a few years to understand what determines the coronal parameters. We will also look at the temporal behavior of Cyg X-1 and GX 339-4 in greater detail, using the Compton shots presented here to get a handle on the system parameters like its size.

For the LMC black holes, the monitoring campaign is going on into its second year. Furthermore, other pointings on these sources will become public during 1998. These data will be subjected to an analysis analogous to that presented in chapter 6. Since the light curve of LMC X-3 appeared special over all of our campaign, these two additional years of data should help in defining whether it was really “special” or whether this object is just changing its appearance in weird ways. Three years of data should also be enough to define a new period, if any, for LMC X-3, and to perform a systematic search for QPOs in LMC X-1, such as the one seen previously by *Ginga*. With the new pointings on LMC X-1 and hopefully a finally converged response matrix and background model, it will also be possible to decide whether this object is really as quiet as I have claimed, or whether there are subtle spectral changes that have been overlooked in the rough analysis performed here. Finally, for the long observations of both objects grids of Comptonization models will be computed that better describe the transitional regime between the soft excess and the power-law component in the spectrum.

Looking at the questions of chapter 1, i.e., what constitutes a black hole and are there any spectral signatures that could be used to decide whether a black hole candidate is a black hole, we have obtained 30 ksec of RXTE data of the black hole candidate V1408 Aql (1957+115), an object that has been in the lists of possible black holes since 1984 but has never been subjected to a detailed broad band analysis. Data presented by Yaqoob, Ebisawa & Mitsuda (1993) lead these authors to the conclusion that the object is a neutron star, but the final word on this question has not yet been spoken.

For massive black holes, like those in the centers of radio quiet AGN, Comptonization



is one of the physical processes that has been invoked for a long time. The spectra of radio quiet AGN appear to be explainable with slab-geometry models, but an application of our models to these data is necessary and very important. Results from a study of the temporal behavior of these sources with the LSSM show that the characteristic time scale of these systems is correlated with the spectral hardness (König, Staubert & Wilms 1997). This behavior can be explained with the Compton shots of section 2.3, but it is not yet clear whether the coronal parameters inferred from the timing models and those inferred from spectral fitting really do agree.

From a programming point of view, the NLMC code will continue to be developed. Physical processes not yet fully included in the code are bremsstrahlung emission and other effects from magnetic fields. Although the inclusion of slightly ionized material is possible in the code, no self-consistent computation of the ionization structure of the material is possible right now. Nayakshin & Melia (1997) have shown that the slab geometry *might* be able to reproduce the observed hard-state BH spectra if an ionized transition layer is put between the cold disk and the corona. The effect of this layer is to reduce the amount of reprocessing, so that the cooling rate of the corona is reduced. The result is that higher coronal temperatures are possible. A self-consistent implementation of this effect is necessary to see whether the reduction of the amount of reprocessing is sufficient to allow coronal temperatures on the order of those observed in the hard-state. We are planning on doing such a simulation in the near future.

## Bibliography

---

- Aab, O.É., Bychkova, L.V., Kopylov, I.M., Kumaigo-rodskaya, R.N., 1984, *Sov. Astron.*, 28, 90 (orig.: *Astron. Zh.*, 61, 152, 1984)
- Abramowicz, M.A., Chen, X.M., Granath, M., Lasota, J.P., 1996, *ApJ*, 471, 762
- Akhiezer, A.I., Berestetskii, V.B., 1965, *Quantum Electrodynamics*, New York: Interscience
- Akritas, M.G., 1997, *Statistical Consulting Center for Astronomy*, available at [http://www.stat.psu.edu/scca/q\\_and\\_a](http://www.stat.psu.edu/scca/q_and_a)
- Allen, C.W., 1973, *Astrophysical Quantities*, London: Athlone, 3<sup>rd</sup> edition
- Anders, E., Grevesse, N., 1989, *Geochim. Cosmochim. Acta*, 53, 197
- Arnaud, K.A., 1996, in J.H. Jacoby, J. Barnes (eds.), *Astronomical Data Analysis Software and Systems V*, *Astron. Soc. Pacific, Conf. Ser.* 101, San Francisco: *Astron. Soc. Pacific*, 17
- Bałucińska-Church, M., Belloni, T., Church, M.J., Hasinger, G., 1995, *A&A*, 302, L5
- Bałucińska-Church, M., Takahashi, T., Ueda, Y., et al., 1997, *ApJ*, 480, L115
- Bałucińska, M., Hasinger, G., 1991, *A&A*, 241, 439
- Baade, W., Zwicky, F., 1934, *Phys. Rep.*, 45, 138
- Balbus, S.A., Hawley, J.F., 1991, *ApJ*, 376, 214
- Balbus, S.A., Hawley, J.F., 1996, *ApJ*, 467, 76
- Balog, N.I., Goncharkii, A.V., Cherepashchuk, A.M., 1981, *Sov. Astron. Lett.*, 7, 336 (orig.: *Pis'ma Astron. Zh.*, 7, 605, 1981)
- Band, I.M., Trzhaskovskaya, M.B., Verner, D.A., Yakovlev, D.G., 1990, *A&A*, 237, 267
- Barr, P., White, N.E., Page, C.G., 1985, *MNRAS*, 216, 65p
- Barret, D., McClintock, J.E., Grindlay, J.E., 1996, *ApJ*, 473, 963
- Barret, D., Mereghetti, S., Roques, J.P., et al., 1991, *ApJ*, 371, L21
- Bearden, J.A., 1967, *Rev. Mod. Phys.*, 39, 78
- Begelman, M.C., Rees, M., 1996, *Gravity's Fatal Attraction: Black Holes in the Universe*, Scientific American Library, New York: Scientific American
- Belloni, T., Hasinger, G., 1990a, *A&A*, 230, 103
- Belloni, T., Hasinger, G., 1990b, *A&A*, 227, L33
- Berestetzki, W.B., Lifschitz, E.M., Pitajewski, L.P., 1989, *Quantenelektrodynamik, Lehrbuch der Theoretischen Physik* 4, Berlin: Akademie-Verlag, 6. edition
- Bevington, P.R., Robinson, D.K., 1992, *Data Reduction and Error Analysis for the Physical Sciences*, New York: McGraw-Hill, 2<sup>nd</sup> edition
- Bianchi, L., Pakull, M., 1985, *A&A*, 146, 242
- Blissett, R.J., Cruise, A.M., 1979, *MNRAS*, 186, 45
- Bochkarëv, N.G., Karitskaya, E.A., Luskutov, V.M., Sokolov, V.V., 1986, *Sov. Astron.*, 30, 43 (orig.: *Astron. Zh.*, 63, 71, 1986)
- Borkus, V.V., Kaniovsky, A.S., Efremov, V.V., et al., 1995, *Astron. Lett.*, 21, 794 (orig.: *Pis'ma Astron. Zh.*, 21, 883, 1995)
- Bowyer, S., Byram, E.T., Chubb, T.A., Friedman, H., 1965, *Science*, 147, 394
- Bradt, H., 1983, *Adv. Space Res.*, 2, 315
- Bradt, H.V., Swank, J.H., Rothschild, R.E., 1990, *Adv. Space Res.*, 10, (2)297
- Bradt, H.V., Swank, J.H., Rothschild, R.E., 1991, *Adv. Space Res.*, 11, (8)243
- Brockwell, P.J., Davis, R.A., 1991, *Time Series: Theory and Methods*, Springer Series in Statistics, New York, Berlin: Springer, 2<sup>nd</sup> edition
- Brown, W.K., Wohletz, K.H., 1995, *J. Appl. Phys.*, 78, 2758
- Burke, D.L., Field, R.C., Horton-Smith, G., et al., 1997, *Phys. Rev. Lett.*, 79, 1626
- Cannizzo, J.K., 1996, *Mem. Soc. Astron. Ital.*, 67, 269
- Cash, W., 1979, *ApJ*, 228, 939
- Chakrabarti, S.K., Titarchuk, L.G., 1995, *ApJ*, 455, 623
- Chandrasekhar, S., 1931a, *Phil. Mag.*, 11, 592
- Chandrasekhar, S., 1931b, *ApJ*, 74, 81
- Coppi, P.S., 1992, *MNRAS*, 258, 657
- Cowley, A.P., 1992, *Ann. Rev. Astron. Astrophys.*, 30, 287
- Cowley, A.P., Crampton, D., Hutchings, J.B., 1978, *AJ*, 83, 1619
- Cowley, A.P., Crampton, D., Hutchings, J.B., et al., 1983, *ApJ*, 272, 118
- Cowley, A.P., Schmidtke, P.C., Anderson, A.L., McGrath, T.K., 1995, *PASP*, 107, 145
- Cowley, A.P., Schmidtke, P.C., Ebisawa, K., et al., 1991, *ApJ*, 381, 526
- Cowley, A.P., Schmidtke, P.C., Hutchings, J.B., Crampton, D., 1994, *ApJ*, 429, 826
- Cui, W., Heindl, W.A., Rothschild, R.E., et al., 1997a, *ApJ*, 474, L57

- Cui, W., Zhang, S.N., Focke, W., Swank, J.H., 1997b, *ApJ*, 484, 383
- Deeter, J.E., Boynton, P.E., 1982, *ApJ*, 261, 337
- Dermer, C.D., Strickman, M.S., Kurfess, J.D., (eds.) 1997, *Proc. 4th Compton Symposium*, AIP Conf. Proc. 410, Woodbury: AIP
- Diem, K., Lentner, C., (eds.) 1970, *Geigy Scientific Tables*, Basel, Ardsley: Ciba-Geigy, 7<sup>th</sup> edition
- Döbereiner, S., Englhauser, J., Pietsch, W., et al., 1995, *A&A*, 302, 115
- Döbereiner, S., Maisack, M., Englhauser, J., et al., 1994, *A&A*, 287, 105
- Dolan, J.F., 1992, *ApJ*, 384, 249
- Done, C., Mulchaey, J.S., Mushotzky, R.F., Arnaud, K.A., 1992, *ApJ*, 395, 275
- Doty, J.P., 1994, *The All Sky Monitor for the X-ray Timing Explorer*, Technical report, Massachusetts Institute of Technology, available at <http://space.mit.edu/XTE/XTE.html>
- Dove, J.B., 1997, *Self Consistent Accretion Disk Corona Models: Application to Black Hole Candidates*, Ph.D. thesis, University of Colorado, Boulder
- Dove, J.B., Wilms, J., Begelman, M.C., 1997, *ApJ*, 487, 747
- Dove, J.B., Wilms, J., Maisack, M.G., Begelman, M.C., 1997, *ApJ*, 487, 759
- Ebisawa, K., 1991, Ph.D. thesis, University of Tokyo, quoted by Schlegel et al. (1994)
- Ebisawa, K., Makino, F., Mitsuda, K., et al., 1993, *ApJ*, 403, 684
- Ebisawa, K., Mitsuda, K., Hanawa, T., 1991, *ApJ*, 367, 213
- Ebisawa, K., Mitsuda, K., Inoue, H., 1989, *Publ. Astron. Soc. Jpn.*, 41, 519
- Ebisawa, K., Ueda, Y., Inoue, H., et al., 1996, *ApJ*, 467, 419
- Einstein, A., 1916, *Ann. Phys. (Leipzig)*, 49, 769
- ESA (ed.) 1997, *The Hipparcos and Tycho Catalogues*, ESA SP 1200, Noordwijk: ESA Publications Division
- Esin, A.A., McClintock, J.E., Narayan, R., 1997, *ApJ*, 489, 865
- Esin, A.A., Narayan, R., Cui, W., et al., 1998, *ApJ*, in press
- Esin, A.A., Narayan, R., Ostriker, E.C., Yi, I., 1996, *ApJ*, 465, 327
- Evans, R.D., 1958, in S. Flügge (ed.), *Korpuskeln und Strahlung in Materie*, Vol. II, *Handbuch der Physik* XXXIV, Berlin, Göttingen: Springer, 218
- Fabian, A., 1997, *Astron. Geophys.*, 38, 10
- Fabian, A.C., 1994, *ApJ Suppl.*, 92, 555
- Fabian, A.C., Barcons, X., 1992, *Ann. Rev. Astron. Astrophys.*, 30, 492
- Fabian, A.C., Blandford, R.D., Guilbert, P.W., et al., 1986, *MNRAS*, 221, 931
- Fabian, A.C., Nandra, K., Reynolds, C.S., et al., 1995, *MNRAS*, 277, L11
- Felten, J.E., Rees, M.J., 1972, *A&A*, 17, 226
- Field, G.B., Rogers, R.D., 1993, *ApJ*, 403, 94
- Ford, H.C., Zsvetanov, Z.I., Ferrarese, L., Jaffe, W., 1997, in *The Central Regions of the Galaxy and Galaxies*, IAU Symp. 184, Dordrecht: Kluwer, in press
- Frank, J., King, A., Raine, D., 1992, *Accretion Power in Astrophysics*, Cambridge: Cambridge Univ. Press, 2<sup>nd</sup> edition
- Franke, R., Nielson, G.M., 1991, in H. Hagen, D. Roller (eds.), *Geometric Modeling: Methods and Applications*, Berlin, Heidelberg: Springer
- Galeev, A.A., Rosner, R., Vaiana, G.S., 1979, *ApJ*, 229, 318
- Gehrels, N., 1986, *ApJ*, 303, 336
- Genzel, R., Eckart, A., Ott, T., Eisenhauer, F., 1997, *A&A*, 291, 219
- George, I.M., Fabian, A.C., 1991, *MNRAS*, 249
- Gierliński, M., Zdziarski, A.A., Done, C., et al., 1997, *MNRAS*, 288, 958
- Gies, D.R., Bolton, C.T., 1982, *ApJ*, 260, 240
- Gies, D.R., Bolton, C.T., 1986, *ApJ*, 304, 304
- Górecki, A., Wilczewski, W., 1984, *Acta Astron.*, 34, 141
- Gorenstein, P., Gursky, H., Garmire, G., 1968, *ApJ*, 153, 885
- Gorshkov, V.G., Mikhaïlov, A.I., Sherman, S.G., 1973, *Sov. Phys. – JETP*, 37, 572 (orig.: *Zh. Eksp. Teor. Fiz.*, 64, 1128, 1973)
- Gran, S., 1992, *A Course in Ocean Engineering, Developments in Marine Technology* 8, Amsterdam: Elsevier
- Grebenev, S., Sunyaev, R., Pavlinsky, M., et al., 1993, *A&A Suppl.*, 97, 281
- Greenhill, L.J., Jiang, D.R., Moran, J.M., et al., 1995, *ApJ*, 40, 619
- Greenstein, G., 1983, *Frozen Star*, New York: Freundlich
- Greiner, J., Morgan, E.H., Remillard, R.A., 1996, *ApJ*, 473, L107
- Gribbin, J., Rees, M., 1990, *The Stuff of the Universe*, London: Heinemann, (reprint: London: Penguin, 1995)
- Gruber, D.E., Blanco, P.R., Heindl, W.A., et al., 1996, *A&A Suppl.*, 120, C641
- Guibas, L.J., Knuth, D.E., Sharir, M., 1992, *Algorithmica*, 7, 381
- Guilbert, P.W., Rees, M.J., 1988, *MNRAS*, 233, 475
- Haardt, F., Done, C., Matt, G., Fabian, A.C., 1993, *ApJ*, 411, L95
- Haardt, F., Maraschi, L., 1991, *ApJ*, 380, L51
- Haardt, F., Maraschi, L., 1993, *ApJ*, 413, 507
- Haardt, F., Maraschi, L., Ghisellini, G., 1994, *ApJ*, 432, L95
- Haardt, F., Maraschi, L., Ghisellini, G., 1997, *ApJ*, 476, 620
- Hawking, S.W., 1988, *A brief history of time*, Toronto, London: Bantam
- Hawking, S.W., Ellis, G.F.R., 1973, *The Large Scale Structure of Space-Time*, Cambridge: Cambridge

- Univ. Press
- Hawley, J.F., Gammie, C.F., Balbus, S.A., 1994, in G.V. Bicknell, M.A. Dopita, P.J. Quinn (eds.), *The First Stromlo Symposium: The Physics of Active Galaxies*, Astron. Soc. Pacific, Conf. Ser. 54, San Francisco: Astron. Soc. Pacific, 53
- Hehl, F.W., Kiefer, C., Metzler, R., (eds.) 1998, *Black Holes: Theory and Observation*, Lecture Notes in Physics, Berlin, Heidelberg: Springer, in press
- Henke, B.L., Lee, P., Tanaka, T.J., et al., 1982, *Atomic Data Nucl. Data Tables*, 27, 1
- Herrero, A., Kudritzki, R.P., Gabler, R., et al., 1995, *A&A*, 297, 556
- Hjellming, R.M., 1973, *ApJ*, 182, L29
- Hjellming, R.M., Rupen, M.P., 1995, *Nature*, 375, 464
- Horne, J.H., Baliunas, S.L., 1986, *ApJ*, 302, 757
- Horowitz, J., 1997, in G.J. Babu, E.D. Feigelson (eds.), *Statistical Challenges in Modern Astronomy II*, New York, Heidelberg: Springer, 254
- Hua, X.M., 1997, *Computers in Physics*, in press
- Hua, X.M., Kazanas, D., Cui, W., 1998, *ApJ*, submitted
- Hua, X.M., Kazanas, D., Titarchuk, L., 1997, *ApJ*, 482, L57
- Hua, X.M., Lingenfelter, R.E., 1992, *ApJ*, 397, 591
- Hua, X.M., Titarchuk, L., 1995, *ApJ*, 449, 188
- Hutchings, J.B., 1978, *ApJ*, 226, 264
- Hutchings, J.B., Crampton, D., Cowley, A.P., 1983, *ApJ*, 275, L43
- Hutchings, J.B., Crampton, D., Cowley, A.P., et al., 1987, *AJ*, 94, 340
- Ichimaru, S., 1977, *ApJ*, 214, 840
- Illarionov, A.F., Syunyaev, R.A., 1972, *Sov. Astron.*, 16, 45 (orig.: *Astron. Zh.*, 49, 58, 1972)
- in't Zand, J.J.M., Pan, H.C., Bleeker, J.A.M., et al., 1992, *A&A*, 266, 283
- Iwasawa, K., Fabian, A.C., Reynolds, C.S., et al., 1996, *MNRAS*, 282, 1038
- Jahoda, K., 1996, *Estimating the Background in the PCA*, Technical report, Greenbelt: NASA GSFC, version dated November 27, 1996
- Jahoda, K., et al., 1996, *BAAS*, 189, 09.06
- Jahoda, K., Swank, J.H., Giles, A.B., et al., 1997, in O.H. Siegmund (ed.), *EUV, X-Ray, and Gamma-Ray Instrumentation for Astronomy VII*, Proc. SPIE 2808, Bellingham, WA: SPIE, 59
- Jelley, J.V., 1966, *Nature*, 211, 472
- Joe, B., 1991, *Adv. Eng. Softw.*, 13, 325
- Kaastra, J.S., Mewe, R., 1993, *A&A Suppl.*, 97, 443
- Kalogera, V., Baym, G., 1996, *ApJ*, 470, L61
- Kazanas, D., Hua, X.M., Titarchuk, L., 1997, *ApJ*, 480, 735
- Kitamoto, S., Miyamoto, S., Tanaka, Y., et al., 1984, *Publ. Astron. Soc. Jpn.*, 36, 731
- Kitchin, C.R., 1984, *Astrophysical Techniques*, Bristol, Philadelphia: Adam Hilger, 1<sup>st</sup> edition
- Klein, O., Nishina, Y., 1929, *Z. Physik*, 52, 853
- König, M., 1997, *Zeitvariabilität in Aktiven Galaxien*, Dissertation, Eberhard-Karls-Universität Tübingen
- König, M., Staubert, R., Wilms, J., 1997, *A&A*, 326, L25
- König, M., Timmer, J., 1997, *A&A Suppl.*, 124, 589
- Kormendy, J., Bender, R., Magorrian, J., et al., 1997, *ApJ*, in press
- Kraft, R.P., Burrows, D.N., Nousek, J.A., 1991, *ApJ*, 374, 344
- Kretschmar, P., 1996, *Hochenergie-Röntgenspektren der akkretierenden Röntgenpulsare Vela X-1 und A 0535+26*, Dissertation, Eberhard-Karls-Universität Tübingen
- Kreykenbohm, I., 1997, *Beobachtungen von Vela X-1 mit RXTE*, Diplomarbeit, Eberhard-Karls-Universität Tübingen, Institut für Astronomie und Astrophysik
- Kreykenbohm, I., Kretschmar, P., Wilms, J., et al., 1998, *A&A*, submitted
- Kreykenbohm, I., Wilms, J., 1997, *RXTE Cheatsheet*, Technical report, Tübingen: Institut für Astronomie und Astrophysik, Abt. Astronomie
- Kroeger, R.A., Strickman, M.S., Grove, J.E., et al., 1996, *A&A Suppl.*, 120, C117
- Kurfess, J.D., 1995, *Adv. Space Res.*, 15, 103
- Kylafis, N.D., Klimis, G.S., 1987, *ApJ*, 323, 678
- Kylafis, N.D., Phinney, E.S., 1989, in Ögelman & van den Heuvel (1989), 731
- Lampton, M., Margon, B., Bowyer, S., 1976, *ApJ*, 208, 177
- Laplace, P.S., 1796, *Le Système du Monde, Vol. II. Des Mouvements Réels des Corps Célestes*, Paris
- Laplace, P.S., 1799, in *Allgemeine Geographische Ephemeriden, Vol. 4(1)*, Weimar, engl. trans. in Hawking & Ellis (1973)
- Lasota, J.P., Abramowicz, M.A., Chen, X., et al., 1996, *ApJ*, 462, 142
- Lasota, J.P., Narayan, R., Yi, I., 1996, *A&A*, 314, 813
- Leahy, D.A., Darbro, W., Elsner, R.F., et al., 1983, *ApJ*, 266, 160
- Lehto, H.J., 1989, in J. Hunt, B. Battick (eds.), *Proc. 23rd ESLAB Symposium on Two Topics in X-Ray Astronomy, Vol. 1*, ESA SP 296, Noordwijk: ESA Publications Division, 499
- Leong, C., Kellogg, K., Gursky, H., et al., 1971, *ApJ*, 170, L67
- Levine, A.M., Bradt, H., Cui, W., et al., 1996, *ApJ*, 469, L33
- Lewin, W.H.G., van Paradijs, J., van den Heuvel, E.P.J., (eds.) 1995, *X-Ray Binaries*, Cambridge Astrophysics Series 26, Cambridge: Cambridge Univ. Press
- Lewin, W.H.G., van Paradijs, J., van der Klis, M., 1988, *Space Sci. Rev.*, 46, 273
- Liang, E.P., Nolan, P.L., 1984, *Space Sci. Rev.*, 38, 353
- Lightman, A.P., Eardley, D.M., 1974, *ApJ*, 187, L1
- Lightman, A.P., Lamb, D.Q., Rybicki, G.B., 1981, *ApJ*, 248, 738
- Lightman, A.P., Rybicki, G.B., 1980, *ApJ*, 236, 928
- Lightman, A.P., White, T.R., 1988, *ApJ*, 335, 57

- Lightman, A.P., Zdziarski, A.A., 1987, *ApJ*, 319, 643
- Ling, J.C., Mahoney, W.A., Wheaton, W.A., et al., 1983, *ApJ*, 275, 307
- Lochner, J., Remillard, R., 1997, The XTE All Sky Monitor Data Products, Technical report, HEASARC/GSFC, version dated August 26, 1997
- Lochner, J.C., Swank, J.H., Szymkowiak, A.E., 1991, *ApJ*, 376, 295
- Lomb, N.R., 1976, *Ap&SS*, 39, 447
- Long, K.S., Helfand, D.J., Grabelsky, D.A., 1981, *ApJ*, 248, 925
- Longair, M.S., 1992, *High Energy Astrophysics*, Vol. 1, Cambridge: Cambridge Univ. Press, 2<sup>nd</sup> edition
- Lutz, J.H., Lutz, T.E., 1972, *AJ*, 77, 376
- Macchetto, F., Marconi, A., Axon, D.J., et al., 1997, *ApJ*, in press
- Magdziarz, P., Zdziarski, A.A., 1995, *MNRAS*, 273, 837
- Maisack, M., Johnson, W.N., Kinzer, R.L., et al., 1993, *ApJ*, 407, L61
- Makishima, K., Maejima, Y., Mitsuda, K., et al., 1986, *ApJ*, 308, 635
- Maloney, P., Begelman, M.C., 1997, *ApJ*, 491, L43
- Maloney, P.R., Begelman, M.C., Pringle, J.E., 1996, *ApJ*, 472, 582
- Marchuk, G.I., Mikhailov, G.A., Nazarialiev, M.A., et al., 1980, *The Monte Carlo Methods in Atmospheric Optics*, Springer Series in Optical Sciences 12, Berlin: Springer (transl. of Метод Монте-Карло в Атмосферной Оптике, Новосибирск: Наука, 1974)
- Marshall, F., Mushotzky, R., Petre, R., Serlemitsos, P., 1993, *ApJ*, 419, 301
- Matt, G., Fabian, A.C., Ross, R.R., 1993, *MNRAS*, 262, 179
- Matt, G., Perola, G.C., Piro, L., Stella, L., 1992, *A&A*, 257, 63 (erratum: *A&A*, 263, 453, 1992)
- Matteson, J.L., 1978, The UCSD/MIT Hard X-Ray and Low Energy Gamma-Ray Experiment for HEAO 1, AIAA 16th Aerospace Sciences Meeting, Huntsville, Alabama, January 16–18, 1978, AIAA paper 78/35
- McConnell, M., Bennett, K., Bloemen, H., et al., 1996, *A&A Suppl.*, 120, C149
- Michell, J., 1784, *Philosophical Transactions of the Royal Society of London*, 74, 35, presented 1783 November 27
- Miller, M.C., 1994, *ApJ*, 441, 770
- Mirabel, I.F., Rodríguez, L.F., 1996, in K.C. Tsinganos (ed.), *Solar and Astrophysical Magnetohydrodynamical Flows*, Dordrecht: Kluwer, 683
- Misner, C.W., Thorne, K.S., Wheeler, J.A., 1973, *Gravitation*, San Francisco: Freeman
- Mitsuda, K., Inoue, H., Koyama, K., et al., 1984, *Publ. Astron. Soc. Jpn.*, 36, 741
- Miyamoto, S., Kimura, K., Kitamoto, S., et al., 1991, *ApJ*, 383, 784
- Miyamoto, S., Kitamoto, S., Iga, S., et al., 1992, *ApJ*, 391, L21
- Miyoshi, M., Moran, J., Herrnstein, J., et al., 1995, *Nature*, 373, 127
- Nakamura, K., Osaki, Y., 1993, *Publ. Astron. Soc. Jpn.*, 45, 775
- Nandra, K., George, I.M., Mushotzky, R.F., et al., 1997, *ApJ*, 477, 602
- Nandra, K., Pounds, K.A., Steward, G.C., et al., 1991, *MNRAS*, 248, 760
- Narayan, R., 1996a, *ApJ*, 462, 136
- Narayan, R., 1996b, *ApJ*, 462, 136
- Narayan, R., Yi, I., 1995, *ApJ*, 452, 710
- NASA 1996, XTE — A Standard of Excellence, available at <http://midex.gsfc.nasa.gov/midex/xte/report.html>
- NASA 1997, Rossi X-ray Timing Explorer Guest Observer Program, Cycle 3, Technical Report NRA 97-OSS-09, Washington, DC: NASA Office of Space Science
- Nayakshin, S., Melia, F., 1997, *ApJ*, submitted
- Negoro, H., Kitamoto, S., Takeuchi, M., Mineshige, S., 1995, *ApJ*, 452, L49
- Neufeld, D.A., Maloney, P.R., 1995, *ApJ*, 447, L17
- Nikishov, A.J., 1962, *Sov. Phys. – JETP*, 14, 393
- Ninkov, Z., Walker, G.A.H., Yang, S., 1987a, *ApJ*, 321, 438
- Ninkov, Z., Walker, G.A.H., Yang, S., 1987b, *ApJ*, 321, 425
- Nolan, P.L., Gruber, D.E., Matteson, J.L., et al., 1981, *ApJ*, 246, 494
- Nousek, J.A., 1992, in E. Feigelson, G.J. Babu (eds.), *Statistical Challenges in Modern Astronomy*, New York, Heidelberg: Springer, 307
- Novikov, I., 1995, in G. Meynet, D. Schaerer (eds.), *Stellar Remnants*, Saas-Fee Advanced Course 25, Berlin, Heidelberg, New York: Springer, 237
- Novikov, I.D., 1990, *Black Holes and the Universe*, Cambridge Univ. Press (transl. of Черные дыры и Вселенная, Москва: Наука, no year)
- Novikov, I.D., Stern, B.E., 1986, in G. Giuricin, F. Mardirossian, M. Mezzetti, M. Ramella (eds.), *Structure and Evolution of Active Galactic Nuclei*, Dordrecht: Reidel, 149
- Nowak, M.A., 1995, *PASP*, 107, 1207
- Nowak, M.A., Dove, J.B., Vaughan, B.A., et al., 1998a, in L. Scarsi, H. Bradt, P. Giommi, F. Fiore (eds.), *The Active X-Ray Sky: Results from Beppo-SAX and RXTE*, *Nucl. Phys. B, Proc. Suppl.*, Amsterdam: Elsevier, in press
- Nowak, M.A., Vaughan, B.A., 1996, *MNRAS*, 280, 227
- Nowak, M.A., Vaughan, B.A., Wilms, J., et al., 1998b, *MNRAS*, in preparation
- Nowak, M.A., Wagoner, R.V., Begelman, M.C., Lehr, D.E., 1997, *ApJ*, 477, L91
- Oda, M., 1977, *Space Sci. Rev.*, 20, 757
- Oda, M., Gorenstein, P., Gursky, H., et al., 1971, *ApJ*, 166, L1
- Ögelman, H., van den Heuvel, E.P.J., (eds.) 1989,

- Timing Neutron Stars, NATO ASI C262, Dordrecht: Kluwer
- Oppenheimer, J.R., Volkoff, G.M., 1939, *Phys. Rev.*, 55, 374
- Orosz, J.A., Bailyn, C.D., 1997, *ApJ*, 477, 876, erratum: *ApJ*, 482, 1086, 1997
- Pakull, M.W., Angebault, L.P., 1986, *Nature*, 322, 511
- Papoulis, A., 1991, *Probability, random variables, and stochastic processes*, Electrical and Electronic Engineering Series, New York: McGraw-Hill, 3<sup>rd</sup> edition
- Payne, D.G., 1980, *ApJ*, 237, 951
- Philips, B.F., Jung, G.V., Leising, M.D., et al., 1996, *ApJ*, 465, 907
- Pietrini, P., Krolik, J.H., 1995, *ApJ*, 447, 526
- Pilla, R.P., Shaham, J., 1997, *ApJ*, 486, 903
- Piran, T., 1978, *ApJ*, 221, 652
- Pooley, G.G., Fender, R.P., 1997, *MNRAS*, 292, 925
- Pottschmidt, K., 1997, *Anwendung linearer Zustandsraummodelle auf die Kurzzeitvariabilität des Schwarzkandidaten Cygnus X-1*, Diplomarbeit, Eberhard-Karls-Universität Tübingen, Institut für Astronomie und Astrophysik
- Pottschmidt, K., König, M., 1997, in D. Maoz, A. Sternberg, E.M. Leibowitz (eds.), *Astronomical Time Series*, Dordrecht: Kluwer, 187
- Pottschmidt, K., König, M., Wilms, J., Staubert, R., 1998, *A&A*, in press
- Poutanen, J., 1994, *J. Quant. Spectrosc. Radiat. Transfer*, 51, 813
- Poutanen, J., Krolik, J.H., Ryde, F., 1997, *MNRAS*, 292, 121
- Poutanen, J., Svensson, R., 1996, *ApJ*, 470, 249
- Poutanen, J., Svensson, R., Stern, B., 1997, in Winkler, Courvoisier & Durouchoux (1997), 401
- Pozdnyakov, L.A., Sobol, I.M., Sunyaev, R.A., 1983, *Astrophys. Rep.*, 2, 189
- Pravdo, S.H., White, N.E., Kondo, Y., et al., 1980, *ApJ*, 237, L71
- Press, W.H., Rybicki, G.B., 1989, *ApJ*, 338, 277
- Rees, M.J., 1984, *Ann. Rev. Astron. Astrophys.*, 22, 471
- Reppin, C., Pietsch, W., Trümper, J., et al., 1983, in G.C. Perola, M. Salvati (eds.), *Non-Thermal and Very High Temperature Phenomena in X-Ray Astronomy*, Roma: Istituto Astronomico, Università "La Sapienza", 279
- Reynolds, C.S., Begelman, M.C., 1997, *ApJ*, 487, 109
- Reynolds, C.S., Fabian, A.C., Makishima, K., et al., 1994, *MNRAS*, 268, L55
- Rodríguez, L.F., Mirabel, I.F., 1995, *Proc. Natl. Acad. Sci. USA*, 92, 11390
- Ross, R., Weaver, R., McCray, R., 1978, *ApJ*, 219, 292
- Rothschild, R., Boldt, E., Holt, S., et al., 1979, *Space Sci. Inst.*, 4, 269
- Rothschild, R.E., 1997, *Developments in Hard X-Ray Astronomy: RXTE Mission and Results*, talk presented at the Golden Jubilee of the Tata Institute for Fundamental Research
- Rothschild, R.E., Blanco, P.R., Gruber, D.E., et al., 1998, *ApJ Suppl.*, in press
- Rybicki, G.B., Lightman, A.P., 1979, *Radiative Processes in Astrophysics*, New York: Wiley
- Scargle, J.D., 1981, *ApJ Suppl.*, 45, 1
- Scargle, J.D., 1982, *ApJ*, 263, 835
- Schandl, S., 1996, *A&A*, 307, 95
- Schlegel, E.M., Marshall, F.E., Mushotzky, R.F., et al., 1994, *ApJ*, 422, 243
- Schlittgen, R., Streitberg, B.H.J., 1995, *Zeitreihenanalyse*, München, Wien: Oldenbourg, 6<sup>th</sup> edition
- Schulz, N.S., Hasinger, G., Trümper, J., 1989, *A&A*, 225, 48
- Schutz, B.F., 1985, *A first course in general relativity*, Cambridge: Cambridge Univ. Press
- Schwarzschild, K., 1916, *Sitzber. Dtsch. Akad. Wiss. Berlin, Kl. Math. Phys. Tech.*, 189
- Shafer, R.A., Haberl, F., Arnaud, K.A., Tennant, A.F., 1991, *XSPEC Users Guide*, ESA, Noordwijk
- Shakura, N.I., Sunyaev, R., 1973, *A&A*, 24, 337
- Shapiro, S.L., Lightman, A.P., Eardley, D., 1976, *ApJ*, 204
- Skibo, J.G., Dermer, C.D., 1995, *ApJ*, 455, L25
- Skibo, J.G., Dermer, C.D., Ramaty, R., McKinley, J.M., 1995, *ApJ*, 446, 86
- Sloan, S.W., 1987, *Adv. Eng. Softw.*, 9, 34
- Smith, A., Turner, M.J.L., 1982, *Nucl. Instrum. Meth.*, 192, 475
- Sobol, I.M., 1991, *Die Monte Carlo Methode*, Berlin: Deutscher Verlag der Wissenschaften, 4. edition (german transl. of *Метод Монте-Карло — Издание четвертое, дополненное и переработанное*, Москва: Наука, 1985), engl. transl.: *The Monte Carlo Method*, Chicago: Univ. Chicago Press, 1974
- Sokolov, V.V., 1987, *Sov. Astron.*, 31, 419 (orig.: *Astron. Zh.*, 64, 803, 1987)
- Stelzer, B., Wilms, J., Staubert, R., et al., 1998, *A&A*, submitted
- Stern, B.E., 1985, *Sov. Astron.*, 29, 306 (orig.: *Astron. Zh.*, 62, 529, 1985)
- Stern, B.E., Begelman, M.C., Sikora, M., Svensson, R., 1995a, *MNRAS*, 272, 291
- Stern, B.E., Poutanen, J., Svensson, R., et al., 1995b, *ApJ*, L13
- Stollman, G.M., Hasinger, G., Lewin, W.H.G., et al., 1987, *MNRAS*, 227, 7p
- Stone, J.M., Hawley, J.F., Gammie, C.F., Balbus, S.A., 1996, *ApJ*, 463, 656
- Strickman, M.S., Johnson, W.N., Kurfess, J.D., 1979, *AJ*, 230, L15
- Sunyaev, R., Churazov, E., 1996, *Astron. Let.*, 22, in press
- Sunyaev, R.A., Titarchuk, L.G., 1980, *A&A*, 86, 121
- Sunyaev, R.A., Titarchuk, L.G., 1985, *A&A*, 143, 374
- Sunyaev, R.A., Trümper, J., 1979, *Nature*, 279, 506
- Svensson, R., 1982, *ApJ*, 258, 335
- Svensson, R., 1987, *MNRAS*, 227, 403
- Svensson, R., 1997, *Conference Summary*, Iceland

- Conference on Accretion Disks, Reykjavik
- Syunyaev, R.A., Gil'fanov, M., Churazov, E., et al., 1990, *Sov. Astron. Lett.*, 16, 55 (orig.: *Pis'ma Astron. Zh.*, 16, 124, 1990)
- Tanaka, Y., Lewin, W.H.G., 1995, in Lewin, van Paradijs & van den Heuvel (1995), Ch. 3, 126
- Tanaka, Y., Nandra, K., Fabian, A.C., et al., 1995, *Nature*, 375, 659
- Tanaka, Y., Shibasaki, N., 1996, *Ann. Rev. Astron. Astrophys.*, 34, 607
- Thorne, K.S., 1994, *Black Holes and Time Warps*, New York, London: Norton
- Thorne, K.S., Price, R.H., 1975, *ApJ*, 195, L101
- Titarchuk, L., 1994, *ApJ*, 434, 570
- Titarchuk, L., Hua, X.M., 1995, *ApJ*, 452, 226
- Toor, A., Seward, F.D., 1974, *AJ*, 79, 995
- Treves, A., Belloni, T., Chiapetti, L., et al., 1988, *ApJ*, 325, 119
- Treves, A., Belloni, T., Corbet, R.H.D., et al., 1990, *ApJ*, 364, 266
- Treves, A., Chiapetti, L., Tanzi, E.G., et al., 1980, *ApJ*, 242, 1114
- Turner, M.J.L., Thomas, H.D., Patchett, B.E., et al., 1989, *Publ. Astron. Soc. Jpn.*, 41, 345
- Turon, C., Cr  z  , M., Egret, D., et al., 1992, *The Hipparcos Input Catalogue*, ESA-SP 1136, Noordwijk: ESA Publications Division
- van der Klis, M., 1989, in   gelman & van den Heuvel (1989), 27
- van der Klis, M., 1994, *ApJ Suppl.*, 92, 511
- van der Klis, M., 1995, in Lewin, van Paradijs & van den Heuvel (1995), Ch. 6, 252
- van der Klis, M., Tjemkes, S., van Paradijs, J., 1983, *A&A*, 126, 265
- Vaughan, B.A., Nowak, M.A., 1997, *ApJ*, 474, L43
- Verner, D.A., Yakovlev, D.G., 1995, *A&A Suppl.*, 109, 125
- Verner, D.A., Yakovlev, D.G., Band, I.M., Trzhaskovskaya, M.B., 1993, *Atomic Data Nucl. Data Tables*, 55, 233
- Walborn, N.R., 1973, *ApJ*, 179, L123
- Weibull, W., 1939, *A Statistical Theory of the Strength of Materials*, Ingenior Ventenskaps Akademien Handlingar 151, Stockholm: Generalstabens Litografiska Anstalts F  rlag
- Whalen, T.M., 1996, *Probabilistic Estimates of Design Load Factors for Wind-Sensitive Structures Using the "Peaks Over Threshold" Approach*, National Institute of Standards and Technology: Technical Report 1418, Washington: U.S. Government Printing Office
- Wheeler, J.A., 1968, *Am. Sci.*, 56, 1
- Wheeler, J.C., 1996, in *Festschrift Igor Novikov*
- White, N.E., Marshall, F.E., 1984, *apj*, 281, 354
- White, T.R., Lightman, A.P., Zdziarski, A.A., 1988, *ApJ*, 331, 939
- Wijers, R.A.M.J., van Paradijs, J., Lewin, W.H.G., 1987, *MNRAS*, 228, 17p
- Will, C.M., 1993, *Theory and Experiment in Gravitational Physics*, Cambridge: Cambridge Univ. Press, 2<sup>nd</sup> edition
- Wilms, J., 1996, *Reprozessierung von R  ntgenstrahlung in galaktischen und extragalaktischen R  ntgenquellen*, Diplomarbeit, Eberhard-Karls-Universit  t T  bingen, Institut f  r Astronomie und Astrophysik
- Wilms, J., Dove, J., Nowak, M.A., Vaughan, B., 1997a, in Dermer, Strickman & Kurfess (1997), 849
- Wilms, J., Dove, J., Staubert, R., Begelman, M.C., 1997b, in Winkler, Courvoisier & Durouchoux (1997), 233
- Wilms, J., Dove, J.B., Maisack, M., Staubert, R., 1996, *A&A Suppl.*, 120, C159
- Wilms, J., Speith, R., Reynolds, C.S., 1998, in Hehl, Kiefer & Metzler (1998), in press
- Winkler, C., Courvoisier, T.J.L., Durouchoux, P., (eds.) 1997, *The Transparent Universe*, ESA SP 382, Noordwijk: ESA Publications Division
- Wu, C.C., Eaton, J.A., Holm, A.V., et al., 1982, *PASP*, 94, 149
- Yaqoob, T., Ebisawa, K., Mitsuda, K., 1993, *MNRAS*, 264, 411
- Zdziarski, A.A., 1980, *Acta Astron.*, 30, 371
- Zdziarski, A.A., 1985, *ApJ*, 289, 514
- Zdziarski, A.A., 1986, *ApJ*, 303, 94
- Zdziarski, A.A., Coppi, P.S., Lamb, D.Q., 1990, *ApJ*, 357, 149
- Zhang, S.N., Mirabel, I.F., Harmon, B.A., et al., 1997, in Dermer, Strickman & Kurfess (1997), 141
- Zhang, W., Giles, A.B., Jahoda, K., et al., 1993, in O.H. Siegmund (ed.), *EUV, X-Ray, and Gamma-Ray Instrumentation for Astronomy IV*, Proc. SPIE 2006, Bellingham, WA: SPIE, 324
- Zhang, W., Jahoda, K., 1996, *Deadtime Effects in the PCA*, Technical report, Greenbelt: NASA GSFC, version dated 1996 September 26
- Zhang, W., Jahoda, K., Swank, J.H., et al., 1995, *ApJ*, 449, 930
- Zombeck, M.V., 1990, *Handbook of Space Astronomy and Astrophysics*, Cambridge: Cambridge Univ. Press, 2<sup>nd</sup> edition

## APPENDIX A

---

### Numerical Methods

The major results presented here were computed using different types of MC codes that are described in greater detail in this appendix. To introduce the general ideas behind the MC method, section A.1 describes the simpler linear MC code which was used, e.g., to compute the time lags of section 2.3 and the reflection features presented in section 2.1.3. In the second section, section A.2, these ideas are expanded in a general description of the NLMC code used for the simulation of the ADC spectra.

#### A.1 Linear Monte Carlo Codes

In the linear MC method, photons are propagated one at a time through a medium with predefined properties. These methods are therefore restricted to the computation of spectra for models where self-consistency is not required. In this case, linear MC codes are to be preferred over the non-linear ones because they are far less CPU intensive. The general procedures applied in a linear MC code are best described by looking at the general structure of such a code (Wilms 1996):

- Generate a photon with an energy drawn from the spectrum of the seed photons, at a certain position and moving in a certain initial direction.
- Generate the distance which the photon is allowed to move, making use of the fact that the probability of a photon to travel an optical depth  $\tau$  is given by  $\exp -\tau$ . This optical depth is translated into a physical length using the scattering cross section  $\sigma$  and the particle density  $n$  of the scattering material:  $l = \tau/n\sigma$ . Here  $\sigma$  is the total cross-section for photo absorption and Compton scattering.
- Decide from the Klein-Nishina cross section,  $\sigma_{\text{es}}$ , and the photoabsorption cross-section,  $\sigma_{\text{bf}}$ , whether the photon is photo absorbed or Compton scattered: the probability for Compton scattering is given by the ratio of the cross sections  $P_{\text{es}} = \sigma_{\text{es}}/(\sigma_{\text{es}} + \sigma_{\text{bf}})$ . If  $\alpha$  is a uniformly on  $[0, 1]$  distributed random number, then the photon will Compton scatter if  $\alpha < P_{\text{es}}$ .
- Simulate the scattering event: either, Compton scattering is simulated using the correct micro-physics, or the photon gets photoabsorbed. If the photon gets absorbed, there is a certain probability that the photon will get reemitted as a fluorescent photon. This probability is given by the fluorescence yield. If the photon is not reemitted, it is killed.
- Simulate the next step.



For low energy photons, the probability that a photon is photoabsorbed is very large so that most photons propagated using such a MC code never escape the system. Furthermore, for low Compton optical depths, the probability that escaping photons have undergone many Compton scatterings is very small. Thus, for low optical depths a very large amount of CPU time would be required to obtain good statistics in the high Compton scattering orders. This is obviously not desirable since the larger scattering orders determine the shape of the spectrum for the astronomical objects that are to be described.

To avoid these shortcomings, the “method of weights” is used. For astrophysical applications this method is extensively described by Pozdnyakov, Sobol & Sunyaev (1983, and references therein), Górecki & Wilczewski (1984), and White, Lightman & Zdziarski (1988). The basic idea behind the method of weights is that the particle propagated in the code is not considered a “real” photon but represents the statistical property that the photon still exists. This statistical property is characterized by the statistical weight  $w$  of the propagated “particle”. The advantage of this paradigm change of not simulating “real” photons but “virtual” photons is that they do not get killed so that all simulated paths contribute to the output spectrum.

In the normal propagation step, use is made of the trivial fact that the probability that a photon escapes without further scatterings is  $P = \exp(-\tau)$  where  $\tau$  is the optical depth to the boundary of the system. Before propagating the particle, the weight  $w \exp(-\tau)$  is added to the output-spectrum. The rest of the particle, with weight  $w(1 - \exp(-\tau))$ , continues to scatter within the corona, i.e., the distance the particle is propagated is simulated under the constraint that it does not leave the system. Obviously, very long path lengths within the corona can be obtained this way. Since the weight of the photon is reduced before each propagation step, its weight can get very small in time and does not contribute appreciably to the output spectrum anymore. Thus, if the particle weight goes below a certain threshold, the particle is killed. For the simulations presented here the threshold was typically taken to be  $10^{-6}$  or smaller. Therefore the photon particle is killed if its weight goes below a threshold, which I have usually taken to be  $10^{-6}$  of its “fresh” weight. The use of the method of weights for obtaining good statistics for the higher scattering orders is called “particle-escape weighting” by Pozdnyakov, Sobol & Sunyaev (1983).

It is also advantageous to use the method of weights when the photon is photoabsorbed. In the method of weights, the particle gets re-emitted after the absorption with a new weight given by  $Yw$ , where  $Y$  is the fluorescence yield of the absorbing element and  $w$  is the weight of the photon before the absorption. The energy of the particle is set to the fluorescence energy of the fluorescence line. Pozdnyakov, Sobol & Sunyaev (1983) call this use of the method of weights “absorption weighting”. For algorithms and many more examples on the use of the method see the references given above, as well as the books by Marchuk et al. (1980) and Sobol (1991). Algorithms for the computation of the mean free path in the case of an inhomogeneous medium are given by Hua (1997).

The linear MC code used in this thesis was programmed from scratch using the ideas above. Compton-scattering is simulated using relativistic formulae and using the differential Klein-Nishina cross section in the computation of the scattering angle. The electrons are assumed to have a relativistic Maxwellian distribution, the effect of which is taken into account in the simulation of the Compton scattering and in the simulation of the mean free path of the photon. Atomic processes are simulated using the fits to the photoabsorption cross sections for the elements from Hydrogen to Zinc given by Verner & Yakovlev (1995), Verner et al. (1993), and Band et al. (1990), as well as the theoretical fluorescence yields published by Kaastra & Mewe (1993). For the simulations described here, fluorescent emission of the Fe  $K\alpha$  (6.4 keV), Fe  $K\beta$  (7 keV), Si  $K\alpha$  (1.7 keV), and S  $K\alpha$  (2.3 keV), lines was included.

The computation of the spectrum and time-lags emerging from the sphere+disk geometry (section 2.3) is complicated by the interaction between the sphere and the disk. Photons leaving the sphere can hit the disk and *vice versa*, while the code is only able to deal with one photon at a time. These photons are put on a stack and dealt with after the weight of the original particle is small enough that it needs not be followed anymore. Photons hitting the accretion disk deposit part of their initial energy  $wE$  within the disk, while another part leaves the disk in the form of reflected photons. To ensure energy conservation, record is kept of the latter amount of energy. When the statistical weight of the reflecting particle is so small that the particle is killed, the energy not reflected from the disk is emitted as thermal photons. This approach of using a photon stack to ensure that all of the primary photon finally leaves the system only works if the model simulated is self consistent: if the corona is too hot, then the stack grows without bounds until the memory is full and the code crashes.

## A.2 Non-Linear Monte Carlo Codes

### A.2.1 Introduction

Contrary to the linear MC codes, in the NLMC methods *all* interactions between the medium and the radiation are taken into account. Thus a NLMC code can be used when the computation of self-consistent models is desired.

The NLMC method is a standard method outside of astrophysics, where it can be used in many engineering applications. For the purposes of simulating accretion disk coronae, the NLMC method was first used in astrophysics by Boris Stern, who also provided the basis for the code used in this thesis. Earlier descriptions of the code have been given by Stern (1985), Novikov & Stern (1986), and Stern et al. (1995b), while the version that is the basis for our work has been described by Stern et al. (1995a). The modifications made for our purposes have been discussed by Dove, Wilms & Begelman (1997), Dove et al. (1997), and Wilms et al. (1997b). A very thorough description of the ideas behind the code and a user's manual to the code is given in the appendix to Jim Dove's thesis (Dove 1997), allowing me to present just a short description of the major ideas behind the code.

The major challenge faced in the simulation of a self-consistent high energy plasma is the large range of energies of the photons and other particles. For a correct simulation, several orders of magnitude of photon energy have to be covered with the code. If this is to be done in parallel, then the “easy” application of the method of weights described above is not sufficient, since the code would be forced to spend a large amount of time in the simulation of many low energy particles. A much better approach is to sample the energy spectra of the particles dealt with in such a way that the number-density of simulated particles is constant over the whole energy range. Obviously this means that each particle within the NLMC code represents a different number of real particles. Extending the idea of weights to cover this problem, Boris Stern invented the concept of the Large Particle (LP). Basically, a LP corresponds to the “photon with weight” described in the previous section, i.e., each photon has a certain energy  $E$  and an energy dependent weight  $w(E)$ , which is chosen such that the number density of LPs is approximately constant with energy. The statistical weight can be thought to be proportional to the number of real particles that are represented by the LP.

To compute the physical properties of the medium, all LPs are allowed to interact with each other. For example, there are electron-LPs that represent the electron plasma. Summing over the number density of electron-LPs gives the total optical depth of the plasma, and Comptonization is dealt with by the interaction of photon LPs with electron LPs. Similarly, the pair production process is represented by the interaction of two photon LPs, while its inverse is implemented as the collision between an electron LP and a positron LP. Due to the Monte Carlo character of the method, it is easy to implement these processes, since the microphysics of the interaction of individual particles is well known. Although the implementation of the microphysics is quite easy, it is complicated by the fact that the statistical weights of the interacting particles represent different numbers of real particles. Therefore, not all particles represented by the LPs can take part in the collision. A consequence of this is that each interaction requires the elimination or creation of new LPs such that energy, momentum, and particle number are conserved in a statistical sense. To ensure that the total number of particles does not grow over all bounds, programming techniques have to be developed to stochastically “destroy” LPs without changing the properties of the physical system simulated. For the details of these techniques cf. Stern et al. (1995a). Since each LP sees all the other LPs as the “background” through which it is propagated, the time step on which the properties of the LP distribution are updated has to be chosen such that the system does not change appreciably over the propagation step. In our simulations the time step for the propagation was chosen such that  $\lesssim 5\%$  of the particles undergo an interaction. While each LP propagates the properties of the system are determined from the state of the system at the end of the previous time step. All properties are updated after the last LP has been propagated.

### A.2.2 Thermal Pools

The major modification of our version of the NLMC code to that described by Stern et al. (1995a) is the implementation of thermal pools. For our thermal accretion disk models it is not necessary to treat all electrons and positrons as LPs since they can be assumed to be thermalized. It is better to use an electron and a positron “reservoir”, or “thermal pool” instead of spending all the computer time on propagating particles which are known to come from a Maxwellian distribution. The volume simulated is split into spatial cells that are chosen such that the physical properties of the cell (e.g., the temperature) can be assumed to be uniform. The temperature of the electron and the positron pool are assumed to be equal to the local temperature of the cell. Each time a photon interacts with an electron (or positron), an electron LP is drawn from the thermal pool using a relativistic Maxwellian distribution for its energy. Then the interaction of the particles is simulated. Depending on the final electron energy the new electron is put back into the pool, or, if the electron energy is larger than a preset cutoff energy, the electron stays “free” as an electron LP. Alternately, after an electron or positron LP interaction or following a pair production event, the electron or positron is inserted into the pool if its energy is less than the cutoff energy. Once an LP is inserted into the pool, its identity is lost, but the pool gains a statistical weight and an energy equal to the LP. After the time step, these changes in energy of the pool are used to determine the new temperature of the pool, by balancing the energy losses (=cooling) with the energy gain from newly created electrons and from the (unspecified) heating source. The use of thermal pools makes the computation much more efficient because it is not necessary to simulate all low energy particle interactions within the pool. These low energy interactions always result in thermalization of the particles so that it is not necessary to simulate them explicitly. See Dove, Wilms & Begelman (1997) for a technical description of the pools.

### A.2.3 Statistical Fluctuations

Due to statistical fluctuations that arise from using a finite number of LPs in the simulations (currently 65 536), the Compton cooling and pair production rates vary between iterations. The result are large temperature and opacity oscillations. Due to the the strong coupling between the temperature and the opacity of the corona, intrinsic fluctuations in the temperature leads to fluctuations in the opacity (and vice versa). These oscillations can lead to an escaping photon spectrum that differs from that of a “steady-state” model, even if the two models have the same “time-averaged” properties. In order to reduce the magnitude of the fluctuations, the temperature of each electron or positron pool is averaged over the previous four iterations. Averaging over a larger number of steps leads to overstable oscillations in both the temperature and pair opacity because the corona cannot adjust to changes in the radiation field quickly enough, causing it to overshoot its equilibrium values. An additional improvement is made by averaging the opacity over the previous ten iterations. This averaging still allows for the correct annihilation and pair production rates, when averaged over all the iterations, and therefore

does not alter the equilibrium pair opacity values. Occasionally, even when averaging, severe fluctuations will cause significant temperature changes. We prevent this occurrence by artificially preventing the temperature of the pool to change by more than 10% between iterations. When the system is in equilibrium, the fluctuations of the cooling rates are symmetric around the equilibrium values. Thus, even though energy is not conserved in the iterations where large temperature changes are artificially prohibited, the energy of the system is conserved in a statistical or “time-averaged” sense.

An additional source of statistical fluctuations of the pool properties is due to unlikely LP–pool interactions. For example, there is a very small probability that a Compton-scattered photon gives all of its energy to a “pool-electron” particle, causing the particle to be ejected from the pool as discussed above. For optically thin models, where the statistical weight of the electron pool is small, these ejection events can lead to large fluctuations in the opacity. In order to reduce the magnitude of these fluctuations, LPs that interact with a pool are “split” into  $N$  mini-LPs, where the mini-LPs have a statistical weight equal to  $1/N$  of the original weight of the LP. Each of the mini-LPs is then propagated in the usual way, and the final state of the LP and pools is determined in a statistical sense. Numerical experiments show that  $N = 25$  allows for adequate statistics without degrading the efficiency of the code too much. For models with a total optical depth of the corona  $\tau \lesssim 0.1$ , a larger number is necessary ( $N = 50$ ).

Using the above methods, the root mean square statistical fluctuations of both the coronal temperature and the total optical depth are  $\sigma_{\text{rms}} \lesssim 5\%$  after the system has reached its steady-state equilibrium values. Note that, although the simulations are integrated in “time”, the true time dependent behavior of the simulations may not be correct since the statistical methods force the timescales for the changes in the temperature and opacity to be longer than their proper values. Thus, time dependent simulations are only meaningful on time scales longer than the time needed for the corona properties to vary smoothly. Since only steady state models are discussed here, this is not a problem. However, the transient behavior of the radiation field, arising from simulating one model by starting from the ending point of a different model, has to be disregarded. Only after the simulation has reached a steady-state the spectrum is recorded and the coronal properties are determined.

#### A.2.4 Generation of Models

In order to reduce the CPU time needed for the computation of model grids, the parameters of the corona are varied in a systematic way, by sweeping the coronal compactness parameter from its minimum to its maximum values while keeping the seed opacity fixed. After each sweep, the seed opacity is incremented. Each new simulation is started using the end-state of the previous simulation. This approach saves CPU time since the system does not have to evolve much prior to reaching an equilibrium state when compared to starting a simulation from scratch. The only caveat in producing the grid is that the relative increments in  $l_c$  should not be more than about threefold; for larger increments, the system is unable to smoothly evolve to the new equilibrium solution

since the transitional behavior will heavily disturb the system. We have verified that the results presented here are independent of the order in which the grid is produced i.e., there is no hysteresis.

## APPENDIX B

---

### Interpolation of Gridded Spectra

#### *B.1 Introduction*

One of the advantages of the popular X-ray fitting package XSPEC is that it is very easily extended with new spectral models. The most straightforward way to extend XSPEC is to write a separate subroutine which returns the spectral model for the desired combination of free parameters. Such a subroutine was written, e.g., to add the new reflection subroutines to the list of available models (Magdziarz & Zdziarski 1995). This approach, however, is possible only for spectral models that are available in analytical form, which is very often not the case. To make the non-analytical models available, an additional possibility had been defined, in which the photon-fluxes of spectral models are given in tabular form as FITS files and where XSPEC interpolates between the given grid-points to obtain the desired model spectra. The current implementation of XSPEC (version 10.0), however, requires the models to be available on an regularly spaced grid of parameters. In other words, for models described by two parameters  $x$  and  $y$ , the models have to be given for all combinations  $(x_i, y_j)$  where the indices  $i$  and  $j$  describe the  $i$ th and  $j$ th parameter number (fig. B.1a). When the CPU time to compute one spectral model is high, the large coverage of the parameter space implied by this interpolation algorithm of XSPEC is not an option. A more natural approach in spectral fitting is to compute a coarse grid of models to acquire a feeling for the general behavior of the spectra and then to iteratively refine the grid spacing in regions of special interest which are, for example, defined by models that are similar to the X-ray spectrum to be studied. In this case, the final grid of models to be computed is similar to that of fig. B.1b. Since it is still desirable to be able to reuse the previously computed models, a more complicated interpolation approach needs to be used. In this appendix I describe such an interpolation algorithm, focusing on the case of two free parameters. A review on the commonly used methods for the interpolation of unevenly spaced data has been given by Franke & Nielson (1991).

#### *B.2 Finite Element Interpolation Using Delaunay Triangularization*

From the many methods available for the interpolation of unevenly spaced data we chose to use the interpolation on the linear surface defined by the corners of a triangle enclosing the desired point. This approach resembles the surface construction algorithms used

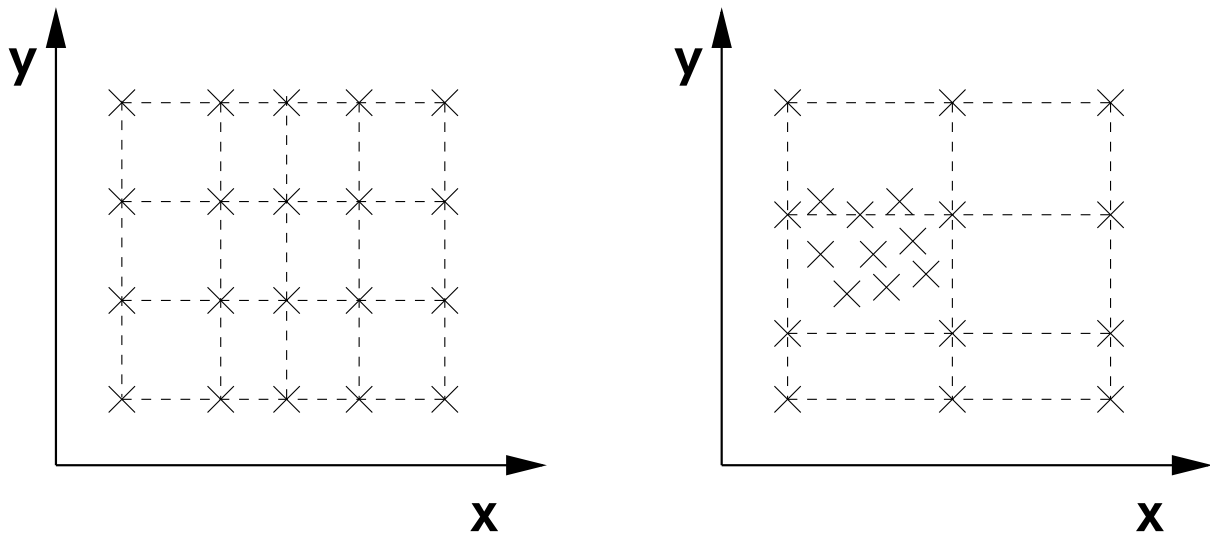


Figure B.1: Examples for parameter combinations for the case of models with two free parameters. The parameters can either form a simple regular grid (a), here sketched by the dashed lines, or they can be distributed in an arbitrary way (b), here shown as a primary grid indicated by the dashed lines plus additional spectral models that have been computed in regions of special interest, presumably since an interesting astronomical source lies in this range of parameters.

in the method of finite elements. Linear interpolation with the “triangular” approach has the advantage of being computationally very efficient while still producing a surface that closely resembles to the real surface, even though the interpolating function is not differentiable on the edges of the triangle. In practice this is not a large problem, provided that the density of the grid points is sufficiently high. It remains the question, however, how to define the triangle defining the interpolating surface.

Although this last question might look trivial at first glance, it turns out that in practice the definition of what exactly constitutes the optimum grid is a very difficult. For example, in the case of the ADC models, whether the interpolation is done with  $\tau$  and  $l_c$  or with  $\tau_{es}$  and  $T_e$  might result in different interpolated functions (Experimenting with our models resulted in us using  $\tau$  and  $l_c$ , since these are the parameters used to characterize a given model and the interpolated spectra looked best this way). More mathematically spoken it is therefore necessary to define a metric on the interpolating grid. After this metric has been decided on (in the case of the ADC models it was just possible to use the Euclidean metric in  $\tau$  and  $l_c$ , other grids might need more complicated metrics), the interpolating triangle can be defined as the most evenly looking triangle *enclosing* the parameters to be interpolated. Here, “most evenly” means that the angles of the triangle computed from the metric are as similar as possible<sup>1</sup>, i.e., that the triangle is given by the Delaunay triangularization of the set of two-dimensional points defined by the grid-points. It turns out that this definition of optimality is also advantageous in an other sense, since there exist fast algorithms for the computation of the the Delaunay trian-

<sup>1</sup>Choosing, e.g., just the three points *closest* to the desired point is not an option since this triangle might not enclose the point.



gularization and its dual, the Voronoi diagram, which can be done with an efficiency of  $\mathcal{O}(n \log n)$  using an divide-and-conquer approach (Guibas, Knuth & Sharir 1992). Moreover, it is possible to locate the triangle  $(x_i, y_i)$ ,  $i \in \{1, 2, 3\}$ , containing a given point  $(x, y)$  with an efficiency better than  $\mathcal{O}(n \log n)$  (see, e.g., Joe 1991; Guibas, Knuth & Sharir 1992; Sloan 1987, and references therein). The interpolated model  $F(x, y)$  is then given by

$$F(x, y) = a + bx + cy \quad (\text{B.1})$$

where

$$c = \frac{(z_3 - z_1)(x_2 - x_1) - (z_2 - z_1)(x_3 - x_1)}{(y_3 - y_1)(x_2 - x_1) - (y_2 - y_1)(x_3 - x_1)} \quad (\text{B.2})$$

$$b = \frac{(z_2 - z_1) - c(y_2 - y_1)}{x_2 - x_1} \quad (\text{B.3})$$

$$a = z_1 - bx_1 - cy_1 \quad (\text{B.4})$$

and where the  $z_i$  are the values of the function to be interpolated,  $z_i = F(x_i, y_i)$ . In the case where the interpolating point is situated on the line segment connecting two triangular points, interpolation is just done along this segment.

The above interpolating algorithm has been implemented into XSPEC using the Delaunay triangularization subroutines and search-routines of the library package GEOMPACK, kindly provided by Barry Joe (Joe 1991). The interfacing between the algorithm and the model points is done using an extension of the standard FITS format for XSPEC tabular models. A subroutine using the present XSPEC FITS files and “hiding” the differences between the previous grids and the current grids in FITS keywords is in preparation. Thanks to the  $\mathcal{O}(n \log n)$  property of the gridding and searching algorithms it was possible to write a program which allows the “by eye” fitting to be done interactively. The interactivity of the program is very useful in visualizing the properties of the corona and its spectra in a much better way than can be done by just providing figures since it is possible to “play” with the physical parameters and see what happens with the spectrum. The fitting of the unfolded spectrum of Cyg X-1 presented in chapter 5, Figs. 5.1 and 5.2, was done using the interactive program.

## APPENDIX C

---

### Properties of the generalized Gamma- and Weibull-Distributions

#### C.1 The Generalized Gamma Distribution

The probability density function of the generalized Gamma distribution is given by

$$P_{\Gamma}(x; \alpha, \beta, \gamma) = \begin{cases} \frac{\alpha}{\beta} \frac{1}{\Gamma(\frac{1+\gamma}{\alpha})} \left(\frac{x}{\beta}\right)^{\gamma} \exp\left(-\left(\frac{x}{\beta}\right)^{\alpha}\right) & \text{for } x > 0 \\ 0 & \text{for } x \leq 0 \end{cases} \quad (\text{C.1})$$

where

$$\Gamma(x) = \int_0^{\infty} t^{x-1} \exp(-t) dt \quad (\text{C.2})$$

is Euler's Gamma function. The generalized Gamma distribution is one of the most studied probability density functions of statistics since many of the important non-discrete density functions can be derived from  $P_{\Gamma}$ . For example,  $P_{\Gamma}(x; 2, \sqrt{2\sigma}, 0)$  is the one-sided normal distribution, and  $P_{\Gamma}(x; 1, 2, n/2 - 1)$  is the  $\chi^2$  distribution. The properties of the generalized Gamma distribution are discussed by Gran (1992, chapter 2.6) to whom the reader is referred for a more extensive discussion<sup>1</sup>.

When integrating  $x^n P_{\Gamma}(x; \alpha, \beta, \gamma)$  with respect to  $x$ , the moments of the distribution are obtained,

$$\langle x^n \rangle = \int_{-\infty}^{\infty} x^n P_{\Gamma}(x; \alpha, \beta, \gamma) dx = \beta^n \frac{\Gamma\left(\frac{\gamma+1}{\alpha} + \frac{n}{\alpha}\right)}{\Gamma\left(\frac{\gamma+1}{\alpha}\right)} \quad (\text{C.3})$$

The moments can be used to compute the mean and the variance of the distribution: The mean of  $P_{\Gamma}$  is given by

$$\langle x \rangle = \beta \frac{\Gamma\left(\frac{\gamma+2}{\alpha}\right)}{\Gamma\left(\frac{\gamma+1}{\alpha}\right)} \quad (\text{C.4})$$

---

<sup>1</sup>The notation used here is different from that used by Gran (1992). His notation can be mapped onto the notation used here by substituting  $a \rightarrow (\gamma + 1)/\alpha$ ,  $h \rightarrow \alpha$ , and  $A \rightarrow \beta$ .

while the variance is

$$\text{Var}(x) = \langle x^2 \rangle - \langle x \rangle^2 = \frac{\beta^2}{\Gamma\left(\frac{\gamma+1}{\alpha}\right)^2} \left( \Gamma\left(\frac{\gamma+3}{\alpha}\right) \Gamma\left(\frac{\gamma+1}{\alpha}\right) - \Gamma\left(\frac{\gamma+2}{\alpha}\right)^2 \right) \quad (\text{C.5})$$

Finally, by computing the maximum of  $P_\Gamma$  it is found that the most probable value of the distribution is located at

$$x_{\max} = \beta \left(\frac{\gamma}{\alpha}\right)^{1/\alpha} \quad (\text{C.6})$$

and has a value of

$$P_{\Gamma, \max} = \frac{\alpha}{\beta} \frac{1}{\Gamma\left(\frac{1+\gamma}{\alpha}\right)} \left(\frac{\gamma}{\alpha}\right)^{\gamma/\alpha} \exp\left(-\frac{\gamma}{\alpha}\right) \quad (\text{C.7})$$

Note that the generalized Gamma distribution used in chapter 2.3 was defined in a slightly different way since the Compton shots of chapter 2.3 did not start with  $x = 0$  but at  $x = x_1$  (cf. eq. 2.53). The moments of the “shifted” generalized Gamma distribution can be obtained from the moments given in eq. (C.3) by

$$\langle x^n \rangle_{\text{shifted}} = \sum_{k=0}^n \binom{n}{k} x_1^k \langle x^{n-k} \rangle_{\text{unshifted}} \quad (\text{C.8})$$

The resulting expression for the variance of the “shifted” distribution is quite messy.

## C.2 The Weibull Distribution

In the special case of  $\gamma = \alpha - 1$  the Gamma distribution is called a Weibull distribution. This distribution was first used in 1939 by Waloddi Weibull as an empirical description for the distribution of the strength of materials to failure. Since then, the distribution has had a widespread use in many fields outside of engineering mechanics, e.g., to describe the mass distribution of crushed materials (Brown & Wohletz 1995), to describe the distribution of the force amplitudes exerted by ocean waves onto swimming platforms and oil rigs (Gran 1992, section 3.7.5), to describe the distribution of wind speeds to produce building codes (Whalen 1996), and many others.

The probability density of the Weibull distribution is given by

$$P_{\text{W}}(x; \alpha, \beta, x_1) = \begin{cases} \left(\frac{\alpha}{\beta}\right) \left(\frac{x-x_1}{\beta}\right)^{\alpha-1} \exp\left(-\left(\frac{x-x_1}{\beta}\right)^\alpha\right) & \text{for } x > x_1 \\ 0 & \text{for } x \leq x_1 \end{cases} \quad (\text{C.9})$$

where  $\alpha, \beta > 0$ . In many applications, the “threshold” or “location parameter”  $x_1$  is implicitly set to zero (as has been done for the generalized Gamma distribution above). For  $\alpha > 1$  the Weibull distribution looks similar to an asymmetric “bell curve”, while

for  $\alpha < 1$  the distribution resembles an exponentially decaying function. Since  $\alpha$  determines the shape of the distribution, it is often called the “shape parameter”. The parameter  $\beta$  is called the “scale parameter” since for a given  $\alpha$  the variance of the distribution is uniquely defined by  $\beta$ :

Using the equations from above it is easy to see that the first moment of  $P_W$  is given by

$$\langle x \rangle = \int_{-\infty}^{+\infty} x P_W(x; \alpha, \beta, x_1) dx = x_1 + \beta \Gamma \left( 1 + \frac{1}{\alpha} \right) \quad (\text{C.10})$$

and the second moment is

$$\langle x^2 \rangle = \int_{-\infty}^{+\infty} x^2 P_W(x; \alpha, \beta, x_1) dx = \beta^2 \Gamma \left( 1 + \frac{2}{\alpha} \right) + 2\beta x_1 \Gamma \left( 1 + \frac{1}{\alpha} \right) + x_1^2 \quad (\text{C.11})$$

so that the variance of the distribution is

$$\text{Var}(x) = \langle x^2 \rangle - \langle x \rangle^2 = \beta^2 \left( \Gamma \left( 1 + \frac{2}{\alpha} \right) - \Gamma \left( 1 + \frac{1}{\alpha} \right)^2 \right) \quad (\text{C.12})$$

For other properties of the Weibull distribution, see Gran (1992).

## List of Abbreviations

ADAF	: Advection Dominated Accretion Flow	LAC	: Large Area Counter
ADC	: Accretion Disk Corona	LMC	: Large Magellanic Cloud
AGN	: Active Galactic Nucleus	LMXB	: Low Mass X-ray Binary
ASCA	: Advanced Satellite for Cosmology and Astronomy	LP	: Large Particle
ASM	: All Sky Monitor	LSSM	: Linear State Space Model
BBXRT	: Broad Band X-Ray Telescope	MC	: Monte Carlo
BHC	: Black Hole Candidate	MIT	: Massachusetts Institute of Technology
BH	: Black Hole	MPE	: Max Planck Institut für Extraterrestrische Physik
CASS	: Center for Astrophysics and Space Sciences	NASA	: National Aeronautics and Space Administration
CGRO	: Compton Gamma-Ray Observatory	NLMC	: Non-Linear Monte Carlo
COMPTEL	: Compton Telescope	NSF	: National Science Foundation
DAAD	: Deutscher Akademischer Austauschdienst	NS	: Neutron Star
DARA	: Deutsche Agentur für Raumfahrtangelegenheiten	OSSE	: Oriented Scintillation Spectrometer Experiment
DFT	: Discrete Fourier Transform	PCA	: Proportional Counter Array
EDS	: Experiment Data System	PCU	: Proportional Counter Unit
EUVE	: Extreme Ultraviolet Explorer	PHA	: Pulse Height Analyzer
EW	: Equivalent Width	PSD	: Power Spectrum Density
FITS	: Flexible Image Transport System	PSPC	: Position Sensitive Proportional Counter
FWHM	: Full Width at Half Maximum	QPO	: Quasi-Periodic Oscillation
GOF	: Guest Observers Facility	RAM	: Random Access Memory
GRT	: General Theory of Relativity	RMF	: Response Matrix Function
GSFC	: Goddard Space Flight Center	ROSAT	: Röntgensatellit
HEAO	: High Energy Astrophysics Observatory	RXTE	: Rossi X-ray Timing Explorer
HEASARC	: High Energy Astrophysics Archive	SAA	: South Atlantic Anomaly
HEXE	: High Energy X-ray Experiment	SOF	: Science Operations Facility
HEXTE	: High Energy X-ray Timing Experiment	SXT	: Soft X-ray Transient
HMXB	: High Mass X-ray Binary	TDRS	: Tracking and Data Relay Satellite
HRI	: High Resolution Imager	TTM	: Coded Mask Imaging Spectrometer
HST	: Hubble Space Telescope	UCSD	: University of California at San Diego
IAAT	: Institut für Astronomie und Astrophysik Tübingen	VLE	: Very Large Event
ISM	: Interstellar Medium	WWW	: World Wide Web
IUE	: International Ultraviolet Explorer	XRB	: X-ray Binary



## Acknowledgements

Many people have directly or indirectly contributed to this thesis. I thank all of them for their help, but first and foremost I want to thank Jim Dove for being the best collaborator I could possibly find. May our collaboration continue for many years!

This thesis would also not be possible without the excellent environment provided by the X-ray astronomy group of the Institut für Astronomie und Astrophysik, for which my advisor Rüdiger Staubert is to “blame” for.

In the past years, my “second home” has been the theory group of Mitch Begelman at JILA in Boulder, whom I thank for his hospitality and support.

My “post docs” Michael Maisack and Michael Nowak taught me the little (?) tricks on how to do research, analyze data, and that a life doing research is fun!

Boris Stern was responsible for writing the NLMC code on which many of the computations of this thesis are based.

Big thanks also go to all the members of the RXTE group in Tübingen for their valuable input (and for their patience . . . ), namely Ingo Kreykenbohm, Peter Kretschmar, Katja Pottschmidt, and Beate Stelzer.

I’m grateful to Duane Gruber, Biff Heindl, and Richard Rothschild for their help and tips concerning the analysis of HEXTE data as well as for their hospitality during my two trips to San Diego.

The analysis of the PCA data was only possible because of the new response matrices provided by Keith Jahoda.

For useful discussions, tips, hints, data, coffee, comments on this thesis, providing code, etc., I thank Keith Arnaud, Steffen Blum, Stefan Dreizler, Ralf Geckeler, Michael König, Markus Kuster, Heinz Lenhart, Phil Maloney, Thomas Rauch, Chris Reynolds, Roland Speith, and Brian Vaughan, as well as all the people at the RXTE help desk and at IAAT, Astronomie, who haven’t been mentioned yet.

“Jugend forscht” got me started into research and the “Studienstiftung des deutschen Volkes” financed many of my books – I thank both institutions for the moral and financial support and hope that they will be able to continue their important work for a long time.

Very often it is forgotten that research is very expensive. I thank the tax payers in Germany and the USA for financing this research, through a salary provided by DARA and through travel funding provided by the DAAD, DARA, the Studienstiftung des deutschen Volkes, NASA, and the NSF. This research has made use of data obtained through the HEASARC online service provided by NASA GSFC, of results provided by the ASM/RXTE teams at MIT and by the RXTE SOF and GOF at GSFC, and of data obtained through the IUE VILSPA data server, operated by ESA.

Finally, the last place in this list of people belongs to Stefanie Kölbl for her patience with me while I spent 25% of the last three years away from her, and for understanding that doing research will never be a 8:00 to 5:00 job.

## Lebenslauf

- 28.04.1969: geboren in Tübingen  
 1975-1976: Grundschule Wurmlingen  
 1976-1979: Eduard-Mörrike Schule, Kirchheim/Teck (Ötlingen)  
 1979-1985: Ludwig-Uhland-Gymnasium, Kirchheim/Teck  
 1985-1988: Schloßgymnasium Kirchheim/Teck  
 1988: Bundessieger "Jugend forscht", Fachgebiet Geo- und Raumwissenschaften  
 1988: Abitur  
 08.1988-09.1988: Dornier System GmbH (Friedrichshafen): Entry-Simulationen für den Huyghens Titan Entry (Phase A Studie)  
 12.1988-08.1990: Zivildienst (Deutsches Rotes Kreuz, KV Stuttgart)  
 08.1990-09.1990: Dornier GmbH (Friedrichshafen): Entry-Simulationen für MARSNET  
 10.1990-04.1996: Eberhard-Karls-Universität Tübingen, Studium der Physik  
 08.1991: ESA/ESOC (Darmstadt): Atmosphere Models for MARSNET  
 10.1991-05.1993: wissenschaftliche Hilfskraft, Wilhelm Schickard Institut, Universität Tübingen  
 06.1993-05.1994: University of Colorado, Boulder, graduate school (astrophysics)  
 06.1993-05.1994: Teaching Assistent, APAS, Boulder  
 06.1994-07.1994: Research Assistent, JILA, Boulder  
 09.1994-04.1996: wissenschaftliche Hilfskraft, Institut für Astronomie und Astrophysik, Tübingen  
 06.1995-07.1995: Research Assistent, JILA, Boulder, CO  
 08.1995-03.1996: Diplomarbeit unter Anleitung von Herrn Prof. Dr. R. Staubert: "Reprozessierung von Röntgenstrahlung in galaktischen und extragalaktischen Röntgenquellen"  
 04.1996: Diplom  
 05.1996- : wissenschaftlicher Angestellter, IAA Tübingen,  
 05.1996-01.1998: Anfertigung der Dissertation mit dem Titel "X-Rays from Galactic Black Holes – Theory and Observation" an der Universität Tübingen, Institut für Astronomie und Astrophysik, Abt. Astronomie, unter Anleitung von Herrn Prof. Dr. R. Staubert  
 07.1997-08.1997: Visiting Member, JILA, Boulder

Meine akademischen Lehrer waren die Professoren, Dozenten und Dozentinnen Dres.

*Angewandte Physik:* K. Gaukler, H. Lichte

*Astronomie und Astrophysik:* M. Begelman, E. Ellingson, A. Hamilton, E. Haug, H. Mauder, R. McCray, H. Ruder, J. Shull, R. Staubert, J. Toomre, K. Werner

*Experimentalphysik:* M. Baumann, M. Brendle, H. Clement, W. Hartmann, R. Hübner, O. Lutz, G. Mertens, W. Nakel, G. Staudt

*Geschichte der Naturwissenschaften:* M. Schramm

*Informatik:* U. Güntzer, H. Klaeren, R. Loos

*Mathematik:* H. Kaul, M. Mathieu, M. Wolff, A. Wörz

*Theoretische Physik:* M. Goldman, H. Müther, H. Reinhardt, H. Wittern



This thesis was typeset in  $\text{\LaTeX}$  by J. Wilms in Bitstream Aldine 401BT (Bembo), Adobe Helvetica, and Computer Modern Typewriter.